UNIVERSITÀ DEGLI STUDI DI MILANO

DEPARTMENT OF CHEMISTRY

PHD SCHOOL IN INDUSTRIAL CHEMISTRY
CYCLE XXXIV

A detailed study of protein – supported phospholipid bilayer systems as model interfaces to investigate biomembrane interactions

PhD Thesis of
Matteo Giannangeli

Tutor: Prof. A. Caselli
Co-Tutor: Prof. A. Podestà

Academic year 2021-2022

Aim of the thesis

The work of this thesis results from an interdisciplinary collaboration involving the Departments of Chemistry, Physics, and the Biosciences at the University of Milan. The activity developed around three correlated subjects.

The main research topic was in the frame of the noMAGIC project (Noninvasive Manipulation of Gating in Ion Channels), an ERC project coordinated by the Prof. Anna Moroni, aimed at creating the first engineered potassium ion channel that can be regulated by the application of a magnetic field. The obtained magneto-genetic tool allows regulating the activity of ion channels overcoming the main drawbacks of optogenetics paving the way to important research applications. The debate on the mechanism that triggers the gating of such channels is still open and significant efforts focus on shedding light on it. In the context of this ERC project, ferritins are key components of the ion channel construct.

A significant part of this thesis was devoted to characterizing ferritins by atomic force microscopy under the supervision of Prof. Alessandro Podestà. To the best of our knowledge, although ferritins have been intensively studied with a variety of techniques, the ferritin from *Pyrococcus furiosus*, that has been selected for this study, was never observed by AFM. This investigation aims at providing details about the morphological features of this protein, as well as information about its aggregation state which are important features to support the creation of the engineered construct.

The second part of the work was aimed at studying, by AFM, the mechanisms involved in the cytotoxicity of imidazolium-based ionic liquids. Indeed, several studies have shown that ionic liquids can be toxic at a given concentration. In particular, the mechanisms involved in the interaction between ionic liquids and phospholipid bilayers were investigated at the microscopic level to improve the understanding of the dynamics related to the toxicity of these compounds. To this purpose, nanomechanical measurements were carried out by AFM on a phospholipid bilayer supported on mica, incubated at various concentrations of two different ionic liquids: 1-Butyl-3-methylimidazolium chloride ([Bmim][Cl]) and 1-Methyl-3-octylimidazolium chloride ([Omim][Cl]). They were chosen to study the effect of the length of the cationic alkyl chain (respectively of 4 and 8 carbon atoms) on the stability of the bilayer. A synthesis protocol was also developed for the functionalization of an AFM probe capable of mimicking the alkyl chain of the imidazole cation of the ionic liquid [Omim][Cl]. This probe was then used in force spectroscopy experiments to investigate the interactions between the alkyl chain and the phospholipid bilayer.

The third part of this thesis focuses on the synthesis and characterization of compounds with interesting photophysical properties. In particular, novel push–pull isoquinolines and their alkynyl precursors, with potential application as polarity-sensitive fluorescent probes or advanced functional materials were introduced.

Compounds containing an extended π-system such as 2-alkenyliden-indolin-3-ones were synthesized in high yields via a cascade reaction between 4H-furo[3,2-*b*]indoles and propargyl esters in the presence of gold(I)-carbenes. Their intense coloration (from yellow to purple) was characterized by UV measurements.

Finally, it has been demonstrated that a catalytic system comprising Cu(I) and a pyridine-containing ligand (PcL) can be efficiently and selectively used in the transformation of several differently

substituted 2-alkenylidene-3-oxoindolines. Two compounds synthesized by this approach are characterized by a second-order nonlinear optical response higher than that of Disperse Red One which found application in electrooptic polymeric poled films.

Chapter 1. Introduction

1.1. Supported lipid bilayer as a model of cell membrane

1.1.1. The Cell

Cells can be defined as the "building blocks of life"[1]. They are the smallest unit of life and constitute all living structures in living organisms. They are complex structures, and the health of living beings depends from their integrity and physiology. For instance, substances that modify the structure and robustness of the cell membrane can be extremely harmful for the living organisms. Likewise, the proper functioning of all components of the cell, such as organelles and transmembrane proteins, is a fundamental requirement for life. Due to their relevance, in the next paragraphs are debated and examined in depth some of the crucial components for the survival of the species. To study these structures, a variety of techniques can be applied and are described in the second part of this introduction.

Cells can be divided into eukaryotic and prokaryotic; the former contains a nucleus while the latter does not, although a nucleoid region is still present. However, eukaryotic or prokaryotic cells are constituted by a membrane (called plasma membrane or cell membrane) enclosing the cytoplasm.

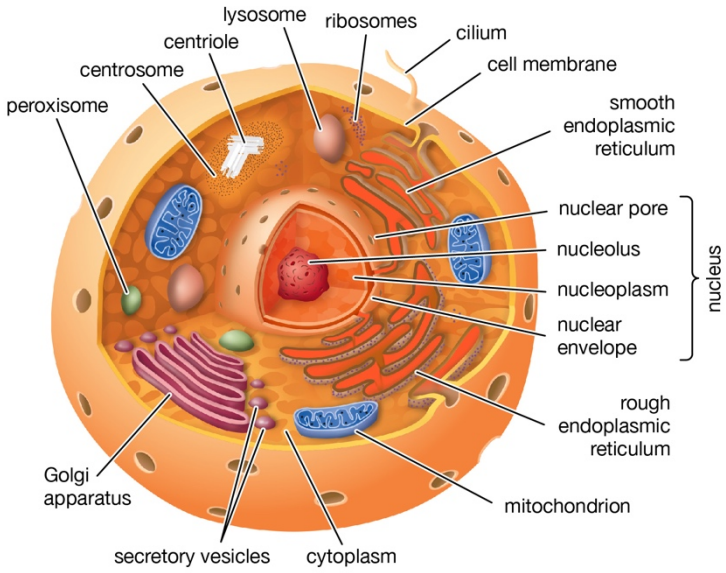

Figure 1 Representation of an eukaryotic cell. Image adapted from Encyclopaedia Britannica (*https://www.britannica.com/science/eukaryote#/media/1/195150/112877)*

The cytoplasm, in turn, is constituted by different organelles embedded by the cytosol, a liquid matrix that contains many molecules and ions involved in cell functions. The organelles are any structure inside a cell that carries out a metabolic function. There is a variety of them, each with a specialized function. Some organelles are separated from the cytosol by membranes similar in structure to the plasma membrane, while others, such as centrioles and free ribosomes, do not have a membrane. An example of a eukaryotic cell containing the primary organelles and internal structures is shown in Figure 1. Mitochondria are involved in the cellular energy production in the form of ATP by oxidative phosphorylation. They occur in various numbers, sizes, and shapes in all eukaryotic cells. Chloroplasts are found only in plants and algae and are involved in photosynthesis. There are different types of vesicles, such as transport vesicles, peroxisomes, and lysosomes, that are small round membrane-enclosed structures. Peroxisomes, for example, are enzymes that catabolize fatty acids and some chemical toxins, surrounded by a lipid bilayer. Lysosomes, instead, contain digestive enzymes in an acidic environment. Ribosomes are a complex of RNA and protein molecules and are involved in the synthesis of proteins. These proteins are then processed and packaged by the Golgi apparatus.

As mentioned above, the eukaryotic cells possess a nucleus, which is separated from the cytoplasm by a nuclear envelope. It contains the DNA that codes for proteins necessary for the cell to function.

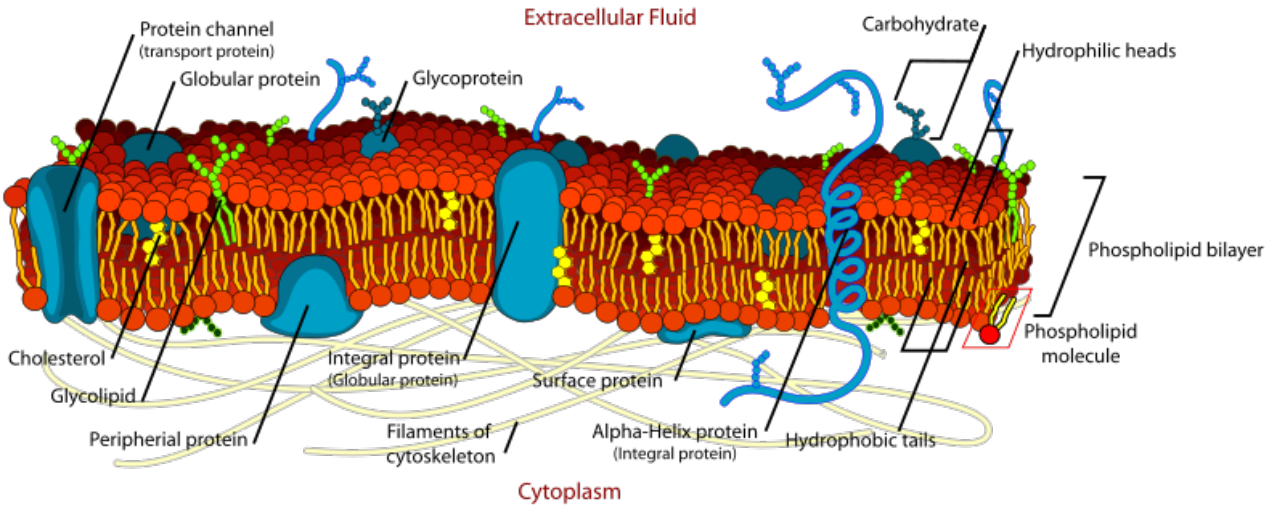

Figure 2 Schematic representation of the structure of the cell membrane. Image by Mariana Ruiz [Public domain], via Wikimedia Commons

In the prokaryotic cell, which has a more primitive structure, the DNA is concentrated in the nucleoid region.

All fluid contained in cytosol, organelles, cytoskeleton and nucleus (in the case of eukaryotic cells) constitute the intracellular fluid (ICF), separated from the environment outside the cell (extracellular fluid, ECF) by the cell membrane.

1.1.2. The Cell membrane

The cell membrane allows the maintenance of the intracellular content compatible with the work and life needs of the cell itself or its constituents thanks to precise and often specific properties of permeability and capacity to transport ions and nutrients. These latter properties also influence the distribution of chemicals between the extra- and intracellular space and between the cytoplasm and intracellular structures. Therefore, biological membranes perform the mechanical function of protecting the cell and are involved in many fundamental activities for the cell itself such as, for example, the recognition of foreign material which is a fundamental phenomenon to the basis of immune recognition processes.

All membranes have the same basic composition consisting of a phospholipid bilayer in which proteins, almost always glycosylated, and other molecules are immersed. These species confer to the cell a specific function that depends on the characteristic of the membrane to which they are linked by non-covalent bonds (Figure 2). The lipid double layer comprises hundreds, if not thousands, of different phospholipid species. Its structure and features are discussed below. Half of the total cell membrane mass, on the other hand, is constituted by proteins that can be of two types: peripherals or integrals. The former are arranged on both membrane faces and can be linked to it through lipid anchors or electrostatic interactions, while the latter penetrate the membrane for a short distance or cross it completely via the transmembrane domain.

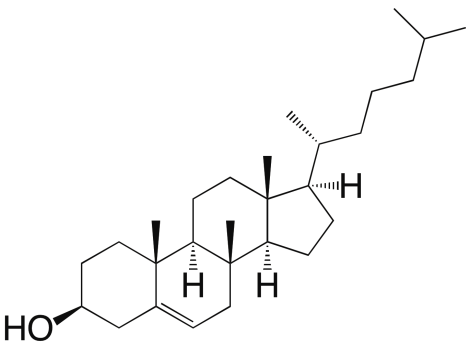

Figure 3 Chemical structure of the cholesterol.

Other lipids and fatty acid species add to this complexity. Of those, sterols (cholesterol in mammals) are the most

abundant in the plasma membrane and can represent up to 40% of total lipid[2]. The structure of cholesterol strongly impacts membrane properties such as viscosity or interleaflet coupling, as described multiple times in comprehensive articles[3,4,5]. Cholesterol indeed is a molecule characterized by the central cyclic structure of the steroid, flat and rigid, in which there is a polar head group (hydroxyl residue) on one side and an apolar hydrocarbon tail group on the other (Figure 3). The bilayer is oriented with the hydroxyl groups close to the polar head groups of the phospholipid molecules. In this position, its rigid, plate-like steroid rings interact with – and partly immobilize – those regions of the hydrocarbon chains closest to the polar head groups. This decrease of the mobility of the first few CH_2 groups of the hydrocarbon chains of the phospholipid molecules makes the lipid bilayer less deformable in this region and thereby decreases the permeability of the bilayer to small water-soluble molecules. Although cholesterol makes lipid bilayers less fluid, at the high concentrations found in most eukaryotic plasma membranes, it also prevents the hydrocarbon chains from coming together and crystallizing. In this way, it inhibits possible phase transitions.

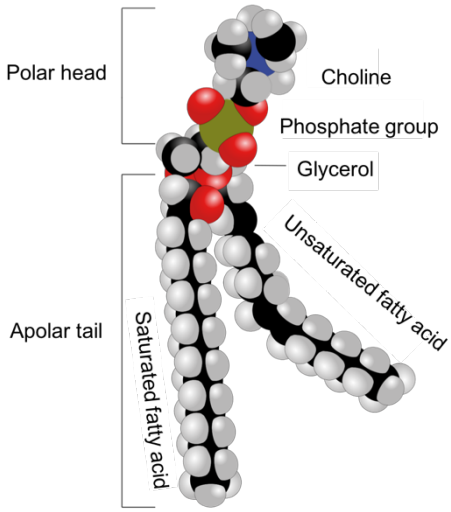

Figure 4 Chemical structure of a phospholipid. Image adapted from Wikipedia (https://it.wikipedia.org/wiki/Fosfolipide#/media/File:Fosfolipide.svg)

In addition to permeability, there are other essential membrane properties, such as fluidity and viscosity. Fluidity is one of the more critical membrane features. It enables the majority of molecules to diffuse over long distances and rotate or re-orientate to adopt optimal conformation. Thus, cells can modify the saturation of their lipid acyl-chains to keep their membranes fluid when adapting to the environment, e.g., different temperatures [6,7]. Indeed, the lipid bilayer fluidity depends on its composition, as it has been demonstrated by studies with synthetic bilayers. A lipid bilayer made of a single type of phospholipid can undergo a *phase transition* (i.e., a change from a two-dimensional rigid crystalline - or gel - state to a liquid state) at a specific temperature. The length and unsaturation number of the hydrocarbon chains influence the temperature of the *phase transition.* A shorter chain length reduces the tendency of the hydrocarbon tails to interact with one another, and *cis*-double bonds produce kinks in the hydrocarbon chains that make them more difficult to pack together so that the membrane remains fluid at lower temperatures. Bacteria, yeasts, and other organisms whose temperature fluctuates with that of their environment adjust the fatty acid composition of their membrane lipids to maintain a relatively constant fluidity. For instance, after a decrease of the temperature, fatty acids with more *cis*-double bonds are synthesized, so the decrease in bilayer fluidity that would otherwise result from the drop of temperature is avoided.

Cell membranes have a certain level of viscosity too (higher than the cytosol[8]) and this influences the mobility of membrane molecules. Membrane viscosity can be modified by the presence of proteins or poorly mobile structures and will thus vary over space.

1.1.3. The lipid bilayer

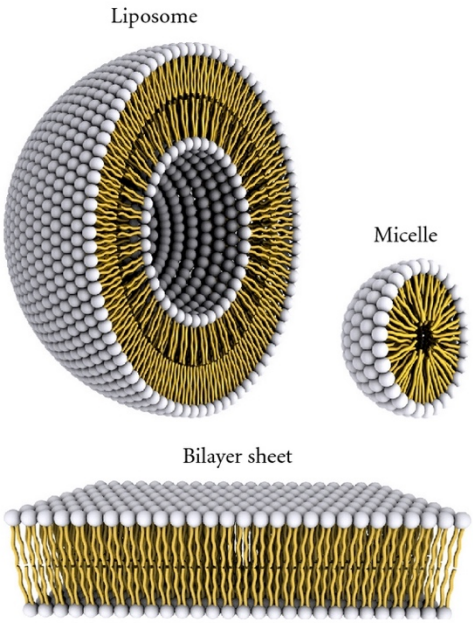

Figure 5 Possible structures of phospholipids in an aqueous environment. Image adapted from *Bitounis D, Fanciullino R, Iliadis A, Ciccolini J. Optimizing Druggability through Liposomal Formulations: New Approaches to an Old Concept. ISRN Pharm. 2012;2012(February):1-11. doi:10.5402/2012/738432*

As anticipated, phospholipids are the most abundant lipids in the membrane. These molecules are constituted by a polar head group and two hydrophobic hydrocarbon tails (Figure 4). The polar head contains a variously substituted phosphate group (typical residues are: choline, serine, ethanolamine, and inositol). The hydrophobic tails are usually fatty acids, and they can differ in length (generally from 14 and 24 carbon atoms). One tail usually has one or more unsaturation (*cis*-double bond), while the other is saturated. Each double bond creates a small kink in the tail. As already discussed, differences in the length and saturation of the fatty acid tails are important because they influence the ability of phospholipid molecules to pack against one another, thereby affecting the membrane's fluidity. The amphipathic character of these molecules is responsible for the self-aggregation properties of the bilayer. When phospholipids are dispersed in water, spontaneous aggregates in which the polar heads are exposed towards the aqueous environment are formed while hydrophobic tails are buried in the interior to minimize the free energy cost. Three types of aggregates can be obtained: micelles, bilayers, and liposomes (Figure 5).

Micelles are spherical structures in which the lipid molecules are arranged with the hydrophobic regions grouped within the sphere and with the polar heads exposed on the surface in contact with the aqueous environment.

In the double layer, two monolayers (sheets) form a two-dimensional sheet. In each monolayer, the hydrophobic parts, excluded from the water, interact with each other. The polar heads are in contact with water on both sides of the bilayer. Since the double layer has its edges still exposed to water, this structure is unstable and spontaneously forms a third type of lipid aggregate: it folds on itself, generating a sphere called vesicle or liposome. In this way, the double layer loses the exposed hydrophobic edges and acquires maximum stability in the aqueous environment.

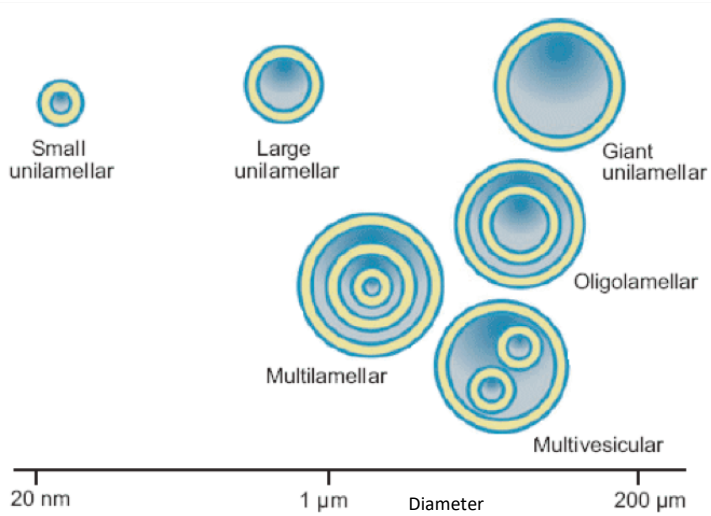

Figure 6 Schematic representation of various types of liposomes. Image adapted from *Rani DT. Liposomes as a potential drug delivery system: a review. Int Res J Pharm. 2013;4(1):6-12.*

Liposomes are hollow microspheres formed by one or more lipid double layers.

Since the 1970s, liposomes have been used - as an experimental form - as drug vehicles. Typically, when the they reach a target membrane, they adhere to it, disintegrating on the cell surface with simultaneous entry into the cytoplasm of the trapped substances.
Liposomes vary in size between 50 and 1000 nm and, as shown in Figure 6; they are classified according to their diameter (ultra-small, small, medium and large) and their structure (unilamellar, multilamellar, multivesicular vesicles).
The main phospholipids involved in forming the lipid bilayer in many mammalian cell membranes are *phosphatidylcholine (PC), phosphatidylethanolamine (PE), phosphatidylserine (PS),* and *sphingomyelin (SPH)*. Note that only phosphatidylserine carries a net negative charge while the other three are electrically neutral at physiological pH, carrying one positive and one negative charge. Together these four phospholipids constitute more than half the mass of lipid in most membranes. Other phospholipids, such as the *inositol phospholipids,* are present in smaller quantities but are functionally important. The inositol phospholipids, for example, have a crucial role in cell signaling.

1.1.4. Supported lipid bilayer

Phospholipid bilayers closely resemble cell membranes in some key respects. For example, they retain two-dimensional fluidity and can be an excellent environment for presenting membrane proteins. For this reason, they are considered a suitable model of cell membrane: model bilayer systems allow for the investigation of biological processes that occur at the cellular level, providing information about ligand–receptor interactions[9,10,11,12], viral attack[13], and cellular signaling events[14,15,16]. Furthermore, it is a simplified model due to the lack of numerous proteins and other molecules that compose the cell membrane. A widespread system used as a cell membrane simplified model is the supported lipid bilayer (SLB), in which the lipid molecules lie on a solid substrate (Fig 7).

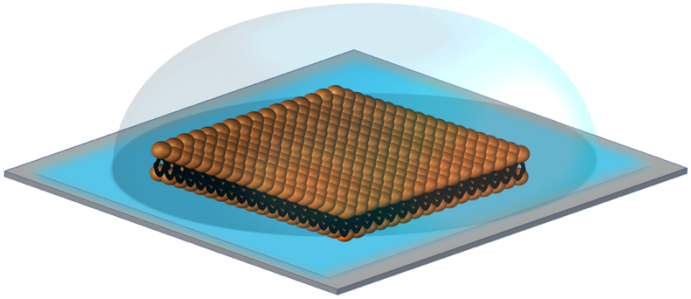

Figure 7 Supported lipid bilayer.

SLBs are more robust and stable with respect to other phospholipid bilayers such as liposomes. Moreover, the solid support also opens the door for using surface-specific analytical techniques, such as AFM.
In these systems, membrane fluidity is maintained by a 10–20 Å layer of trapped structured water between the substrate and the bilayer[17,18]. To be able to support the phospholipid bilayers, the surface must be hydrophilic, smooth and clean. The best substrates are fused silica[17,19], borosilicate glass[17,20], mica[21], and oxidized silicon[17]. Thin films can be used as solid supports as observed with TiO_2[22,23,24], indium-tin-oxide[25,26], gold[27,28], silver[28], and platinum[29].
The formation of the SLB can be obtained in three ways[30,31]:

1. transfer of the monolayer;
2. fusion of vesicles;
3. single double layer diffusion.

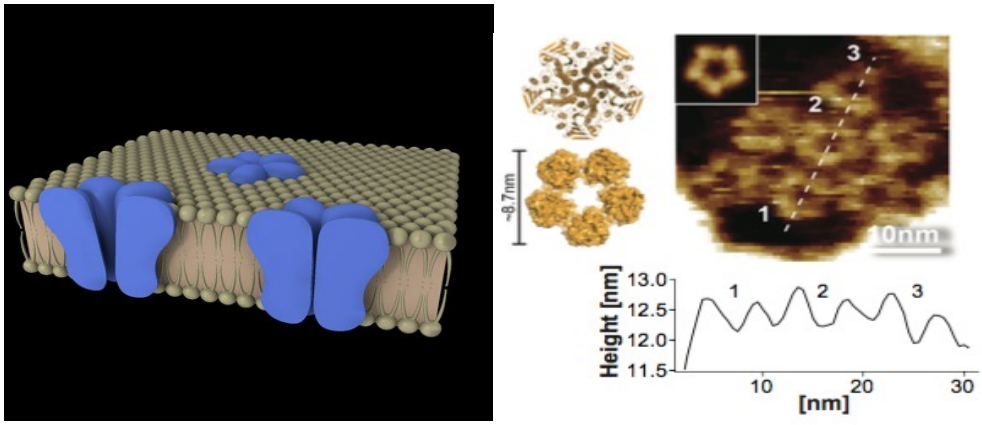

Figure 8 (left) schematic representation of an ion channel and (right) AFM micrograph and height profile of ion channels. Image adapted from *Rangl M, Schmandt N, Perozo E, Scheuring S. Real time dynamics of gating-related conformational changes in CorA. Elife. 2019;8:1-17.*

The first method uses a Teflon container containing the aqueous solution, with two movable Teflon barriers.

The Teflon barriers slowly push the film molecules to compact them and guide them towards the solid substrate. The substrate with the first leaflet is then slowly extracted. The second lipid bilayer leaflet is subsequently transferred by dipping the solid support covered with the first leaflet vertically (Langmuir-Blodgett transfer).

The transfer of the monolayer from the air-water interface of a Langmuir balance (Langmuir-Blodgett technique) is laborious but allows the deposition of asymmetrical double layers.

In the second method, lipid vesicles are deposited on the substrate by vesicular suspensions. By regulating the adhesion strength to the substrate (for example through electrostatic forces deriving from the presence of a certain percentage of charged lipids), the vesicles open and form adherent double layers that fuse into continuous double layers.

In the third method, diffusion of the single bilayer is spontaneously achieved by depositing a lipid reservoir in a solid (from an organic solution). After adding water, a single double layer is spontaneously retained on the surface by adhesion forces (if it is hydrophilic and sufficiently attractive). The double layer is continuous and self-healing because the local pores heal quickly due to the strong diffusion pressure provided by the lipid reservoir. In this thesis, we used the easily implementable vesicle fusion method. For this technique, it is essential to carry out an extrusion or sonication step of the solution to break the multi-lamellar vesicles that spontaneously form to obtain unilamellar vesicles. The rupture and fusion of the multilamellar vescicle would lead to the formation of superimposed lipid double layers.

1.2. Ion channels

A representative family of integral proteins in the cell membrane are ion channels. Ion channels are transmembrane proteins that allow the flow of ions across membranes, either cell membranes or the membranes of intracellular organelles (Fig. 8).

They are generally multimeric assemblies of three to six pore-forming subunits that possess cyclic symmetry. These subunits are arranged around the central axis that forms the pathway for ion conduction.

Ion channels are open and close in response to a range of stimuli. The main types of stimuli that are known to cause ion channels to open are a change in the voltage across the membrane (voltage-

gated channels), mechanical stress (mechanically gated channels), or the binding of a ligand (ligand-gated channels). The ligand can be either an extracellular mediator — specifically, a neurotransmitter (transmitter-gated channels) — or an intracellular mediator, such as an ion (ion-gated channels) or a nucleotide (nucleotide-gated channels). More precisely, ion channels are not continuously open. Instead, they are gated, i.e., closed, ready to open briefly and then close again. As a consequence of the channel opening and the relative flow of a specific ion (some channels are more ion-selective than others), the changes in ion distribution can activate a variety of intracellular signaling cascades. The signals generated by these proteins are among the fastest found in biological systems and occur on the timescale of tens of microseconds to hundreds of milliseconds. The flux through a channel pore can be as high as 10^9 ions per second. Other classifications that can be done of these proteins are by type the of ions passing through the pore, or by cellular classification, e.g., across the cell membrane or intracellular organelles membrane. More than one hundred types of ion channels have been described thus far, and new ones are still being added to the list. They are present in all animal cells and are found in plant cells and microorganisms. In humans, they play key roles in a plethora of cellular activities. These range from the basic function of cell volume regulation to the sophisticated control of development, cardiac rhythm generation, and neural activity. Sodium and potassium ion channels, for example, which belong to the voltage-gated ion channels class, are involved in neuron firing. In physiology, the term “to fire” is referred to a neuron that emits an action potential or a nerve impulse. The action potential contributes to the propagation of a signal along the neuron’s axon, thus permitting cell-to-cell communication. Cell membranes are characterized by a membrane potential: a (typically negative) voltage difference between the exterior and interior of the cell. A voltage-gated ion channel tends to be open for some values of potential and closed for others. In the absence of perturbations, the membrane potential is constant and is called resting potential. If the membrane potential increases, a depolarization occurs, while a potential decrease is termed hyperpolarization. When the membrane potential exceeds a certain value (threshold potential), the action potential is triggered, propagating the signal. This process, characterized by an abrupt depolarization followed by a hyperpolarization as reported in Figure 9, is permitted by the opening and closing of the ion channels.

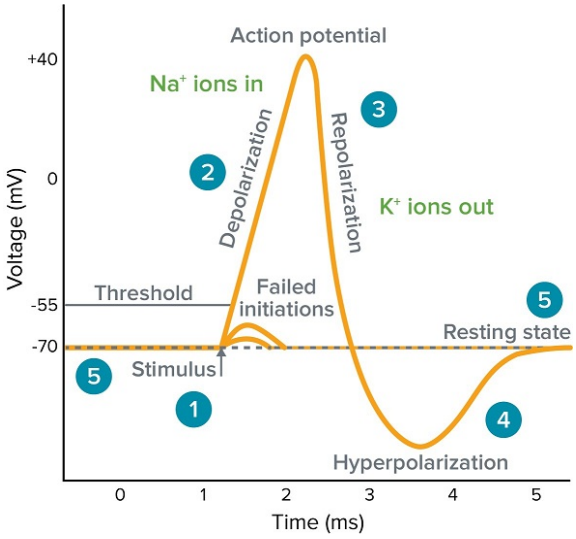

Figure 9 Diagram of the voltage vs. time during the action potential. Image adapted from https://www.moleculardevices.com/applications/patch-clamp-electrophysiology/what-action-potential

1.3. Ferritins

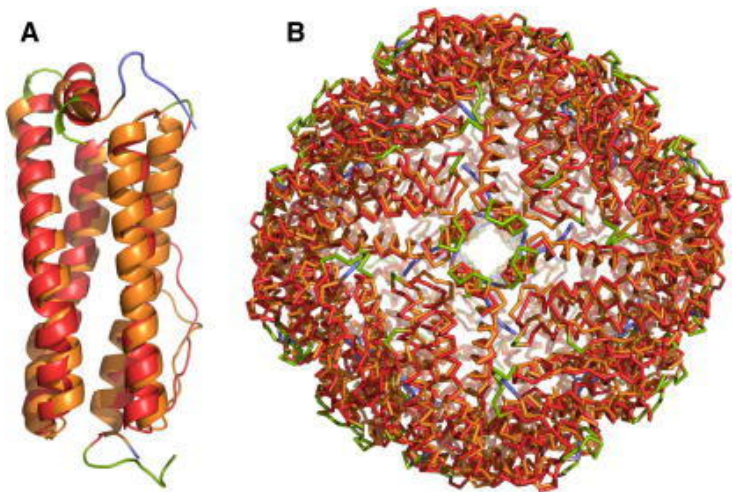

Figure 10 a) ferritin subunit and b) self-assembled ferritin..

Ferritins are iron storing proteins that can be found in animals[32], plants[33,34], and bacteria, but despite the different origins, they possess similar structures. The most extensively studied ferritin is that of horse spleen (HSF), traditionally considered the mammalian ferritin model. It consists of 24 identical subunits (~20 kDa each) that self-assemble in a roughly spherical protein (~480 kDa) with an outer diameter of about 12 nm and an internal cavity with a diameter of approximately 8 nm (Fig. 10). The protein shell has various ca. 0,3 – 0,5 nm wide channels, which connect the cavity with the surrounding environment[35]. The electrostatic potential generated by the negatively charged residues in these channels helps iron to enter and exit the protein inner cavity[36]. This space can accommodate up to 4500 iron atoms as an iron(III) mineral, traditionally described as ferrihydrite $[Fe(III)_{10}\ O_{14}\ (OH)_2]$. Indeed, the role of ferritin is to store, transport, and release iron in a controlled manner. In the brain, for example, iron is crucial for neuronal development, gene expression, enzyme function, dopamine, heme and iron–sulfur cluster synthesis, as well as electron transport. Despite its importance for life, excess iron is highly toxic. Iron(II) promotes the formation of highly reactive oxygen species (ROS), which are extremely powerful oxidizing agents capable of causing irreversible cell damage, organ failure and eventually death[37]. Therefore, both excess and deficiency of iron are harmful. Ferritin stores the excess of this metal by oxidizing Fe(II) to Fe(III); once required, iron can be recovered from the store to participate in cell metabolism. However, the behavior of ferritin is still not fully understood.

The ferroxidase activity produces hydrogen peroxide and diferric oxo/hydroxo mineral precursor[38]. The former moves away from the catalytic sites so to prevent reactions with incoming ferrous substrates, since few free radicals can be detected during the reaction[39]. The latter goes from the catalytic site to the protein cavity since minerals are formed only in the cavity. As the mineral fills the cavity, oxidation can occur at the protein catalytic sites and mineral surface. In the simplest ferritin reaction mechanism, the dioxygen bridge is retained in the hydrogen peroxide product[40]. However, the apparent protein-protein cooperativity observed during ferroxidation reactions suggests a more complex reaction pathway in which multiple catalytic sites may participate.

Reversing the biomineralization process in ferritin is very slow, emphasizing the safety of iron and oxidants stored in ferritin and reflected in the slow rates of iron removal from ferritin with chelators *in vitro*. The *in vivo* mechanism of iron release from ferritin is still undetermined. However, it has already been made patently clear that the ferroxidase centers of the H-subunits, which are central to the mechanism of ferritin's iron uptake, are not involved in the iron release. Therefore, iron uptake and release are two processes that utilize distinct pathways[41].

The ferritin superfamily can be divided into three sub-families: the classical ferritins (Ftn), the bacterioferritins (Bfr), and the DNA-binding proteins from starved cells (Dps). The Ftn and Bfr proteins are considered maxi-ferritins, whereas Dps proteins are mini-ferritins. These three sub-families share the same characteristic four-helix bundle fold[42]. The Ftn proteins are found in all three domains of life (eukarya, archaea, and bacteria). The Bfr proteins have a quaternary structure identical to the Ftn proteins, but they are restricted to bacteria and archaea. The Dps proteins form a smaller molecule with a lower iron storage capacity than Ftn and Bfr and utilize unique ferroxidase sites. The 24 polypeptide chains, that self-assembly to give the protein shell, can be classified into two types: the H (heavy) and the L (light) subunits, 21 kDa and 19 kDa, respectively that differ in functionality. Whereas the H subunit plays a key role in the rapid detoxification of iron, since it contains a catalytic ferroxidase center for rapid iron(II) oxidation, the L subunit is associated with iron nucleation, mineralization, and long-term iron storage in the ferritin cavity[43].

1.4. Ionic liquids

1.4.1. Definition and main features of ionic liquids

Ionic liquids (IL) are the most studied "green" solvents in recent decades. They are defined as organic salts which are liquid at room temperature; they consist of asymmetrical and hindered ions that make difficult the packing necessary for crystallization. Since the possible combinations between all the anion and cation are huge, the term ionic liquid identifies an enormous variety of chemical entities. The most common are cations such as imidazolium, pyridinium, quaternary ammonium and quaternary phosphonium, and of anions such as alkyl sulfate, triflate, tetrafluoroborate and hexafluorophosphate. In Figure 11 are reported the chemical formula of some cation and anion of ionic liquids.

Research in this field started in the early twentieth century when it was discovered that ethyl ammonium nitrate is liquid at room temperature.

During the sixties and seventies, ionic liquids were studied for applications in electrochemistry, while the analysis of their chemical-physical properties started more recently.

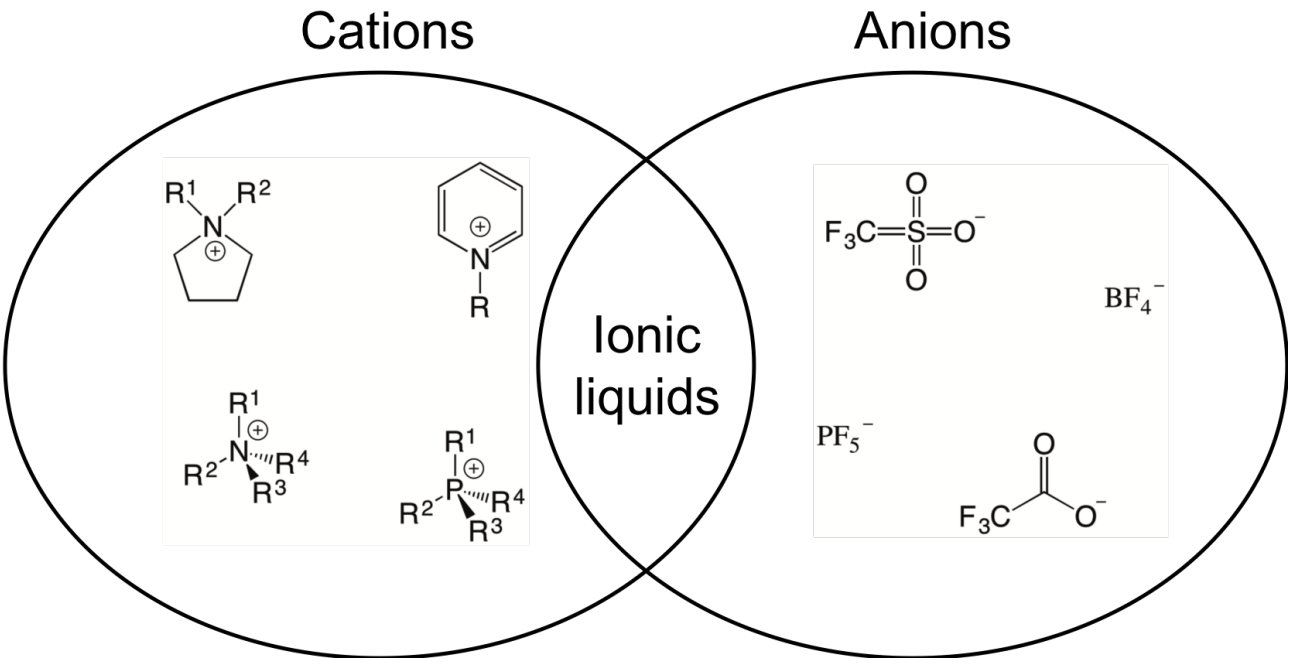

Figure 11 Chemical structure of cations and anions of ionic liquids.

Until now, the attention towards this class of solvents and compounds has mainly focused on the synthesis of substances with particular chemical-physical properties (first generation ILs), such as the absence of volatility or greater thermal stability, and on the design of new substances that possess particular properties (second generation ILs).
Interest in the synthesis of ionic liquids with specific biological properties (third generation ILs) has recently grown, becoming one of the main objectives driving the design of specific substances[44].
The choice of the cation and anion profoundly influences the chemical-physical properties of these substances, determining their toxicity towards living organisms and their persistence in the environment[45].
The main characteristics of ionic liquids are very low vapor pressure, non-flammability, non-combustibility, high thermal stability, the existence of a wide range of temperatures at which they are in a liquid state and a high ionic conductivity.
Some physico-chemical properties of these compounds, such as being liquid at room temperature and almost zero vapor pressure, avoid the release into the atmosphere, unlike many organic solvents commonly used in the synthesis of chemical products and other industrial applications[46].

1.4.2. Industrial application of ionic liquids

In 2002, BASF developed the Basil process (Biphasic Acid Scavenging utilizing Ionic Liquids), which exploits the properties of ionic liquids on an industrial scale. During a step of the synthesis of alkoxyphenylphosphines, raw materials in the production of lucirins (photo-initiators in the protection of inks from exposure to ultraviolet light), the released hydrochloric acid is neutralized with methylimidazole forming the ionic liquid methylimidazolinium chloride.
IoLiTec developed another interesting application for the electronics industry in the field of surface cleaning; this treatment can be particularly difficult since charged particles, often metallic, must be eliminated.The ionic liquids used in the process form a thin sheath adhered to the surfaces to be cleaned which allows the removal of particles without forming crusts.
In recent years, research has paved the way for the use of ionic liquids in the treatment and dissolution of cellulose, the most abundant organic polymer of natural origin. Cellulose can be dissolved in very few organic solvents, such as NMNO (N-methylmorpholine N-oxide), and is industrially processed and recovered with large amounts of acid and basic, such as in the Lyocell process® or in the treatment of ink removal (deinking).
Some ionic liquids, such as imidazolinium and pyridinium salts with chlorides and acetates as anions, are instead able to effectively solubilize the cellulose pulp, which can then be recovered by dilution with water[47]. Ionic liquids have also been used in the manufacture of liquid mirrors for telescopes, allowing to avoid the use of mercury[48]; other promising applications concern the field of third generation photovoltaics, where they are studied and used as electrolytes[49].
Finally, recently, new types of “reversible” ionic liquids called “switchable solvents” have found interesting applications. These solvents, generally consisting of combinations of amines with alcohols or water, can be converted from a nonpolar form, suitable for the extraction of lipophilic substances, such as vegetable oils, into a polar ionic form consisting of ammonium carbonate, simply by adding and removing CO_2. Thus, the lipophilic compounds can be recovered and the solvent recycled[50].

The use of ionic liquids on an industrial scale faces the scientific world with the problem of determining the risk related to the use of these compounds.
In fact, despite the “green” features mentioned above, many ionic liquids have proved to be eco-problematic, as evidenced by the numerous eco-toxicological studies in recent years[51–54].

1.4.3. Toxicity of ionic liquids

Recent studies have highlighted the importance of designing ionic liquids considering their toxicological and eco-toxicological aspects, particularly the release into the environment, biodegradability, and biological activity.
Toxicity studies carried out on simple biological systems such as fungi, bacteria, algae, terrestrial plants or on more complex systems such as fish, mammals, and amphibians[55–58], have shown that ionic liquids could be harmful to aquatic, and terrestrial organisms and a linear relationship was found between the lipophilicity of cation and the toxic effects of ionic liquids.
Other studies have been performed on the effect of ILs on cellular and subcellular structures at different biological levels, using different cell lines at various exposure conditions[59–62]. In all cases, at different levels of biological organization, using cells or whole organisms as a target, an increase in the lipophilicity of the cation is corresponded to an increase in toxicity.
For example, in alkyl methylimidazolinium salts the presence of a carbon side chain (C12 MIM) increases toxicity by three orders of magnitude compared to a chain with 4 carbon atoms (C4 MIM) [63]. Also, the structure of the cation plays an important role: aromatic heterocyclic cations, such as imidazolinium or pyridines, are more toxic than cyclic aliphatic cations, such as morpholins and sulfonium salts, which are practically harmless. Long-chain phosphonium and quaternary ammonium salts, similar to cationic surfactants, are both highly toxic. On the other hand, the influence of the anion on the toxicity of a series of imidazolinium salts was found to be low. One of the ways how the toxicity of a substance towards cellular structures can be expressed is through non-specific interactions with the lipid structures of the membrane itself. Therefore, given that the cytotoxicity of ionic liquids is closely correlated with their lipophilicity, some works have focused on studying their interaction with cell membranes to identify the microscopic mechanism underlying their toxicity in in pharmacology, biomedicine, and more generally in bio-nanotechnology. Nevertheless, the detailed mechanism has not yet been fully elucidated and represents one of the main objectives in understanding ionic liquids' toxicity mechanisms.

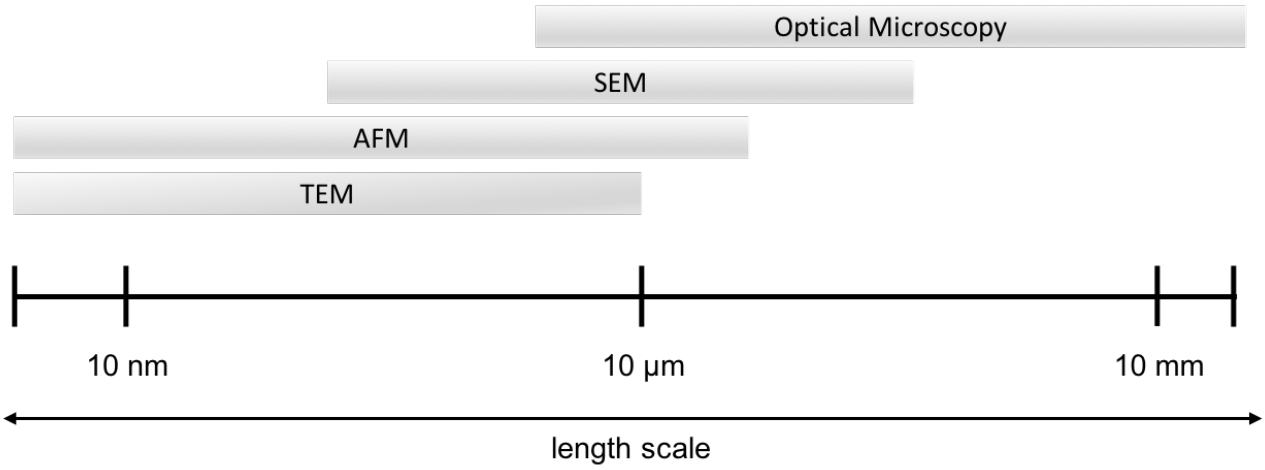

Figure 12 Comparison of lenght-scale of various microscopes.

1.5. Microscopy techniques

Except for some egg cells, the majority of cells require magnification under a microscope to be observed. A typical animal cell indeed is 10 - 50 µm in diameter, which is about one-fifth the size of the smallest particle visible to the naked eye. Microscopy can be divided into three main branches: optical, electronic, and scanning probe microscopy. Figure 12 compares the imaging ranges of different types of microscopies. The human eye can distinguish objects down to a tenth of a millimeter while Optical microscopy reaches one micrometer. In contrast, electron microscopy as well as the various types of scanning probe microscopy (SPM), such as scanning tunneling microscopy (STM) and atomic force microscopy (AFM), provide resolution in the atomic range. In addition to the resolution limits, other characteristics must be considered, such as the time to obtain an image, the contrast mechanisms (topography, chemical contrast, etc.), the surface sensitivity, the working environment (ambient, vacuum, liquid). Also, the price of the microscope and its ease of use are important parameters.

As well as every analytical method, each microscopy technique has its advantages and disadvantages for a particular application. For instance, while SPM is the method of choice if surface sensitivity is needed, TEM is the best choice if features below the surface area must be imaged. And again, for quick imaging down to the nanoscale, SEM should be used. In the next paragraphs, different types of microscopes are discussed.

1.5.1. Optical microscopy

The optical microscope, also called light microscope, uses visible light transmitted through, refracted around, or reflected from a specimen. The magnification of an object is obtained with a system of lenses and, in particular, it depends on how much the lenses bend the light waves[64].

However, magnification is not the only important parameter in microscopy: another crucial aspect is the limit of resolution. It is the ability to distinguish two separate points or objects as independent. The resolution of a microscope provides a measure of the level of detail it can be used to reveal. As a general rule, a given type of radiation cannot be used to probe structural details much smaller than its own wavelength. Indeed, the limit of resolution of an optical microscope, i.e., the minimum distance at which two points can be resolved, is 0.2 µm (under the best conditions). This is related to the optical diffraction effect: when light waves move through an optical system, they interfere with each another. They can be *in phase,* with crests and troughs matching, thus reinforcing each other, or *out of phase*, interfering in such a way as to cancel each other partly or entirely. When light interacts with an object, a change of the phase relationship occurs producing complex interference effects. At high magnification, for example, a circular spot appears as a set of concentric rings. For the same reason, a single point seen through

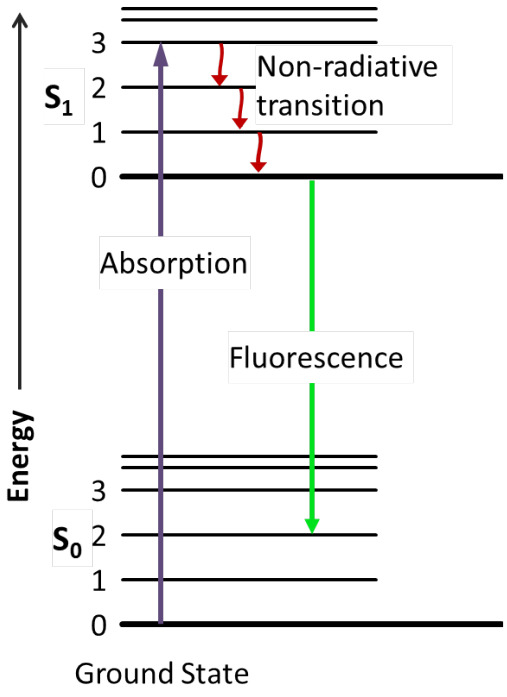

Figure 13 Jablonski energy diagram of fluorescence.

a microscope appears as a blurred disc, and two objects close together give overlapping images and may merge into one.

Another limitation is that this technique can only image dark or strongly refracting objects effectively. For example, since the internal structures of live cells are colorless and transparent, they need to be stained with selective dyes, but this often involves killing and fixing the sample.

A technique developed to overcome this limitation is fluorescence microscopy. It is most often used to detect specific proteins or other molecules in cells and tissues. A fluorescence microscope is designed for viewing material stained with fluorescent dyes. It is similar to a light microscope, but the illuminating light is passed through one set of filters before the specimen to select those wavelengths that excite the dye, and through another set of filters before it reaches the eye, to select only those wavelengths emitted when the dye fluoresces. Indeed, when a a photon of the excitation light hits a fluorescent molecule (fluorophore) , an electron can absorb it, thus raising its energy from the ground state level to an excited state level, as shown in the Jablonski energy diagram of fluorescence (Figure 13). This energy is then emitted as a photon to bring the electron back to its ground states, but a small amount of energy is dissipated by molecular collision or transferred to a proximal molecule. Since the emitted photon carries less energy and therefore has a longer wavelength than the excitation photon, the emitted fluorescence can be distinguished from the excitation light. The excitation and emission wavelengths are specific characteristics for each fluorophore, and for polyatomic fluorophores, broad excitation and emission spectra are exhibited. In Figure 14, an example of fluorescence spectrum is reported. The wavelength is plotted on the abscissa, and both the excitation absorption and emission intensity are plotted on the ordinate. The distance between the excitation and emission wavelengths is called the Stokes Shift; a fluorophore with a large stock shift is preferable as it is easier to distinguish.

The brightness of a fluorescent molecule is an important factor, too. Two parameters determine it: the molar extinction coefficient (ε) and quantum yield (Φ). The former is defined as the quantity of light absorbed by a fluorophore at a given wavelength and is measured in M^{-1} cm^{-1}. The latter is calculated as the number of photons that are emitted by the fluorophore divided by the number of photons that are absorbed. This calculation provides the efficiency of a fluorophore and has a maximum of 1. The brightness of a fluorophore is then calculated as the product of ε and Φ. Any process that lowers the fluorescence intensity causes quenching. Collisional quenching, contact quenching, and energy

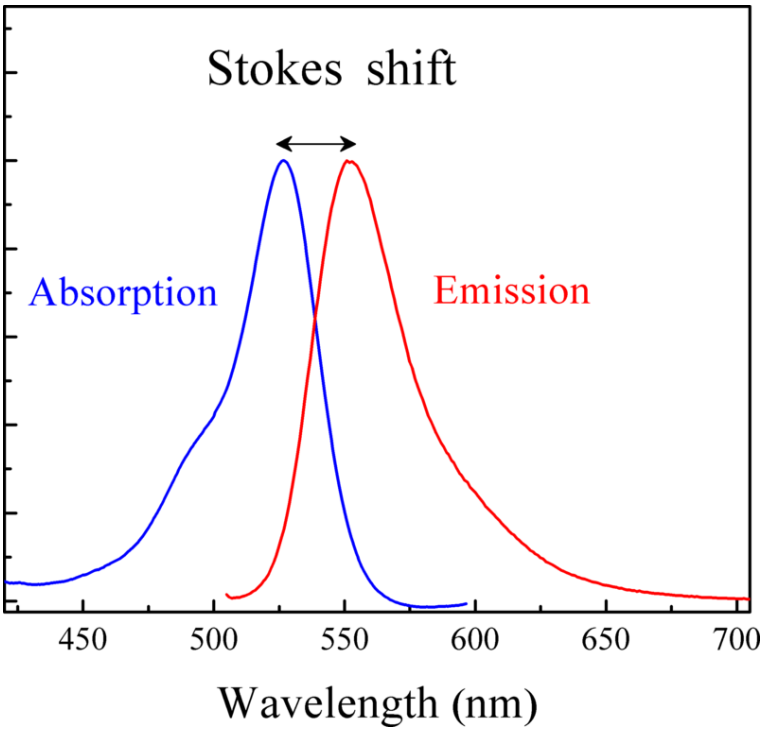

Figure 14 Example of fluorescence spectrum. Image adapted from https://en.wikipedia.org/wiki/Stokes_shift

transfer are just some examples of these processes.

As the second filter of the microscope allows only light of the emitted wavelength to pass, it is seen to glow against a dark background. Therefore, even a small amount of fluorescent dye can be detected. The same quantity of molecules of an ordinary stain observed conventionally, would be practically indistinguishable because they would give only the faintest tinge of color to the light transmitted through this stained part of the specimen. For detecting specific molecules in cells, as mentioned above, an effective approach is to couple a fluorophore to an antibody. An antibody is a Y-shaped protein that can recognize and bind an antigen present on the external of a pathogen. This enables to obtain specific staining reagents capable to bind selectively a suitable macromolecule in the cell. This technique can be applied not only to antibodies but also other molecules and proteins. Indeed, antibodies can be labelled using a chemically reactive derivative of a fluorophore and then detected by fluorescence microscopy. Common reactive groups include amine-reactive

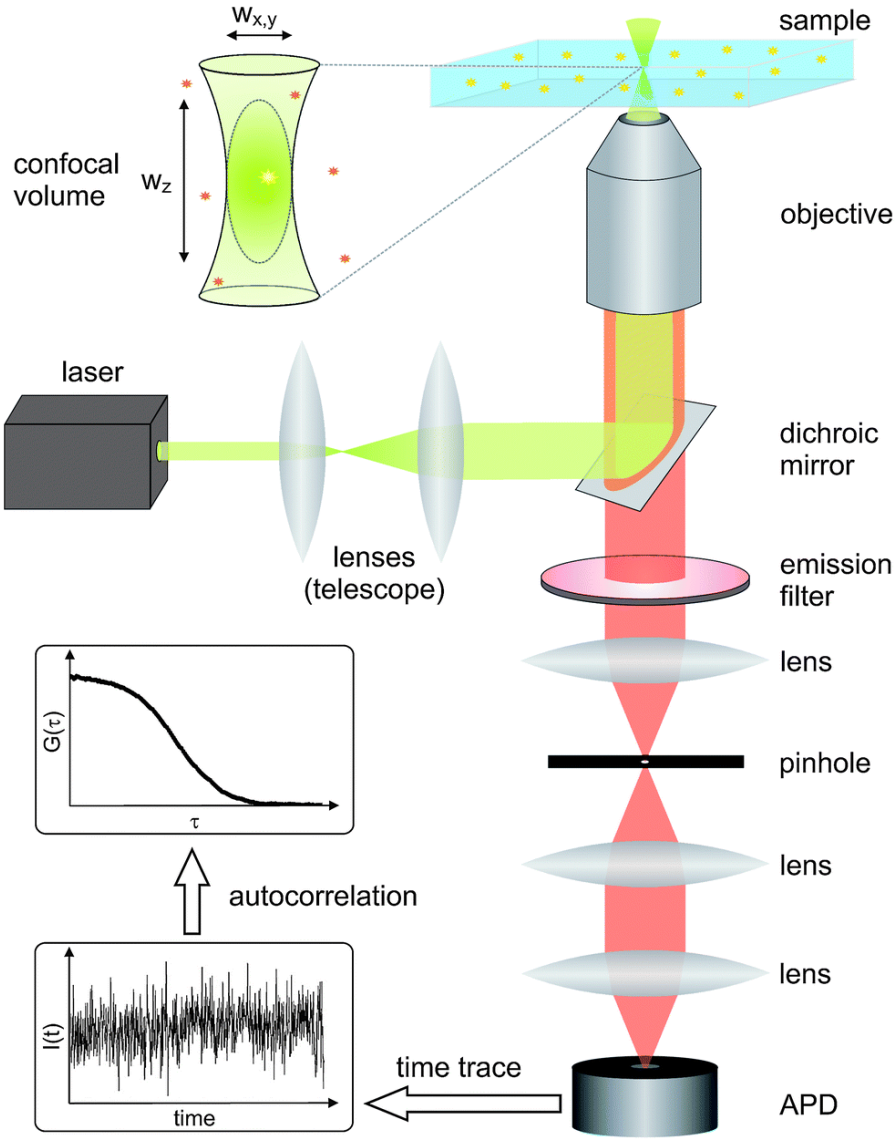

Figure 15 Experimental setup of Fluorescence Correlation Spectroscopy. Image adapted from *Caccia M, Nardo L, Santoro R, Schaffhauser D. Silicon Photomultipliers and SPAD imagers in biophotonics: Advances and perspectives. Nucl Instruments Methods Phys Res Sect A Accel Spectrometers, Detect Assoc Equip. 2019;926(November 2018):101-117. doi:10.1016/j.nima.2018.10.204*

isothiocyanate derivatives such as FITC (fluorescein isothiocyanate), amine-reactive succinimidyl esters such as NHS-fluorescein or NHS-rhodamine, and sulfhydryl-reactive maleimide-activated fluorophores such as Fluorescein-5-maleimide or ATTO 488 maleimide.

Fluorescence microscopy has been improved to determine molecular dynamics in biological systems: this technique is known as fluorescence correlation spectroscopy (FCS). FCS is a powerful tool for detecting molecular dynamics through analyzing the intensity fluctuation emitted by biomolecules diffusing in and out of a focused light[65]. It enables to measure the local concentration, hydrodynamic radius, diffusion coefficient, and the interaction of different proteins.

The experimental setup of FCS, often performed in a confocal system, is illustrated in Figure 15.

The fluorescence emitted by the fluorescently-labeled molecules in the observation volume is collected by the same objective and propagates along the opposite direction of the excitation/depletion light. After passing through a long-pass dichroic mirror, the fluorescence is focused through a pinhole onto an avalanche photodiode (APD). Since this is a confocal system, the fluorescence emitted in the out-of-focus region is rejected by the pinhole, and therefore, it does not reach the detector. Consequently, the pinhole reduces the axial extension of the observation volume. Such confined observation volume significantly enhances the signal-to-noise ratio and also reduces the measurement time needed to obtain a decent correlation curve[66].

1.5.2. Electron microscopy

In paragraph 1.5.1, it has been pointed out that the limit of resolution depends on the wavelength of the illuminating radiation used to probe the sample, which, in the case of optical microscopy, cannot be lower than 0.2 µm. To decrease this limit a different electromagnetic radiation, with a smaller wavelength, is required. For this reason, in electron microscopy, which has a resolution of 0.1 nm due to the objective lens system limitation, a beam of electrons to create magnified specimens is used. The wavelength of electrons is 2.5 pm at 200 keV (the wavelength of an electron decreases as its velocity increases). The beam of electrons can be used in a transmission mode (transmission electron microscopy, TEM), passing through a very thin sample (*ca* 100 nm), or it can scan a surface and be collected in reflection (scanning electron microscopy, SEM). TEM and SEM can reach a magnification of up to 10000000x and 500000x, respectively. SEM resolution can be as good as 1 nm, TEM resolution is atomic.

An electron microscope is composed of a high vacuum system in which the electrons can travel due to a difference of potential, an electron source, a condenser lens, a specimen holder, an objective lens, a projector lens, and a screen/camera.

The lenses are electromagnets, able to focus the beam into an image and control its position on the sample. The beam of electrons is generated by a filament of various types, including tungsten or lanthanum hexaboride, heated by a high-voltage anode (up to 300 kV).

A limitation of this technique is that the sample must be conductive so that the negative charge of the electron does not build an electric field, deflecting the beam and preventing the acquisition of the image. Nonconductive samples can be coated with a thin layer of a conductive material such as gold/palladium or carbon.

Another major limitation is that the high vacuum requires specialized sample preparation, particularly for biological samples, to render them fixed, dehydrated, and stable under vacuum.

Today, eSEM (environmental SEM) can work in moderate vacuum or water vapor with reasonable resolution to image bio samples.

1.5.3. Scanning probe microscopy

Scanning probe microscopy (SPM) is conceptually different from optical and electron microscopy. While in these techniques an electromagnetic beam is used to obtain a 2D image of the sample, in SPM a small probe is used to detect the local properties of a surface or interface. The interaction between the probe and the surface gives information about the morphology, and physico – chemical characteristics of the sample. Moreover, if the interaction between the probe and the substrate is strong enough, the substrate can be modified on the nanoscale.

For this reason, more than any other method, scanning probe microscopy reflects the close ties between physics, chemistry, and biology, and it is probably the only instrument that can be found in the labs of all three disciplines around the world.

The principal SPM instruments are scanning tunneling microscopy (STM) and atomic force microscopy (AFM). They rely on the same concept: a probe scanning the sample's surface that provides information. The probe is kept at a fixed distance from the surface through a feedback circuit that, responding to information coming from the probe, such as a current or a force, acts on a piezoelectric actuator to maintain the distance constant.

1.6. Atomic force microscopy

In atomic force microscopy (AFM), a nanometric tip, placed at the end of an elastic lever called cantilever, is raster-scanned over the surface of a sample along the x-y plane. The deflection of the cantilever (along the z-axis) is kept constant by a feedback control circuit that controls a piezoelectric actuator. By recording the vertical position of the piezoelectric as a function of the x-y position of the tip, a 3D topographic image is reconstructed.

While the Scanning Tunneling Microscopy probe requires a conductive sample being controlled by a current, the movement of an AFM probe depends on the force applied by the tip on the sample.

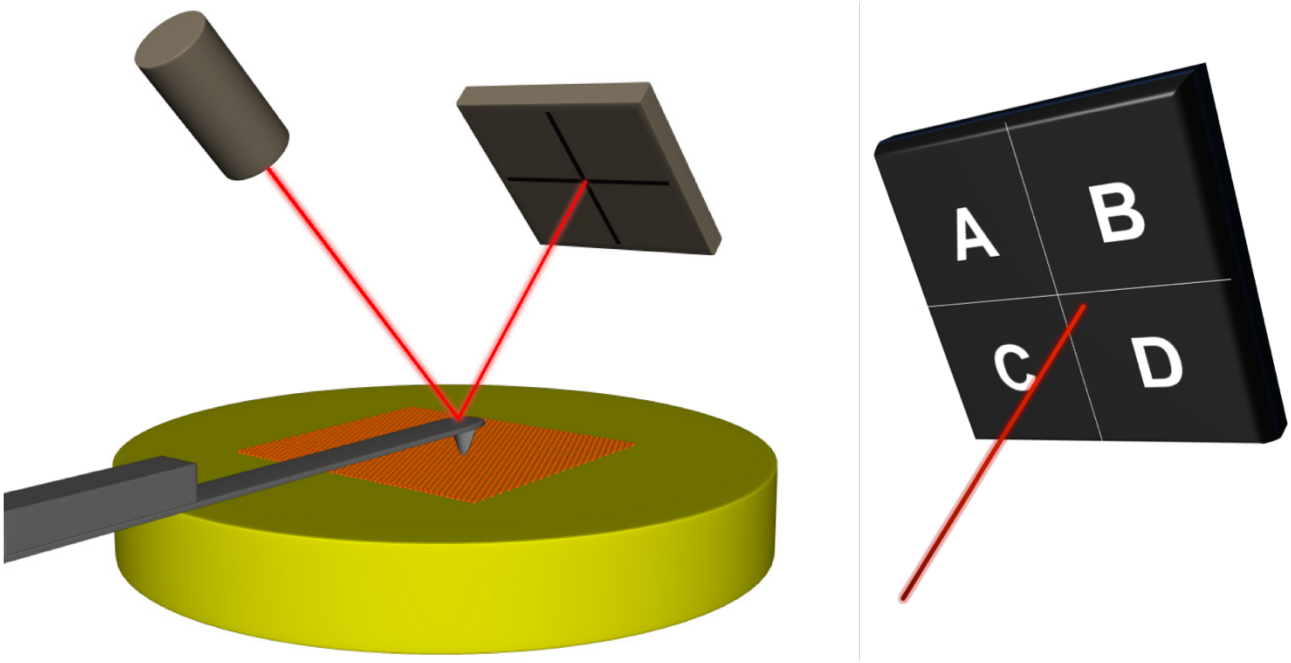

Figure 16 (left) Representation of the optical lever sensor of an AFM and (right) detail of the four-segment photodetector.

This feature overcomes one of the major limits of scanning tunneling microscopy, allowing using AFM also on insulating samples.

To monitor the force sensed by the tip, different force sensors can be employed. All these force sensors must be able to measure very low forces. Since extremely sharp probes are needed to perform high-resolution imaging, a very low applied force is required to apply little pressure to the tip and thus not damage it. A suitable force sensor, responding to this requirement and currently employed in nearly all AFM instruments, is the optical lever sensor. The principle of this system is as simple as it is effective. A laser beam is reflected from the backside of the cantilever often coated with gold to enhance its reflective properties, onto a four-segment photodetector (Figure 16). The lever deflects as the tip interacts with the sample, thus changing the reflected light path and the laser spot on the photosensor. The force is then measured by monitoring the change in light (and hence in voltage) detected by the four quadrants of the photodetector. The higher the force applied by the tip, the higher the deflection and thus the movement of the laser spot. The detector's quadripartition also enables to evaluate whether the deflection is vertical (due to asperities of the sample) or there is a torsion of the lever (due to friction phenomena). Naming the four quarter A, B, C and D as shown in Figure 16b, the vertical deflection is calculated as

$$\Delta V_{vert} = \frac{(A+B)-(C+D)}{(A+B+C+D)} \quad (1)$$

while the horizontal deflection is calculated as

$$\Delta V_{lat} = \frac{(A+C)-(B+D)}{(A+B+C+D)} \quad (2)$$

Depending on the intended application, the cantilever should have the following features: a low constant force, high resonant frequency, high lateral stiffness, short lever length, reflective surface, and a sharp protruding tip[67]. To register a measurable deflection with small forces, the cantilever must flex with a relatively low force constant (k). The k values vary from 0.35 N/m for contact mode (vide infra for AFM imaging modes) to 40 N/m for tapping mode. The mechanical resonance frequency must be > 10 kHz and can reach values of hundreds of kHz, such as in the tapping mode. High lateral stiffness in the cantilever is desirable to reduce the aforementioned effects of lateral forces that can introduce artifacts. The dimensions of the elastic levers are generally between 50 and 300 microns long, 20-60 microns wide, and between 0.2 and 1 micron thick. The most common shapes for these devices are v-shaped or rectangle shaped (see Figures 17a and 17b). The two main materials used for their manufacture are silicon (Si) and silicon nitride (Si_3N_4). Silicon enables to create levers with low force constants, but they can easily bend due to

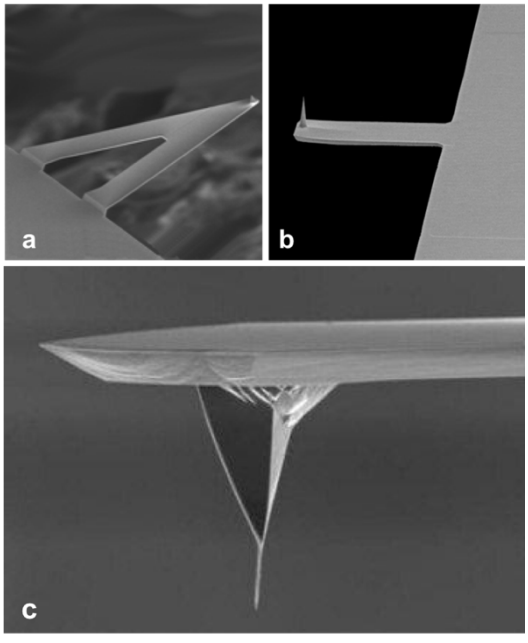

Figure 17 Different shaped cantilever: a) v-shaped and b) rectangle shaped; c) sharpened AFM probe.

stress. On the other hand, silicon tips can be brittle and can be more likely to chip when they contact a surface. Also, the sharpening of the tip, which allows higher resolution, influences its brittleness. New types of probes are constantly under development since one of the major challenges is the production of tips with a reproducible radius below 10 nm at a reasonable cost. Si_3N_4 probes are sharpened by adding an extra process step that changes the shape of the pit on which the Si_3N_4 film is deposited. Another option is an additional oxidation/etching process after the probe is manufactured. Si probes can be sharpened by chemical etching, ion milling, or adding a carbon nanotube (see Figure 17c). Each of these techniques can create a sharper probe but also increase the probe's manufacturing price.

As introduced above, the motion of the probe is controlled by a feedback control circuit. The error signal (Z_{err}), i.e., the difference between the signal from the force sensor and a set-point value, is sent to the feedback controller, which, in turn, controls the Z piezoelectric actuator. This system enables the probe to "track" the surface as it is scanned, keeping Z_{err} minimal, thus following the profile of the sample as closely as possible.

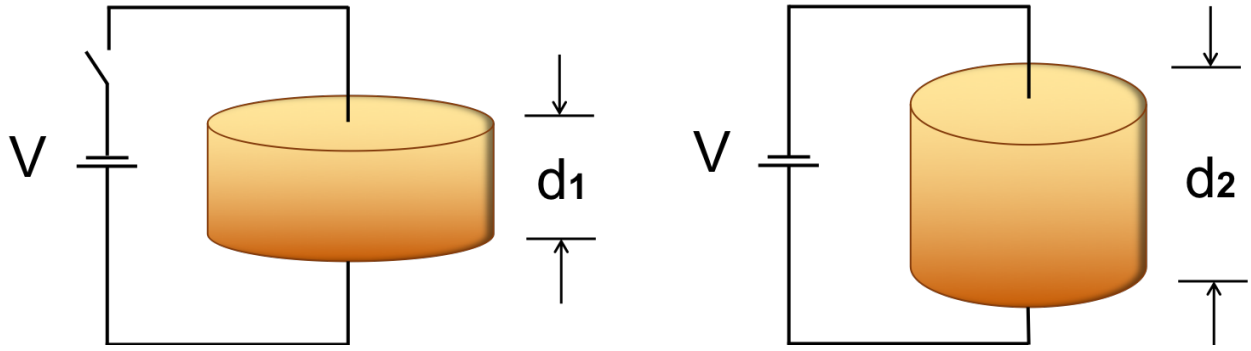

Figure 18 A piezoelectric disk that expands radially ($d_2 > d_1$) when a voltage potential is applied to the top and bottom electrodes.

A piezoelectric material accumulates electric charges in response to applied mechanical stress. A typical example of the use of this effect is the ignition of pocket lighters. The reverse effect can also occur: an externally applied electrical field can deform a crystal unit cell. If a voltage ΔV is applied across a piezoelectric material (Fig. 18) of dimensions *x*, *y,* and *z* (polarized in the *z*-direction), a strain is generated along the z-direction. Similarly, the actuator can be deformed along x and y upon polarization along x and y. This effect is used in piezoelectric actuators that control the AFM probe or the sample relative displacement.

Over the years, a variety of AFM modes have been developed. In the next paragraphs are described only the most adopted ones, attainable with commercial AFMs without significant modification. These methods, which prove the versatility of this instrument, will be divided into topographic modes, non-topographic modes and surface modification modes. Each AFM mode has pros and cons, and the operator must choose the most suitable mode depending on the circumstances.

1.6.1.Topographic modes

1.6.1.1. Contact mode

Contact mode (CM) AFM is the simplest mode conceptually and was the first to be developed. In this technique, during the acquisition of an image, the tip is always in contact with the sample. The probe pushes against the surface with a constant and controlled force which is determined by setting a set-point value for the deflection. As soon as the probe bumps into an asperity, the tip is moved by the feedback system to keep the deflection set-point constant. Contact mode enables a

very high resolution on smooth samples, and it is also the fastest of all topographic modes. On the other hand, since the tip is always in contact with the sample, it can get dirty or damaged more easily compared to the other modes. Also, the sample may be damaged. Moreover, the applied normal force leads to a high lateral force applied to the sample as well. In the case of weakly adsorbed samples, or soft, easily deformed samples, this can lead to sample distortion, damage, or even removal from the substrate[68,69]. Although this mode can be used on soft and delicate samples, paying attention to applying a low force, this may not be possible in ambient conditions: due to air moisture, a capillary meniscus of water forms between the tip and the surface. This causes the pull of the AFM tip onto the surface resulting in a force greater than that set by the operator. On the contrary these forces do not exist in water. Imaging in liquid can be problematic with non-contact modes (vide infra) making contact mode preferable .

Three main signals that can be obtained with this technique: i) the motion of the Z piezo that provides the topographic image, ii) the vertical deflection of the cantilever before the feedback system response (which cannot be instantaneous), that provides the error image, and iii) the lateral deflection caused by the lateral twisting of the elastic lever due to the surface friction. This latter signal is typically used to assess material properties due to its sensitivity to material features rather than as a measure of sample topography; therefore, this topic will be covered in the non-topographic mode section.

The error signal, which is a measure of how much the cantilever deflects before the deflection is 'corrected' by the feedback circuit, in an ideal situation should be zero. However, the action of the controller takes some time, therefore this signal can only be minimized. A low error means e good "tracking" of the surface.

1.6.1.2. Tapping mode

Today there are a large number of dynamic modes, but they rely basically on the same principle. The cantilever is oscillated, usually with an additional piezoelectric element, typically at its close resonance frequency. When the oscillating probe approaches the sample surface, the oscillation amplitude changes due to the interaction between the probe and the sample, i.e. a change of resonance frequency. The effect is a damping of the cantilever oscillation. The optical lever monitors the oscillation, and the scanner adjusts the z height via the feedback loop to maintain the constant oscillation in the repulsion regime keeping a fixed distance from the sample, just as in contact-mode AFM. One of the most used of these techniques is tapping mode (TM). In TM the probe oscillates with a larger amplitude (1-100 nm) [70]. This implies that the tip can pass through a contamination layer or water, often present on the sample in ambient conditions, and also easily detach at each tap.

Moreover, lateral forces are strongly decreased, as the tip interacts perpendicularly with the surface as it scans. These features make tapping mode one of the most used techniques for imaging in the air. In liquid, however, the cantilever's mechanical excitation can induce the fluid's excitation in the fluid cell[71] and is, therefore, less used.

Often, the delay in the phase of the probe oscillation is recorded, and since it is strongly affected by the tip-sample interaction (energy dissipation), it can be used to distinguish among different materials.

1.6.1.3. Peak Force Tapping mode

Peak Force Tapping mode, like tapping mode, interacts with the sample intermittently. The probe is ramped inertially (vide infra) in adjacent points, with vertical movements towards and away from the sample, at frequency in the range of 0.5-8 KHz. Therefore, it is a vertical approach scanning mode, in which the probe does not interact with the sample during lateral movement. The force curves are used to recreate the topographic map of the surface. This imaging mode allows to work with extremely low forces, especially in liquid, and it is ideal to be applied on delicate samples, such as phospholipid bilayers or biological samples. This mode can be as fast as TM.

1.6.2. Non-topographic modes

AFM is a highly versatile instrument. Indeed, it can be used to obtain more than just topographic information because AFM is primarily a force sensor (and transducer). The possibility of controlling the AFM probe through the *piezo*, and designining and using suitable tips that can interact with the sample, recording very low forces, pave the way for many applications.

1.6.2.1. Nanoindentation

In this technique, the probe is ramped in the z axis while measuring the cantilever deflection as the tip contacts and presses onto the sample surface. This can reveal a variety of sample properties. The output of this interaction is a force curve (FC), which is a plot of the force applied by the probe as a function of the distance travelled by the z-piezo towards/from the surface. More in detail: the tip is brought closer to the sample until contact is made. At this point, there is a deflection of the cantilever which increases up to a maximum, which the operator can control via the *trigger threshold* value. When this value is reached, the probe moves away until it returns to the starting position. Figure 19 shows the typical trend of a force curve obtained on a hard sample, for example, a substrate of mica.

The tip-sample approach phase is termed *approaching,* while the withdrawal phase is termed *retracting* phase.

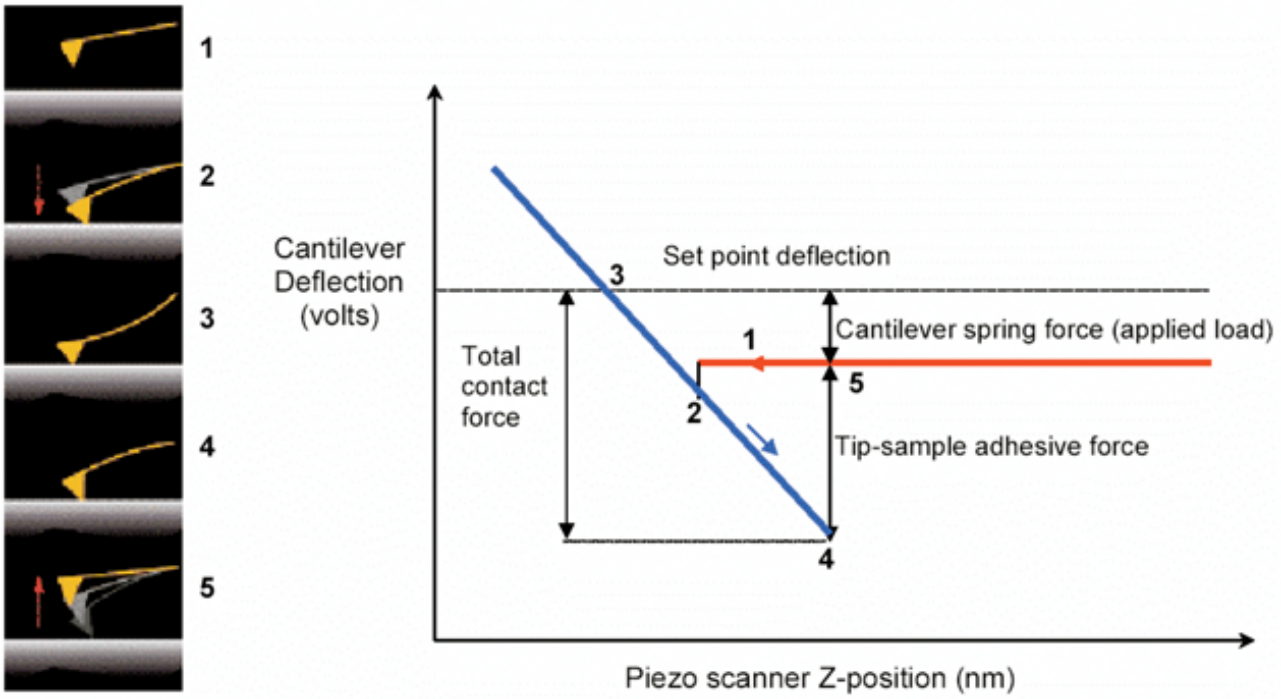

Figure 19 Typical force curve acquired on a rigid substrate in abient conditions. Image taken from https://www.bruker.com/en/products-and-solutions/microscopes/materials-afm/afm-modes/forcedistance.html

It is possible to divide the curve into five phases that make up the entire ramp (that is the approaching and retracting movement along the z axis):

1. The tip is far from the sample, and during the extension of the piezo, no deflection is measured (baseline);
2. The tip comes into contact with the sample due to attractive forces established (typically van der Waals forces, electrostatic or capillary forces). This event is defined as *jump-in*;
3. In the contact area, repulsive forces are established leading to cantilever deflection up to the trigger threshold value. At this point, the piezoelectric inverts its motion;
4. The tip moves away from the sample;
5. Adhesion forces are triggered that keep the tip in contact with the sample beyond the initial contact threshold, until the moment of detachment (*pull-off*) in which the lever returns to rest;

The adhesion force in Figure 19 (point 5) is generally observed in ambient conditions rather than in liquid, and it is caused by capillary forces due to the aqueous meniscus between the tip and the surface. The conversion from the cantilever deflection (volts) vs piezo scanner Z-position (nm) to the Force (nN) vs tip-sample distance, d (nm) is described in detail in the paragraph 5.2.3.
The qualities of the atomic force microscope mentioned above, such as high load sensitivity and high positioning resolution of the probe, allow detecting forces as low as piconewton, in specific regions of micro-organisms[72,73], living cells[74] or ultra-small samples such as nanoparticles[75,76].
Nanoindentation can be achieved both on hard materials, with very stiff cantilevers and hard probes, and on soft samples, where this setup may be inappropriate, with a normal AFM probe. For quantitative results, however, the tip radius and the cantilever must be accurately characterized. These experiments can be carried out in a grid pattern. For instance, the *auto ramp* mode enables acquisition of FCs in a grid of n x m rows and columns at a selected distance between them.
Data analysis for nanoindentation is an essential part of the experiment and is often achieved through the Hertz model[77].

1.6.2.2. Force spectroscopy

Force spectroscopy is one of the most well-known examples of non-topographic modes. It is used to measure the interaction between the sample and the probe, observed in the retracting part of FCs acquired during the experiment. To this purpose, AFM probes are often functionalized with molecules of interest[78,79,80] that can interact with a specific part of the sample, although experiments with bare AFM tips[81,82], colloidal probes (e.g. silica spheres, which may be themselves chemically modified), and even micro-organisms[83,84] are reported . A wide variety of surfaces can be probed, from cell membranes[85], micro-organisms[86,87], whole living cells[88], and a range of solid surfaces such as metals[89], ceramics[77], and polymers[90,91].

In an ideal situation, the tip is functionalized with a single suitable molecule, and at each FC, the specific interaction event can be clearly recognized. Real conditions are different: generally, after the AFM tip functionalization, a large number of molecules that interact with the sample are bound to the probe and not necessarily at its far end. Therefore, a statistical variation in results is typically very large. This means that, typically, a very large dataset needs to be generated, and a lot of data analysis is required. Figure 20 shows an example of real force spectroscopy retracting FC. A major application of force spectroscopy is protein unfolding, which uses the AFM force sensitivity to probe the mechanical unfolding of large protein molecules.

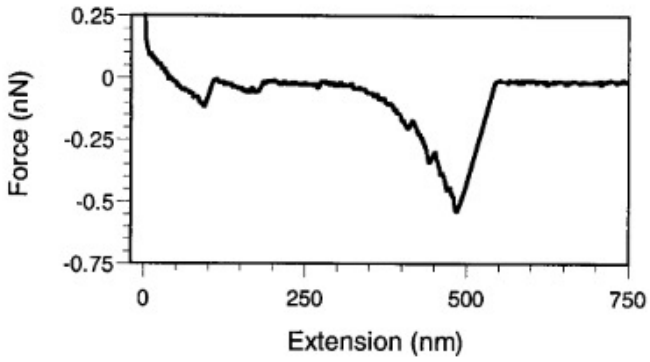

Figure 20 Example of *retracting*-phase force curve in a force spectroscopy experiment. Image adapted from *Dufrêne YF. Atomic force microscopy, a powerful tool in microbiology. J Bacteriol. 2002;184(19):5205-5213. doi:10.1128/JB.184.19.5205-5213.2002*

1.6.2.3. Mechanical property imaging

The measure of the interaction of the probe with the sample while it acquires topographical data allows obtaining mechanical information about the sample surface. It also allows overcoming some drawbacks of the previous techniques, such as complicated data analysis and relatively slow data acquisition. There are a vast number of modes that correlate mechanical information with the measured topography.

For example, lateral force microscopy (LFM) measures the lateral deflection signal from the photodiode (generated by the twisting of the cantilever) during the acquisition of an image. This gives information about the mechanical interaction of the probe with the sample, that depends on the friction faced by the tip as it scans over the sample. For this reason, LFM is sometimes also called friction force microscopy (FFM).

Another mode is Phase imaging, in which the phase shift signal is recorded during Tapping mode. Phase contrast shows adhesion and viscoelastic properties[92]. This is one of the most used techniques for 'mechanical' characterization of sample surfaces, probably due to the popularity of tapping mode, and the fact that obtaining the data is very simple and does not require post-processing of the data.

1.6.2.4. Magnetic force microscopy

Magnetic fields decay quickly with distance, so to measure local properties, the probe must be very close to the sample. For this reason, the use of AFM for these measurements is optimal. In magnetic force microscopy (MFM), a magnetic field is detected through a magnetic probe. This is obtained by coating a silicon cantilever with a thin magnetic layer, typically using cobalt, cobalt-nickel, and cobalt-chromium[93].

Since the materials used for the coating are generally softer than the underlying silicon, the wear rate of the probe is increased. Moreover, this coating causes an increase of the tip radius and thus decreases the resolution of the probe.

As the magnetic forces are negligible compared to the tip-sample forces when in contact, these measurements must be performed at a distance of the order of 5-50 nm from the surface to reduce

the interference from the undesired forces. These modes can be carried out in many different ways, but all of them have a resolution lower than 30 nm laterally due to the lifting of the tip[93].

The data storage industry is largely based around creation of magnetic nanodomains of the size range of a few hundreds of nanometers, and there is no other technique to accurately measure such features. Therefore, MFM has seen much use industrially, particularly in data storage applications[94].

Other application of AFM that is worth mentioning are

- electric force microscopy (EFM): it is similar to MFM, but instead of magnetic fields, electrical fields are measured;
- electrochemical AFM: it study a surface as a function of applied potential using the AFM[95];
- thermal modes: it acts as a thermometer by measuring the temperature locally with a resisting probe[96].

1.6.3. Surface modification

As already mentioned, AFM is a versatile instrument. In addition to topographic and non-topographic modes, it can be used for surface modification. Since the probe motion can be controlled with remarkable precision, surfaces can be modified at the nanoscale. In the next section, some nanolithography techniques are described.

1.6.3.1.Local oxidation

The sample surface can be oxidized while scanning it with the probe[97]. A suitable bias (several volts) applied to the tip in humid environment causes oxidation of silicon to silicon oxide. This process is deeply influenced by humidity since the meniscus between the tip and the surface provides the electrolyte for oxidation. Therefore, the size of the meniscus affects the dimension of the feature that it's possible to manufacture[98].

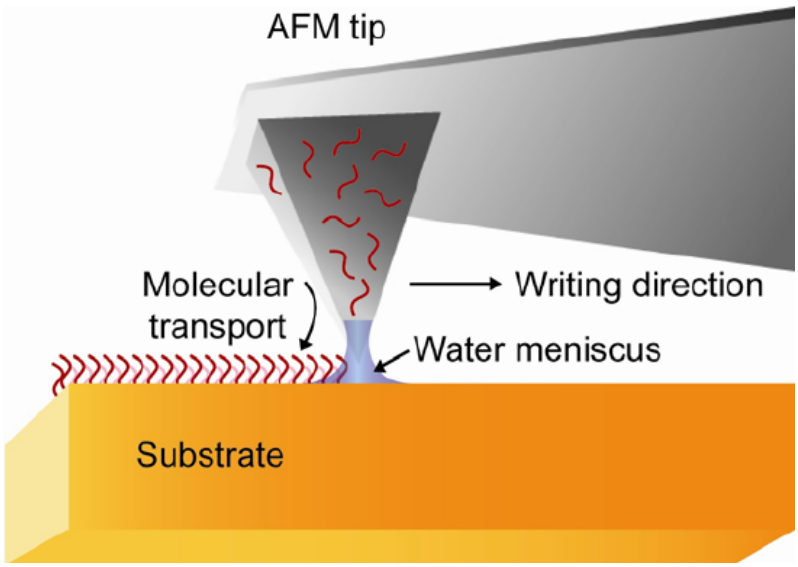

Figure 21 Mechanism of action of the dip-pen nanolithography. Image taken from https://www.researchgate.net/profile/Harald-Graaf/publication/236606266/figure/fig1/AS:299458064601092@1448407774759/Dip-Pen-Nanolithography-principle-Molecules-are-transferred-from-an-AFM-tip-onto-the.png

1.6.3.2. Scratching techniques

The fine control of the probe motion also allows applying a high normal force to the sample to obtain scratches with the desired pattern. This simple technique can be performed on various surfaces, although its application is less common than local oxidation.

1.6.3.3. Dip-pen nanolithography

Using the AFM tip as a pen, dipping it in a solution of the molecule to be grafted, it is possible to depose almost any material on a sample exploiting the capillary water layer that forms between the tip and the surface[99] (see Figure 21). Like with a macroscopic pen, tip radius, scanning speed and set-point influence the written pattern's dimension. The "inks" that can be used vary among organic molecules[99], proteins[100,101], synthetic peptides[102], DNA[103], polymers[101], inorganic nanoparticles[104]

and more[103,105]. A major application of dip-pen nanolithography is in the creation of arrays of receptors for parallel testing, e.g., proteomics, genomics, etc.

1.7. NMR

Nuclear magnetic resonance (NMR) is the most effective spectroscopic method for determining molecular structures in solution. It can also give information about geometry and symmetry, and provide mechanistic details when used to study the reactions.

Many nuclei of atoms have a spin angular momentum, defined as spin quantum number *I*. The value of *I* is always positive and can be integer or semi-integer. Atoms with *I* = 0, such as ^{12}C and ^{16}O have

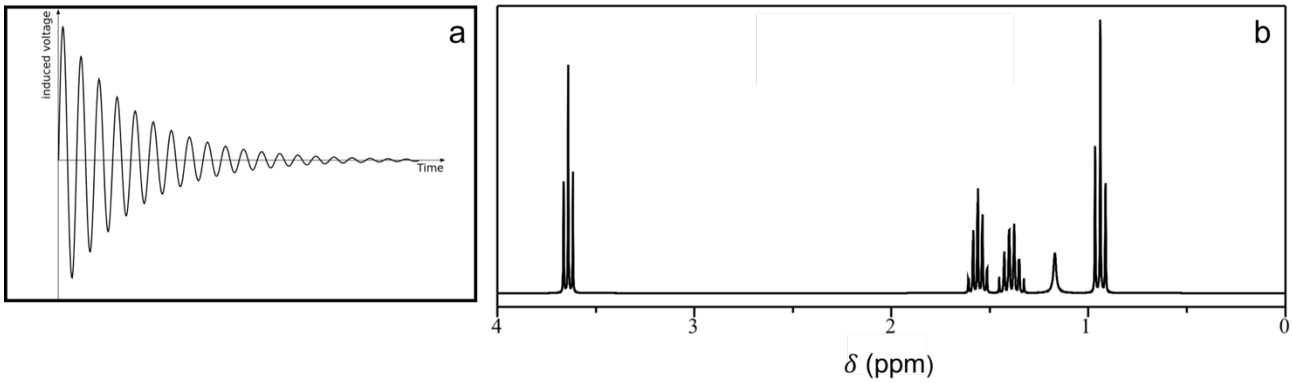

Figure 22 a) Free-induction decay (FID) and b) NMR spectrum obtained by the fourier transorm applied to the FID. Image adapted from https://it.wikipedia.org/wiki/Decadimento_libero_dell%27induzione

a null magnetic moment. Only the atomic nuclei with *I* > 0, manifest a magnetic dipole and are NMR-active. The nucleus analyzed most frequently by NMR is ^{1}H, with *I* = ½. Other nuclei with *I* = ½ are ^{13}C, ^{15}N, ^{19}F and ^{31}P. Atoms with *I* > ½ have a quadrupole moment, i.e., a non-uniform distribution of the electric charge, which broadens the signals and degrades the spectra, making these atoms more difficult to analyze.

Ordinarily, nuclei are oriented randomly, but if a strong magnetic field is applied, the nuclei line up and start to precess with the same orientation. A nucleus with spin *I* can assume 2*I* + 1 orientations with respect to the direction of an applied magnetic field. Therefore, nuclei with *I* = ½ can exist in one of the two possible spin states. The precession frequency (or Larmor frequency) is given by the equation

$$\nu = \frac{\gamma B_0}{2\pi} \tag{3}$$

where γ is the gyromagnetic ratio, and B_0 is the magnetic field strength[106].

If a short radiofrequency (RF) pulse is applied at a right angle to the direction of B_0, the nuclei flip down to the x-y plane in unison and continue to precess. The magnetization vector is therefore rotating in the x-y plane at the Larmor frequency. The rotating magnetization induces a current in a receiver coil, which can be detected and amplified. Over time, the signal weakens as the nucleus re-aligns with B_0. The oscillating and decreasing signal is the *free-induction decay*, FID (Figure 22a). In a system composed of several nuclei, each with its characteristic frequency, the FID is the sum of the oscillating and declining functions. Its components can be analyzed and separated using the Fourier transform, transforming the signal into a spectrum in which each line represents the Larmor frequency of the different nuclei (Fig. 22b).

In modern NMR spectrometers, a superconducting magnet cooled with liquid helium generates the magnetic field (with a magnitude of 10 T or greater). An outer Dewar filled with liquid nitrogen serves to avoid boil-off of the much more expensive, cooler liquid helium. The sample is quickly rotated to mediate any magnetic inhomogeneities.

The introduction of a second frequency dimension brought to two-dimensional nuclear magnetic resonance spectroscopy (2D NMR), a set of NMR methods in which data are plotted as a function of two frequency axes rather than one. This gives more information about a molecule than 1D NMR, and therefore, these experiments are especially useful in determining the structure of complicated molecules.

Correlation spectroscopy (COSY), exchange spectroscopy (EXSY), and nuclear Overhauser effect spectroscopy (NOESY) are some examples of 2D NMR.

A sequence of radio frequency pulses is generated with delay periods in between them, and depending on the frequencies, intensities, and timing, different experiments are performed. However, all of them are constituted by four steps:

1. the preparation period, where a set of RF pulses creates a magnetization coherence;
2. the evolution period, a determined length of time during which no pulses are delivered, and the nuclear spins are allowed to freely precess (rotate);
3. the mixing period, where another series of pulses manipulate the coherence into a state which will give an observable signal;
4. the detection period, in which the FID signal from the sample is observed as a function of time, in a manner identical 1D-NMR.

The output is a plot showing an intensity value for each pair of frequency variables. The intensities of the peaks in the spectrum can be represented using a third dimension.

Additional NMR dimensions that depend on molecular properties such as size, shape, mass, and charge could give important information, but these overall molecular properties are not well represented in conventional NMR as spin interactions tend to be relatively local.

Nuclear relaxation times depend on correlation times for molecular motion, which depend on molecular sizes and shapes, but they can be quite different for different nuclei in the same molecule because of site-specific magnetic interactions and because local or segmental motions may obscure overall molecular motions. As determined by diffusion measurements and electrophoresis, the transport properties of molecules and ions have the same effect on all nuclei in a given molecule.

Diffusion-ordered spectroscopy (DOSY) aims to separate the NMR signals of different species according to their diffusion coefficient. A series of spin echo spectra are measured with different pulsed field gradient (PFG) strengths, and the signal decays are analyzed to extract a set of diffusion coefficients with which to synthesize the diffusion domain of a DOSY spectrum. Therefore, the idea is to increment an experimental variable that modulates the detected signal and then transform the data with respect to that variable to produce a ‘‘spectrum’’ related in this case to molecular translation[107,108].

1.8. Dynamic light scattering

Dynamic light scattering (DLS) is a widely used technique for measuring *in situ* the sizes of nanoparticles in liquids and their size distributions. DLS has many variations, but all of them can be classified as “hydrodynamic” techniques since they directly measure hydrodynamic quantities, such

as rotational diffusion coefficients, which are then related to sizes and shapes via theoretical relations.

The Brownian motion theory states that particles are subjected to random forces due to collisions with solvent molecules resulting in random motion of particles. The friction exerted by a moving particle is proportional to its radius and the viscosity of the solvent surrounding particles. When a monochromatic beam of light encounters solution containing particles, light scatters in all directions due to their size and shape. Dynamic light scattering, also known as photon correlation spectroscopy, is based on the intensity of this scattered light resulting from interference on the surface of a square-law detector between the light scattered from different particles in the medium. In a DLS instrument, a laser light is directed toward a solution and the scattering intensity is recorded by a detector. At a given instant, the total scattered intensity at a certain scattering angle depends on the positions of the particles (structure). Since the particles are moving with Brownian motion, the scattered intensity fluctuates. Therefore, the scattered intensity is a stochastic signal that reflects the thermal motion of the molecules.

To extract useful information from this signal, its time correlation function is computed. This is usually done using an autocorrelator: a computer equipped with special boards to allow rapid real-time calculation of the scattered intensity time correlation function.

By correlating the intensity fluctuations of scattered light with respect to time (ns-µs), the digital autocorrelator determine how rapidly the intensity fluctuates, which is related to the diffusion behavior of macromolecules.

Figure 23 depicts a schematic diagram of a DLS instrument: light from a laser is focused on a sample, and the light scattered is collected by a photomultiplier (or an avalanche photodiode[109]). An autocorrelator receive the output of the photomultiplier (PMT) digitized by a photon counting

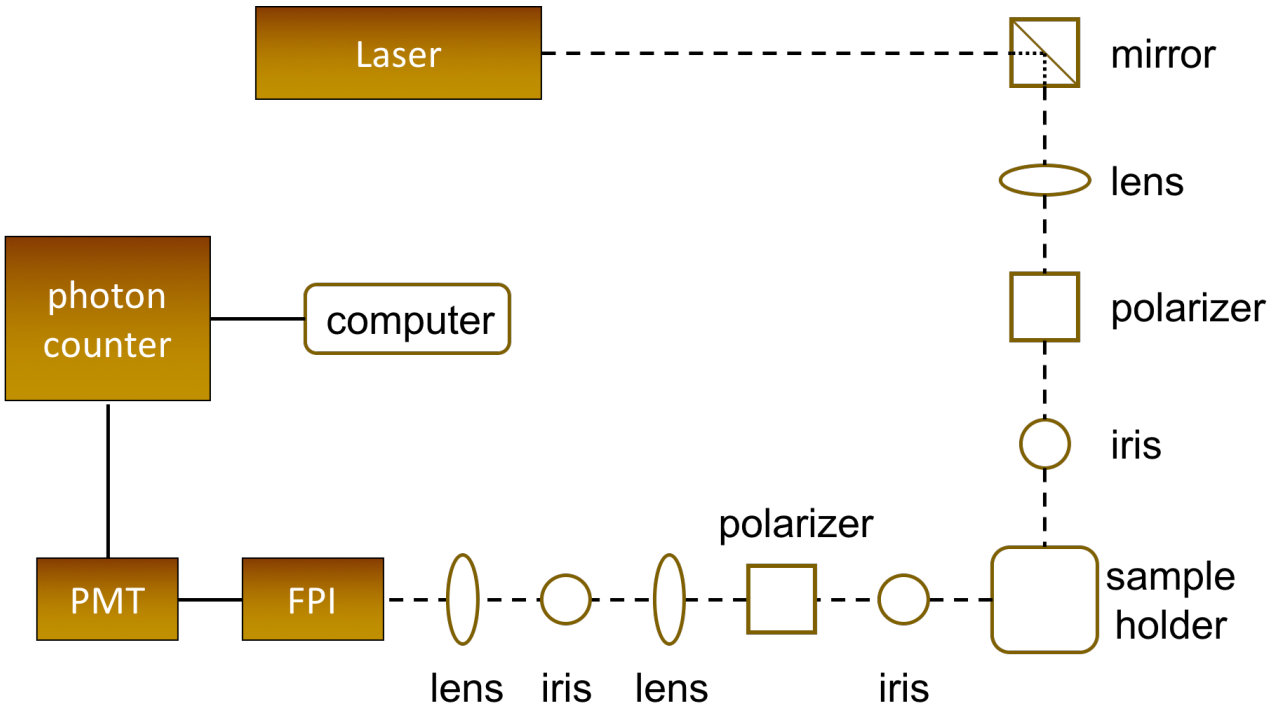

Figure 23 Schematic representation of the experimental setup of a Dinamic Light Scattering instrument.

system. Fiber optics guides are used to deliver the light to the sample, collect the scattered light and bring it to the detector.

1.9. Small-angle X-ray scattering

Small-angle X-ray scattering (SAXS) belongs to a family of non-destructive analytical techniques that provides information about the structure, chemical composition, and physical properties for a variety of 1-100 nm and beyond particle systems by characterizing average particle sizes and shapes[110,111].

In a SAXS experiment, the scattered intensity of an X-ray beam of a specific wavelength hitting a sample, with an angle between 0 and 5 degrees, is observed. When a monochromatic wave hits an object, the electrons of its atoms become sources of secondary waves. Unlike crystallography, in which the macromolecules are regularly positioned, in SAXS the molecules are randomly oriented in solution and free to move. Therefore, instead of the typical crystallographic diffraction peaks, from which 3D electron density $\rho(r)$ and high-resolution structure can be reconstructed, no peaks are observed, and the orientation information is lost. Still, information on the shape and size of macromolecules, characteristic distances of partially ordered materials, pore sizes, and other data can be obtained.

The SAXS experimental profile is composed of three distinct regions, as shown in Figure 24.

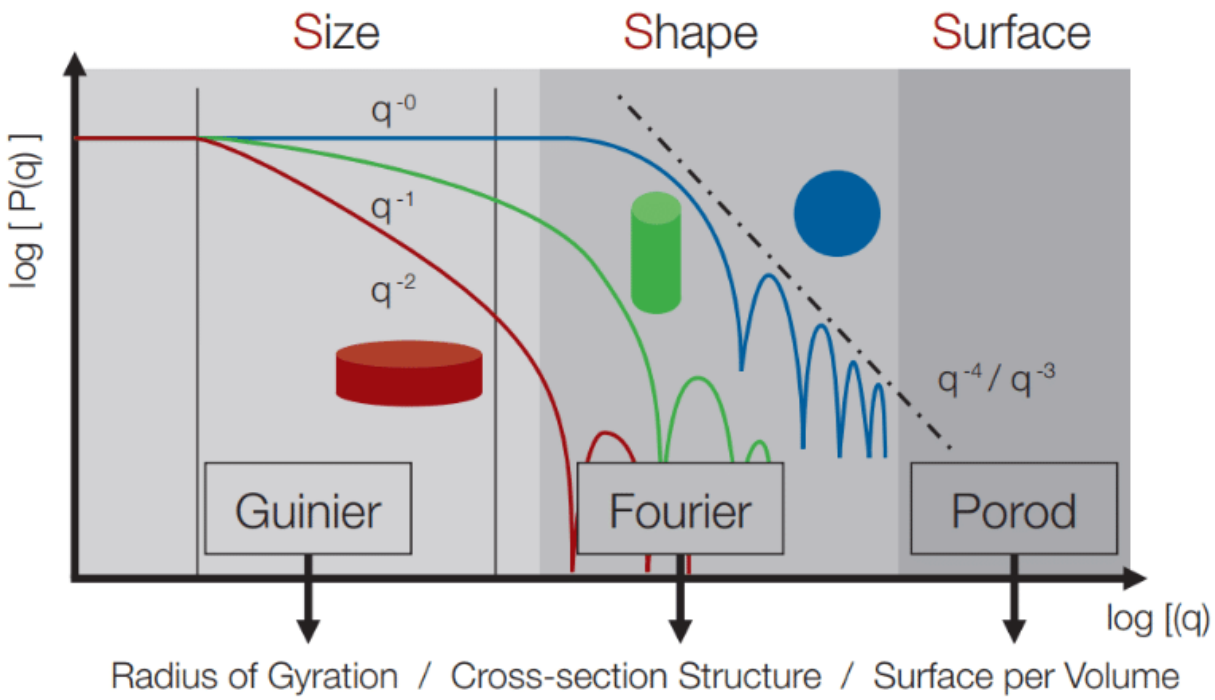

Figure 24 Experimental profile of a SAXS experiment. Image taken from *https://www.researchgate.net/figure/Left-Regime-of-information-for-the-form-factor-Left-Pair-Distribution-Function-plots_fig8_326259034*

The Guinier region is influenced by interactions between the particles in solution. The experimental radius of gyration R_g may be approximated by fitting a line to the natural log of the intensity as a function of the square of the scattering vector q^2.

In the Fourier region, an indirect Fourier transformation of the experimental form factor provides information regarding the particle shape *P(q)* (Equation 4).

$$\rho(r) = \frac{1}{2\pi^2 r}\int_0^\infty qP(q)\sin(qr)dq \quad (4)$$

It refers to the distribution of electrons averaged over a radius *r*; *ρ (r)* curves are used to determine the general particle shape, provided all the particles in the sample are of similar shape[112].

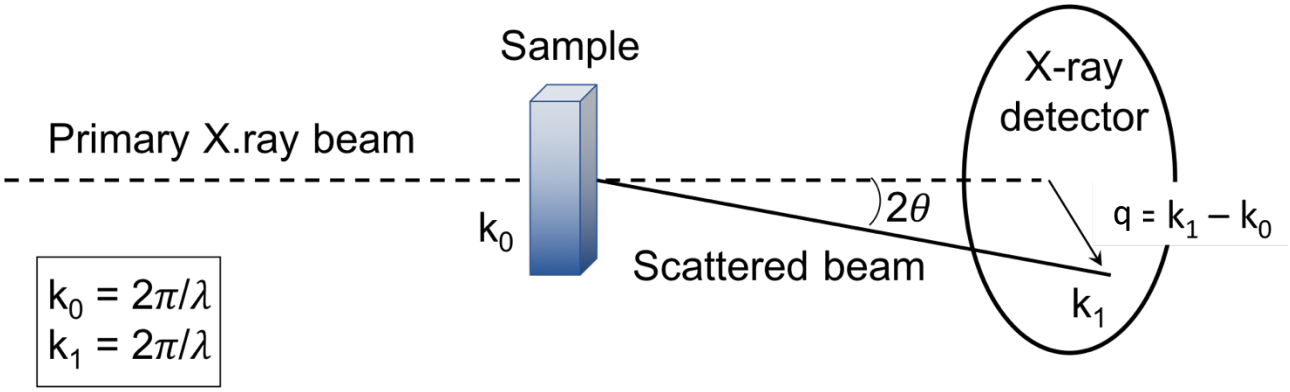

Figure 25 Setup of a SAXS experiment.

Lastly, the Porod invariant *Q* (equation 5), in the homonymous region, gives information such as the surface to volume ratio and specific surface estimation for compact particles.

$$Q = \int_0^\infty q^2 I(q)dq \quad (5)$$

The setup of a SAXS experiment is showed in Figure 25: a solution of the sample is placed in a quartz capillary and illuminated by a collimated monochromatic X-ray beam. The intensity of the scattered X-rays is recorded by an X-ray detector. After the subtraction of the scattering pattern of the pure solvent, the signal from the particles of interest is obtained. This signal is related to the overall shape and size of the particles under investigation[113]. Typically, 10-100 µL of sample per measurement are required. This technique is used to characterize both ordered and disordered proteins in solution, nanoparticles, nanoporous materials, polymers and so on.

1.10. Small-angle neutron scattering

Small-angle neutron scattering (SANS) is based on concepts similar to those of SAXS. Also, this technique enables to probe the structure of materials on a typical size range lying from 1 nm up to a few 100 nm such as nanoparticles, polymers, pores, proteins, etc. Some of the information that can be obtained about the sample are the gyration radius, shape, volume, mass, fractal dimension, specific area. In addition, information about the sample organization, e.g., aggregated or homogeneously dispersed, can be obtained. As well as SAXS, and unlike microscopy techniques, which allow observing a specific detail of the sample, the obtained information with SANS is statistically averaged on the whole sample.

In a SANS experiment, a neutron beam is used to probe the sample. By interacting with the atomic nuclei, it is scattered over all directions. The scattered intensity, I(Q) is reported as a function of the scattering vector q, defined as:

$$q = 4\pi sin\frac{\theta}{\lambda} \quad (6)$$

Where λ wavelength of the incident radiation and θ is the scattering angle.

In some cases, neutrons can be a better choice than X-rays.

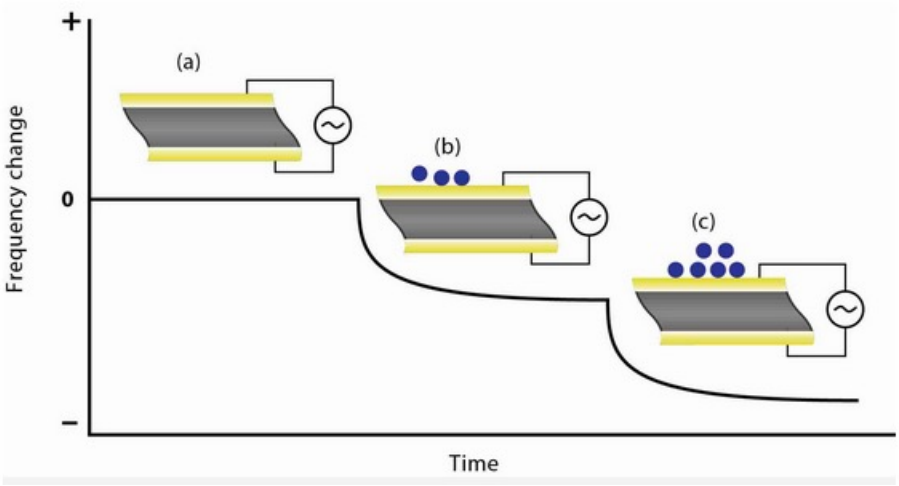

Figure 26 Diagram of the variation of the frequency vs. time in a Quartz Crystal Microbalance when mass is added. Image taken from https://www.nanoscience.com/techniques/quartz-crystal-microbalance/

Neutrons interact with the atomic nuclei, and not with the electronic cloud, as for X-rays. Each atomic type has a defined scattering length. While for X-rays the scattering length grows with the number of electrons, for neutrons, it changes somewhat irregularly, and importantly, the scattering length of hydrogen is significantly different from that of deuterium. This unique property of neutrons enables contrast variation experiments where some molecules are labeled by deuterium to create a neutron contrast in the system.

A second advantage of the use of neutrons is that, since they bear a spin ±½, they interact with the magnetic moments of molecules. Moreover, their very weak absorption by matter enables them to

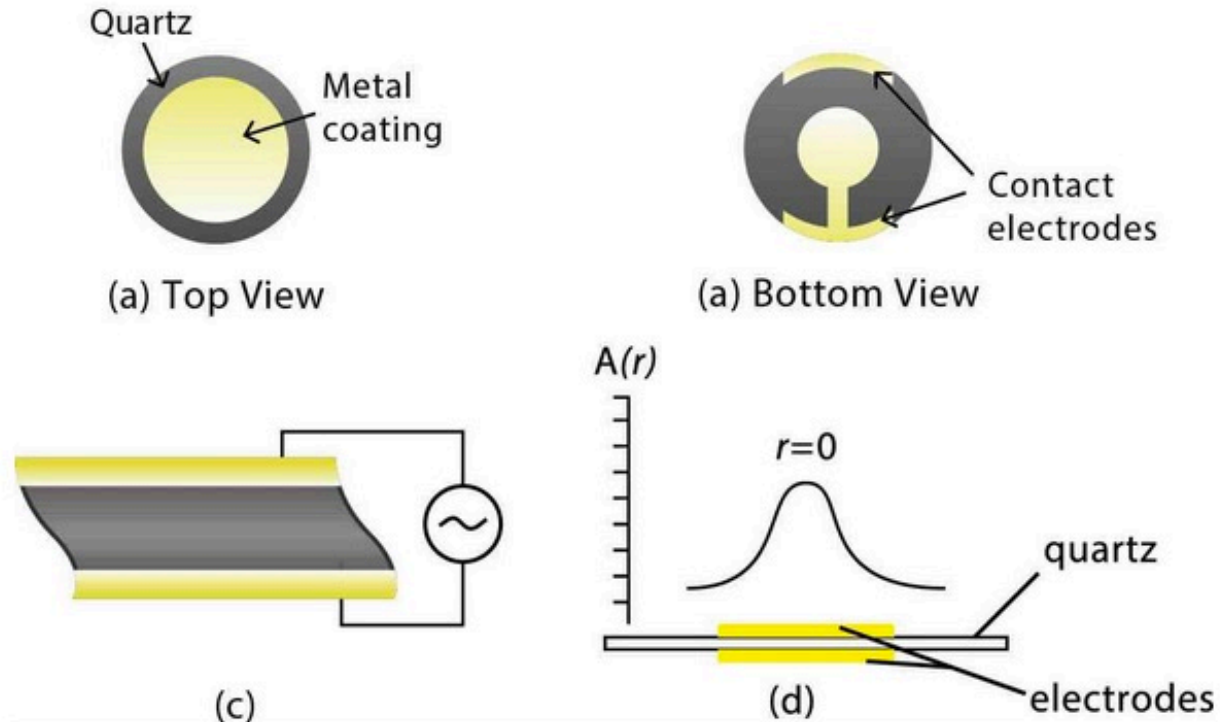

Figure 27 Piezoelectric in a QCM. Image taken from https://www.nanoscience.com/techniques/quartz-crystal-microbalance/

make in situ experiments even within devices made of metallic components. Last but not least, their weak energy makes SANS experiments absolutely not destructive, which is of great importance in biology or for the expertise of industrial devices.

1.11. The Quartz Crystal Microbalance

The Quartz Crystal Microbalance (QCM) is an extremely sensitive dynamical mass balance able to measure changes in mass per unit area in the range of microgram and even nanogram. This technology is based on the piezoelectric properties of the quartz (see section 1.6). A quartz disc is made to oscillate at a defined frequency by applying a suitable voltage through metal electrodes. The addition or removal of mass onto the electrode surface causes a change in the piezo-electrode system thickness and, therefore, in the oscillation frequency. In particular, when the mass increases, the frequency decreases (Fig. 26); by monitoring it in real time, information about molecular interactions or reactions occurring at the electrode surface can be obtained.

Besides the piezoelectric behavior, quartz also possesses a unique combination of properties that make it an ideal candidate for ultrasensitive devices. It is abundant in nature, and it is easy to grow and process. In addition, α-quartz, the phase of quartz that can be used as a resonator, is thermodynamically stable up to 573 °C. Quartz wafers are obtained by cutting a bulk quartz crystal at specific orientations with respect to the crystallographic axis. The metal electrodes (usually gold) are directly evaporated on both sides of the wafer. The common 5 MHz quartz crystal has a corresponding thickness of approximately 330 µm.

The basic principle on which this technique relies, i.e. the relation between the frequency oscillation and the mass on the surface electrode, is described by the Sauerbray equation:

$$\Delta m = -C \cdot \frac{\Delta f}{n} \tag{7}$$

where Δm is the mass change, C is the sensitivity constant and depends on the property of the crystal used, Δf is the resonance frequency change and n is the number of the odd harmonic (1,3,5,7… etc).

This equation assumes that a small mass added to the crystal can be treated as an equivalent change in the mass of the quartz crystal itself. Therefore, to consider the Sauerbray equation valid, the added mass must be rigidly adsorbed on the quartz surface with no slip.

Another limitation is that the added mass must be uniformly distributed over the active area, i.e., the area where the electrodes overlap. The crystal vibration occurs only in this region: the amplitude of vibration, A(r), peaks in the center of the electrode, r = 0, and tapers off in a Gaussian fashion towards the edges of the electrodes (Fig. 27).

To summarize, the Sauerbrey equation is valid under the following three conditions:

1. the added mass is small compared to the mass of the crystal itself
2. the added mass is rigidly adsorbed
3. the mass is equally distributed over the active area of the crystal.

In a QCM instrument, the quartz crystal described above is secured by a crystal holder that also provides the electrical connection. An oscillator drives the crystal to its resonance frequency, and a controller reads the frequency change and stores process parameters.

The quartz crystal holder is usually placed in a thermostated chamber since the oscillation frequency stability is affected by temperature changes. The chamber can be customized to perform measurements either in air, vacuum, or liquid media.

Chapter 2. Characterization of ferritins

2.1. Introduction

2.1.1. Gating of ion channels in medicine

The control over the gating of ion channels is essential in medicine. Currently, they represent the second largest drug targets after G protein-coupled receptors (GPCRs)[114]. Many ion channels, for example, are involved in nociception (the sensory process that brings to the pain sensation) and represent the target for focused analgesia[115]. Drugs targeting Na^+, K^+, Ca^{2+} and Cl^- ion channels influence all organs or systems related to neuronal activity, including the central nervous system (CNS), the peripheral nervous system, and the cardiovascular system[116]. Precise inhibition or activation of a distinct type of ion channel is also crucial in research, particularly in neurobiology, where it is used to study the role of a specific cell type within a circuit and the role of this circuit in complex neural networks. Francis Crick observed that to assemble a general theory of the mind, "a method by which all neurons of just one type could be inactivated, leaving the others more or less unaltered" would be required[117]. Since one fundamental goal of modern neuropharmacology is to causally link ion channel activity in given neuronal pathways with alterations of circuit physiology and ultimately of behavior, the utility of classical pharmacology in vivo in achieving this goal is limited, due to inadequate temporal precision on the timescale of neural signaling and lack of selectivity[115]. In addition, most of the drugs cannot reach the brain since they are not able to pass the blood-brain barrier. In the next sessions, approaches to control ion channels are discussed.

2.1.2. Optogenetics

In the last years, the development of optogenetics has been a revolution in neuroscience. This technology allows controlling ion channel activity with unprecedented spatial and temporal precision and thus overcoming the pharmacological approach's main limits. It uses genetic methods to express light-sensitive ion channels that can be controlled in vitro and in vivo by a suitable light source. An example of these light-activated proteins are microbial opsins. When these proteins are covalently bound to retinal – a vitamin A–related organic cofactor that serves as the antenna for photons –a photon's adsorption induces the retinal isomerization and triggers a sequence of conformational changes within the opsin partner. The combination between opsin and retinal is called rhodopsin. It is characterized by a unitary nature, as it combines the two tasks of light sensation and ion flux into a single protein. With the development of optogenetics, single-component optogenetics tools for neuronal excitation or inhibition have been implemented. Optogenetics began with a channelrhodopsin, introduced into hippocampal neurons in 2005[118] and developed thanks to the work of Hegemann, Bamberg, and Nagel[117] who discovered and characterized the first single-component optogenetic channels (ChR1 and ChR2) in unicellular algae and bacteria. This discovery was followed by the visionary work of Deisseroth, who expressed ChR2 channel in the central nervous system, showing that it was possible to control the firing of neurons by light[117]. Since the early works, the optogenetic toolbox has been vastly expanded including dozens of single-component proteins activated by various wavelengths of light, with various ion conductance regulation properties that operate in neurons over a wide range of speeds (from milliseconds to tens of minutes), enabling broad experimental configurations and opportunities.

The major advantage of this technique is that through genetic manipulation, light sensitive channels can be expressed in specific type of neurons in model organisms. In addition to the fundamental

scientific understanding of how specific cell types contribute to the function of biological tissues such as neural circuits in vivo (e.g. in the amygdala[119]), optogenetics has been used to study Parkinson's disease and other neurological and psychiatric disorders and constitutes the most powerful experimental approach to study the complexity of the brain[120]. Light-delivery technology is clearly central in optogenetics. In vitro, the main sources of light are mercury arc lamps[118,121,122], lasers[120,123–125] and light-emitting diodes (LEDs)[126,127]. In vivo, stimulation of behaving animals has been conducted primarily with laser light delivered to the transduced tissue via optical fibers inserted through chronically implanted cannulas[128–130]. These invasive implants are necessary due to the high frequency wavelengths of the used lights, which are poorly penetrating into tissues. Indeed, all the relevant light-gated proteins which are so far available for optogenetics, are activated by wavelengths which peak in the blue-green region of the light spectrum. All that, combined with the need of precise surgical skills, represents a severe drawback of the technique. Moreover, the wavelengths of these lights are absorbed by flavins, hemoglobin and other chromophores producing radicals and hence toxic side effects[131].

2.1.3. Magneto-genetics: the noMAGIC project

The further evolution of optogenetics would be the possibility to control the ion channel activity using non-harmful stimuli able to penetrate deeply into tissues. Overcoming the limits mentioned above would pave the way to a new study in research and medicine. Among the possible stimuli, the magnetic field (MF) is a promising option. Indeed, it is already used in the medical field, for diagnosis and in therapy. In Magnetic Resonance Imaging (MRI) and Transcranial Magnetic Stimulation (TMS), it can reach values even up to 8 T[132]. Moreover, many animals can perceive the magnetic field of the earth, like migrating birds, mollusks, and arthropods[133]. A large number of behavioral experiments has established the existence of a magnetic sense in animals; nevertheless, so far only little is known about the biophysical principles behind this ability[134]. Since channels controlled by MF have not yet been identified in natural organisms, the most convenient pathway is the synthetic one. Therefore, a suitable magnetic receptor to be coupled to an ion channel must be identified. Extracellular iron nanoparticles could be good candidates as they are affected by the action of a magnetic field. However, their injection in living organisms is invasive, time-limited owing to particle internalization[135], and, as the applied particles only decorate cells locally, they cannot be used to activate dispersed cells. Instead, the paramagnetic iron contained in the protein ferritin can be employed as an endogenous nanoparticle magnetic receptor.

In a recent work of Stanley et al.[136], a genetically encoded system for remote regulation of gene expression by low-frequency radio waves (RFs) or a magnetic field was designed. They co-expressed a modified TRPV1 channel with an N-terminal fusion to an anti-GFP nanobody, and a ferritin protein with an N-terminal fusion to GFP. TRPV1 are cation selective channels belonging to the superfamily of transient receptor potential ion channels (TRP)[137]. This results in the tethering of GFP-tagged ferritin to the modified TRPV1 at the cell membrane. This engineered ion channel was tested *in vitro* and *in vivo* on diabetic nude mice. In both cases, the results showed that RF or a magnetic field could gate the ion channel. A similar construct was designed in the ERC project noMAGIC (noninvasive manipulation of gating in ion channel) by Prof. Moroni's group. They are the first to use a potassium channel in the design of a magneto-genetic tool. In particular, they took advantage of a viral

potassium channel (Kcv) to build a K^+ temperature sensitive channel using a synthetic biology approach.

The K^+ temperature sensitive channel with an EGFP-nanobody attached at the N-terminus was co-transfected in HEK 293 cells with mouse ferritin (mFT) linked to EGFP thus obtaining a construct of a temperature sensitive ion channel linked to the iron-storing protein ferritin.

2.2. Results and discussion

2.2.1. Analysis of ferritins by AFM

Part of this work was to characterize, by atomic force microscopy, one of the key components of the construct mentioned above: ferritins.

Three different types of ferritins were analyzed:

1. *Pyrococcus furiosus* ferritin (in the apo- and holo- form)
2. Horse spleen holo-ferritin
3. *Humanized Archaeoglobus fulgidus* apo-ferritin

The AFM characterization of ferritins was performed through the morphological analysis. AFM images were acquired to obtain information about the size of this protein, as well as its self-assembly equilibrium. To this purpose, the analysis of a statistically relevant number of ferritins in the micrographs was performed on MATLAB, by means of custom data analysis routines.

The preparation of the sample, the imaging buffer and the substrate are essential parameters that must be carefully selected to obtain useful images.

It is important to highlight that this is a statistical analysis. For this reason, the concentration of the protein on the substrate must be carefully tuned: a high concentration is required in order to have enough statistical data. On the other hand, a suitable portion of the substrate must be exposed, and ferritins must be isolated and divided (clusters must be avoided) so that their height can be calculated from the substrate to the top of the particle. Since these iron storage cages are spherical in shape, it can be assumed that the height of the sphere corresponds to its diameter. As the AFM resolution along the z axis is remarkably high, the size of the proteins can be obtained with high accuracy and precision.

2.2.2. Choice of the experimental parameters

2.2.2.1. The substrate

To tune the substrate density, three parameters are particularly important: the sample concentration, the incubation time, and the substrate.

The sample concentration is generally kept in a range between mg/mL and µg/mL. In the case of self-assembling proteins it can be a critical parameter as it will be discussed later.

At the same sample concentration, the incubation time can modify the density of protein particles on the surface: reducing the incubation time, decreases surface concentration as proteins have less time to reach the surface before the rinsing step.

The choice of the substrate also plays a crucial role. To ensure surface adhesion of the proteins, electrostatic interactions are typically exploited. Therefore, the surface charge of a given substrate, related to the isoelectric point (IEP) of PfFt, can make a huge difference. The IEP of apo-ferritin (without iron core), and holo-ferritin (with iron core) is around 4.5. This means that, at a physiological pH (*ca* pH 7), the protein is negatively charged. Among the possible AFM substrates, mica was selected. Substrates such as SiO_2, flat gold and HOPG are also reported in the literature.

However, SiO_2 requires a cleaning procedure more complicated than mica while HOPG and flat gold allows taking advantage of gold-thiol (from cysteine residues) bonds formation. However, $PfFt_s$ do not possess cysteines. HOPG can easily expose a clean surface when it is required but the planar areas are quite small.

Mica, instead, due to its lamellar structure, can be cleaved with a small piece of adhesive tape, thus exposing a freshly clean and atomically flat surface. This substrate, at pH 7 is negatively charged. As already mentioned, also ferritins are negatively charged at physiological pH, therefore a repulsion between sample and substrate occurs. For this reason, a second substrate was prepared incubating the mica with a solution of poly-L-ornithine, thus obtaining a positively charged adsorbed layer. Indeed, poly-L-ornithine is a polyamine, and at physiological pH the NH_2 groups are protonated, bearing a positive charge. It is worth noting that at a certain distance from the substate, the electrostatic interaction is influenced by the protein net charge. When the protein is close to the surface, local electrostatic interactions come into play, due to the individual residues and the readjustment of the protein structure. Therefore, it is very difficult to predict the adhesion of ferritins to the substrate only on the basis of the isoelectric point and the surface charge of the substrate. Nevertheless, the substrate charge influences the surface concentration, as reported below.

2.2.2.2. The imaging buffer

AFM allows to perform protein analysis in a liquid environment. Evidently, the imaging buffer plays a role in the sample behavior. The ionic strength influences the screening length, as long as specific adsorption is negligible, and therefore the interactions between the surface and the sample will be different depending on the buffer composition. Moreover, In-liquid imaging permits to use a buffer solution suitable to a particular protein. In the present work, the experiments were performed with three imaging buffers:

1. Milli-Q water (pH ≈ 6, ionic strength < 10^{-6} mM)
2. PBS (pH ≈ 7.4, ionic strength ≈ 150 mM)
3. HEPES 20 mM, NaCl 150 mM (pH 7, ionic strength ≈ 150 mM)

All the analyses performed in liquid resulted in being rather complicated. The proteins proved to be weakly bonded to the surface. In-liquid imaging was difficult as the proteins were often displaced by the tip during the scan. For this reason, imaging conditions had to be carefully regulated. Peak Force Tapping (PFT) was selected as the imaging mode. Indeed, this is the most suitable mode for biological samples in liquid. The setpoint was kept as low as possible (in the range of 150-300 pN) also in order not to deform the proteins. The scan rate was set at 0.4 Hz, requiring around 20 minutes to acquire a single image. Since the FCs acquisition frequency in PFT can reach 4 kHz, there was a fear that it could disturb the aqueous environment locally. Therefore, experiments were carried out at various frequencies, ranging from 0.5 to 4 kHz. However, up to 2 kHz, no relevant differences were observed. 2 kHz was therefore selected as ramp frequency to increase the resolution as much as possible with the same scan rate.

2.2.3. AFM of *Pyrococcus furiosus* holo-ferritin

The highly thermostable ferritin from the hyperthermophilic archaeal anaerobe *Pyrococcus furiosus*, referred to as PfFt, was chosen due to its thermostability properties, as it retains its activity even after several hours of incubation in boiling water[138]. It can be purified from *E. coli* with a relatively

simple procedure and obtained in high yields. For these reasons, and since a characterization of this ferritin is missing in the literature, PfFt was selected as a model system for this study.

2.2.3.1. AFM of Pyrococcus furiosus holo-ferritin in Milli-Q water

Pyrococcus furiosus holo-ferritins were observed in milli-Q water, both on mica and on polyornithine. From these experiments, the effect of the surface charge of the substrate is evident. As the charges of ferritins and polyornithine have an opposite sign at the pH of the analisys (pH 6-7), the expected interaction during the incubation time is higher. The results confirmed this hypothesis. Indeed, at the same concentration and incubation time, the particle density on polyornithine was remarkably higher than on mica. To obtain a similar surface density for both substrates, the concentration of PfFt settled down was reduced from hundreds of ng/mL to tens of ng/mL.

Figure 28 shows the height distributions of the holo-ferritins analyzed in PFT mode both on mica and polyornithine, at the concentration of 500 µg/mL and 4 µg/mL, respectively (Figure 28a and 28b). On both substrates, a peak around 10-12 nm is observed, which is consistent with the dimension of a 24-*mer*, as reported in the literature[139,140]. Smaller particles around 1-2 nm are also observed on both the height distributions, while a peak at *ca* 7 nm is observed only in Figure 28a. Only a few studies on the self-assembly mechanism of ferritins have been conducted, but they suggest that the 24-*mer* is formed by a series of concentration-dependent association reactions

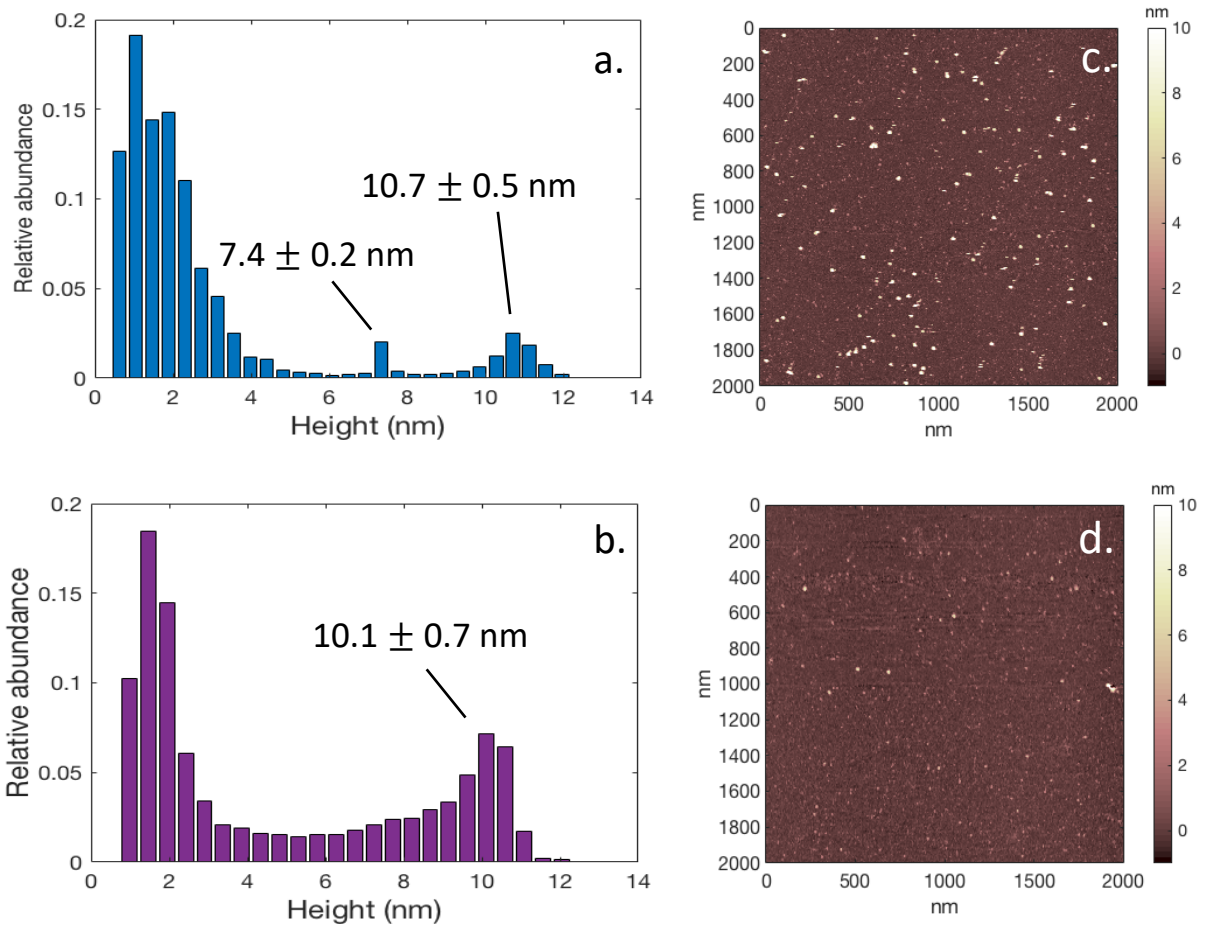

Figure 28 a) Height distribution of PfFt holo 500 µg/mL on mica, b) height distribution of PfFt holo 4 µg/mL on polyornithine in Milli-Q water, c) micrograph of PfFt holo 500 µg/mL on mica, d) micrograph of PfFt holo 4 µg/mL on polyornithine in Milli-Q water.

involving a mixture of oligomeric subunits, with dimers that act as assembly intermediates[141]. These subunits include the monomers, dimers, trimers, hexamers and dodecamers, as suggested by intrinsic fluorescence, far-UV circular dichroism data, and glutaraldehyde cross-linking experiments[142]. The dimer appears to be the most populated species[142], and its stability in solution was demonstrated by sedimentation velocity and analytical ultracentrifugation of this protein at various pHs[143].

The peak at 7 nm, therefore, could be one of these forms, likely the 12-*mer*. As already discussed, it is interesting to note that even if ferritins have a net negative charge, given the large size (their molecular weight is around 500 kDa), it is possible that the protein has interacted with the substrate with suitable amino acid residues. Therefore, adhesion might have occurred even in cases that would seem to be electrostatically unfavored. This could explain the presence of a 24-*mer* (negatively charged at pH 6-7) on the negatively charged mica. Indeed, beyond the net charge, the protein readjusts its structure in order to expose the suitable residues to the surface once it gets close enough, thanks to the van der Waals interactions.

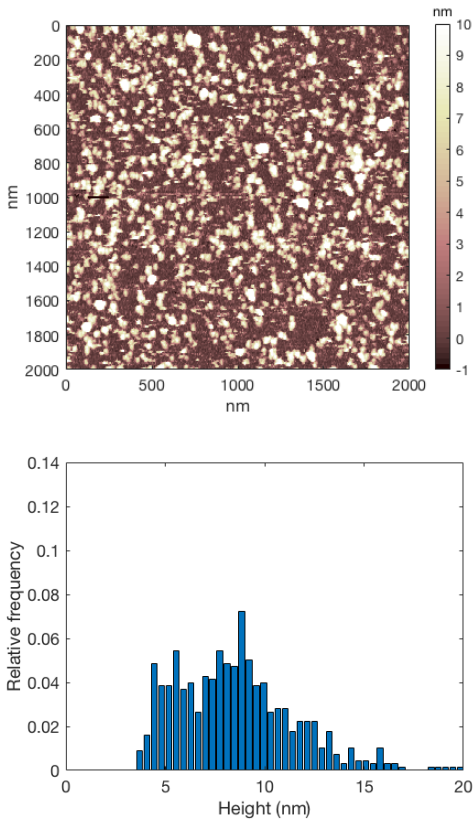

Figure 29 (top) Micrograph of PfFt holo 60 µg/mL on mica in PBS, and (bottom) related height distribution obtained from the micrographs.

The same batch was analyzed after one year in the same experimental conditions to confirm the sample stability, and the same results were obtained.

2.2.3.2. AFM of Pyrococcus furiosus holo-ferritin in PBS Buffer

Biological samples are sensitive to the solvent in which they are suspended. This is particularly true for ferritins, which are formed by the self-assembly of 24 monomers and where an equilibrium between various oligomeric forms occurs. For this reason, a phosphate-buffered saline (PBS) was tested as an imaging buffer. PBS is an isotonic, non-toxic buffer solution commonly used in biological research.

Despite expectations, PBS did not turn out to be a good buffer for the sample. Several concentrations were tested, but a tendency of the proteins to aggregate was always observed. The best result, obtained with PfFt holo 60 µg/mL on mica, is reported in Figure 29, where the height distribution covers a wide range from 4 nm to 16 nm. From the images obtained, clusters can be observed. The tendency of the sample to aggregate in the PBS buffer was also observed with DLS analysis (data not shown).

2.2.3.3. AFM of Pyrococcus furiosus holo-ferritin in HEPES

HEPES (4-(2-hydroxyethyl)-1-piperazineethanesulfonic acid) is also a buffer used for biological samples and is one of the twenty "Good's buffers" (twenty buffering agents for biochemical and biological research selected during 1966-1980 by Norman Good and colleagues)[144,145].

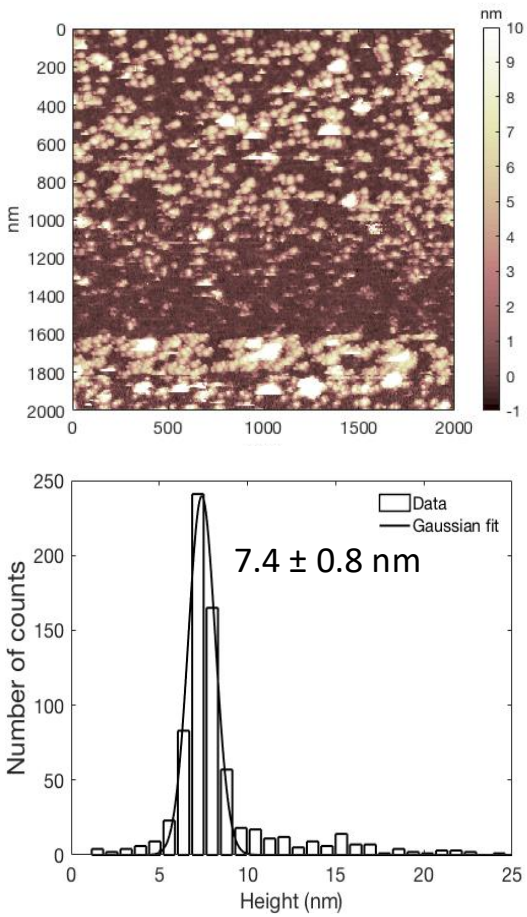

Figure 30 (top) Micrograph of PfFt holo 200 µg/mL on polyornithine in HEPES, and (bottom) related height distribution obtained from the micrographs.

In-liquid imaging in HEPES was highly challenging. In these conditions the proteins are so little bound to the substrate that a quality image was never acquired. In addition, the AFM tip became dirty during almost every imaging acquisition. When a particle such as ferritin sticks to the tip, an artifact is observed in the topography. Since the image results from the interaction between the probe and the sample, artifacts are introduced if the shape of the probe is modified. Consequently, a dull tip will provide a lower resolution image because the tip will not track some details of the surface, while a dirty tip such as the one reported in Fig. 30 (top) will reproduce the particle twice. This particular artifact is called "double tip" and occurs because the probe interacts with the sample both with the tip and with the particle stuck to it (that results as an extension of the tip) during the scan.

Although each image shows a double tip phenomenon, it's still possible to accurately measure the particles' height: the double tip is an artifact that involves the x-y axes but not the z axis which is the one considered for the height calculation.

After several attempts, a sufficient number of micrographs that guarantee enough statistics were acquired. The result of the sample at a concentration of 200 µg/mL in HEPES on polyornithine is reported in Figure 30 (bottom). A dominant peak at 7.4 ± 0.8 nm is observed.

Due to the complexity of the In-liquid imaging, the sample was also analyzed in ambient conditions. In-air imaging is performed without any solution, therefore it does not allow carrying out the analysis in a physiologic environment. In addition, the rinsing phase after the incubation of the sample must be performed using milli-Q water as the salts contained in buffers such as PBS or HEPES would crystallize on the surface once the solution is dried, preventing the observation of the sample. However, a layer of hydration remains despite the drying phase, thus locally maintaining the ferritins in an aqueous-like environment. On the other hand, in-air imaging requires a simpler experimental setup, and is easier to perform. Indeed, the particles are held in position by an aqueous meniscus that forms between the sample and the substrate, avoiding their shift along the surface.

PFT and Tapping Mode (TM) were selected to perform the analysis in ambient conditions. The sample was observed both on mica at a concentration of 250 µg/mL and on polyornithine at a concentration of 4 µg/mL.

A broad peak could be observed in both conditions, but heights of respectively 8 nm and 7 nm emerged. A possible explanation of the 1 nm difference is that the particles may be partially embedded in the polyornithine layer, thus resulting in an underestimation of the height, or that PFT allows the application of smaller forces on the sample than TM, with consequent reduction of sample compression, these effects causing a decrease at the measured height.

2.2.4. AFM of *Pyrococcus furiosus* apo-ferritin

Pyrococcus furiosus ferritins were observed in the apo- form (PfFt-apo), i.e., without iron in the inner cavity. Analogously to PfFt-holo, they were analyzed in various imaging buffers, either in fluid or in ambient conditions. It soon became apparent that this sample was more challenging to investigate.

2.2.4.1. AFM of Pyrococcus furiosus apo-ferritin in Milli-Q water

The experimental conditions chosen for the analysis were decided on the basis of the results obtained with the holo- form. PfFt apo was therefore analyzed in milli-Q water on polyornithine at a concentration of 4 µg/mL using PFT mode in fluid. The results obtained were substantially different from those obtained with the holo form: no proteins with the expected size were observed, while a background of small particles with a diameter of *ca* 2 nm

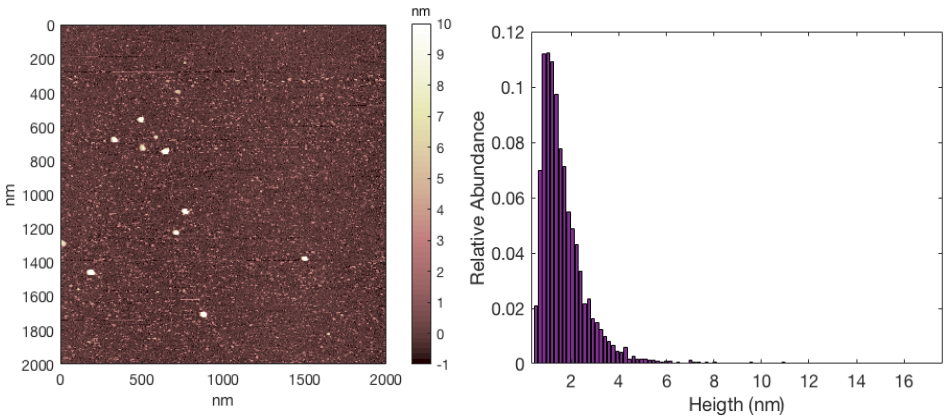

Figure 31 (left) Micrograph of PfFt apo 4 µg/mL on polyornithine in Milli-Q water, and (right) related height distribution obtained from the micrographs.

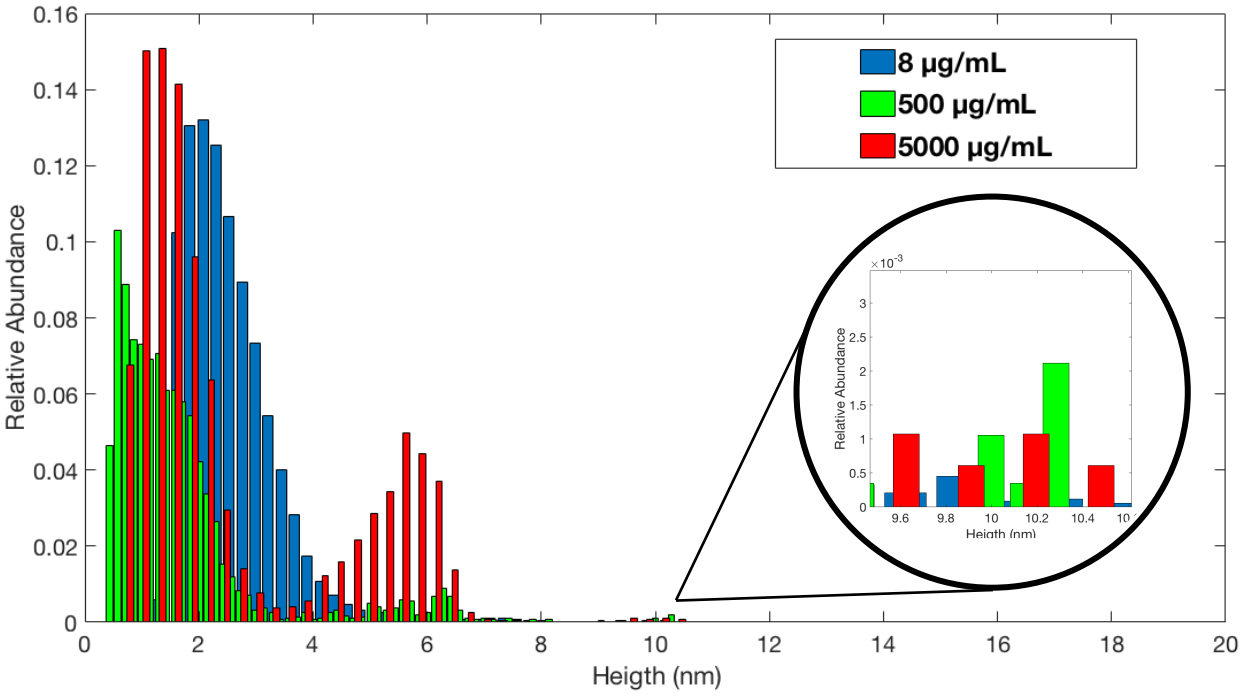

Figure 32 Comparison between the height distribution of PfFt apo with increasing concentration in milli-Q water.

covered the majority of the substrate (Fig. 31). These small particles are not artifacts and are likely the smaller stable subunits (the dimers) that constitute the fully assembled ferritin (the 24-*mer*). Looking for the suitable sample concentration, samples at 1.3, 3, 4, 8, 20, 40, 60 µg/mL concentrations were prepared by dilution of a stock solution and analyzed by AFM.

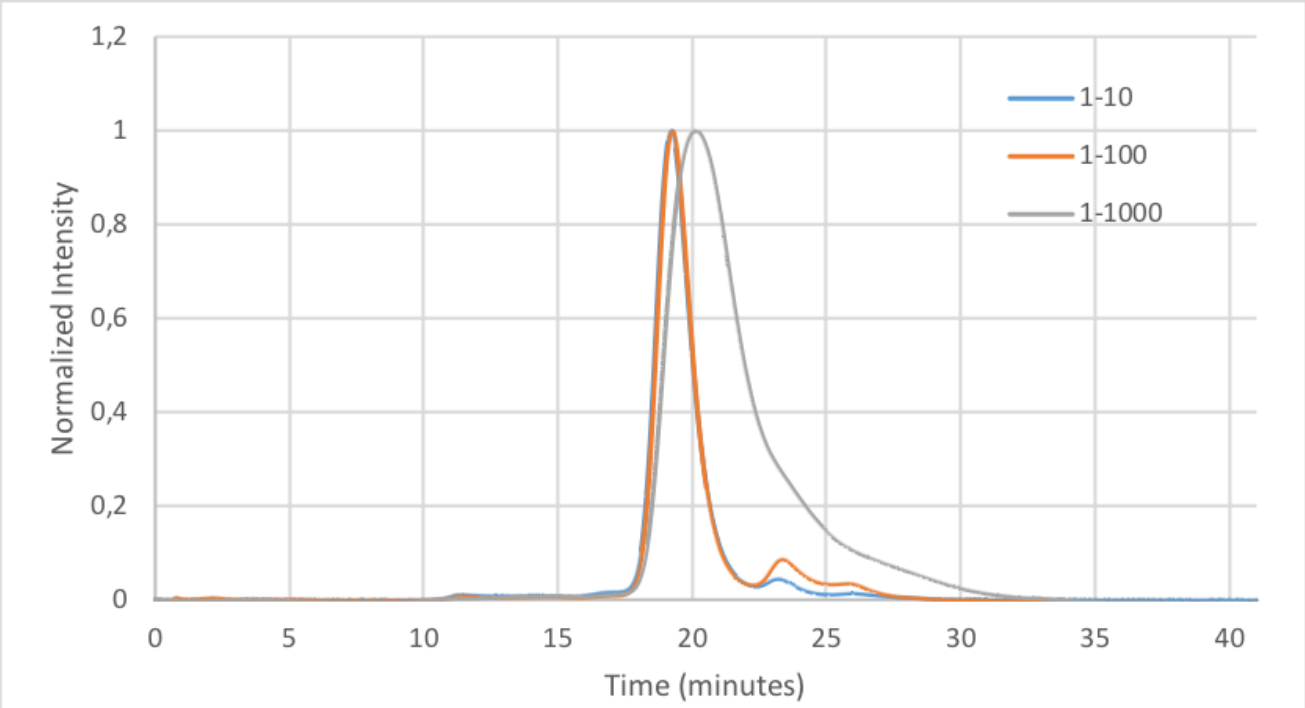

Figure 33 Gel filtration of PfFt apo 800 µg/mL (blue), 80 µg/mL (orange) and 8 µg/mL (grey).

The height histograms of all these samples are similar, showing a peak at around 2 nm and no peaks at 10-12 nm.

The sample was then analyzed on bare mica. The suitable surface concentration of the sample was found to be 500 µg/mL (for the already mentioned effect of the polyornithine's surface positive charge). The results were encouraging, showing bigger particles with a height of 5-6 nm and few particles of 10 nm. The concentration of the sample was further increased to 5000 µg/mL and the relative abundance of observed particles with a height of 5-6 nm increased. However, the relative abundance of the proteins of 10-12 nm was the same. In Figure 32, a comparison between the height distribution of PfFt apo with increasing concentration in milli-Q water is shown. The aggregation state of ferritins appears to be concentration-dependent, as reported in the literature[36]. These results are supported by the PfFt apo gel filtration analysis reported in Fig. 33. The peak related to the sample concentration of 8 µg/mL is right-shifted, indicating a smaller size.

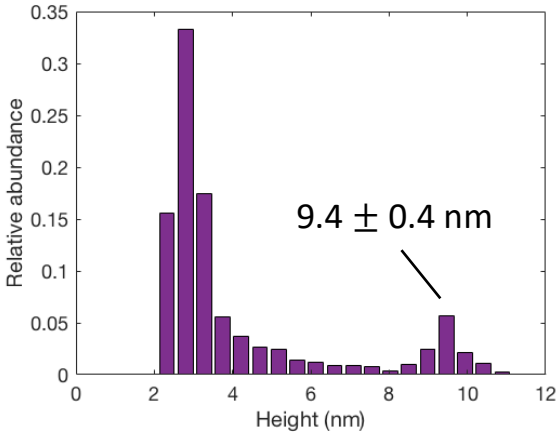

Figure 34 Height distribution of PfFt apo 500 µg/mL on polyornithine 4.5 µg/mL in Milli-Q water.

Once this concentration dependency has been identified, the aim was to investigate the protein on polyornithine at higher concentrations. Increasing the sample concentration was not possible as a low protein concentration was

required on the positively charged substrate, as already discussed.

The first approach was to reduce the incubation time before the rinsing step so that less protein could reach the surface. The time was reduced from 3 minutes to 15 seconds, but the surface concentration was still too high.

Therefore, a second strategy was to reduce the concentration of the polyornithine solution used to functionalize the mica. The tested concentration ranged from 0,1 mg/mL to 4.5 µg/mL. Figure 34 shows the height distribution obtained from In-liquid imaging of PfFt apo (500 µg/mL) on polyornithine (4.5 µg/mL). Besides the peak related to small particles, which is always present, the peak at 9.4 nm indicates the presence of bigger particles, with dimensions close to that observed with PfFt holo. The height difference of a few nanometers could be due to the compression of the protein by the tip, caused by a higher softness of the apo ferritin. Indeed, it is likely that the inner iron core makes the holo ferritin less compressible.

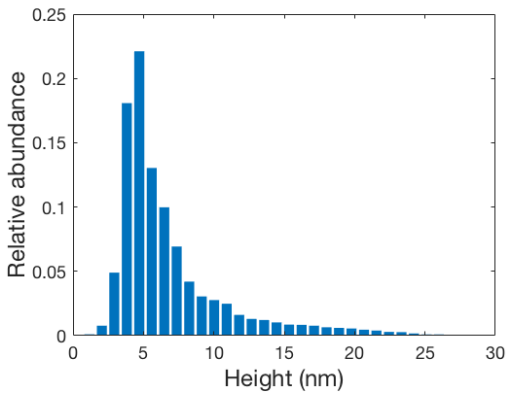

Figure 35 Height distribution of PfFt apo 0.5 mg/mL on mica in PBS

2.2.4.2. AFM of Pyrococcus furiosus apo-ferritin in PBS buffer

In-liquid imaging of PTF was performed on mica using PBS as imaging buffer, at a protein concentration of 0.25, 0.5, 1, 2, 5 mg/mL.

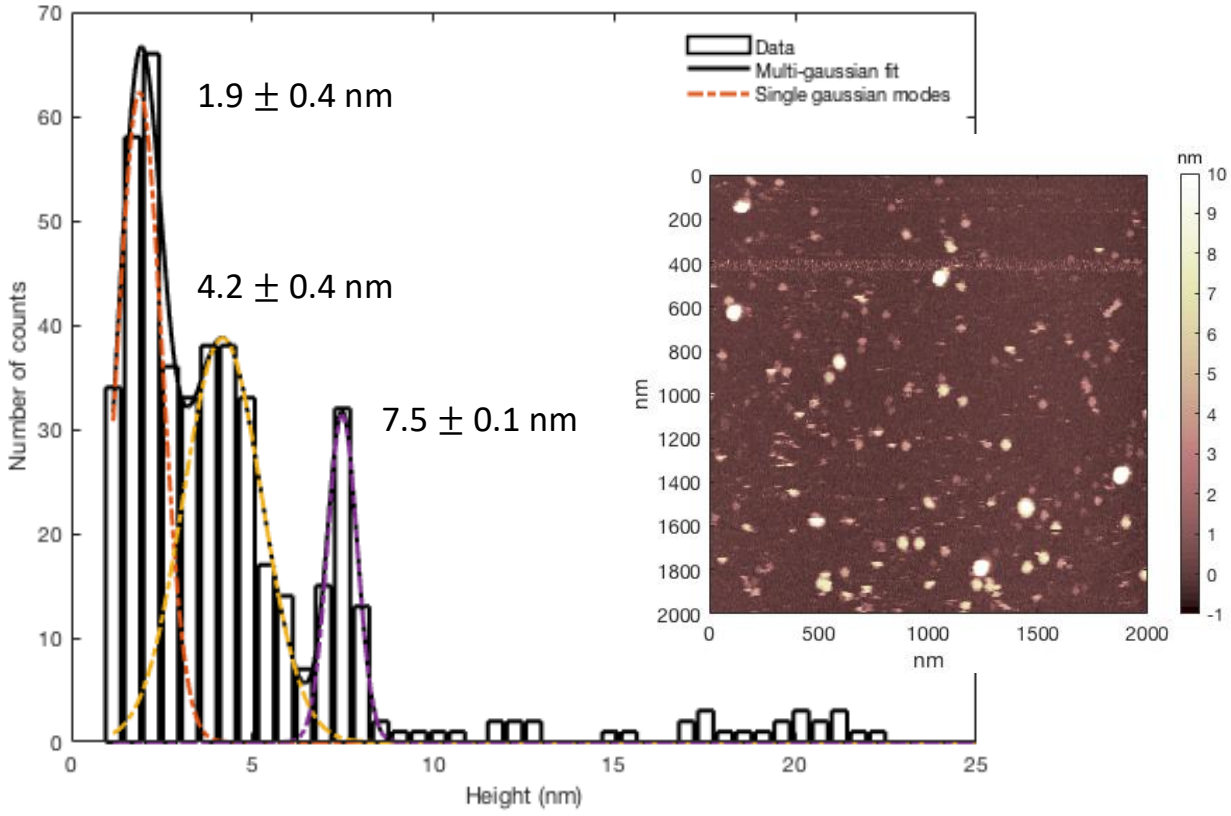

Figure 36 Micrograph of PfFt apo 200 µg/mL on mica in HEPES and related height distribution

Analogously to what was seen with PfFt holo in PBS, a wide range of height distributions was obtained. The histogram reported in Fig. 35 refers to PfFt apo 0.5 mg/mL in PBS on mica, but it is representative of all the sample concentrations tested.

2.2.4.3. AFM of Pyrococcus furiosus apo-ferritin in HEPES

HEPES buffer solution 20 mM, NaCl 150 mM pH 7.4 was then tested as imaging buffer both on polyornithine and bare mica as substrates.

On bare mica, the protein was observed at 200 µg/mL, and the results are reported in Fig. 36. The presence of aggregates larger than 24-*mer* could be observed. In addition to these aggregates, three main peaks could be observed, respectively at 1.9 nm, 4.2 nm, and 7.5 nm. This experimental result might indicate the presence of different oligomers, smaller than 24-*mer*.

2.2.5. Humanized *Archaeoglobus fulgidus* ferritin

All ferritins can be reversibly disassembled at low pH values (pH = 2.0). The re-assembly – at physiologic pH – of human ferritins in the presence of highly payload compounds enables their use as a tool for cell targeted delivery, by enclosing and sheltering suitable compounds, thus preventing immunogenic responses[146]. However, the extreme pH values required to disassemble the protein reduces the type of molecules that can be loaded only to the pH resistant ones.

The chimeric construct humanized apo-ferritin from *Archaeoglobus fulgidus*, from now on referred to as HumAfFt, is characterized by unique self-assembly properties. In fact, in neutral buffers they are disassembled as dimeric species, but they can be easily form a 24-mer aggregate in the presence of divalent metal cations[147] such as Mg^{2+}.

The self-assembly properties of HumAfFt as a function of divalent cations were investigated by analyzing ferritins both in milli-Q water, where the protein disaggregation was expected, and in a solution of 40 mM $MgCl_2$ in milli-Q water where the protein is expected to self-assemble. HumAfFt was diluted at 1.3 µg/ml concentration in the two imaging buffers and incubated for 30 minutes before the In-liquid imaging. The analysis was performed on a polyornithine coated substrate using PFT mode. The size of the observed particles is the same with both buffer solutions (Fig. 37). In particular, mostly small particles with a height of around 1 nm were detected.

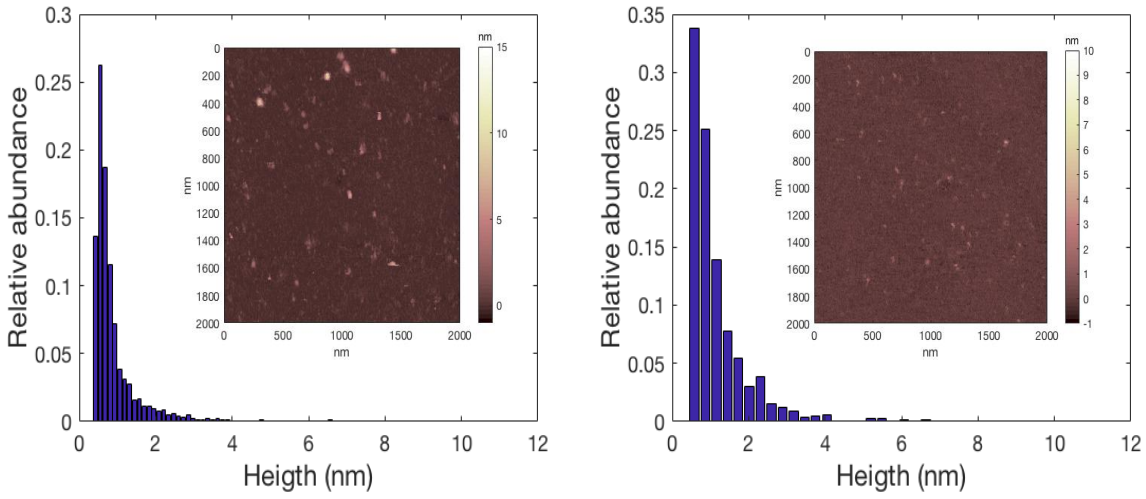

Figure 37 (left) HumAfFt apo 1,3 µg/mL on polyornithine in Milli-Q water and (right) HumAfFt apo 1,3 µg/mL on polyornithine in $MgCl_2$ 40 mM

The concentration of $MgCl_2$ was then increased from 40 mM to 100 mM. Moreover, to avoid the interference of polyornithine's positive charges, bare mica was used as the substrate. The optimal sample concentration was found to be 60 µg/mL. The results obtained in this condition were encouraging: the sample analysed in $MgCl_2$ showed a well-defined peak at 4 nm, and a population of particles ranging from 4 nm to 8 nm. The protein in milli-Q water was still disaggregated, as expected.

A third experiment was performed, keeping the same conditions of the previous experiment, but

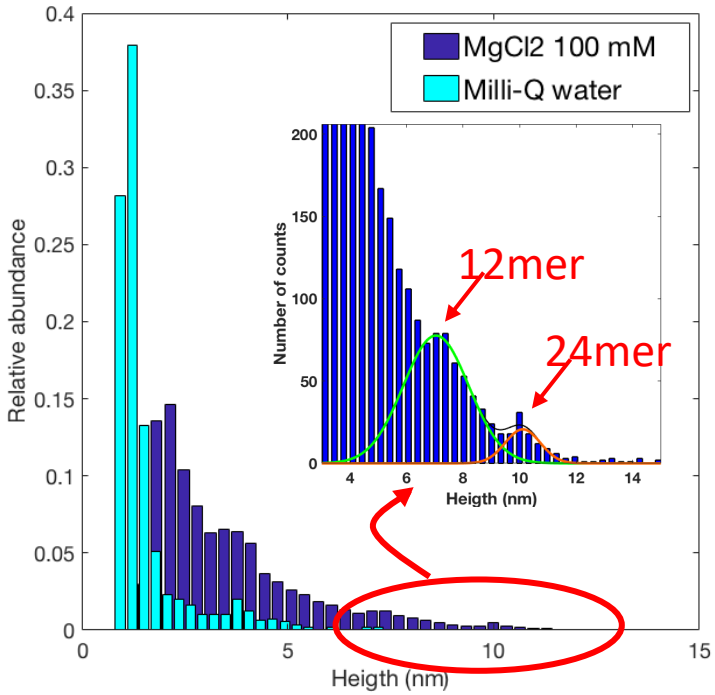

Figure 38 Comparison between HumAfFt apo 60 µg/mL on mica in Milli-Q water (light blue) and in $MgCl_2$ 100 mM, overnight.

increasing the incubation time from 30 minutes to overnight. HumAfFt incubated in divalent cations shows particles with a height of 7 nm (more abundant) and 10 nm, consistent with the size of the 12-mer and the 24-mer (Fig. 38). The equilibrium, once again, appears shifted towards smaller oligomers, likely tetramers and dimers. Worth to note, the sample, incubated overnight in milli-Q water, shows a small fraction of particles with a size around 4 nm, suggesting that an equilibrium between the various oligomers is always present.

2.2.6. AFM of Horse Spleen Ferritin

Horse Spleen ferritins (HSF) are among the most studied ferritins, beeing the first ferritins isolated in 1937[36]. HSF are the most commonly ferritins reported in AFM articles[139,148–153]. It is interesting to note that careful analysis of the works reported in the literature reveals that there is no agreement about the size of HSF.

Holo-ferritins from horse spleen were investigated by AFM. In-liquid imaging was performed in Peak Force Tapping, while In-air imaging was performed in Tapping mode. Mica and mica functionalized with a layer of polyornithine were used as substrates. Milli-Q water was used as the dilution buffer for TM, while 20 mM HEPES with 150 mM NaCl at pH 7.4 was used for In-liquid imaging. The results obtained with PfFt prompted us to discard PBS.

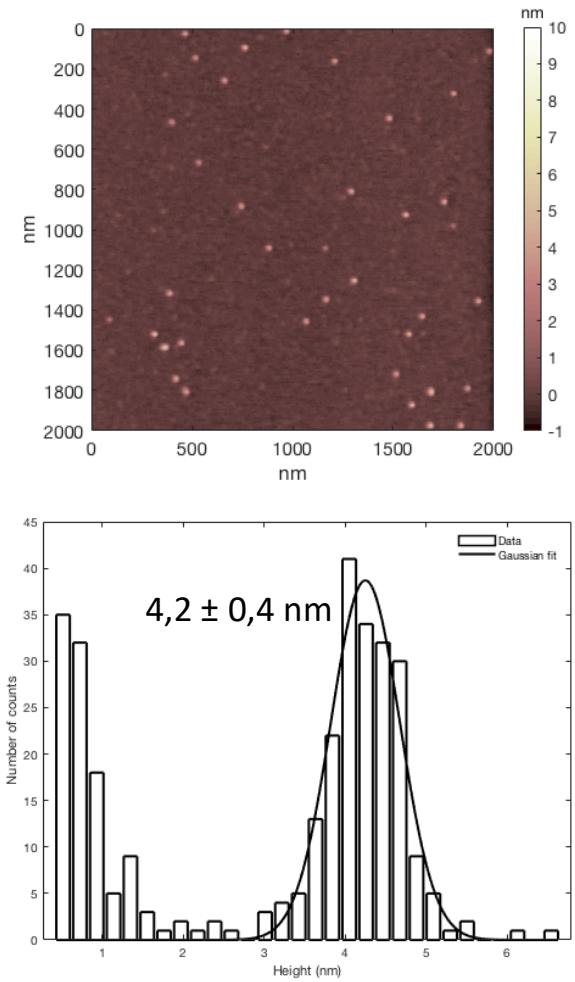

Figure 39 Micrograph of HSF 6.3 mg/mL on mica in ambient conditions and related height distribution

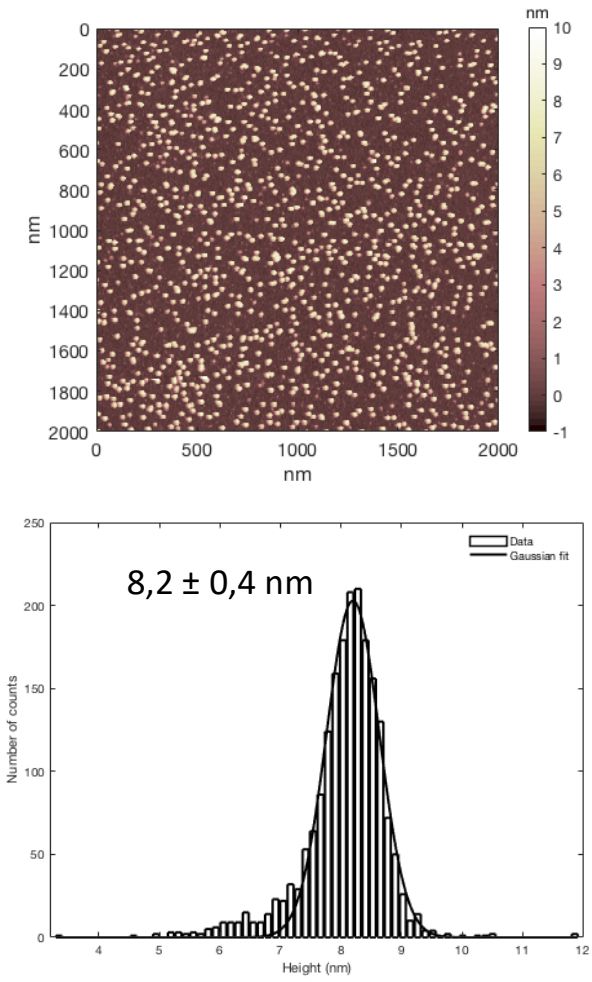

Figure 40 Micrograph of HSF 63 µg/mL on polyornithine in ambient conditions height distribution

HSF was analyzed on bare mica at 6.3 mg/mL concentration in Tapping mode after careful optimization of the sample concentration. The relatively high protein concentration made it impossible to get rid of a homogeneous hydration layer that initially prevented tracking the surface. To overcome this problem high forces were applied in order to pierce the aqueous layer. The proteins were finally imaged. However, an anomalous size of 4.2 nm was observed, as showed in Fig. 39. A possible explanation may be the high applied forces, although is not very likely to induce such a large compression of holo-ferritin.

The sample was then analyzed in TM on polyornithine, reducing the concentration at 63 µg/mL. Quality images were acquired and, as depicted in the height distribution histogram (Fig. 40), a single peak at 8.2 nm is present.

Analogously to PfFt, In-liquid imaging of HSF was quite tricky: the quality of the acquired images was low, and weakly bound proteins caused frequent contamination of the AFM tip. The HSF stock solution was diluted with HEPES to the final concentration of 63 µg/mL and observed on polyornithine using PFT. The results are shown in Figure 41. It is interesting to note that the peak at 10 nm is one of the main peaks, in addition to the one at around 2 nm (probably attributable to dimers). Minor peaks can be observed at 6 nm and 8.8 nm.

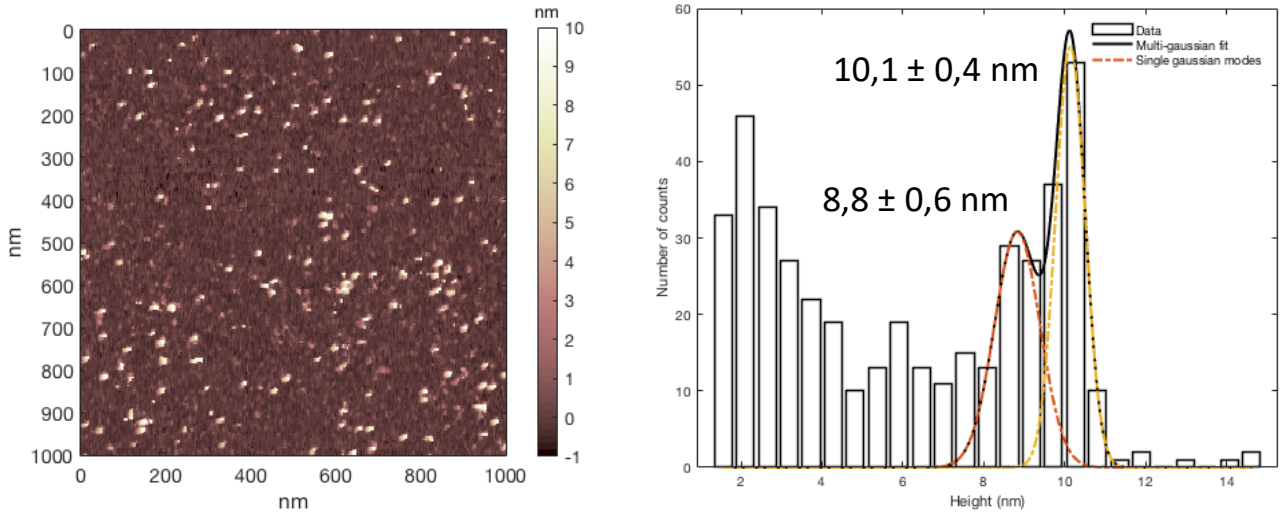

Figure 41 Micrograph of HSF 63 µg/mL on polyornithine in HEPES and related height distribution

2.2.7. Labelling strategies for apo- and holo-ferritins

Although the opening of Stanley's magneto-genetic construct has been proved, the debate about its mechanism is still open. The main hypotheses that have been proposed are:

1. Activation through a thermal effect: the radio-frequency (RF), or a magnetic field moved with respect to the magneto-genetic construct, heats the iron oxide nanoparticles contained into ferritins. The local rising of temperature induces the temperature-sensitive ion channel to open.
2. Activation through mechanical forces: ferritins interact with the magnetic field, thus generating a force that causes the mechanical opening of the channel.
3. Activation through reactive oxygen species (ROS): it has been shown that RF can induce the release of iron from ferritins. This iron can generate ROS via redox reactions or react with membrane lipids generating oxidized lipids that cause the opening of the channel[154].

To investigate whether a mechanical force can activate the ion channel, the first point to check is whether ferritins actually undergo the effect of the magnetic field and move when exposed to it. For this purpose, fluorescence correlation spectroscopy was selected by the group of Prof. Moroni. This technique enables to investigate the diffusion coefficient of a fluorescent particle. The experimental idea was to observe the ferritin's behavior with and without applying a magnetic field and verify if there is a difference in their diffusion coefficient. To be observable, therefore, the ferritins had to be labeled with a fluorescent molecule, which would make them visible under the microscope. PfFt was selected as model protein for this study.

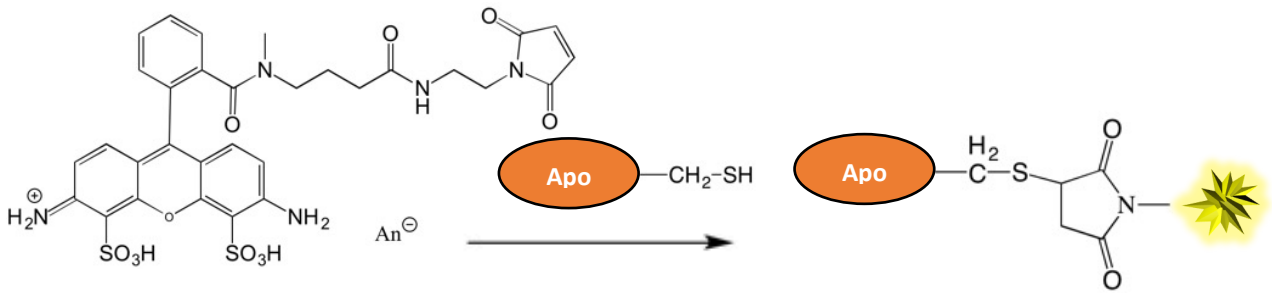

Figure 42 Reaction of Atto 488 maleimide with Cys-PfFt

Fluorescein isothiocyanate (FITC) is a fluorophore often used to visualize proteins in biochemical assays and fluorescence microscopy. It promptly reacts with a primary amine on the protein to form a covalent amide bond[155]. This reaction can easily occur, and apo-ferritins were quickly labelled. They served as the control for holo-ferritins. The reaction also proceeded for holo-ferritins, but the iron core inside these proteins caused the static quenching of the fluorophore, thus preventing the observation with FCS.

A new batch of apo-ferritins was kindly provided by Prof. A. Boffi's group, Department of Biochemical Sciences "A. Rossi Fanelli" from University of Rome "Sapienza". to overcome this problem. The new proteins were mutated to introduce 24 cysteines in the outer part (Cys-PfFt apo). The idea was to label the Cys with a fluorophore spaced from the iron core to avoid the quenching. Maleimides are well suited for the selective reaction with thiol groups. Atto 488 maleimide is a fluorophore with high molecular absorption and quantum yield and a suitable length chain that keeps the fluorescent part of the molecule far enough from the iron core so that quenching is avoided (Fig. 42). Apo-ferritins were therefore successfully labeled. However, the experiment also required the holo- form to perform the FCS analysis. Unfortunately, attempts to apply the experimental conditions previously optimized (*vide infra*) for the iron loading of PfFt apo to PfFt apo labelled with Atto 488 maleimide (from now on named Atto-Cys-PfFt apo for simplicity) were not successful. Indeed, in the centrifugation step, after the addition of iron, the proteins precipitated. The attempt to load with iron Cys-PfFt apo also failed. The hypothesis is that the Cys residues reacted to form disulfide bridges that caused the precipitation of the protein during centrifugation. A new strategy was then devised: since the free thiols interfered with the iron loading, the idea was to force the reaction with the maleimide so to label all thiols. To achieve this, a reagent cheaper than Atto 488 maleimide was chosen. The reaction was carried out with a large amount of 6-maleimidohexanoic acid. This molecule is not fluorescent, but it is cheaper than Atto 488 melemide and thus could be used in large excess with respect to the ferritin and was selected only to prove that what prevents the loading of Cys-PfFt apo is the thiol's condensation. The experiment was not fully conclusive, since the iron loading of the obtained product failed again. However, the Ellman's assay, which is used to quantify the number of free thiols group in a sample, revealed the presence of a large number of free thiols, and this could explain the protein precipitation.

Eventually, due to the complexity of the labelling, this strategy was abandoned, and different techniques were chosen.

2.2.8. DOSY NMR analysis

A new approach was to take advantage of the magnetic field generated in DOSY NMR to obtain information on the behavior of ferritins when a MF is applied. The rationale behind this experiment

was the following: since PfFt apo and holo have the same size, and are exposed to the same MF, a variation in the diffusion coefficient in the two samples should indicate that the holo form is influenced by the MF.

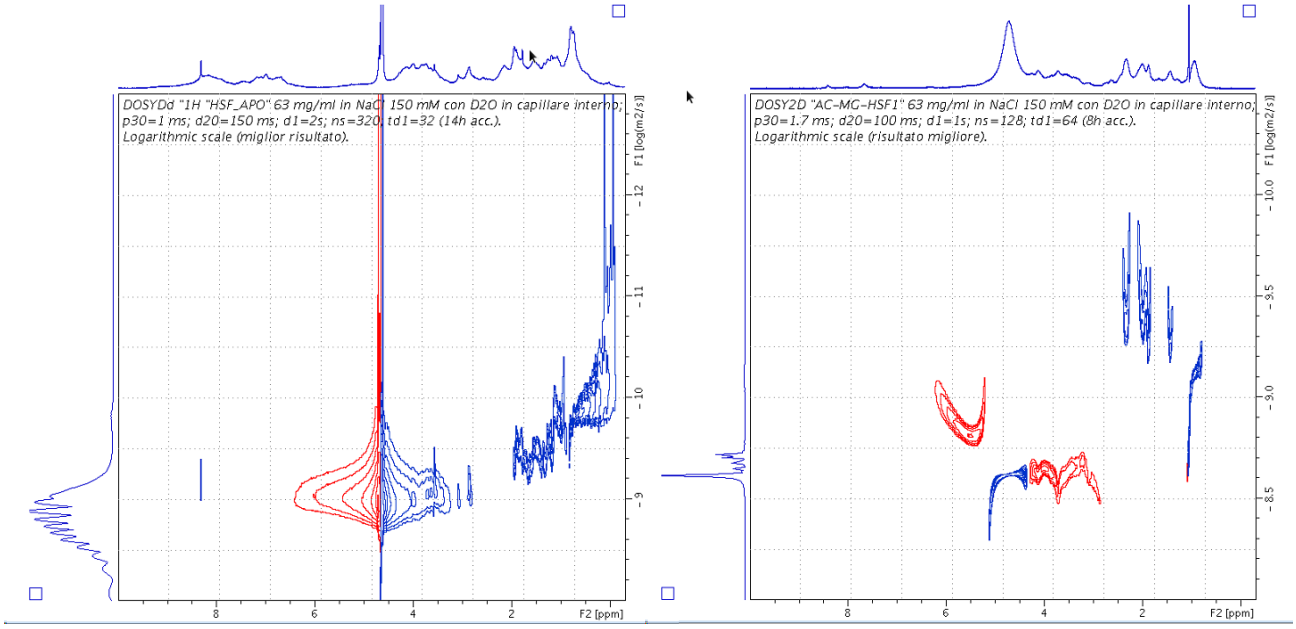

Figure 43 DOSY NMR spectra of HSF 63 mg/mL apo (left) and holo (right) in NaCl 150 mM with 600 MHz NMR equipped with the high-resolution reverse probe (BBI).

A preliminary NMR spectrum (500 MHz) of 10 mg/mL PfFt holo in PBS was acquired but the signals were not visible being covered by broad signals probably generated by the presence of contaminants in the sample. To overcome this problem, a more concentrated solution was required. The purification of PfFt, although easier than that of other ferritins, is still delicate and the production of the required amount of protein was extremely challenging. For this reason, we performed the DOSY NMR experiment on HSF, a protein that can be purchased in large amount.
Two samples of HSF in the apo- and holo- forms, 0.5 mL, at the concentration of 63 mg/mL in 150 mM NaCl were analyzed with a 600 MHz NMR, with the high-resolution reverse probe (BBI). The results are shown in Figure 43. The signals present broad peaks along diffusion axis. The order of magnitude of the obtained diffusion coefficients, $6 \cdot 10^{-10}$ m^2s^{-1}, are in agreement with the expected values but there are no differences between apo- and holo- ferritins. These results suggest that ferritins are not attracted by the MF under the experimental conditions employed. However, we are aware that this is just a preliminary study, and more experiments should follow, in particular by studying the proteins behaviors as a function of the medium viscosity.

2.2.9. Iron loading optimization

To study the behavior of ferritin in the magnetic field, the comparison between apo- and holo- ferritins was required. To this purpose, an experimental procedure to load the PfFt apo with iron was optimized. During the ferritin iron uptake, Fe(II) moves through a hydrophilic channel of the protein shell, where it is oxidized to Fe(III) by a reaction with cellular oxygen in a ferroxidase center (Fig. 44), to form a diferric peroxo complex inside the cavity[156]. To provide Fe(II) to the protein, a 10 mM solution of $FeSO_4$ and 0.5 mM HCl degassed and stored under nitrogen was added dropwise to the apo-ferritin. Working in the Schlenk line avoided the premature oxidation of Fe(II). The pH was monitored with a pH meter and maintained between 6.5 and 7.5 by adding drops of a 1 M NaOH solution. The monitoring of the pH was challenging due to the small volumes of sample with respect to the dimension of the electrode of the pH-meter, and the setup required several attempts before the procedure was optimized. Eventually, loading of PfFt at various loading factors was successful, leading to production of the protein with different amount of iron inside the inner cavity. The amount of iron loaded was characterized through Inductively Coupled Plasma Optical Emission Spectroscopy (ICP-OES). Table 1 reports the values of iron measured by ICP-OES at the different loading factors (see paragraph 5.1.2. for experimental details). The possibility to tune the iron loading of ferritins was interesting from an experimental point of view. Indeed, it is reasonable to assume that ferritins are not fully charged in physiological conditions, and intermediate states of loading are more likely to be a better representation of the reality. A new batch of ferritins loaded at various loading factors was prepared and analyzed by SANS and SAXS in collaboration with Dr. Caterina Ricci from the group of Prof. Del Favero, from Department of Medical Biotechnology and Translational Medicine of the University of Milan.

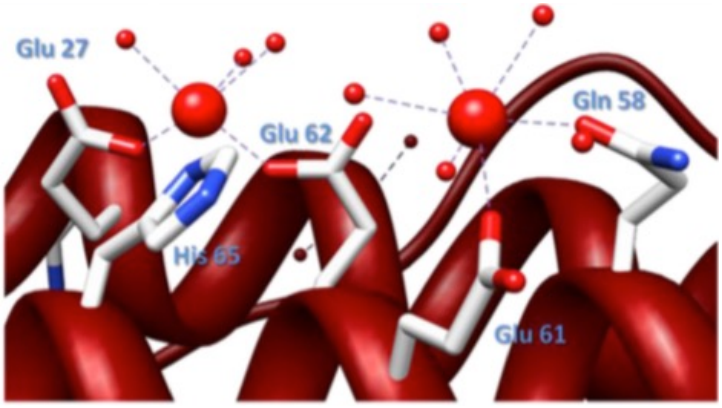

Figure 44 The two iron coordination sites at the ferroxidase center. Image adapted from *1Carmona F, Palacios Ò, Gálvez N, et al. Ferritin iron uptake and release in the presence of metals and metalloproteins: Chemical implications in the brain. Coord Chem Rev. 2013;257(19-20):2752-2764. doi:10.1016/j.ccr.2013.03.034*

Table 1. Iron loading of PfFt at various loading factors

Sample	Volume of $FeSO_4$[a] (µL)	Atoms of Fe per ferritin
Ft1	21	27
Ft2	42	61
Ft3	125	188
Ft4	292	341

[a] $FeSO_4$ 10 mM in HCl 0.5 mM was added to 2 mg of PfFt apo, maintaining pH around 7.

As shown in Figure 45, the progressive loading of the proteins was observed in the results.

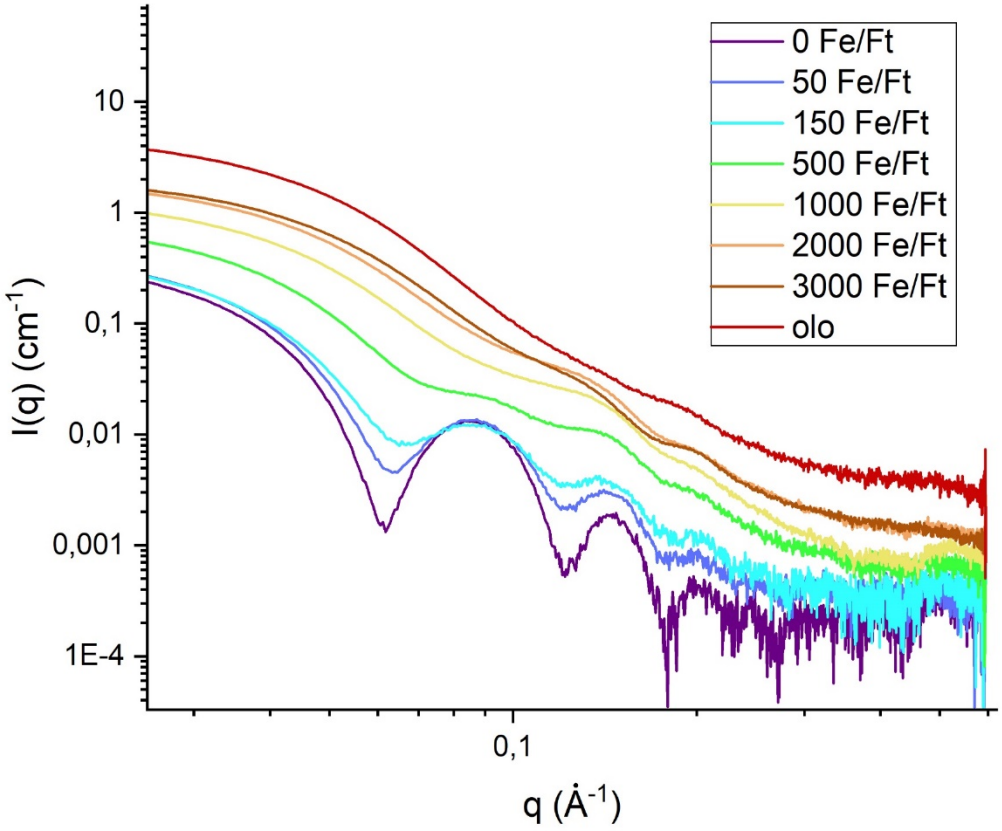

Figure 45 Results of SANS experiments on PfFt at various loading factors.

2.3. Conclusions

The aim of the ERC project noMAGIC (noninvasive manipulation of gating in ion channel) coordinated by Prof. Moroni was to use a potassium channel in the design of a magneto-genetic tool. In noMAGIC, a viral potassium channel (Kcv) was exploited to build a K^+ temperature sensitive channel using a synthetic biology approach. The K^+ temperature sensitive channel with an EGFP-nanobody attached at the N-terminus was co-transfected in HEK 293 cells with mouse ferritin (mFT) linked to EGFP thus obtaining a construct of a temperature sensitive ion channel linked to the iron-storing protein ferritin.

The aim of the work described in this chapter was to contribute to the characterization of ferritins, the key components of the construct mentioned above, by Atomic Force Microscopy, Fluorescence Correlation Spectroscopy and DOSY NMR.

Three different types of ferritins, *Pyrococcus furiosus* ferritin (in the apo- and holo- form), Horse spleen holo-ferritin, and *Humanized Archaeoglobus fulgidus* apo-ferritin were analyzed to obtain information about the size of these proteins, as well as their self-assembly equilibrium. In the AFM analysis, parameters such as sample preparation, imaging buffer composition, and substrate features were carefully selected to obtain meaningful micrographs.

The best results with *Pyrococcus furiosus* holo-ferritins were observed in milli-Q water, both on mica and on polyornithine coated mica. The study confirms the presence of fully self-assembled ferritins

(24-*mer*). Smaller particles around 1-2 nm were also observed. The use of other imaging buffers such as PBS or HEPES did not introduce significant improvements in the quality of the images or in the self-assembly equilibrium. The use of AFM revealed the simultaneously presence of other oligomeric forms (probably examers and dodecamers).

Pyrococcus furiosus apo-ferritin, analyzed in the conditions identified above for the holo-ferritin, provided results substantially different from those obtained with the holo form: no proteins with the expected size were observed, while a background of small particles with a diameter of *ca* 2 nm covered the majority of the substrate. Results obtained at various concentration suggested that the aggregation state of ferritins could be concentration-dependent.

In-liquid imaging of PfFt apo (500 µg/mL) on polyornithine (4.5 µg/mL) showed, in addition to the peak related to small particles which is always present, a peak at 9.4 nm that indicates the presence of bigger particles, with dimensions close to that observed with PfFt holo. The height difference of a few nanometers could be due that fact that the inner iron core makes the holo-ferritin less compressible.

The self-assembly properties of Humanized *Archaeoglobus fulgidus* ferritin, as a function of divalent cations were investigated in solutions of different composition. The salt dependent aggregation of the protein was confirmed.

Horse Spleen ferritins (HSF) were analyzed by AFM. In-liquid imaging was performed in Peak Force Tapping mode, while in-air imaging was performed in Tapping mode. In-liquid imaging of HSF was quite challenging. Significant results of HSF were obtained at a concentration of 63 mg/mL in HEPES where a peak at 10 nm was observed. Various peaks attributable to other oligomeric forms were visible in the height distribution histogram.

Ion channel activation though a mechanical force was investigated by exposing ferritins to a magnetic field and using fluorescence correlation spectroscopy. This technique required Labeling of ferritins with a fluorophore. Apo- and holo-ferritins were labelled with Fluorescein isothiocyanate (FITC) but the iron core inside these proteins caused the static quenching of the fluorophore, thus preventing the observation with FCS. Various approaches were applied to space the fluorophore from the iron core, but none of the strategies used allowed successful labeling of holo-ferritins.

As an alternative strategy to obtain information on the behavior of ferritins under a magnetic field, DOSY NMR was performed on HSF in the apo- and holo- form to measure variation in their diffusion coefficient. The preliminary results showed that no difference is observed.

Lastly, the loading of the apo-PfFt with iron was optimized and characterized through Inductively Coupled Plasma Optical Emission Spectroscopy (ICP-OES). The protocol developed allowed tuning the iron loading. The possibility to control the amount of iron loaded is interesting as it allows reproducing physiological conditions where ferritins are not fully loaded.

Chapter 3. AFM investigation of ionic liquids' toxicity

3.1 Introduction

Ionic liquids (ILs) are salts generally liquid at room temperature[157]. Due to their negligible vapor pressure, controlled miscibility and flammability, and versatility in designing the molecular structure, they are considered "green solvents"[158], and are recently replacing volatile organic solvents in several large-scale industrial syntheses processes[159]. However, despite their "green" reputation, ILs have a certain level of toxicity, confirmed by several studies, mainly based on EC_{50} values[160]. Indeed, most cations of ionic liquids contain linear alkyl chains of various length, and it is supposed that these chains penetrate in the cell membrane, according to a "tail first" mechanism, causing its weakening or even disruption[161]. However, this mechanism has not yet been fully elucidated. Generally, to explore the toxicity of a substance, a standard cell viability assay is used. This type of test measures the percentage of live cells within a population. AFM is also a powerful technique to investigate ionic liquids' toxicity mechanisms. Using supported phospholipid bilayers as a simplified model to mimic the cell membrane, AFM allows studying, at a microscopic level, the interaction between ILs and phospholipid bilayers, to improve understanding of the dynamics related to the toxicity of these compounds.

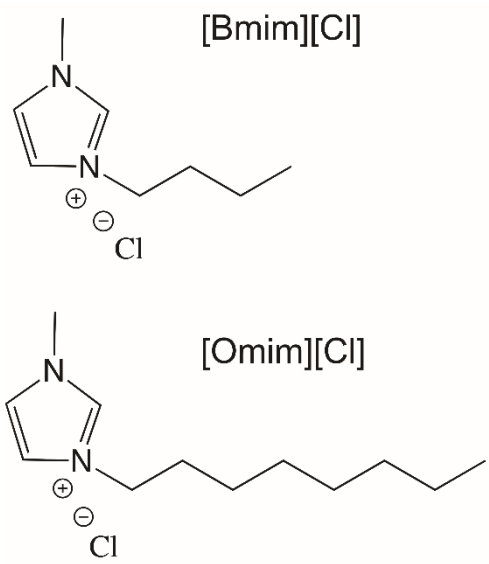

Figure 46 Chemical structure of [Bmim][Cl] and [Omim][Cl].

The present work chose 1,2- dioleoyl-sn-glycero-3-phosphocholine (DOPC) as the phospholipid to prepare the supported phospholipid bilayer. DOPC was selected as it is among the most abundant lipids present in eukaryotic membranes and adequately reproduces some of the properties of the cytomembrane.

Two different experiments using atomic force microscope were designed to study the interaction of a membrane with ionic liquids:

1. Nanomechanics experiments were performed by incubating the sample with two different ionic liquids, varying the concentrations.
2. Specific interactions between the SLB and an eight carbon atoms alkyl chain of a functionalized AFM tip were analyzed using force spectroscopy.

3.2. Results and discussion

3.2.1. Nanomechanics experiments

In order to investigate the effect of the length of the alkyl chain of the cation, two ionic liquids were selected: 1-Butyl-3-methylimidazolium chloride ([Bmim][Cl]) and 1-Methyl-3-octylimidazolium chloride ([Omim][Cl]). As can be seen from Figure 46, [Bmim][Cl] has a chain consisting of 4 carbon atoms, while [Omim][Cl] has a chain of 8 carbon atoms. This experimental design's rational is that the longer the chain, the higher the weakening effect on the SLB.

A phospholipid bilayer was prepared (as described in section 5.2.1.). This sample was then analyzed in peak-force tapping mode, using a ScanAsyst Fluid tip to obtain topographic maps of the surface.

These images provide information on the status of the bilayer. Indeed, it can be homogeneous or have holes or lipid islands. This latter can be both on the substrate and on the underlying bilayer. However, this information is not sufficient since it is impossible to distinguish between the substrate and the SLB only on the basis of the topographic image.
The most important experimental data is the *approaching* force curve. A typical FC that indicates the existence of a single bilayer on the substrate is shown in Figure 47: the tip pushes against the bilayer until its breaking occurs; during the breakage, the force experienced by the tip decreases abruptly and this corresponds to a peak in the approaching FC.

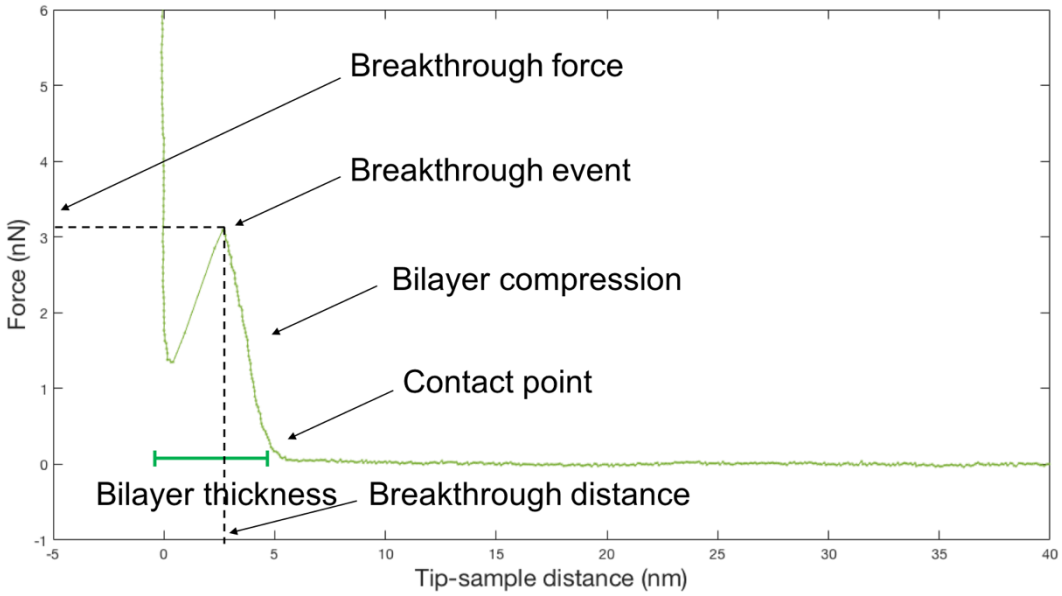

Figure 47 Approaching-phase force curve acquired on DOPC bilayer supported on mica.

Therefore, from the analysis of the *approaching* FCs it is possible to establish whether the sample is a single bilayer, two bilayers superimposed on each other or if what is seen in the image is only the atomically flat surface of mica. In the first case, a single breaking event will be observed (Figure 47) whereas in the second case, the events will be as many as the number of overlapping double layers. In the case of mica since the tip will immediately enter in contact with the rigid substrate, there will be no disruptive events.
From these breaking events, it is possible to obtain the breakthrough force value, *i.e.* the force necessary for the tip to penetrate the bilayer, and the breakthrough distance, *i.e.* the distance of the tip from the mica substrate to the which penetration takes place.
A statistically relevant number of FCs was acquired on the SLB using the auto ramp mode (see section 5.2.1. “nanomechanics measurements” for details).
After collecting a sufficient number of force curves, the phospholipid bilayer was conditioned with [Bmim][Cl] and [Omim][Cl] at various concentrations for 20 minutes, and each experiment was conducted similarly to that described for the sample in the absence of ILs.
The acquired data were expressed as ratio between values measured before and after the addition of the ionic liquid. This normalization rendered such values independent from the radius R of the probe and from both deflection sensitivity and spring constant. In fact, the accurate characterization of the tip’s radius is difficult which makes inaccurate the comparison between the data acquired

with different probes. Furthermore, mechanical-elastic parameters change according to the pressure exerted on the sample, which, in turn, depends on the radius R of the tip. It was then preferable to present the relative variations of the quantities taken into consideration, acquired in the same measurement set and with the same tip. This is possible since the native bilayer, without ionic liquid, is always characterized during each measurement session.

Therefore, the normalized *breakthrough* force was defined as

$$F_b' = \frac{F_b^{IL}}{F_b^0} \tag{8}$$

where F_b^0 is the *breakthrough* force measured before the addition of the ionic liquid and F_b^{IL} is the *breakthrough* force measured after the addition of the ionic liquid.

Similarly, the normalized breakthrough distance was defined as

$$d_b' = \frac{d_b^{IL}}{d_b^0} \tag{9}$$

The decrease of F_b' indicates that a lower force is required to break the phospholipid bilayer relatively to the sample without ionic liquid.

Table 2. Breakthrough force values normalized as a function of the [Bmim][Cl] concentration

Concentration (mM)	F_b'
5	0.913 ± 0.009
10	0.889 ± 0.008
50	0.863 ± 0.012
300	0.705 ± 0.006
400	0.563 ± 0.064
500	0.418 ± 0.027

Table 2 shows, for the different concentrations of [Bmim][Cl], the normalized breakthrough force values and the relative error, calculated as the standard deviation of the mean.

These values, which show a decreasing trend appreciable in Figure 48, agree with the results obtained through numerical simulations[162] as well as through experimental techniques such as the neutron reflectometry experiment[163].
These data seem to confirm the hypothesis that the alkyl chain of the imidazole cation, due to its lipophilicity, penetrates inside the phospholipid bilayer, thus weakening the structure of the bilayer. In fact, as the concentration increases, the forces necessary to break the double layer decrease. In order to look for further evidence supporting the "tail-first" mechanism, new measurements were made by contacting the sample with [Omim][Cl], whose alkyl chain is eight carbon atoms long, compared to 4 of [Bmim][Cl]. Table 3 shows the F_b' values for the different concentrations of [Omim][Cl].

Table 3. Breakthrough force values normalized as a function of the [Omim][Cl] concentration

Concentration (μM)	F_b'
1	0.961 ± 0.077
10	0.912 ± 0.104
100	0.847 ± 0.088

The following considerations can be drawn from the data obtained:

1. analogously to the case of [Bmim][Cl], when the [Omim][Cl] concentration increases, a reduction in the force required to break the phospholipid structure is observed. This indicates that the relationship between the concentration of ionic liquid and the weakening effect of the bilayer is directly proportional.
2. The values of F_b' for concentrations of [Omim][Cl] 10 μM are comparable with those of [Bmim][Cl] at a concentration of 3 orders of magnitude higher. This is consistent with what has been discussed above: the alkyl chain linked to the imidazole ring of a cation of

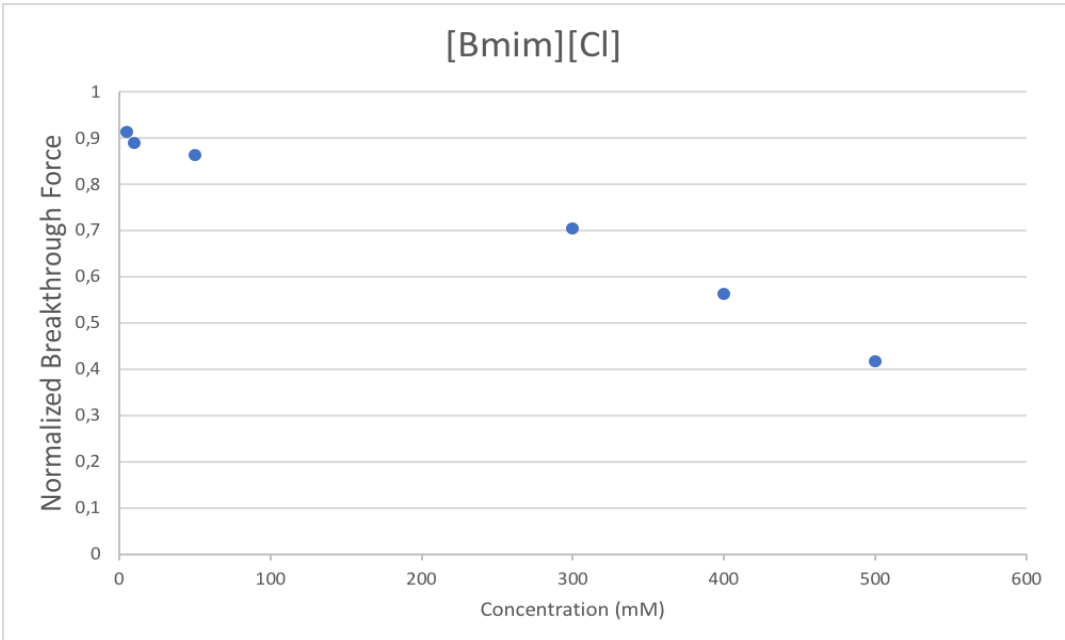

Figure 48 Normalize Breakthrough force values as a function of [Bmim][Cl] concentration.

[Omim][Cl] is twice as long as that of [Bmim][Cl], therefore it is more hydrophobic, and the effect on the phospholipid structure occurs at significantly lower concentrations.

Concerning the normalized *breakthrough* distance values relative to [Omim][Cl], as seen in Table 4, there are no significant variations depending on the concentration and this is in agreement with the fact that ionic liquids do not interact by stratifying above the lipid layer but causing interstitial or substitute defects, which do not change the value of this distance.

Table 4. Breakthrough distance values normalized as a function of the [Omim][Cl] concentration

Concentration (μM)	d_b'
1	1.055 ± 0.007
10	1.082 ± 0.010
100	1.109 ± 0.010

3.2.2. Force spectroscopy experiments

To further confirm the existence of the "tail-first" interaction mechanism discussed in the previous paragraphs, an experiment based on atomic force spectroscopy was designed. An AFM tip was functionalized with a linear alkyl chain of 8 atoms, analogous to that linked to the imidazole ring of the cation of [Omim][Cl], and used to acquire FCs on the DOPC supported phospholipid bilayer.
In this way, instead of letting the ionic liquid diffuse towards the phospholipid bilayer, the alkyl chain is mechanically brought into contact with the bilayer. Since the movement of the probe can be controlled through the piezoelectric transducer, it is possible to move the alkyl chain towards and away by modifying the parameters such as contact time, approach, and departure speed, and observing the interactions between the hydrocarbon and the bilayer by analyzing the force curves during the *retracting* phase.
These curves should show a trend similar to that shown in Figure 49: phenomena of non-specific adhesion are observed due to the tip-sample interaction (1) and specific adhesion interactions between the alkane bound to the tip and the lipophilic tails of the DOPC (2).
The characteristic shape of this interaction is due to the fact that the alkyl chain is linked to a molecule of polyethylene glycol (PEG) which acts as a spacer and allows the two types of adhesion to be separated by a distance equal to the length of the PEG, on the abscissa axis. As the probe moves away from the surface, the PEG molecule completely stretches until it becomes tensioned due to the interactions between the alkyl chain and the bilayer. This behavior generates a recall force that reaches its peak at the maximum extension of the PEG. When the pulling force exceeds the interaction between the lipophilic molecules, detachment occurs. What has just been described is defined by the worm-like chain (WLC) model, used in the physics of the polymer to describe the behavior of semi-flexible polymers in solution. To simplify with an analogy, the cantilever can be assimilated to a fishing pole, the PEG molecule to the line, the alkyl chain to the hook, and the bilayer to the fish.

A heterobifunctional N_3-PEG-NHS commercially available was used to functionalize the AFM tip. The PEG acts as a spacer. Amino functional groups were introduced by covalently modifying the probe tip surface with with APTES ((3-aminopropyl) -triethoxysilane) . This PEG moiety bears a succinimide esther (NHS) at one end that can be exploited to functionalize the surface with an alkyl chain. The alkyl chain is bound to the spacer via click chemistry reaction (Huisgen reaction) between the azide present at the other end of the PEG and the terminal alkyne on the alkyl chain.

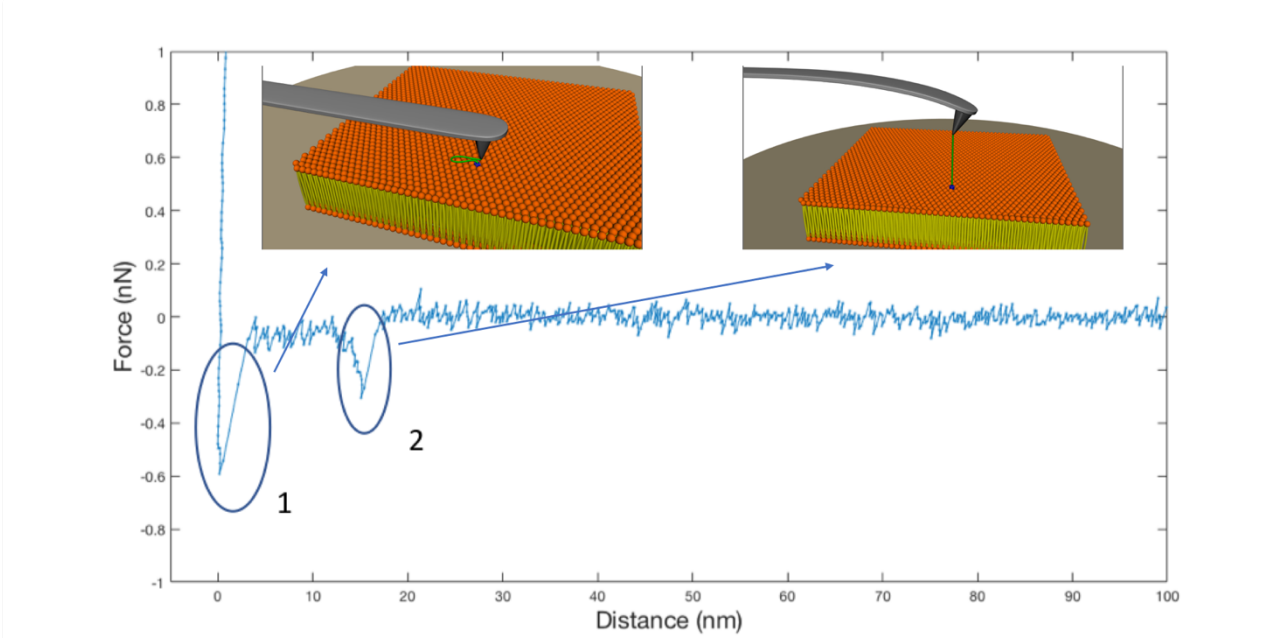

Figure 49 Retracting-phase force curve showing a tip-bilayer aspecitfic interaction (1) and an alkyl chain-bilayer specific interaction (2).

The term click chemistry was introduced by K. B. Sharpless[164] in 2001 to describe reactions that possess the following characteristics: they lead to high yields, have a wide application, create only by-products that can be removed without chromatography, are stereospecific, simple to do, and can be made in easily removable or non-toxic solvents.

The possibility of using the thiol-maleimide reaction for the alkyl-PEG coupling was also initially evaluated. There are similarities between the functionalization method that employs maleimido- and azido- linkers.

Both methods exploit reactions that take place in an aqueous solution, use reagents that are not susceptible to hydrolysis in the time scale in which the reaction takes place, and are very efficient. The high efficiency of the reaction allows using low concentrations of binder and short reaction times. These aspects are very important if we consider that the coupling with traditional methods such as for example the reaction between amine and aldehyde, have slow reaction kinetics and require high concentrations of ligand.

The high selectivity of the thiol-maleimide and azide-alkyne reactions is a further advantage.

Eventually, the azide was selected over thiol due to its greater chemical stability and high reaction rate with the alkyne promoted by the Cu (I) catalyst, which leads to a practically quantitative coupling yield.

A disadvantage of this strategy is the need to use Cu (I) as a catalyst, but the problem can be easily solved by reducing the Cu (II) (coming from $CuSO_4$) with sodium ascorbate, generated in situ from ascorbic acid and NaOH. The susceptibility to oxidation of Cu (I) species and ascorbate requires

operating in an inert atmosphere. For this reason, the tip functionalization reactions were performed in a Schlenk line.

In Figure 50 a schematic representation of the sequence of reactions used in the functionalization of the tip is reported.

The functionalization of the tip was performed through three steps:

1. Amino-functionalization of the tip.
   Standard amino-silanization protocols (in ethanol or other polar solvents) are not applicable due to the possible formation of polysiloxane polymers which make the probes sticky and unusable. The problem can be avoided by using two alternative methods:
   a. the reaction with ethanolamine in dimethyl sulfoxide
   b. amino-silanization with APTES vapors.

   According to what is reported in the literature[165], the functionalization process with vapors of APTES gives better results regarding AFM measurements, therefore this strategy was selected. The silicon nitride tips have numerous silanol groups, in particular after oxidation with a piranha solution. These groups react readily with APTES in the vapor phase.
2. Conjugation of the PEG with the amino groups of the probe.
   The presence of amino groups on the surface of the cantilever allows the binding of PEG-NHS molecules by nucleophilic addition of the amine to the terminal active ester of the PEG.
3. Click chemistry reaction between PEG-N_3 and 1-decyne.
   The last step of functionalization uses a variant of the Huisgen 1,3-dipolar cycloaddition. Indeed, the thermally promoted Huisgen 1,3-dipolar cycloaddition of alkynes with azides requires high temperatures. The process is simplified by using a copper-catalyzed reaction that follows a different mechanism and can be conducted in aqueous conditions, even at room temperature.

Several probes, one functionalized with APTES, one with PEG and one with the alkil chain were obtained by performing the functionalization procedure up to the step 1,2 and 3 respectively. From now on, these probes are named APTES, PEG and C8 for simplicity. A non-functionalized probe (Si probe) was used in the experiments.

Si, APTES and PEG probes were used as controls to prove that the interactions observed with the C8 probe is attributable to the type of interaction hypothesized.

Probes characterization was challenging due to their fragility. Therefore, an indirect characterization method was applied: as AFM tips are made of Si, silicon slides were functionalized with the same protocol used for the probes. A sample obtained after each step of the functionalization was stored for further analysis. The slides were then characterized by XPS spectroscopy and ATR-FTIR. XPS confirmed the presence of APTES.. ATR-FTIR confirmed each step of the functionalization except for the one with PEG.

For each cycle of measurement, auto ramps were acquired in different areas of the sample in order to produce statistically significant FCs.

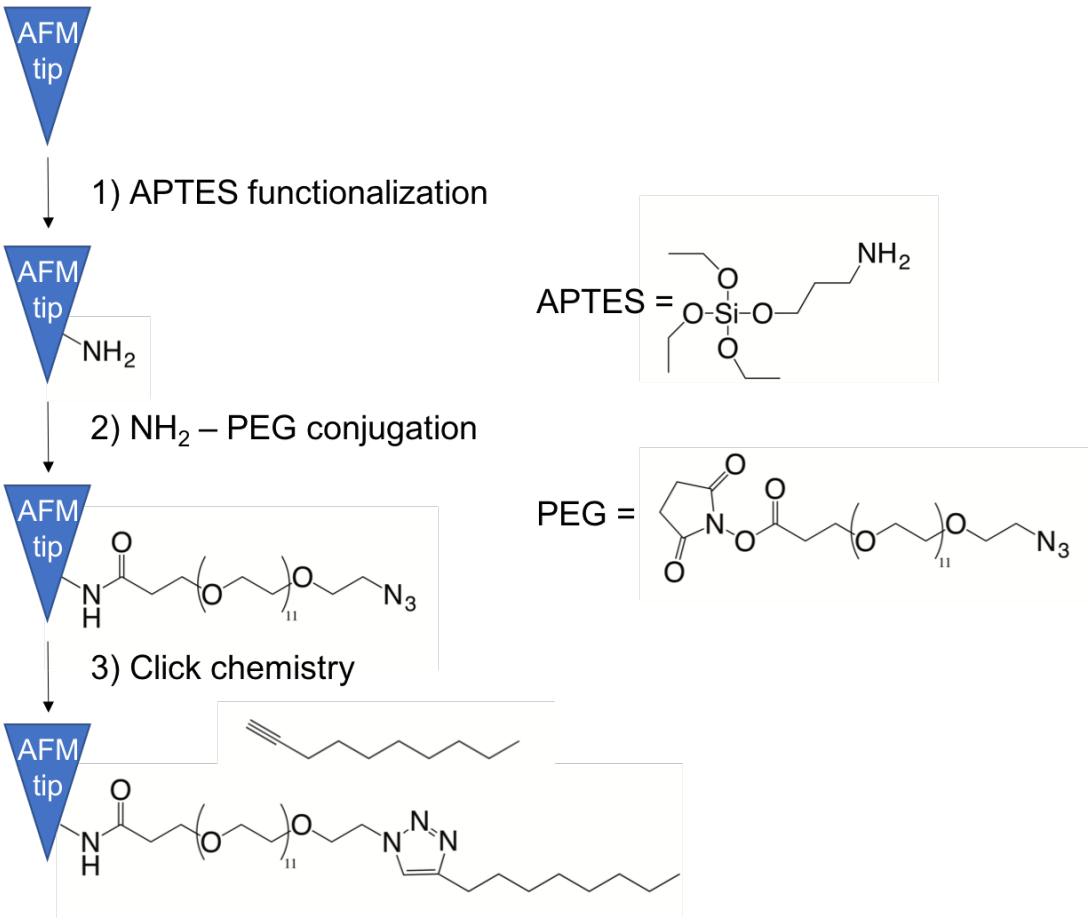

Figure 50 Scheme of the probe functionalization reactions.

Each auto ramp consists of 144 force curves taken in a matrix of 12x12 points spaced at 100 nm each.
The experiments were performed by applying a low force, around 2 nN, to prevent the rupture of the lipid bilayer, yet allowing a close interaction of the carbon chain with the phospholipid bilayer. The “Hold Time” parameter, that refers to the contact time between the tip and the sample, was set at 2 seconds to promote the interactions between the SLB and the probe.
The preliminary results suggested the presence of different modes of interaction depending on the type of tip used.
As expected, in the control experiment with the Si and APTES probes, no specific adhesion interactions between the tip and the sample were observed. Retracting FCs obtained with the PEG probe showed few specific interactions, but with lower adhesion forces respect to the C8 probe (Fig. 51). Some specific interactions with the PEG probe are not particularly surprising due to the partially hydrophobic character of the PEG chain. However, the distribution in the interaction distance suggested that the chains were not precisely linked to the tip. On one hand this is physiological as PEG can be linked through the entire height of the AFM tip. On the other hand, this may indicate a

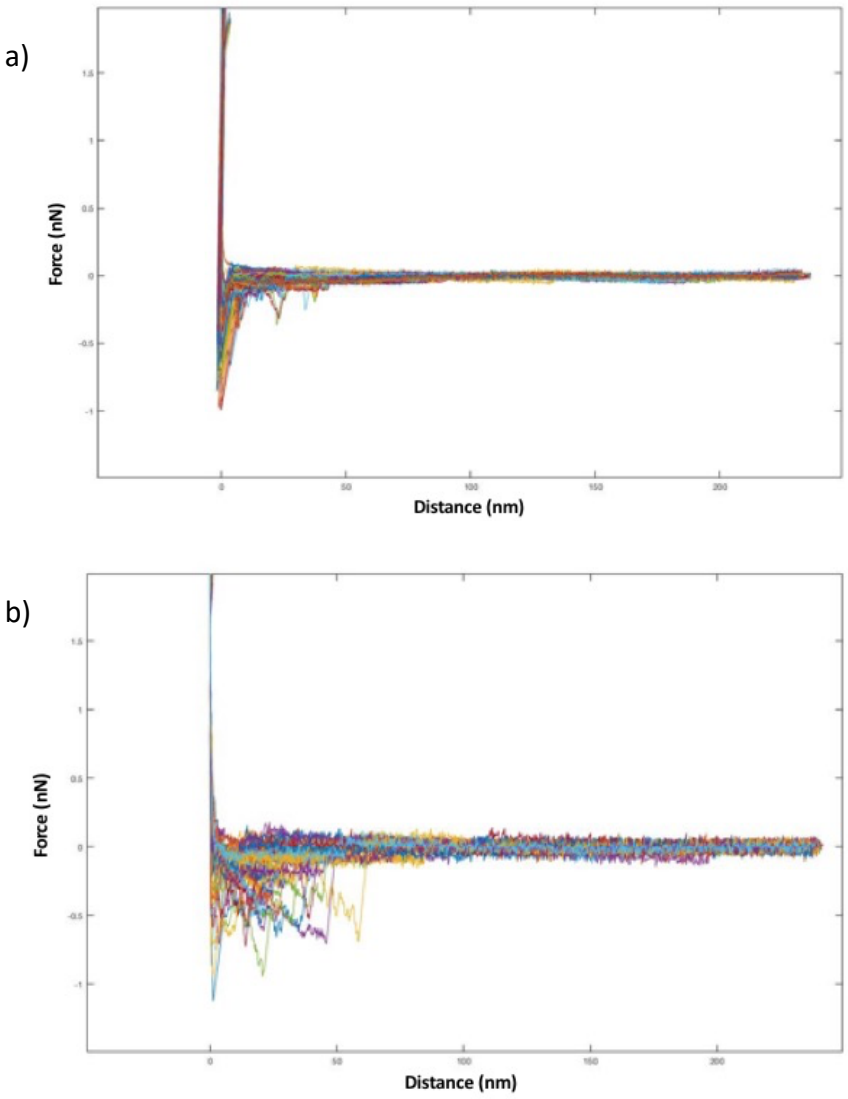

Figure 51 Retracting-phase force curves acquired with (a) the PEG-probe and (b) the C8-probe.

polymerization of APTES molecules with the formation of a network connected in series and in parallel. Indeed, the first step of the functionalization (APTES), is the most delicate and parameters such as exposure time, reaction atmosphere, reagent purity can strongly affect the results.
For this reason, the optimization of this step was performed. New APTES was purchased, divided in smaller aliquots using a glove-box and stored under nitrogen at -20°C. Various exposure time to the APTES vapors were tested. The role of the atmosphere for the functionalization was also investigated: nitrogen or static vacuum. The optimized procedure is reported in the paragraph 5.2.2. "AFM probe functionalization".
A script for custom data analysis was developed on MATLAB in order to perform the punctual analysis of thousands of retracting force curves. By manually selecting the interaction events, the script provided the force of each event, as well as the distance of the probe from the surface when it occurs, and other parameters. The results of the analysis of the retracting FCs obtained with the Si, APTES, PEG and C8 probes are reported in Fig. 52. From these charts, the following observations can be deduced:

- The aspecific event, due to the interaction between the tip and the SLB is observed in all the tested probes.
- The population of events observed only with the C8 probe ad around 10 nm indicates specific interactions between the 8 carbon atoms alkyl chain and the bilayer.

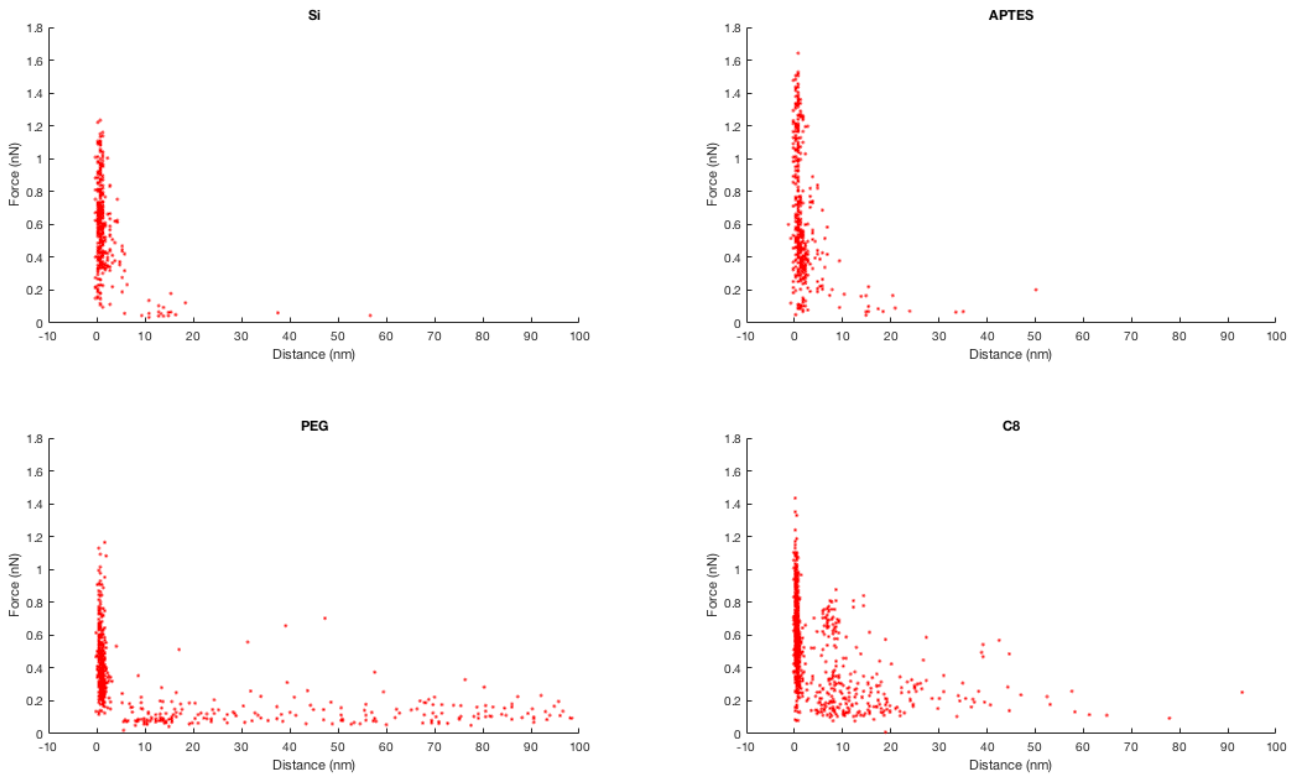

Figure 52 Interaction events (aspecific and specific) plotted as the interaction forces as a function of the distance at which they occur, for Si-probe (top left), APTES-probe (top right), PEG-probe (bottom left), C8-probe (bottom right).

3.3. Conclusions

In the work described in this chapter, nanomechanics studies were carried out to investigate the mechanisms of interaction between supported phospholipid bilayers and ionic liquids. In particular, the procedure for the formation of a DOPC phospholipid bilayer by fusion of unilamellar liposomes was optimized.

An innovative procedure for functionalization of AFM tips with a linear alkyl chain of 8 carbon atoms was also developed, in order to mimic the alkyl chain of the imidazole cation of the ionic liquid [Omim] [Cl].

The probe thus obtained was used in atomic force spectroscopy measurements to investigate the microscopic mechanisms of interaction between ionic liquids and phospholipid bilayers.

In the future, it will be necessary to expand the case history of nanomechanical measurements by further increasing the length of the alkyl chain, to develop characterization strategies for functionalized probes and to optimize force spectroscopy measurements, developing data analysis models that allow quantitative analysis, as well as qualitative, of the results obtained.

The aim of the work reported in this chapter was to investigate the ionic liquids toxicity mechanisms by AFM through nanomechanics and force spectroscopy experiments. A supported phospholipid bilayer was prepared using 1,2- dioleoyl-sn-glycero-3-phosphocholine (DOPC). Two ionic liquids, 1-Butyl-3-methylimidazolium chloride ([Bmim][Cl]) and 1-Methyl-3-octylimidazolium chloride ([Omim][Cl] with chains of 4 and 8 carbon atoms respectively were selected to investigate the effect of the chain length on the weakening effect produced on the SLB. Initially, the morphology of the SLB was assessed by AFM using peak-force tapping mode and by analyzing approaching force curve. Then, the phospholipid bilayer was conditioned with [Bmim][Cl] and [Omim][Cl] at various concentrations and force curves were acquired. The results confirm the hypothesis that the alkyl chain of the imidazole cation, due to its lipophilicity, penetrates inside the phospholipid bilayer with a "tail-first" mechanism, thus weakening the structure of the bilayer.

The "tail-first" interaction mechanism was confirmed by an AFM experiment in which an alkyl chain was covalently bound to the AFM tip that was mechanically brought into contact with the bilayer. The profile of the force curves during the *retracting* phase depends on the interactions between the hydrocarbon chain and the bilayer. Parameters such as contact time, approach and departure speed were varied. The experiments show that a specific interaction event is clearly observed in the case of C8 probe, respect to Si, APTES and PEG probes, thus contributing to confirm the “tail-first mechanism”.

Chapter 4. Synthesis and characterization of highly conjugated heterocyclic molecules with interesting photophysical properties

4.1. Synthesis and photophysical evaluation of polarity sensitive push – pull isoquinolines and their alkynyl precursors

4.1.1 Introduction

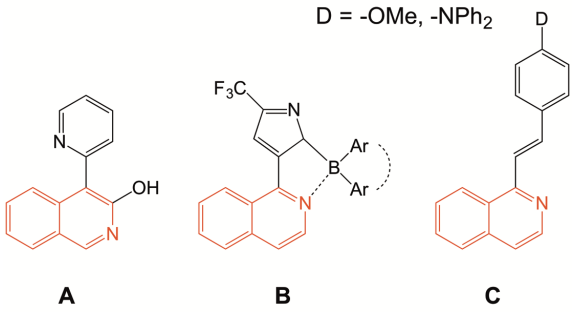

Figure 53 Polarity-sensitive isoquinoline-containing compounds.

Polarity-sensitive fluorescence probes carry chromophores that change their emission characteristics depending on the local polarity of their surroundings[166]. Therefore, they are useful to investigate the structural and dynamical properties of biological and model membranes. For example, monitoring cellular polarity is essential to understand physiological and pathological processes.

Fluorescent probes that can sense the environment are generally composed of an aromatic ring system with electron-donor and electron-acceptor groups; when these groups are at the greatest possible distance, maximal effects are expected[167]. An ideal polarity-sensitive dye must be characterized by: strong solvatochromism, absorption near the visible range, wide Stokes shift, high extinction coefficient (ε), quantum yield (QY), and photostability. As solvatochromic dyes can vary their color in response to polarity, a large class of environmentally sensitive probes were constructed based on these dyes. Typically, they belong to push–pull dyes that perform intramolecular charge transfer. After light absorption, the push–pull structure ensures that the charge is transferred to the acceptor group from the donor group, which creates a highly dipolar excited state. In more polar solvents, its emission shifts to longer wavelengths through the interaction of the highly dipolar excited state with the dipoles of the solvent[168]. Given their biological relevance, the synthesis and characterization of fluorescent probes have increasingly attracted research interest. Many fluorescent probes have been designed and synthesized in response to the variation of these parameters in vitro and in vivo.

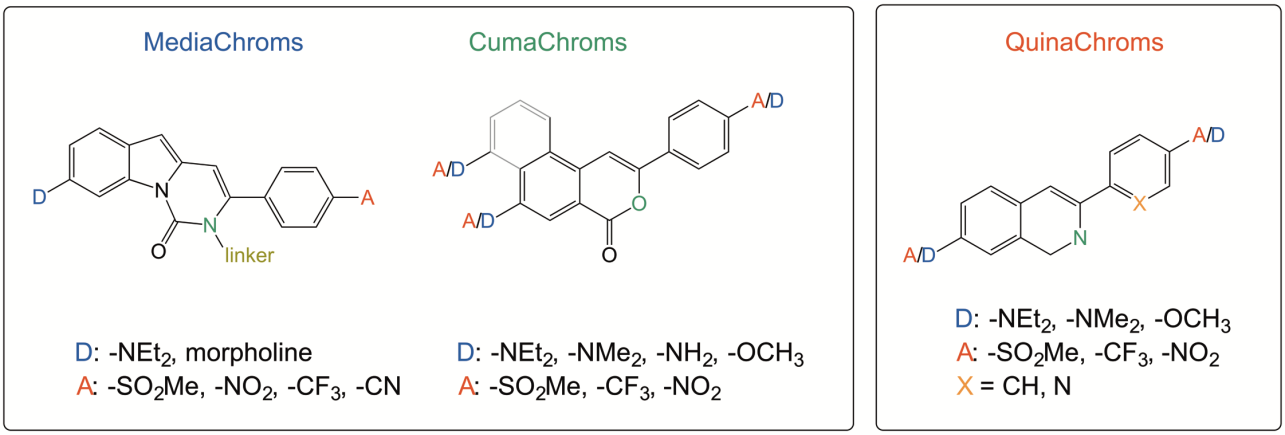

Figure 54 The D-π-A systems previously developed (left) and developed in this work (right).

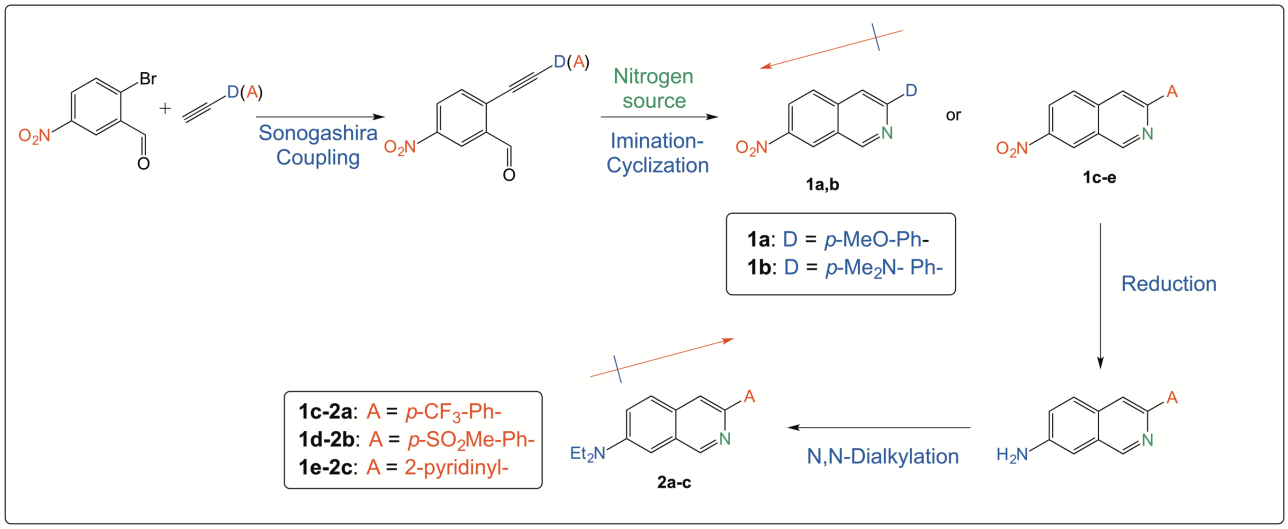

Scheme 1 Planned synthetic approaches.

During my PhD program I worked on the characterization of fluorescent molecules with interesting spectroscopic properties, synthetized by the group of Prof. G. Abbiati from the Department of Pharmaceutical Sciences of the University of Milan.

The study of (hetero)polycyclic aromatic molecules end-capped with conjugated electron-donating and electron-withdrawing groups (D-π-A or push–pull systems) has increased in the last ten years, due to the particular properties of these compounds[169].

Five years ago, the group of Prof. Abbiati synthesized a small library of polarity-sensitive fluorescent dyes – nicknamed MediaChroms[170] – characterized by a pyrimidoindolone backbone, which exhibited promising photophysical profiles. One of them was tested as a probe for biological analyses. More recently, they developed ten unprecedented D-π-A isocoumarin-based derivatives – nick- named CumaChroms[171] – with interesting spectroscopic properties.

At the same time, they have also been active in the development of new domino and multicomponent reaction (MCR) strategies for the synthesis of functionalized heterocycles starting from alkynes bearing a contiguous nucleophile. From a methodological point of view, the use of other sources of energy (*e.g.* microwaves) and the catalysis promoted by metals such as silver and gold are effective tools to reach the goals. In particular, in the last few years, they developed some approaches to isoquinolines – and closely related N-heterocycles – through a domino imination/cycloisomerization of γ- and δ-ketoalkynes in the presence of an ammonia source[172–175], also called a MCR[176].

The fluorescence properties of isoquinolines, in particular, those characterized by the presence of a nitrogen[177–180] or an oxygen[181] on the C-3 position, are well known. Contrariwise, the environment-sensitive properties of suitably functionalized isoquinoline nuclei have been little explored. Recently, the preparation of nine 3-hydroxy-4-pyridyl-3-isoquinolines has been reported by Ihmels and co-workers. One of this compound displayed interesting solvatochromic and halochromic properties (Fig. 53, A)[182]. Another example shows that the 1-isoquinolinyl fragment was used to chelate the boron atom in a series of five boron compounds characterized by a dual emission, where the solvent polarity influences the charge transfer emission (Fig. 53, B)[183]. In 2020, the synthesis and photophysical characterization of some new push–pull isoquinoline chromophores in which

isoquinoline was the pulling unit was performed by the research group of Rodríguez–López (Fig. 53, C)[184].

To the best of our knowledge, the synthesis and the evaluation of photophysical features of push–pull isoquinolines, where the isoquinoline is the π-unit, is practically unexplored. For this reason, the spectroscopic properties of some original D-π-A isoquinolines, – nicknamed QuinaChroms – were prepared and evaluated as potential polarity-sensitive fluorophores and/or organic structures for optoelectronic applications (Fig. 54). In the next paragraph, the obtained results are described.

4.1.2. Results and discussion

An effective push–pull system was created by selecting the electron-donating (D) and electron-withdrawing (A) groups to connect to the isoquinoline backbone, taking into account the advices reported in the review of Bures[169], and the recent experience of the group of Prof. Abbiati[170,171]. Therefore, dialkylamino groups and the methoxy group were chosen as EDGs. About the selection of the EW groups, those groups that displayed more interesting features in their previous studies were selected. In particular, (i) the methylsulfonyl group, which gave notable results in the CumaChrom series[171], (ii) the nitro group, for its availability and versatility in subsequent transformations, (iii) the trifluoromethyl group, a substituent rarely investigated in this context[185] that provided unexpected outcomes in the MediaChrom series[170], and (iv) the pyridine, which gives solvatochromic and halochromic properties to the isoquinoline nucleus, as recently revealed[182].

Therefore, the preparation of five original push–pull isoquinolines was planned (Scheme 1). The new QuinaChroms can be divided into two series, **1a,b**, and **2a–c**, respectively, according to an inverted "dipolar moment" with respect to the longitudinal axis of the molecule. This choice arises from the interesting result obtained in the CumaChrom series[171], in which a reversed position of the functional groups resulted in a switch from positive to negative solvatochromic behavior.

Table 5. Synthesis of starting materials.

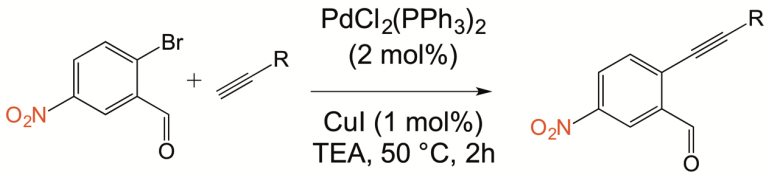

3a-e

Entry	3	R	Yield[a] (%)
1	**a**	p-MeO-Ph-	95
2	**b**	p-MeN_2-Ph-	92
3	**c**	p-CF_3-Ph-	88
4	**d**	p-$MeSO_2$-Ph-	95
5	**e**	2-pyridyl-	76

[a] Referred to pure isolated product

Isoquinolines **1a** and **1b** could be obtained by a standard Sonogashira coupling between 5-nitro-2-bromobenzaldehyde and suitable electron-rich acetylenes, (i.e., 4-methoxyphenylacetylene and 4 dimethyl-aminophenylacetylene, respectively), followed by an imination/ cyclization sequence (Scheme 1). To synthesize compounds **2a–c**, after the coupling with the appropriate electron-poor arylacetylene (i.e., 4-trifluorophenylacetylene, 4-methyl- sulfonyl-phenylacetylene, and 2-

ethynylpyridine, respectively) and the subsequent imination/cyclization domino reaction to obtain A-π-A isoquinolines **1c–e**, the approach required the reduction of the nitro to an amino group, followed by N-alkylation (Scheme 1). Therefore, under the reaction conditions already optimized in Prof. Abbiati's laboratory, 2-alkynyl-5-nitrobenzaldehydes **3** were prepared by a Sonogashira cross-coupling reaction[186,187], using a cheap and commercially available 2-bromo-5-nitrobenzaldehyde and suitable aryl alkynes as starting materials. The reactions was performed in freshly distilled

Table 6. Screening of the optimal imination/cyclization conditions

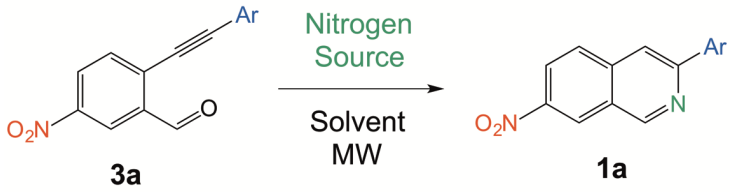

Ar = *p*-MeO-Ph-

Entry	Nitrogen source	Solvent	Time	MW (T)	Yield[a] (%)
1	$AcONH_4$ 20 equiv.	DMSO	30 min	80 °C	15
2	$AcONH_4$ 20 equiv.	DMF	30 min	80 °C	20
3	$AcONH_4$ 20 equiv.	CH_3CN	30 min	80 °C	14
4	$AcONH_4$ 20 equiv.	Toluene	30 min	80 °C	31
5	$AcONH_4$ 20 equiv.	MeOH	30 min	80 °C	29
6	NH_3 2M	MeOH	30 min	80 °C	39
7	NH_3 2M	MeOH	1 h	80 °C	40
8	NH_3 2M	MeOH	2 h	80 °C	52
9	NH_3 2M	MeOH	4 h	70 °C	44
10	**NH_3 2M**	**MeOH**	**2 h**	**100 °C**	**56**
11	NH_3 2M	MeOH	4 h	100 °C	53
12	NH_3 2M	MeOH	2 h	120 °C	18

[a] Referred to the pure isolated product.

trimethylamine (TEA) at 50 °C under a nitrogen atmosphere and in the presence of bis(triphenyl-phosphine)palladium(II) chloride and copper iodide as catalysts, and the desired 2-alkynyl-5-nitrobenzaldehydes **5** was obtained in good yields (Table 5).

2-((4-methoxyphenyl) ethynyl)-5-nitrobenzaldehyde **3a** was selected as a model substrate to find the best reaction conditions for the cyclization of 2-alkynyl-5-nitrobenzaldehydes **3a-e** to give the corresponding isoquinolines. The influence of the strong EWG nitro group on the benzaldehyde moiety suggested a possible adverse effect that could make the reaction trickier. Therefore, the reaction was tried in the presence of different nitrogen sources, solvents, and temperatures.

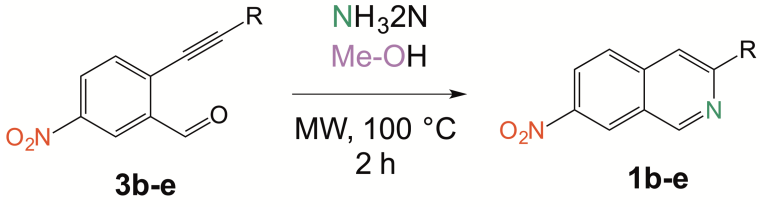

1b: R = *p*-Me_2N-Ph-; (58%)
1c: R = *p*-CF_3-Ph-; (19%)
1d: R = *p*-$MeSO_2$-Ph-; (0%)
1e: R = 2-pyridyl; (0%)

Scheme 2 Scope and limitation of the approach.

As an energy source, microwaves were selected due to their well- established efficiency[173–175]. The results are summarized in Table 6.

Based on the recent results concerning the imination/cyclization of 2-propargyl benzaldehydes[173], the

reaction was tried in DMSO with ammonium acetate as a nitrogen source and 80 °C by microwave heating for 30 min, but **1a** was obtained in poor yields (Table 6, entry 1). The effect of the solvent under these conditions was explored (Table 6, entries 2–5): methanol and toluene gave the best results, although still unsatisfactory (Table 6, entries 4 and 5 respectively). As a nitrogen source 2 M ammonia in methanol was used[175] (Table 6, entries 6–12). Among different temperatures (ranging from 70 to 120 °C) and times (ranging from 0.5 to 4 h), microwave heating at 100 °C for 2 hours (Table 6, entry 10) was selected as the best reaction conditions.

However, despite the optimized reaction conditions the reaction yields do not exceed 56%, probably due to the already aforementioned unfavorable effect of the nitro group on the alkynyl benzaldehyde, able to decrease the reactivity both at the carbonyl terminus as well as at the triple bond level.

Next, the cyclization approach was extended to other 2-alkynyl- 5-nitrobenzaldehydes **3b–e**. The results are depicted in Scheme 2.

As observed for **3a**, the effect of an EDG on the alkyne terminus favours the cyclization of alkynylbenzaldehyde **3b** to give the desired isoquinoline **1b** in 58% yield. Conversely, the presence of an EWG seems to strongly prevent the reaction. The isoquinoline **1c** was obtained in very poor yield (19%) starting from aldehyde **3c**, characterized by the presence of a trifluoromethyl group. Moreover, the reactions of aldehydes **3d** and **3e** failed to give the desired isoquinolines, and mixtures of unidentified by-products were obtained. It is possible that the two conjugated strong EWGs at the opposite sides of diarylalkyne strongly perturbs the electronic properties of the CuC π system, quenching its reactivity toward the intramolecular nucleophilic addition of the imine intermediate to the triple bond.

To overcome this problem, some additional experiments on **2c** by further fine-tuning of the reaction conditions were carried out. However, not even the presence of a silver salt as the catalyst[174] allowed to obtain yields over 15%.

A different route to obtain isoquinolines **2a–c** was then planned. The idea was to obtain an amino group from the nitro group (Scheme 3). The number of reducible π-systems on the 2-alkynyl-5-nitrobenzaldehydes (the nitro, the aldehyde, and the alkyne) could cause some problems to the reduction of the nitro group. For this reason, the nitro group of 5-nitro-2-bromobenzaldehyde was directly reduced, after proper protection of the aldehyde as acetal that was performed under

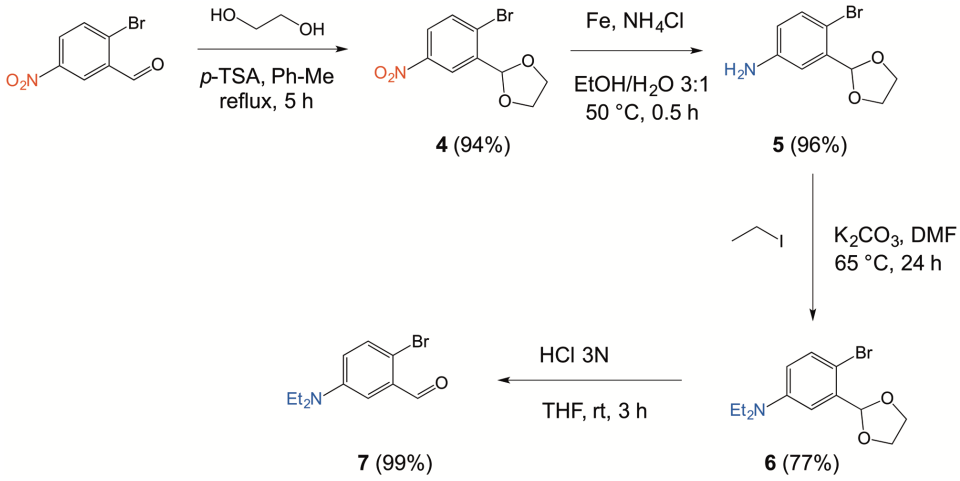

Scheme 3 Synthesis of the key-intermediate **7**.

standard conditions to give the 2-(2-bromo-5-nitrophenyl)-1,3-dioxolane **4** in 94% yield. The chemical reduction in the presence of iron and ammonium chloride was the best among various methods tested. The desired 4-bromo- 3-(1,3-dioxolan-2-yl)aniline **5** was obtained in a satisfactory 96% yield. The corresponding 4-bromo-3-(1,3-dioxolan-2-yl)-N, N-diethylaniline **6** was obtained by treatment with an excess of iodoethane under basic conditions in good yield (77%). The following deprotection proceeded in a quantitative yield to render the key starting material, 2-bromo-5-(diethylamino) benzaldehyde **7**, sufficiently pure such that no further purification was needed.

Table 7. Absorption peak wavelength (λ_{abs}) and fluorescence emission peak wavelength (λ_{em}) of QuinaChroms 1a,b and 2a-c in different solvents (c = 0.014 mg mL^{-1})

		1a		**1b**		**2a**		**2b**[a]		**2c**	
Solvent	$E_T(30)$[4a]	λ_{abs} (nm)	λ_{em}[b] (nm)	λ_{abs} (nm)	λ_{em}[b] (nm)	λ_{abs} (nm)	λ_{em}[b] (nm)	λ_{abs} (nm)	λ_{em}[b] (nm)	λ_{abs} (nm)	λ_{em}[b] (nm)
Toluene	33.9	371	476[e]	431	601[d]	347	431	357	429	347	427[d]
THF	37.4	366	506[d]	428	648[d]	348	439	359	445	347	434
EtOAc	38.1	365	509[d]	423	650[d]	346	437	355	444	345	434
DCM	40.7	368	548	433	700[e]	348	439	364	449	350	437
Acetone	42.2	365	549	425	513[e]	349	445	303	464[e]	348	443
DMF	43.2	371	568	432	554[e]	352	454	362	477	351	448
DMSO	45.1	375 (18643)[c]	585[d]	438 (23985)[c]	438[e]	356 (30885)[c]	457	367 (25412)[c]	487	354 (23436)[c]	454
EtOH	51.9	361	561[e]	419	575[e]	346	451	359	468	348	449
Water	63.1	387	551[d]	412	570[e]	340	431[d]	367	523[d]	344	473[d]
Solvatochromic shift		**14**	**109**	**19**	**n.d.**	**10**	**26**	**11**	**58**	**7**	**27**
Stokes shift (toluene)		**105**		**170**		**84**		**72**		**80**	

[a] c em = 0.007 mg mL^{-1}. [b] The excitation has been carried out at the λ corresponding to the absorption maxima. [c] ε expressed as M^{-1} cm^{-1}. [d] Moderately fluorescent. [e] Extremely little fluorescent.

The desired push–pull 2-alkynyl-5-dietylaminobenzaldehydes **8a–c** were obtained from the Sonogashira reaction between aldehyde **7** and the selected alkynes. The standard Sonogashira reaction conditions were modified in order to obtain good yields. Indeed, it is reasonable to assume that the presence of the amino group on the aldehyde moiety and the electron-poor nature of the alkynes involved. The

cyclization step also required some modifications with respect to the standard conditions. However, despite the efforts, the desired D-π-A isoquinolines **2a–c** were obtained only in modest yields, but in high purities, (Scheme 4) besides unidentified by-products. These probably arised from

8a: (67%) - Reax. Cond.: MeCN, 5 h
8b: (41%) - Reax. Cond.: MeCN, 2 h
8c: (76%) - Reax. Cond.: K_2CO_3, DMF, 4 h

2a: (26%) - Reax. Cond.: 180 °C, 1 h
2b: (18%) - Reax. Cond.: 80 °C, 1 h
2c: (28%) - Reax. Cond.: 100 °C, 2 h

Scheme 4 Synthesis of QuinaChroms **2a-c**.

polymerization processes. Since all QuinaChroms isoquinolines are not reported in the literature, they and have been fully characterized through mono and/or bidimensional NMR spectroscopy, elemental analysis and mass spectrometry.

Then, the photophysical properties of QuinaChroms **1a–b** and **2a–c** were evaluated. Nine different solvents with different polarities (toluene, dichloromethane, tetrahydrofuran, ethyl acetate, acetone, ethanol, *N,N*-dimethylformamide, dimethylsulfoxide, and water) were used to collect the UV/Vis absorption spectra. Most of the molecules synthesized are well soluble in the explored solvents. A mother solution of 0.5 mg mL^{-1} in DMSO was prepared for all compounds., The ε value was obtained, using the linear regression method, from the absorbance values in DMSO. The UV absorption and emission spectra in different solvents were recorded by dissolving 28 µL of the stock DMSO solution (1 mg mL^{-1}) in the suitable media, to obtain a final concentration of 0.014 mg mL^{-1} (Table 7). Moreover, the absolute QYs in three solvents with different polarities was also measured (Table 8).

High ε in DMSO were observed for all isoquinolines **1a,b**, and **2a–c**. These values are comparable to those of other well-established fluorescent molecular probes, such as 1,8-ANS (8-anilinonaphthalene-1-sulfonic acid, ε = 18 000). All compounds are characterized by strong absorbance in all tested solvents except for water which experienced solubility problems, less pronounced only in the case of **2c**. As expected, the range of absorption maxima in the different solvents is quite tight, ranging from 7 nm for **2c** to 19 nm for **1b**.

Table 8. Absolute QYs of QuinaChroms 1a,b and 2a-c in three solvents with different polarities (c = 0.014 mg mL^{-1})

	Solvent		
Compound	Toluene QY (%)	DMSO QY (%)	EtOH QY (%)
1a	45.8	15.7	2.4
1b	77.8	Not determinable	Not determinable
2a	14.2	28.1	13.8
2b	24.2	62.6	35.7
2c	17.6	27.2	13.5

The more red-shifted absorption maxima are observed in DMSO by all isoquinolines, but whereas **1a** and **2a–c** have their maximum absorption peaks in the UV-A region (from 354 to 375 nm), **1b** displays more pronounced red-shifted maxima in the visible region (438 nm). Thus, it is reasonable to assume that the isoquinoline scaffold allows a more efficient ICT from position 3 to 7 rather than to the opposite arrangement. Isoquinolines were irradiated at their maximum absorption wavelength for the specific solvent and fluorescence emission peaks were recorded. Moderate to good intensities were obtained, except for **1b** whose fluorescence is moderate for toluene, THF, and ethyl acetate and extremely poor for all the other seven solvents. This low fluorescence makes the emission data of **1b** unreliable and problematic to translate. The fluorescence in water for all compounds is moderate or poor, but this might be explained by the already discussed poor solubility observed in this medium.

A bathochromic effect of the emission maxima according to the increase of the polarity of the medium was observed for compounds **1a** and **2a–c**, while **1b** seems to display a particular reversed hypsochromic shift. However, as already mentioned, the fluorescence of **1b** is very low in almost all solvents strongly undermining the reliability of these data. The poor emissive properties of **1b** in all other solvents represent a strong drawback for whatever possible application as environment-sensitive probe or advanced materials.

The widest solvatochromic shift (Δλ = 109 nm) is displayed by isoquinoline **1a** but the intensity of fluorescence is modest and vary among the solvents (in particular in toluene and ethanol is very low). Compounds **2a–c** are characterized by strong fluorescence in almost all solvents and, in particular, **2b** has the widest solvatochromic shift (Δλ = 58 nm) and the highest QY in all the solvents tested. Referring to the above mentioned features that distinguish an optimal polarity sensitive probe (i.e. fluorescence intensity, solubility, wide solvatochromic shift, absorption close to the visible range, large Stokes shift, and high QY), compounds **1a** and **2b** are the more interesting compounds prepared in this work. The solvatochromic features of **2b** are somewhat predictable in agreement with the behavior of the corresponding CumaChrom[171]. Conversely, the pronounced

Table 9. Absorption peak wavelength (λ_{abs}) and fluorescence emission peak wavelength (λ_{em}) of QuinaChroms 3a,b and 8a-c in different solvents (c = 0.014 mg mL^{-1})

		3a		**3b**		**8a**		**8b**[a]		**8c**	
Solvent	$E_T(30)$[4a]	λ_{abs} (nm)	λ_{em}[b] (nm)	λ_{abs} (nm)	λ_{em}[b] (nm)	λ_{abs} (nm)	λ_{em}[b] (nm)	λ_{abs} (nm)	λ_{em}[b] (nm)	λ_{abs} (nm)	λ_{em}[b] (nm)
Toluene	33.9	440	476[d]	374	570[d]	347	472	355	475	342	473
THF	37.4	440	506	369	619[d]	345	481	352	480	340	477
EtOAc	38.1	434	509[d]	367	613[d]	343	482	350	482	338	480
DCM	40.7	447	548	371	554[e]	347	503	357	504	344	503
Acetone	42.2	437	549	367	542[e]	343	498	351	501	339	497
DMF	43.2	447	568[d]	373	544[e]	347	508	354	508	342	507
DMSO	45.1	454 (16483)[c]	585[d]	376 (18824)[c]	579[e]	348 (24943)[c]	521	356 (26319)[c]	521	345 (29000)[c]	517
EtOH	51.9	437	561[e]	362	554[e]	343	546[e]	352	557[e]	343	562[e]
Water	63.1	416	551	403	546[e]	345	547[e]	360	531[e]	344	612[e]
Solvatochromic shift		**20**	**109**	**14**	**n.d.**	**5**	**49**	**5**	**46**	**7**	**44**
Stokes shift (toluene)		**67**		**196**		**125**		**121**		**131**	

[a] c em = 0.007 mg mL^{-1}. [b] The excitation has been carried out at the λ corresponding to the absorption maxima. [c] ε expressed as M^{-1} cm^{-1}. [d] Moderately fluorescent. [e] Extremely little fluorescent.

solvatochromism of **1a**, characterized by the presence of a weaker EDG such as the methoxy group[169], is rather surprising and unexpected, in particular if compared with the similarly unpredicted poor performances of **1b**. Two ^{1}H NMR spectra of **1a** in DMSO five days apart from each other were recorded showed no degradation of the sample, thus confirming that the lack of fluorescence of **1b** was not related to fast degradation of the molecule in solution (data not shown). The photophysical properties of 3-(4-methoxyphenyl)isoquinoline were compared with the work of Rodríguez–López[184]. The isoquinoline, whose synthesis was reported by the Prof. Abbiati's group in 2010[176], represents the pulling unit. As expected, the lack of a conjugated π-system strongly affected

the photophysical properties. The UV-Vis absorption maxima in many cases overlap the absorption of the solvents and the molecule displays neither fluorescence nor solvatochromic properties when pulled under a UV lamp at 254 nm.
UV / Vis absorption and emission spectra were recorded in nine different solvents, as was done for isoquinolines, and ε was calculated from the absorbance values in DMSO (Table 9). Absolute QYs were also measured in three solvents with different polarities (Table 10).

Table 10. Absolute QYs of Alkynylbenzaldehydes 3a,b and 8a-c in three solvents with different polarities (c = 0.014 mg mL^{-1})

	Solvent		
Compound	Toluene QY (%)	DMSO QY (%)	EtOH QY (%)
3a	67	Not determinable	Not determinable
3b	Not determinable	25.1	Not determinable
8a	65.5	71	3.4
8b	71.4	88.5	4.4
8c	73.6	84.6	3.6

The alkynylbenzaldehyde **3b,** similarly to the isoquinoline **1b,** displayed poor fluorescence too in almost all solvents, and the QY is undeterminable in toluene and ethanol. This strengthened the hypothesis of a sort of "fluorogenic incompatibility" between nitro and dimethylamino groups at the margins of a highly conjugated system. This in accordance with the reduced fluorescence solvatochromism generally observed in 4-amino-7-nitro-2,1,3-benzoxadiazole (NBD) analogues[188,189]. Once again, compounds with the EDGs on the benzaldehyde moiety (**8a–c**) are characterized by brighter fluorescence and high QY in toluene and DMSO. The results obtained with the alkynylbenzaldehydes in water are unreliable due to the poor solubility of this compound in this solvent. The performances of **3a** resulted to be worse than those of the corresponding isoquinoline **1a** (also testified by the indeterminability of QY in polar solvents), while aldehydes **8a–c** exhibited broader Stokes shifts compared to the corresponding isoquinolines **2a–c**. However, while **8a** and **8c** also displayed larger solvatochromic shifts, for **8b** this value is comparable to that of **2b**.

4.1.3. Conclusions

Five novel isoquinolines – nicknamed QuinaChroms – endowed with a conjugated D-π-A system were synthesized. Highly regioselective imination/cyclization domino sequence of suitably substituted 2-alkynylbenzaldehydes in the presence of methanolic ammonia are promoted by microwaves. The conjugated strong ED and EW groups on the far end of the starting alkynyl benzaldehydes affect the electronic asset of the molecules and such perturbation on the triple bond makes the cyclization steps trickier. The polarity-sensitive properties of the D-π-A isoquinolines and their alkynyl precursors were investigated using nine solvents of increasing polarity. Among the QuinaChroms, compounds **1a** and **2b** exhibited the more interesting spectroscopic properties, whereas alkynylbenzaldehydes **8a–c** – which bear a free aldehyde group suitable for conjugation – showed an intense fluorescence and a wide Stokes shifts. Potential applications of these compounds are in the field of polarity-sensitive probes for the study of biological interactions and the production of novel nonlinear optical materials.

4.2. Gold-catalyzed cascade reactions of 4H-furo [3,2-b]indoles with propargyl esters: synthesis of 2-alkenylidene-3-oxoindolines

4.2.1. Introduction

During my PhD program, in the context of chromophores and dyes, I collaborated with the group of Prof. E. Rossi, from the Department of Pharmaceutical Sciences of the University of Milan to the synthesis and characterization of 2-alkenylidene-3-oxoindolines via a gold-catalyzed cascade reaction between 4*H*-furo[3,2-*b*]indoles and propargyl esters. In the frame of this work, I performed

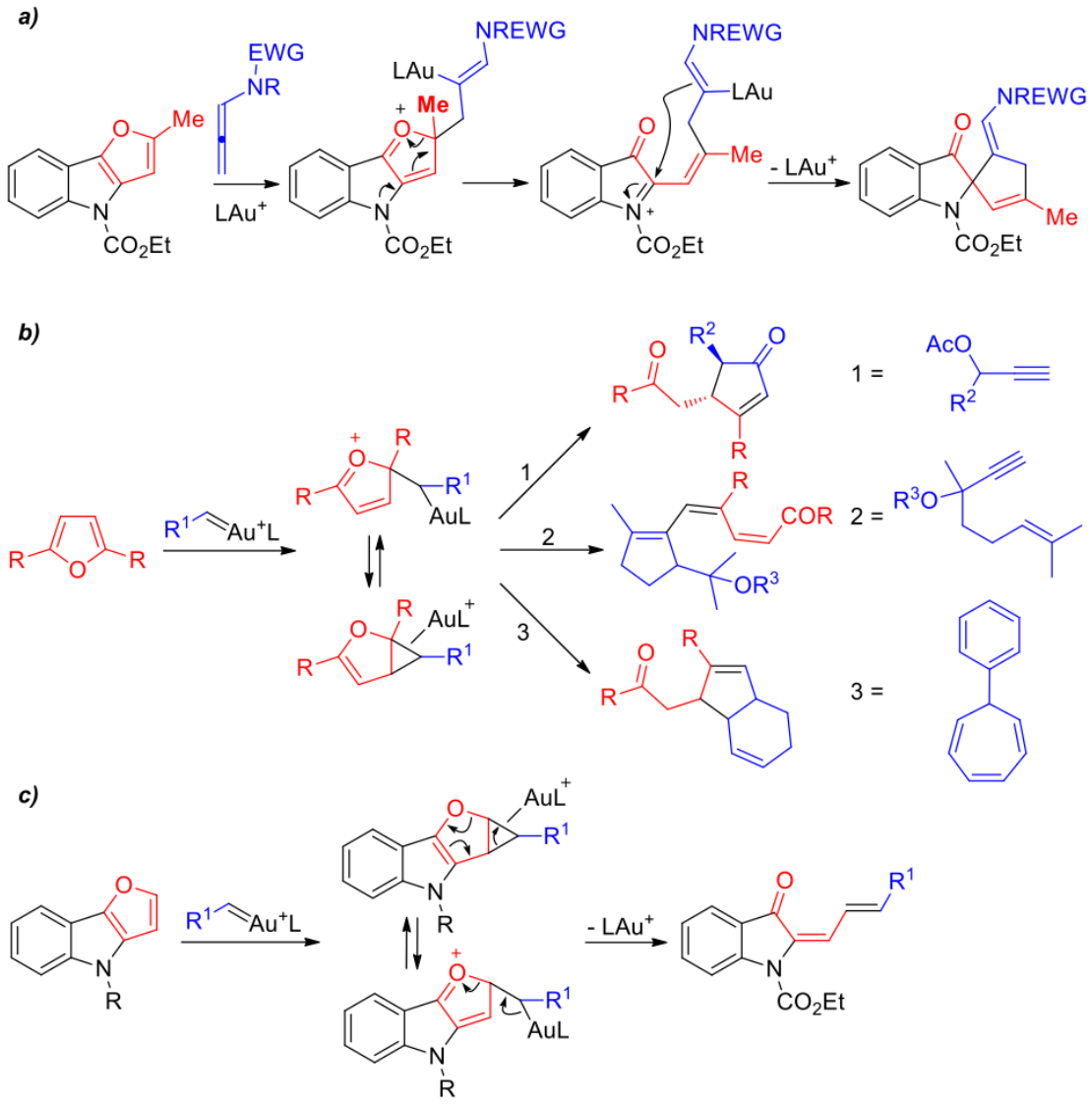

Scheme 5 Previous and proposed work.

the characterization of these compounds by UV/Vis spectroscopy.

A powerful tool in synthetic organic chemistry[190] is homogeneous gold catalysis. Among other factors, the importance of the developed chemistry is the capacity of gold species to activate π-

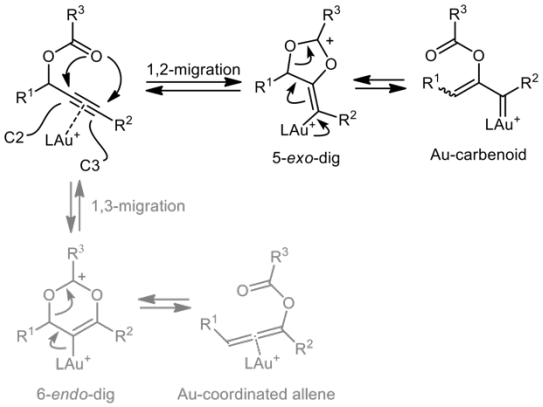

Scheme 6 Propargyl esters and their general reactivity patterns.

systems under mild conditions with tunable selectivity allowing for the synthesis of highly substituted and complex structures[191–194]. In particular, processes of homogeneous gold-catalyzed cascade have been widely used for the e synthesis of complex heterocycles and natural products[195–198]. Prof. Rossi's group has recently published results on the gold-catalyzed cascade rearrangement of 2-methyl-4H-furo[3,2-b]indoles to indolin-3-one derivatives in the presence of gold-activated allenamides I (Scheme 5a)[199]. The reaction involves a cascade sequence implying the addition of a gold-activated allene to the C2 furan moiety of the starting furoindole followed by a ring-opening/ring-closing event affording 2-spiro- cyclopentane-1,2-dihydro-3H-indolin-3-ones. In a similar perspective, Echavarren and co-workers reported the reactions of furans with gold(I)-carbenes II generated in situ from propargyl esters, 1,6-enynes and 7-substituted-1,3,5-heptatrienes (Scheme 5b)[200]. The reactions initiated with the electrophilic addition of gold(I)-carbenes to furans followed by furan ring opening. These results prompted us to investigate the opportunity of involving the C2–C3 bond of C2 unsubstituted furoindoles in a gold(I) catalyzed cascade reaction using gold(I)-carbene complexes II generated in situ from suitable propargyl esters via gold-catalyzed 1,2-acyloxy migration (Scheme 5c). The results indicated that the reaction proceeds via the addition of gold-carbene to furoindole followed by the furan ring-opening reaction providing 2-alkenyliden-indolin-3-ones.

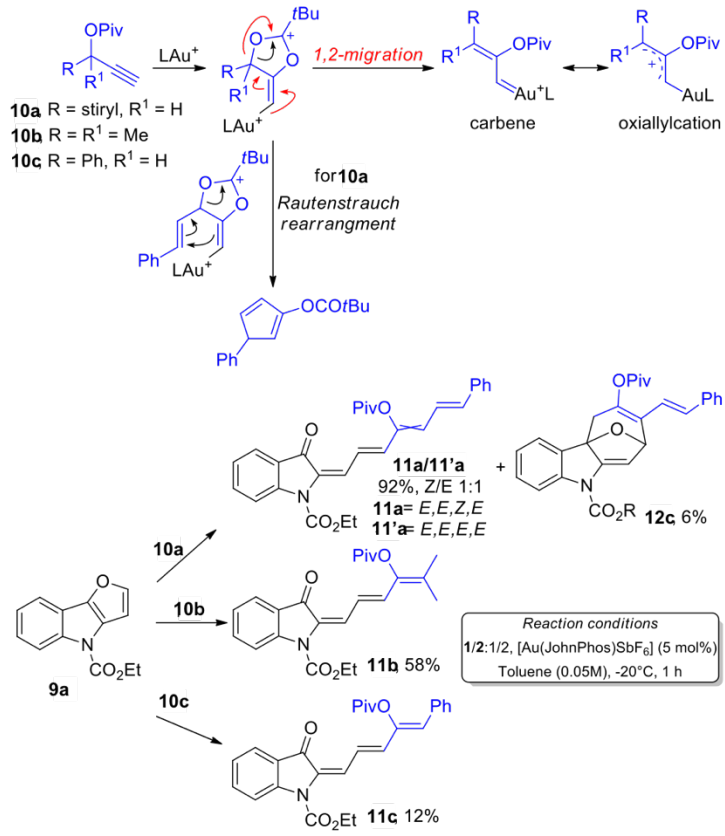

Scheme 7 Preliminary results.

Propargyl esters are advantageous substrates for cascade reactions due to their capacity to generate gold-coordinated allenes I and gold- carbenes II able to participate in cascade processes (Scheme 6)[201], via gold-catalyzed 1,2-or 1,3-acyloxy migration.

Furthermore, these structurally varied intermediates proved to be in equilibrium with each other. Generally, 1,3-migration is favored for internal alkynes, whereas 1,2-migration predominates for terminal alkynes and EWD-substituted alkynes. The next paragraph reports details on the investigation.

4.2.2. Results and discussion

The synthesis of 4H-furo[3,2-b]indoles employed in this work was reported in a paper recently published by Pirovano et al[199]. As a proof of concept, the reactivity of furoindole **9a** with propargyl esters **10a–c** bearing different substituents at the α-position was tested (Scheme 7) and, in the presence of gold(I) catalysts, the corresponding carbene–oxyallyl cation species was obtained[202–204]. In addition, propargyl ester **10a** complicates the reaction outcome due to the formation of the Rautenstrauch rearrangement product (Scheme 7)[201,205]. The planned model reactions was carried out in toluene at −20 °C, in the presence of two equivalents of **10a–c** and 5 mol% of the preformed cationic JohnPhosAuSbF$_6$ catalyst. With propargyl ester **10a,** a separable 1:1 mixture of Z/E isomeric 2-(hepta-2,4,6-trien-1-ylidene)-3- oxoindolines **11a** and **11'a** was obtained in excellent yield, together with a small amount of tetracyclic compounds **12a**.

Analytical (MS) and spectral data (1D and 2D NMR) confirmed the structures of all isolated

Table 11. **Optimization of the reaction conditions**

Entry	Au(I)[b]	Solvent	**10a**	Temp. (°C)	Time (h)	**11a** (%)[c]	**11'a** (%)[c]	**12a** (%)[c]
1	A	Toluene	2	-20	1	45	47	6
2[d]	B	Toluene	2	-20	43	15	6	6%
3	C	Toluene	2	-20	1	36	12	28%
4[d]	D	Toluene	2	-20	1	25	/	21%
5	E	Toluene	2	-20	1	40	41	7%
6	A	TFE	2	-20	1	38	43	/
7	A	DCM	2	-20	1	47	46	4
8	**A**	**Toluene**	**1.2**	**-20**	**1**	**58**	**36**	**6%**
9	A	Toluene	1.2	-35	10	/	/	/

[a] All reactions were carried out using **9a** (0.2 mmol) and **10a** (0.24-0.4 mmol, manual dropwise adition) in the stated solvent (0.05 M). [b] 5 mol%, performed catalysts. [c] Isolated yield. [d] Some decomposition products were observed desides the starting 9a.

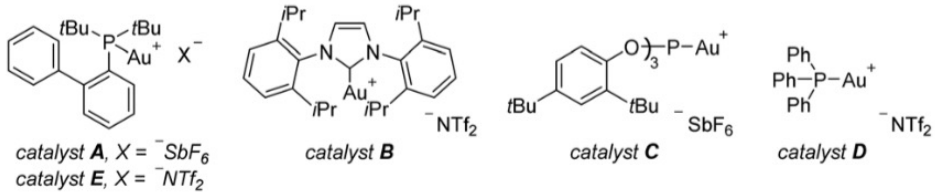

catalyst ***A****, X =* $^-SbF_6$ *catalyst* ***E****, X =* $^-NTf_2$ | *catalyst* ***B*** | *catalyst* ***C*** | *catalyst* ***D***

compounds. Besides, the geometries around the double bonds of the heptatrienyl moieties were assessed by 2D NOESY NMR spectroscopy and ^{3}J Z/E coupling constant analysis. Analysis of 2D COSY, TOCSY, HSQC and NOESY spectra defined the regiochemistry of compound **12a**. With propargyl ester **10b,** the reaction afforded 2-((E)-5-methyl-hexa-2,4-dien-1-ylidene)-3-oxoindoline **11b** in a moderate yield.

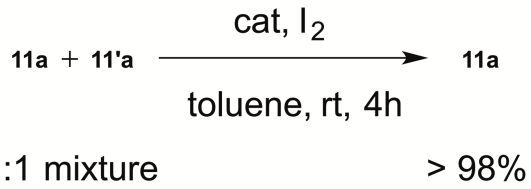

Scheme 8 Isomerization of a **11a/11'a** mixture to pure **11a**.

The structure was assigned for compounds **11a** and **11'a** as reported above. It is worth noticing that at the end of the reaction, after the usual work-up, the ^{1}H NMR analysis of the crude mixture revealed the presence of two Z/E isomers. However, the chromatographic purification step allowed to observe

the complete conversion towards **11b**. Finally, with propargyl ester **10c** the reaction led to the isolation of 2-((2E,4Z)-5-phenyl- penta-2,4-dien-1-ylidene)-3-oxoindoline **11c** in a poor yield. Besides **11c**, the starting unreacted furoindole **9a** and some decomposition compounds were detected. Based on the results, the reactivity of α-styryl substituted propargyl esters was
investigated. The influence of different gold(I) ligands, counterions, solvents and stoichiometries on the reaction outcome (Table 11) were assessed. The reaction between **9a** and **10a** was chosen (Scheme 7 and Table 11, entry 1) as a model.

Worst results were obtained with less electrophilic catalyst[206] such as the cationic gold(I) carbene complex B. The starting **9a** was recovered after a prolonged reaction time, together with small amounts of the desired compounds and some decomposition products (Table 11, entry 2). More electrophilic cationic catalysts such as gold(I) phosphite C or triphenyl- phosphine D complexes provided better yields but poorer selectivity compared to the model reaction (Table 11, entries 3 and 4). Then, JohnPhos ligand was used changing the counterion from SbF6 to NTf2 with practically no effect on the reaction outcome (Table 11, entry 5). The use of solvents such as trifluoroethanol or dichloromethane (Table 11, entries 6 and 7) did not affect the reaction outcome. However, toluene was selected as the reaction medium due to its lower cost compared to TFE, and improved ability to dissolve reaction products compared to DCM. Moreover, reducing the equivalents of **10a** to 1.2 did not affect the reaction outcome (Table 11, entry 8). The influence of temperature on the reaction outcome was investigated in the last two experiments (Table 11, entries 9 and 10). The reaction carried out at 20 °C led to the isolation of **11a** and **11'a** in poor yields, together with a series of tarry and unidentified compounds, whereas no reaction occurred at −35 °C . It is noteworthy, that the analysis of the crude reaction mixture did not allow detecting the Rautenstrauch rearrangement product (see Scheme 7)[205,207–210]. It can be reasonable assumed that, starting from the gold activated propargyl ester **10a**, the 1,2-migration and the subsequent carbene addition to furoindole **9a** are faster than the Rautenstrauch rearrangement process even at room temperature. To hypothesis was confirmed by repeating the reaction between the Rautenstrauch rearrangement product and propargyl ester **10a**[207] in the absence of **9a.** In this condition, the [4 + 3] cycloadduct was isolated. The screening of the best synthesis conditions of **12a** were not investigated to in-depth. The outcomes of this screening allowed establishing the best conditions for the synthesis of **11a** and **11'a.**

Then, the potential of obtaining the 3-oxo-2- (hepta-2,4,6-trien-1-ylidene)indolines 3/3' as single isomers was investigated by quenching the reaction with 15 mol% of triphenylphosphine, followed by a treatment of the solution with a catalytic amount of iodine. The conversion of a mixture of **11a**/**11'a** isomers to the **11a** isomer was completed (>98%) in 4 hours (Scheme 8).

Based on these results, the scope of the reaction was then explored by performing all the experiments in the conditions mentioned in the footnote of Table 1 (entry 8). At the end, triphenylphosphine quenched the reaction mixtures which was then treated with iodine. Compounds **11a–n,** purified by chromatography, were isolated and characterized (Scheme 9).

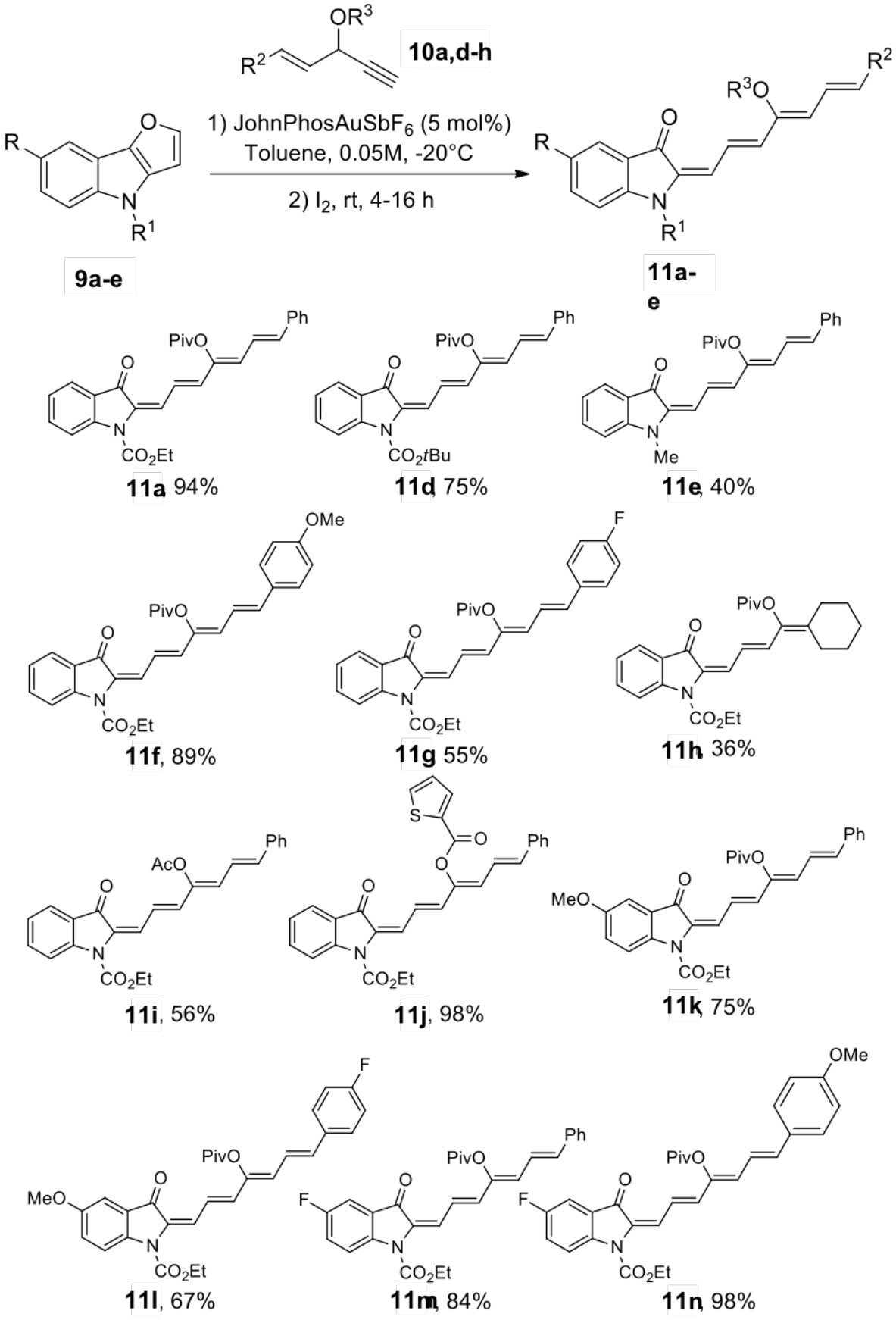

Scheme 9 Reaction scope.

The reaction between **9a** and **10a** provided **11a** as a single isomer with an excellent yield. Then, the influence on the yield of the protecting group on the nitrogen was investigated. In particular, it was

seen that a bulkier electron-withdrawing group such as N-Boc led to the formation of the corresponding product **11d** in a lower yield. Moreover, the substitution of the starting furoindole with an electron-donating N-methyl group was poorly tolerated. The yield was down to 40% due to the formation of **11e**. Next, it was observed that the reaction outcome was strongly affected by the substitution pattern of the starting propargyl esters **10a,d–h.** The introduction on the styryl ring of an electron- donating methoxy group, in fact, provided great results both with the standard

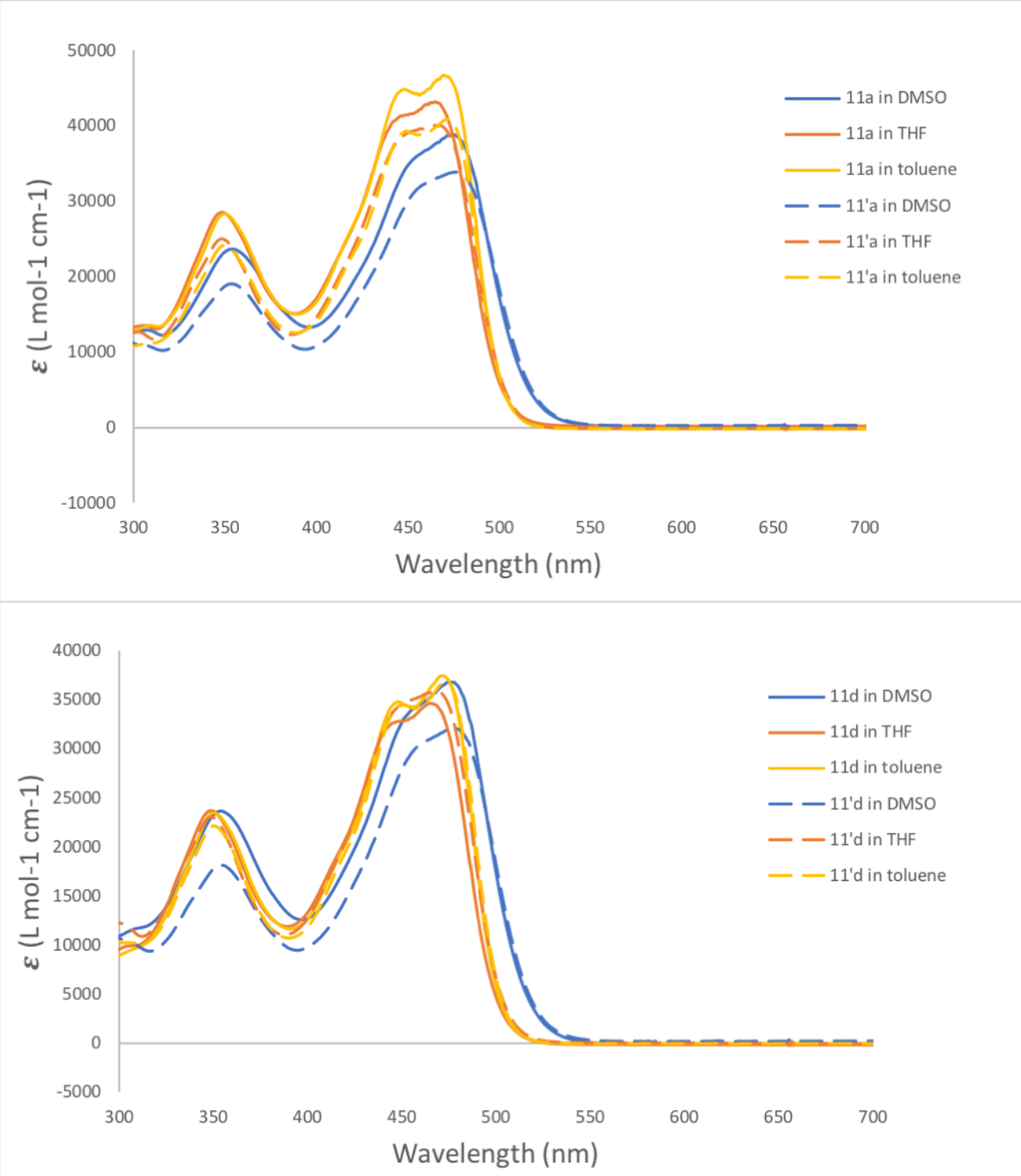

Figure 55 (Top) Extinction coefficient of both **11a** (bold lines) and **11'a** (dotted lines) and (bottom) extinction coefficient of both **11d** (bold lines) and **11'd** (dotted lines) measured in solvents of different polarities (DMSO in blue, THF in red and Toluene in yellow).

furoindole **9a,** and 7-fluorine-substituted furoindole **9e** (**11f** 89% and **11n** 98% respectively). On the contrary, the substitution with an electron-withdrawing group had a negative influence on the formation of compounds **11g** and **11l**, which were isolated in lower yields (55% and 67%, respectively). As previously shown (Scheme 7), the reaction with a disubstituted propargyl ester was less efficiently leading to formation of corresponding product **11h** in a yield of 36%. The modification of the OR^3 group in the ester led to excellent results. By replacing pivalate with the less hindering compound acetate, **11i** was isolated in 56% yield, while a more electron-withdrawing thienyl derivative afforded **11j** with a high yield of 98%. Finally, the attention focused on the modification of indole core of **9a–g**. It was noted that substituents with different electronic properties at the C7 position were well tolerated. Notably, methoxy-substituted indoles provided **11k** and **11l** with a yield of 75% and 67%, respectively. These values are slightly diminished, but still good. However, fluorine-substituted products **11m** and **11n** were synthesized with excellent yields of 84% and 98%, respectively, starting from the corresponding fluorinated indole **9e**. In most cases, traces of the corresponding tetracyclic compounds **12** were detected in the crude reaction mixtures via ^{1}H NMR spectroscopy. Moreover, a preliminary set of photophysical properties were established for the highly conjugated compounds **11a**/**11'a** (isolated during the preliminary reactivity tests) and **11d**/**11'd** (isolated while performing the standard reaction, avoiding the iodine mediated isomerization step). UV/Vis spectra in solvents of increasing polarity, toluene, THF and DMSO were recorded. The molar extinction coefficient was calculated from absorbance values using the linear regression method. The spectra show two peaks at about 350 and 470 nm (Fig. 55).

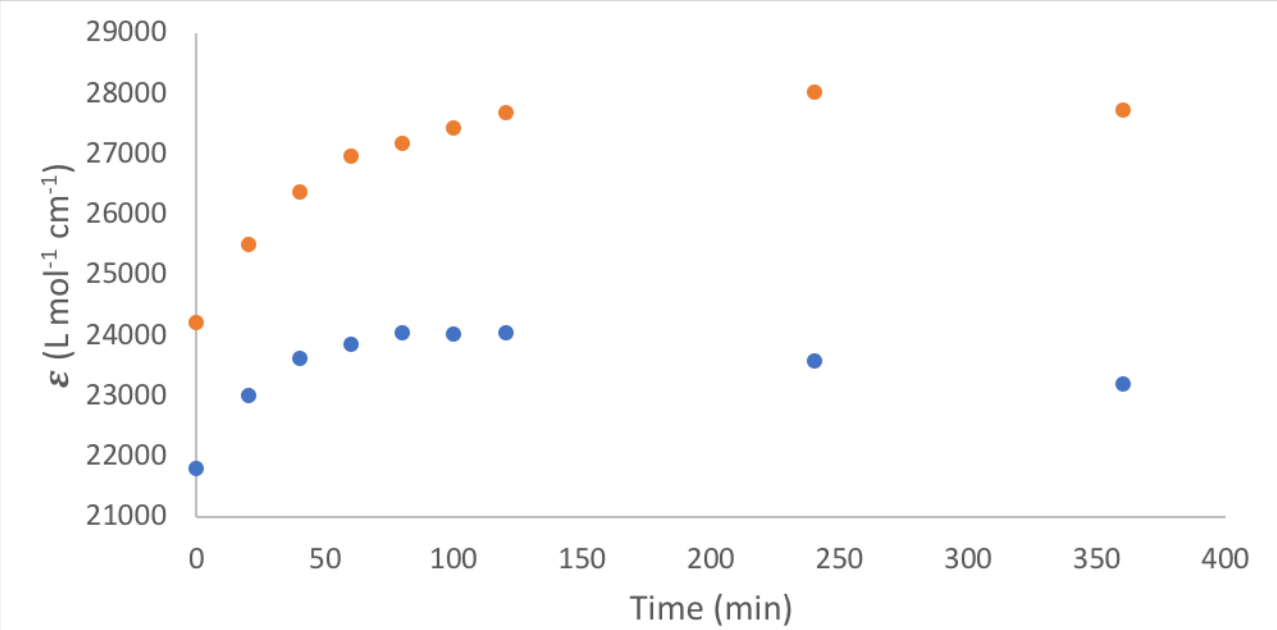

Figure 56 Extinction coefficient vs. time at 354 nm for **11a** (blue) and **11d** (orange) measured in DMSO at a concentration of $2 \cdot 10^{-5}$ M.

Table 12. Extinction coefficient for 11a/11'a and 11d/11'd measured in solvents of different polarities

Compound	DMSO			THF		Toluene
	ε (L mol^{-1} cm^{-1})			ε (L mol^{-1} cm^{-1})		ε (L mol^{-1} cm^{-1})
11'a	ε_{353} 17873	ε_{474} 32504	ε_{348} 24985	ε_{468} 40446	ε_{349} 23324	ε_{472} 39580
11a	ε_{354} 22988	ε_{474} 38170	ε_{348} 26630	ε_{466} 40636	ε_{350} 27593	ε_{470} 45751
11'd	ε_{355} 18604	ε_{479} 33831	ε_{349} 22986	ε_{466} 36935	ε_{350} 20826	ε_{474} 35413
11d	ε_{354} 24052	ε_{476} 37628	ε_{349} 24209	ε_{465} 35417	ε_{351} 24945	ε_{471} 39690

The absorption wavelengths are essentially the same for both isomers of compounds **11a** and **11d**. The value of absorbance (and therefore the extinction coefficient) is the main difference between the Z/E spectra. As reported in Table 2, molar extinction coefficient values for both Z compounds are greater than those for E isomers, with the only exception of the more red-shifted **11d** peak of in THF. The solvatochromism is rather small for all derivatives. Different solvents induce a variation of the extinction coefficient rather than the absorption wavelength. In particular, the larger variations are observed in derivative **11'a**, when switching from DMSO to THF.

The photoisomerization reaction was followed by the UV irradiation of pure **11'd** and **11'a** solution in DMSO (2 × 10−5 M) with a 200 W lamp to promote the complete conversion to the Z isomer. To avoid solvent evaporation during the conversion the photoisomerization was carried out in a rotaflo-equipped cuvette. In this condition the concentration of the species in solution remains constant. Measurements were taken every 20 minutes to monitor the isomerization from E to Z. As expected, an increase in the extinction coefficient was observed. In both cases, by plotting the intensity of the peak at 354 nm vs. time (Fig. 56) it was found that reaching the equilibrium requires about 2 hours. Upon extending the time (6 h), a slight decomposition of the products was observed. Finally, some simple transformations were realized; compounds **11a** and **11d** as substrates, and two indoles (**9f** and **9g**), different from standard furoindoles, were subjected to standard reaction conditions (Scheme 10).

N-CO2Et and N-Boc protected compounds **11a** and **11d** were deprotected in alkaline and acidic conditions, respectively. The corresponding 2-alkylydene-3- oxoindole **11o** was isolated in moderate to good yields. Then, the same compounds **11a** and **11d** were reduced under catalytic conditions. Hydrogenation of the entire trienylidene moiety was observed and the compounds **13a** and **13b** were isolated as a 1 : 1 mixture of diastereoisomers. Finally, the reactions of 2-vinyl and 2-methyl indoles **9f** and **9g** with **10a,** under standard reaction conditions, provided the cyclopropanation

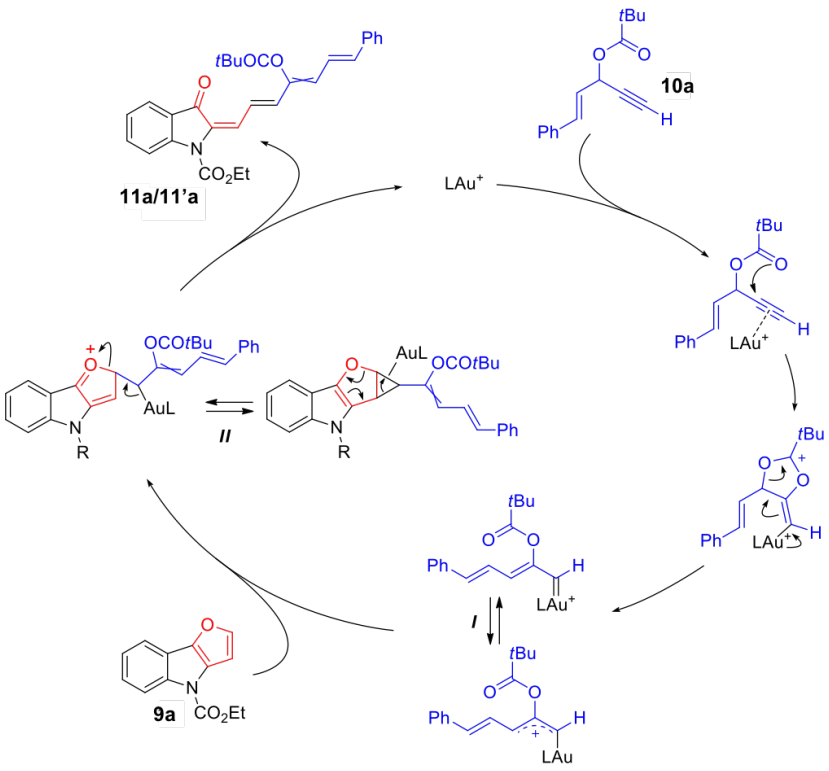

Scheme 11 Proposed reaction mechanism.

adduct (**14**) at the exocyclic double bond of 1f and the hydroarylation product (**15**) with **9g**. The geometries around the cyclopropane moiety and diene system of **14** were tentatively assigned via 1D and 2D NMR spectroscopy.

Moreover, the reaction mechanism was confirmed by considering the data reported in the literature concerning reactivity of gold–carbene complexes[211] and electrophile driven furan ring opening reactions (Scheme 11)[209,212–214]. The cationic gold(I) catalyst activates the terminal propargyl ester. This triggers the reversible[215] 1,2-acyloxy migration leading to formation of the derivative I, which can be described as a gold-carbene or as an oxy- allyl cation. Therefore, I reacts as a pure electrophilic carbene with the C2–C3 furan carbons of **9a** to provide the corresponding cyclopropanated species II. Alternatively, considering intermediate I as an oxyallyl cationic specie, intermediate II could be formed due to the electrophilic attack on the C2 carbon atom of furoindole **9a**. Finally, both arrangements of intermediate II evolve via the furan ring-opening reaction affording the final products **11a**/**11'a** and restoring the gold(I) catalyst. Probably, the E/Z geometry around position 4 at the trienylidene moiety of **11a**/**11'a** results from the dual nature of the intermediate I which possesses a fixed geometry merely in the carbenic form dictated by the mechanism of 1,2-migration.

4.2.3. Conclusions

The work reports on an efficient and high yielding methodology for the synthesis of polyconjugated 2-alkylidene-3-oxoindoles. Cationic gold(I) catalysts allow promoting the selective formation of gold-carbenes from propargyl esters under mild reaction conditions. Moreover, the gold catalyst is implicated in the electrophilic addition/ ring opening sequence with furoindoles. The results demonstrate the usefulness of these catalysts in promoting complex cascade reactions. In addition, these catalysts allow to improve and expande the synthetic concept indroduced by Prof. Rossi's group in a previous work[199] on the electrophile-driven ring- opening reactions of furoindoles for the synthesis of 3-oxo- indole derivatives. The compounds synthesized represent a new class of 2-alkylyden-3-oxoindoles. To the best of our knowledge, while a great deal of articles report the synthesis of simple 2-methyleneindolin-3-one13 (indigo derivatives) and 2-allylideneindolin-3-one[216], only few outdated references deal with trienylidene derivatives [217].

4.3. Synthesis of 2-alkenylidene-3-oxoindolines: cascade reactions of 4*H*-furo[3,2-*b*]indoles with diazoacetates catalyzed by a Cu(I) macrocyclic pyridine-containing ligand (PcL) complex

4.3.1. Introduction

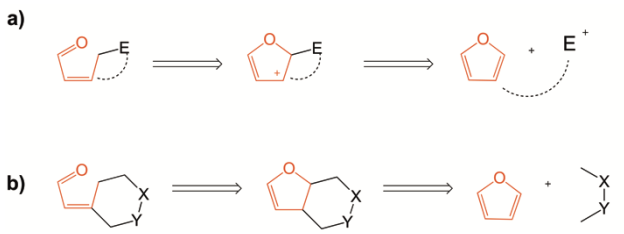

Scheme 12 Ring opening reactions of furans.

Ring opening reactions of furans are a well documented class of organic transformations[212]. They mostly occur by intra- or intermolecular addition of electrophiles at C2, followed by a ring-opening event[213,218–221], Scheme 12a, or imply the C2 C3 bond in annulation reactions with suitable partners followed by ring rearrangement[214,222], Scheme 12b.

Prof. Rossi's group has recently exploited this type of reactivity with 4*H*-furo[3,2-*b*]indoles, compounds with a furan ring embedded in a tricyclic framework[199,223]. For example[223], as shown in Scheme 13a, *E,E,Z,E*-(hepta-2,4,6- trien-1-ylidene)-3-oxoindolines were synthesized starting from 4*H*-furo[3,2-*b*]indoles via a cascade sequence involving gold-carbene complexes ***I***. The reaction starts with the formation of a gold-carbene species via cationic gold(I) catalyzed 1,2-acyloxy migration of properly substituted propargyl esters followed byaddition of gold-carbene to furoindole and successive furan ring-opening.

However, adequate yields were obtained only with α-styryl substituted propargyl esters whereas alkyl or aryl substituted derivatives provided the corresponding alkyliden-3-oxoindolines in poor yields. Thus, in order to expand the applicability of these transformations, copper- carbene complexes generated in situ from diazoalkanes under copper(I) catalysis were tested for the

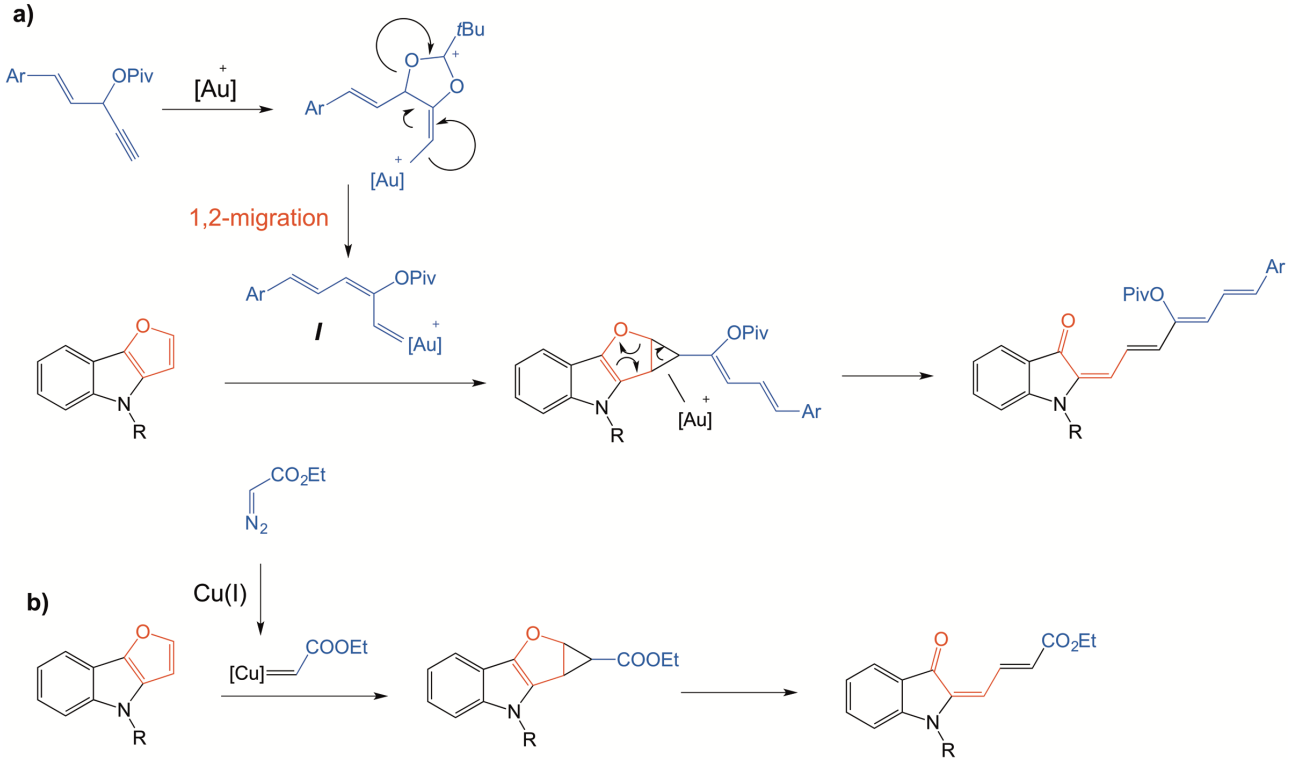

Scheme 13 Reactivity of 4H-furo[3,2-*b*]indoles with: a) gold-carbene and b) copper-carbene complexes (this work).

synthesis of 2-(penta-2,4-dien-1-ylidene)3-oxoindolines, Scheme13b. In this field, Prof. Rossi has recently reported on the coordination chemistry of pyridine containing macrocyclic cyclen-type ligands (PcL) and the catalytic activity of their copper(I) complexes[224]. Due to the importance in organic synthesis of the reactions involving metal catalyzed carbene transfer starting from diazoalkanes [225–227], a series of [Cu$^{(I)}$(PcL)] complexes was evaluated in alkene cyclopropanation[228–231] and X-H bond insertion reactions[232]. More recently, the ability of those [Cu$^{(I)}$(PcL)] complexes to efficiently catalyze the reaction between 2-vinylindoles and diazoesters to yield a series of 2-vinylcyclopropa[*b*]indolines with excellent levels of regio- and stereocontrol[233] was demonstrated.

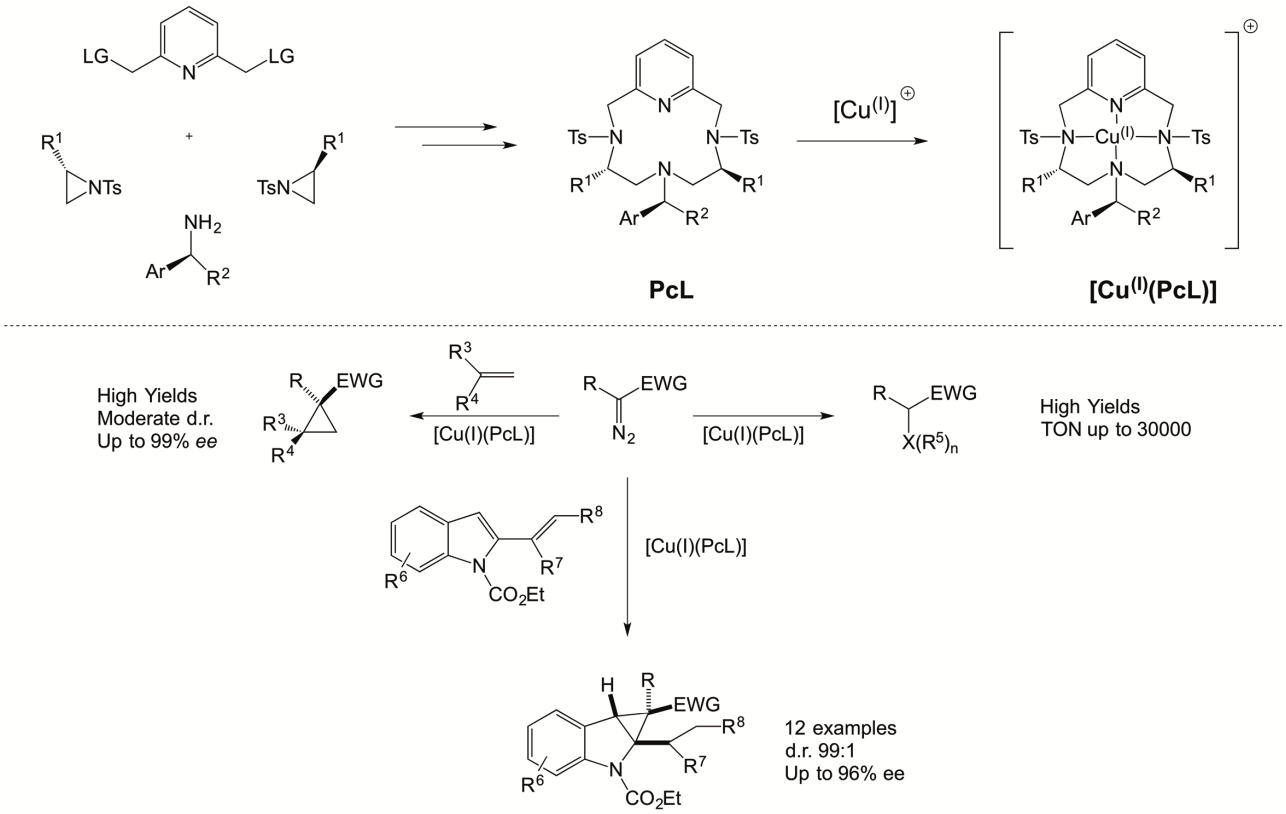

Scheme 14 Synthesis of pyridine-containing ligands (PcL) and their applications in copper(I)-catalyzed cyclopropanations with diazo compounds.

The synthetic path used to obtain the target macrocyclic complexes, including chiral non racemic ones, is flexible and high yielding, starting from cheap materials, Scheme 14.

4.3.2. Results and discussion

Initially, the reactivity of furoindole **16a** with EDA (EDA = ethyldiazoacetate) was evaluated, by screening several metal catalysts, Table13. The slow addition of EDA to a dichloromethane solution of furoindole **16a,** in the presence of classical rhodium(II) octanoate dimer complex ($Rh_2(Oct)_4$, 2.5 mol%), a well-established precursor for the Rh(II)-carbenoid mediated cyclopropanation of alkenes, with diazocarbonyl compounds[234], provided a separable 2.5 : 1 mixture of *E/Z* isomeric 2-(penta-2,4-dien-1-ylidene)3-oxoindolines **17a** and **17'a** (entry 1, Table 13) in good yield . The structure of the isolated compounds was confirmed by analytical (HRMS) and spectral data (1D NMR). The

TABLE 13. OPTIMIZATION OF THE REACTION CONDITIONS.[A]

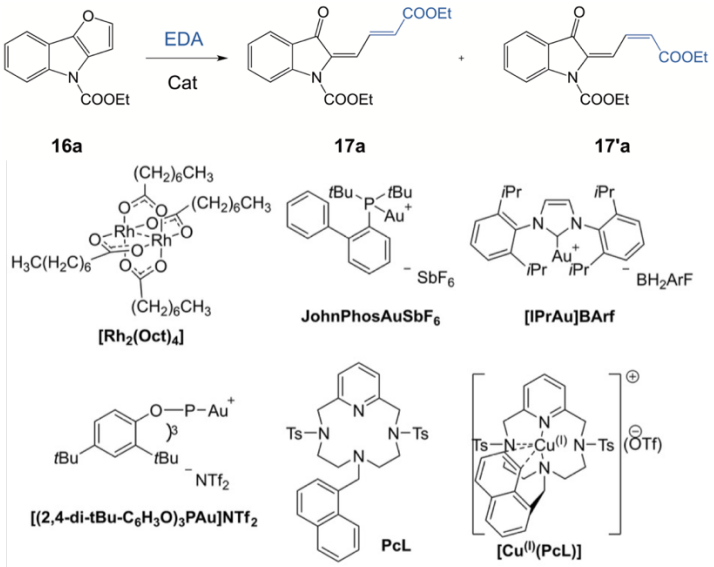

Entry	catalyst	Solvent [M]	Equiv EDA	t [°c]	t [h]	**17a**[b] [%]	**17'a**[b] [%]
1	$Rh_2(Oct)_4$ 2.5 mol%	DCM 0.05	2[c]	rt	1.5	49	20
2	$Rh_2(Oct)_4$ 1.0 mol%	DCM 0.05	2[c]	rt	1.5	41	17
3	JohnPhosAuSbF$_6$ 5 mol%	DCM 0.05	2[c]	rt	1.5	/[d]	/
4	IPrAuCl 5 mol% NaBArF 5 mol%	DCM 0.1	2[e]	rt (2h) 40 (3h)	5	/[d]	/
5	$(ArO)_3PAuNTf_2$[f] 5 mol%	DCM 0.1	2[e]	rt (2h) 40 (3h)	5	/[d]	/
6	$Cu(OTf)_2$ 15 mol% Ph-$NHNH_2$ 15 mol%	DCM 0.05	2[c]	rt	1.5	29	12
7	$Cu(OTf)_2$ 8 mol%	DCE 0.07	1.5[g]	rt	2	19	6
8	$[Cu(OTf)]_2$*C_6H_6 (5 mol%) PcL (10 mol%)	DCE 0.07	2.5[g]	rt	1	75	12
9	[Cu(I)(PcL)] (8 mol%)	DCE 0.07	1[g]	rt	1	30	6
10	[Cu(I)(PcL)] (8 mol%)	DCE 0.07	1.5[h]	rt	2	74	25

[a] All reactions were carried out using **1a** (0.2 mmol) and EDA (0.2-0.5 mmol) in the stated solvent (0.1-0.05 M) in the presence of 4 Å MS. [b] isolated yield. [c] EDA added with syringe pump in 1h in 1 mL of solvent. [d] **1a** and EDA recovered unreacted at the end of the reactions. [e] EDA added manually dropwise. [f] Ar = (2,4-di-*t*Bu-C_6H_3). [g] EDA added with syringe pump in 1h in 2 mL of solvent. [h] EDA added with syringe pump in 2h in 2 mL of solvent.

reduction of the catalyst load to 1.0 mol% caused a slight yield decrease (entry 2, Table 13). Next, the model reaction was run, in the presence of 5 mol% of preformed cationic JohnPhosAuSbF_6 catalyst[235]. In this conditions, no traces of products were detected and only the starting furoindole **16a** was quantitatively recovered (entry 3, Table 13). Other cationic gold(I) catalyst, namely chloro[1,3-bis(2,6-diisopropylphenyl)imidazol-2-ylidene]gold(I), [IPrAu]BArF, and [(2,4-di-*t*Bu-C6H3O)3PAu]NTf2 were also ineffective, even in refluxing DCM (Table 13 entries 4 and 5).

Instead, copper(II) triflate in the absence of any reducing agent, lowered the yield (entry 7).

When the in situ formed copper(I)/PcL complex was used[229], the yield of the desired oxoindolines **17** was increased to 87 % with a diastereoisomeric *E/Z* ratio of 6.25 to 1 (entry 8, Table 13). A further optimization of the reaction conditions was carried out by slowly adding the isolated copper complex a 1.5 fold molar ratio over the starting EDA. Under these conditions, an almost quantitative yield of the desired products was obtained, in a d.r. of 3 (entry 10, Table 13). It is possible to obtain **17a** as a single isomer just treating the solution after the complete addition of EDA with a catalytic amount of iodine as already reported for 3-oxo-2-(hepta-2,4,6-trien- 1-yilidene)indolines[223],. The conversion of a mixture of **17a**/**17'a** stereoisomers to the **17a** isomer was completed (> 98 %) in 2hours (Scheme 15).

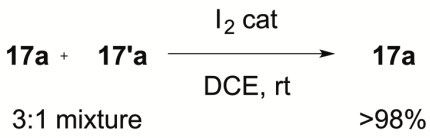

Scheme 15 Isomerization of a **17a**/**17'a** mixture to pure **17a**.

Once the reaction conditions were optimized, the applicability of the reaction was explored. All the reactions were carried out under the conditions reported in the footnote of Table 13 (entry 10). Once the reaction mixture was treated with iodine to fully convert the *Z* isomer into the more stable *E* compound, Scheme 16, the compounds **17a**–**m,** purified by chromatography**,** were characterized.

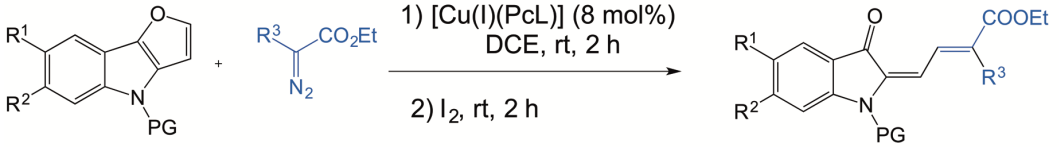

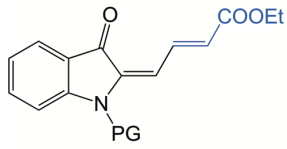

17a: PG = CO_2Et, 99%
17b: PG = Boc, 68%
17c: PG = Me, 77%

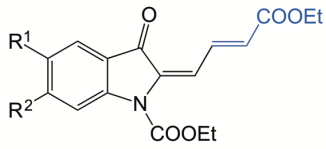

17d: R^1 = OMe, R^2 = H, 73%
17e: R^1 = Me, R^2 = H, 94%
17f: R^1 = H, R^2 = OMe, 66%
17g: R^1 = F, R^2 = H, 73%
17h: R^1 = H, R^2 = F, 61%

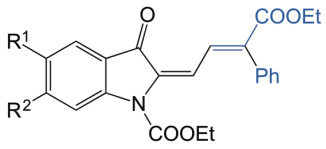

17i: R^1 = H, R^2 = H, 69%[a]
17j: R^1 = OMe, R^2 = H, 93%
17k: R^1 = H, R^2 = OMe, 95%[b]
17l: R^1 = F, R^2 = H, 92%[c]
17m: R^1 = H, R^2 = F, 80%[d]

Reaction conditions: **16** (0.2 mmol) and diazocompound (0.3 mmol) in DCE (0.07 M), *E/Z* > 98:2.
[a] *E/Z* = 95:5. [b] *E/Z* = 88:12. [c] *E/Z* = 85:15 .[d] *E/Z* = 96:4.

Scheme 16 Reaction scope.

Firstly, the reaction between **16a** and EDA provided **17a** in almost quantitative yield as a single isomer. Then, the influence of the protecting group at the nitrogen position on the yield was investigated. In particular, it was acertained that a bulkier electron-withdrawing group such as N-Boc lower the yield of **17b** (68%). Instead, the substitution of the starting furoindole with an electron-donating N-methyl group was tolerated, and compound **17c** was obtained in 77 % yield.
A study on the influence of the substitution pattern of the starting furoindole indicated that the introduction of a methyl substituent at C7 of the indole core did not alter the reaction outcome. The compound **17e** was obtained in excellent yield (94%). The presence of the more coordinating methoxy group at the same position decreased the yield of the isolated compound **17d** (73%). Similar effect on the yield was observed also when the methoxy group was in C8 position, leading to the desired product **17f** in 66% yield. When electron-withdrawing groups were present on the indole core, either at C7 or at C8, a drop in the isolated yield of the product was observed, and the corresponding product **17g** and **17h** were obtained in 73% and 61% yield respectively. The substituent in C8 is less tolerated than in C7 position, in both cases regardless the nature of substituent.
Finally, the reactivity of a donor/acceptor carbenoid precursor was tested, namely methyl phenyl diazoacetate. Due to its superior stability, this compound is far less susceptible to dimer formation[236]. Good to excellent yields were observed with all tested furoindoles. Thus, the model furoindole **16a**, reacting with methyl phenyldiazoacetate, gave rise to the single isomer **17i** in 69 % yield, whereas excellent yields were obtained for all C7 and C8 substituted furoindoles. In these cases, changing the position of the methoxy group did not cause differences on the outcome of the reaction, and the corresponding products **17j** and **17k** were obtained in 93% and 95% yield, respectively. The same trend reported for EDA was seen with the fluorine derivatives with a lower yield for compound **17m** than for **17l** (80% and 92% yield respectively). It is worth noting that the yield for all methoxy and fluorine derivative products was higher than that obtained for the corresponding compound using EDA, showing enhanced selectivity of methyl phenyldiazoacetate.

Table 14. Main absorption bands in the UV-Vis spectra and second-order NLO response

Compound	Absorption[a] $\lambda_{max/nm}$ (ε[$M^{-1}cm^{-1}$])	$\mu\beta$ [x 10^{-48} esu][b]
17a	246(14898), 283(13033), 317(8362), 396(2993)	230
17c	247(5379), 308(19024), 316(1849), 509(3929)	190
17d	287(1879), 317(7274), 330(6598), 426(2793)	410
17e	246(18388), 310(10333), 322(18326), 417(5029)	400
17g	284(14646), 295(15141), 320sh (11436), 413(3559)	480
17h	250(19419), 289(25362), 315sh (16742), 330sh (10016), 393(5291)	540
17l	289(15846), 343(11980), 416sh (8861), 432(9516)	640
17m	252(2218), 289(26299), 332(19758), 409(17182)	680

[a] In $CHCl_3$; UV-Vis spectra recorded in toluene are almost identical to the ones recorded in $CHCl_3$ solution. [b] in $CHCl_3$ 10^{-3} M working at 1.907 μm; estimated uncertainty in EFISH measurements is ± 20%.

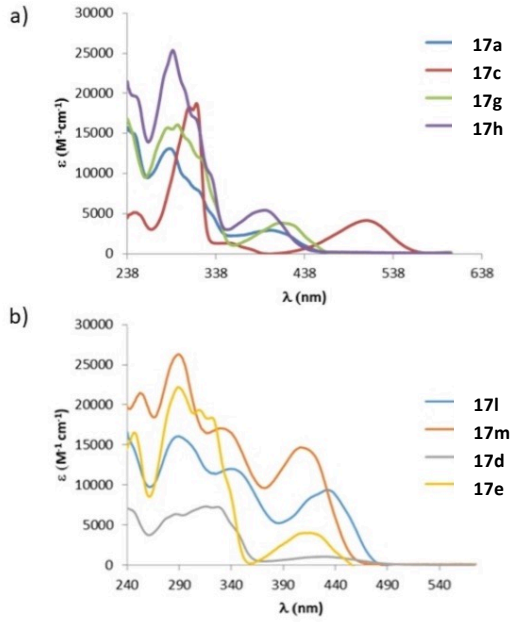

Figure 57 Absorption spectra in chloroform solution of compounds a) **17a**, **17c**, **17g**, **17h** and b) **17l**, **17m**, **17d**, **17e**.

The second-order nonlinear optical (NLO) properties of the target 2-(penta-2,4-dien-1- ylidene) 3-oxoindolines **17 were investigated.** These compounds have a peculiar structure, in which a quite long π-conjugated system with enforced coplanarity is accompanied by the presence of both electron donor and electron acceptor groups. It is known that chromophores with second-order NLO properties are important as molecular building block materials. They find application in molecular photonics, in particular for optical communications, optical data processing and electro-optical devices[237,238]. To provide a second-order NLO response, a molecule must not be centrosymmetric. Good quadratic hyperpolarizabilities, β, characterize *Push-pull* 1D dipolar molecules, in which an electron donor group (EDG) is separated from an electron acceptor (EWG) group by means of a π-conjugated polarizable spacer. As a general rule, the use of strong electron donors and acceptors and the incorporation of a bridge with a large conjugation length lead to a strong second-order NLO response[237–242].

Thus, this work investigates the NLO properties in solution of a selection of 2-(penta-2,4-dien-1-ylidene) 3-oxoindolines **17** by means of the EFISH (Electric Field Induced Second Harmonic generation) technique. EFISH affords the product μβ where μ is the ground state dipole moment[243–245]. UV-visible absorption spectra and μβ measurements of on compounds **17a**, **17c**, **17d**, **17e**, **17g**,

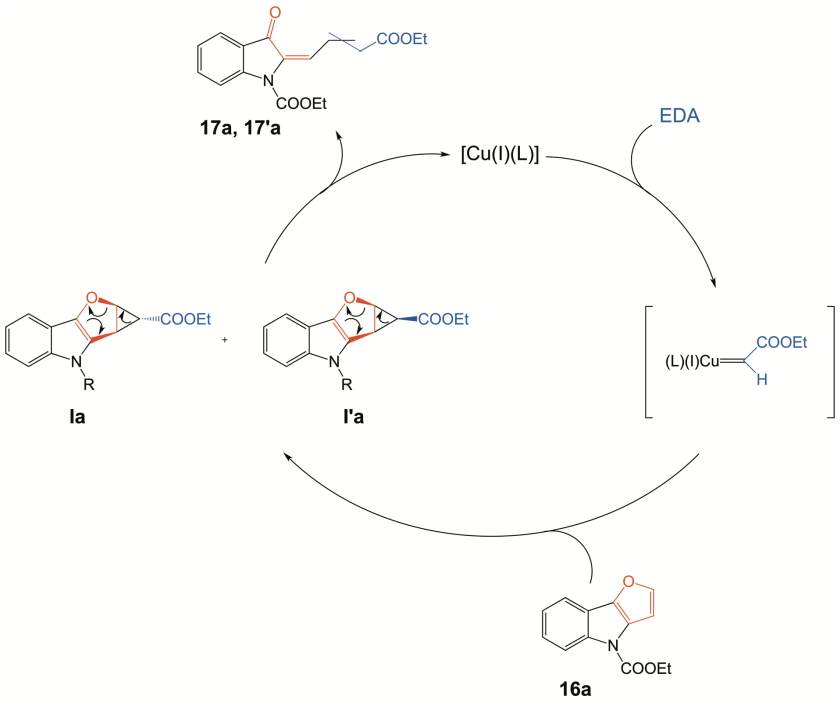

Scheme 17 Proposed reaction mechanism.

17h, **17l** and **17m** in chloroform solution were recordered and the results are summarized in Table 14. The main absorption maxima are reported in Table 14. By changing the substituent on the nitrogen atom from an ethyl-ester to a methyl group, from 17a to 17c, a relevant red shift of the band at lower energy is observed (Figure 57) . A Comparison of the **17a**, **17g** and **17h spectra** reveals the effect of a fluorine atom as substituent on the phenyl ring. In both **17g** and **17h compounds**, the presence of a fluorine atom increases the epsilon values.

Figure 57b shows the effect of MeO compared to Me (**17d** and **17e**): with the Me substituent, the epsilon values increase. A phenyl substituent on the terminal double bond causes a red-shift of the band at lower energy (compare **17g** with **17l** and **17h** with **17m**).

As reported in Table 14, all molecules are characterized by a fair to good second-order NLO response.

A clear dependence from the substituents on the core of the investigated compounds on the μβ values is present. Comparing compounds **17a** and **17d**, the positive effect of a donor group (MeO) on the phenyl ring (μβ goes from $230 \cdot 10^{-48}$ to $410 \cdot 10^{-48}$ esu) is clearly visible. However, even a slightly donor group such as Me (**17e**) gives a good response ($400 \cdot 10^{-48}$ esu). As previously observed[246], substitution of methyl by fluorine has a significant positive effect on the NLO properties (for **17g**, μβ is $480 \cdot 10^{-48}$ esu). Still, the position of the fluorine substituent has an influence: from **17g** to **17h**, μβ goes from $480 \cdot 10^{-48}$ to $540 \cdot 10^{-48}$ esu. As expected[237–242], a larger π-delocalization, obtained by adding a phenyl group on the terminal double bond, leads to a significant increase of the second-order NLO response: μβ is $640 \cdot 10^{-48}$ and $680 \cdot 10^{-48}$ esu for **17l** and **17m**, respectively. The two compounds characterized by the most intense bands at low energy in the UV-visible region (Table 14) provide the best second-order NLO response , in agreement with the two-level model[247]. Finally, from an application point of view, the μβ values of **17l** and **17m** are of interesting. They are superior to the value reached by Disperse Red One ([*trans*-4,4'-$O_2NC_6H_4N$= $NC_6H_4NEt(CH_2CH_2OH)$], $500 \cdot 10^{-48}$ esu) which has found application in electrooptic polymeric poled films[248].

Finally, a mechanism could be easily underlined looking at the studies reported in the literature on both the reactivity of copper carbene complexes[249] and the electrophiles-driven furan ring opening reactions[199], Scheme 17.

Activation of the diazoacetate by means of cationic copper (I) catalyst leads to the formation of the copper-carbene complex that reacts with the nucleophilic C2 C3 furan carbons of **16a** to give the corresponding cyclopropanated species **Ia**/**I'a**, which evolves via furan ring-opening to final products **17a**/**17'a**.

4.3.3. Conclusions

In conclusion, this work demonstrated that several differently substituted 2-alkenylidene-3-oxoindolines can be efficiently and selectively synthesized by using a catalytic system comprising Cu(I) and a pyridine-containing ligand (PcL). The results obtained improve and expand the synthetic pathway reported for the gold(I)catalyzed cascade reaction yielding to highly conjugated oxoindolines. In particular, the reported methodology allows for the installation of a double conjugated system at the C2 carbon atom of the oxoindoline which resulted unfeasible with gold(I) carbenes. The catalytic system used relies on the use of an economic metal source coordinated to an easy to assemble macrocyclic ligand under extremely mild reaction conditions. Substitution of the starting furoindole is well tolerated and, expecially when using a donor/acceptor carbenoid

precursor, excellent yields are obtained, regardless if an electron/donating (OMe) or an electron/withdrawing (F) atom are present. Interestingly, two of the 2-(penta-2,4-dien-1-ylidene) 3-oxoindolines are characterized by a second-order nonlinear optical response higher than that of Disperse Red One which has found application in electrooptic polymeric poled films.

Chapter 5. Materials and methods

5.1. Characterization of ferritins

5.1.1. Ferritin imaging

The samples were incubated on mica discs prepared as described in paragraph 5.2.1 “subtrate preparation”. A positively charged surface, was obtained through mica functionalization with poly-L-ornithine hydrobromide, purchased from Sigma. 10 µL of a solution of poly-L-ornithine 0,1 mg/mL in Milli-Q water were drop casted on a freshly cleaved mica disc for 3 minutes. The substrate was then gently rinsed with Milli-Q water (1 mL, 3 times) and dried under a stream of nitrogen. As imaging buffer for the measurements in liquid, Milli-Q water, PBS 1x pH 7,4 and HEPES 20 mM, NaCl 150 mM, pH 7,4 were used.

Humanized Archaeoglobus fulgidus ferritin (expressed by E. coli cells), apo- and holo-ferritin from Pyrococcus furiosus (expressed by E. coli cells) and horse spleen ferritin (purchased from Sigma Aldrich) samples were prepared at a concentration ranging from 1 µg/mL to 5000 µg/mL by dilution from a stock protein solution.

The proteins were placed on freshly cleaved mica or freshly cleaved mica functionalized with poly-L-ornithine. For in-liquid imaging: 30 µL of ferritin solution were drop casted on the substrate and incubated from 20 s to 10 mins to let the protein reach the surface, before rinsing with a suitable imaging buffer (1 mL, 3 times). For imaging in ambient conditions, 30 µL of ferritin solution were drop casted on the substrate and incubated from 20 s to 10 mins to let the protein reach the surface, before rinsing with Milli-Q water (1 mL, 3 times). The sample was then dried with a gentle stream of nitrogen.

AFM images were obtained using a multimode atomic force microscope Nanoscope 4.

Fluid imaging was performed in Peak Force Tapping mode with a Bruker MTFML-V2 fluid cell. ScanAsyst-Fluid AFM probes (tip radius: nominal 20 nm, max 60 nm) with a spring constant of 0,35-1,4 N/m and ScanAsyst-Fluid+ AFM probes (tip radius: nominal 2 nm, max 12 nm) with a spring constant of 0,35-1,4 N/m were used. ScanAsyst-Fluid+ AFM probes allowed a better resolution while ScanAsyst-Fluid AFM probes (with a bigger tip radius) were selected to prevent damaging the proteins. Air imaging was performed in Tapping mode with NCHV-A AFM probes (nominal tip radius: 8 nm) with a spring constant of 40 N/m, mounted on a MMEFCH (Bruker) tip holder.

5.1.2. Data analysis for protein morphological characterization

The surface density of the proteins in the micrographs obtained must be such as to have a high number of molecules (in order to have a good statistic), but at the same time they must be separated from each other. Once the image is processed to remove sample tilt and scanner bow, by means of a custom MATLAB functions, a mask file that identify the background is created. The mean value of the background is subtracted to the image and all the particles that emerge from the background are identified and labelled. Morphological properties such as volume, area, height, eccentricity and many others are obtained for each identified particle.

5.1.3. Ferritin iron loading

A solution of $FeSO_4$ 10 mM, HCl 0.5 mM were added dropwise to 2 mL of a solution of apoferritin from Pyrococcus furiosus 1 mg/mL in HEPES 50 mM, pH 7. In order to avoid the oxidation of Fe(II),

the solution of $FeSO_4$ was degassed and kept under nitrogen atmosphere during the whole procedure. The pH of the ferritin solution was constantly monitored during the addition of $FeSO_4$ and kept between 6,5 and 7,5 adding dropwise a solution of NaOH 0,1 M. To obtain ferritins loaded at various loading factors, different amounts of $FeSO_4$ solution were added to the protein solution, respectively: 20,8 µL, 41,7 µL, 125,1 µL, 291,1 µL and 1876 µL. After 30 min the reaction was interrupted and the sample centrifugated at 16000 rpm at 4°C for 20 min. The supernatant was transferred in an Amicon® Ultra Centrifugal Filter 30k (Merck Millipore) and the buffer exchanged with HEPES 20 mM, NaCl 150 mM, pH 7.

5.1.4. Labelling of ferritin

Labelling with Atto 488 maleimide

Working under nitrogen atmosphere, the reducing agent tris(2-carboxyethyl)phosphine (TCEP, 5 mg) was added to a degassed solution of Pyrococcus furiosus ferritin 8,5 mg/mL in HEPES 20 mM, NaCl 150 mM, pH 7,4 (500 µL, 8,85E-06 mmol Ft), mutated with 24 cys. After 20 min of stirring at RT, a solution of Atto 488 maleimide (1 mg) in DMSO (100 µL) was added dropwise and the solution was degassed again and stirred for 2 hours at RT. The solvent was then exchanged with HEPES 20 mM, NaCl 150 mM, pH 7 using an Amicon® Ultra Centrifugal Filter (30k) and concentrated at 300 µL.

Labelling with 6-maleimidohexanoic acid

Working under nitrogen atmosphere, 3,7 mg of TCEP were added to a degassed solution of Pyrococcus furiosus ferritin 8,5 mg/mL in HEPES 20 mM, NaCl 150 mM, pH 7,4 (300 µL, 5,31E-06 mmol Ft) under stirring at RT. After 20 min, a solution of 6-maleimidohexanoic acid (3,3 mg) in DMSO (100 µL) was added dropwise and the reaction proceeded under stirring for 2 hours at RT. The buffer was exchanged with HEPES 20 mM, NaCl 150 mM, pH 7 by means of a gravity desalting column and the sample concentrated at 300 µL with an Amicon Ultra Centrifugal Filter (30k).

Table 15. Standard solution and protein samples prepared for the Bradford essay

Solution	**From stock solution**	**Hepes**
Std 1	0 µL of Stock	1000 µL
Std 2	20 µL of Stock	980 µL
Std 3	40 µL of Stock	960 µL
Std 4	60 µL of Stock	940 µL
Std 5	80 µL of Stock	920 µL
Std 6	100 µL of Stock	900 µL
Std 7	120 µL of Stock	880 µL
Std 8	140 µL of Stock	860 µL
Std 9	160 µL of Stock	840 µL
Std 10	180 µL of Stock	820 µL
Holo 1:100	5 µL	495 µL
Holo 1:50	10 µL	490 µL
100 Fe/Ft 1:1000	1 µL	999 µL
100 Fe/Ft 1:500	2 µL	998 µL

Ellman essay

The essay was accomplished on (1) a solution of Pyrococcus furiosus ferritin mutated with 24 cys, (2) a solution of the same protein labelled with 6-maleimidohexanoic acid and (3) on a blank, prepared respectively as follow: (1) 18,8 µL of protein 8,5 mg/mL in HEPES 20 mM, NaCl 150 mM, pH 7,4 made up to volume (200 µL) with the same buffer pH 8,9, (2) 29,6 µL of protein 5,4 mg/mL in HEPES 20 mM, NaCl 150 mM, pH 7,4 made up to volume (200 µL) with the same buffer pH 8,9 and (3) 29,6 mL HEPES 20 mM, NaCl 150 mM, pH 7,4 and 170,4 µL of the same buffer pH 8,9. A solution of DTNB 10 mM in Milli-Q water (20 µL) was added. The samples were mixed for 5 mins and their UV-Vis spectra acquired with a Spectrophotometer (BioSpectrometer®, Eppendorf).

Bradford essay

From a freshly prepared BSA Stock solution 6,6 mg/mL in HEPES 20 mM, NaCl 150 mM pH 7,5, a solution of 0,1 mg/mL was obtained by dilution (15 µL to 1 mL). As reported in the following table, 10 standard solutions were obtained. Each standard solution (0,5 mL) was mixed with 0,5 mL of RT Bradford reagent. After 10 mins, the UV-Vis spectra of each solution were acquired with a Spectrophotometer in order to obtain a calibration curve. Within the same timescale (the Bradford staining is time depending, so it is important to prepare the standard solution and the samples at the same time), the protein samples were prepared as reported in the Table 15.

5.2. AFM investigation of ionic liquids' toxicity

5.2.1. Nanomechanics experiments

Substrate preparation

A 10 mm diameter mica disc (Highest quality grade V1 muscovite mica, Ted Pella Inc.) was glued with a bicomponent epoxy resin adhesive (RS, 850-940, Quick Set Epoxy Adhesive) on a 15 mm diameter Teflon disc, which in turn was glued on a 15 mm diameter metal disc (AFM specimen discs, Ted Pella, Inc.). The mica was cleaved with adhesive tape immediately before deposing sample solutions to expose an atomically smooth, clean surface to the phospholipids.

HBS buffer preparation

A solution of NaCl 150 mM, HEPES 20 mM, $CaCl_2$ 3 mM, $MgCl_2$ 5 mM in Milli-Q water (18,2 MΩcm at 25°C) was prepared and the pH adjusted to 7,4 with NaOH 1 M in Milli-Q water. The ionic strength of the solution is ≈150 mM.

Supported lipid bilayer (SLB) preparation by vesicle fusion

A 10,6 mM stock solution of the phospholipid DOPC (1,2-dioleoyl-sn-glycero-3-phosphocholine) in chloroform was prepared by dissolving 25 mg of DOPC in 3 mL of chloroform. The DOPC solution was stored under nitrogen atmosphere at -20 °C.

A solution containing unilamellar phospholipid vesicles was prepared. To this purpose, 283 µL of the stock solution were evaporated in a 10 mL pear-shaped flask with a nitrogen flow, reclining and rotating the flask during the operation so that the DOPC spreads homogeneously on the inside of the flask. The evaporation was finalized in a desiccator under vacuum overnight. Then, 3 mL of HBS buffer were added, resuspending the DOPC with a vortex mixer, thus obtaining a cloudy milky suspension. The suspension was sonicated in an ice bath with an immersion ultrasonic sonicator (Omni Ruptor 200, Omni International Inc.) until it became clear (1 minute at 85 % of the maximum power and 1 minute rest, 10 cycles). Samples for AFM were prepared fresh just after sonication, to

be sure that the unilamellar vesicles were still present and not aggregated into larger multi-lamellar vesicles. The obtained solution of DOPC 1 mM in HBS could be stored for 3-4 days at 4 °C. After few days, multi-lamellar vesicles tend to reform, therefore it is necessary to sonicate again before deposition.

To prepare samples for AFM investigation, 40 µL of DOPC in HBS were placed on a freshly cleaved mica disc and incubated for 30 minutes, heating with an incandescent lamp to favour the organization of the fused unilamellar vesicles into an ordered, extended, supported lipid bilayer. To avoid the sample evaporation, the disc was placed under a double enclosure, obtained by the far end of a cut Falcon tube and a transparent plastic cup placed on it. After 30 minutes the lamp was turned off and the sample incubated for 1 hour, then rinsed with HBS buffer (300 µL, 3 times) and let thermalized for 30 minutes. During this process, care was taken not to allow the solution to evaporate.

Nanomechanics measurements

All measurements were performed using a Multimode 8 AFM from Bruker. A fluid cell (MTFML-V2, Bruker) was used to carry out the measurements in solution. Inlets and outlets allowed to exchange the solution, and in particular to inject the IL when needed.

A 2 µm x 2 µm image of the SLB was acquired in Peak Force Tapping mode using a ScanAsyst Fluid probe (Bruker) with a nominal tip radius of 20 nm (max 60 nm) and a spring constant of 0,35-1,4 N/m, to check the condition of the bilayer. After every image, a set of force – distance curves (15 x 15 grid, 50 nm step) in auto ramp mode was acquired. Then, the probe was manually moved on a new area of the bilayer using the designated screw and the optical microscope. For each sample, 3-4 auto ramps were collected. Force curve sets were acquired both before and after the exposition of the lipid bilayer to the IL. For each IL condition, a set of force curves was collected without the IL on the same bilayer, in the same experimental conditions, to serve as control.

Preparation of [Bmim][Cl] solutions at various concentrations

1-butyl-3-methylimidazolium chloride 99%, [Bmim][Cl] (purchased from IoLiTec) is solid at room temperature; the IL was heated in the oven at 70 °C for 3 hours until complete melting of the ionic liquid was obtained. A stock solution of [Bmim][Cl] 500 mM in HBS buffer was prepared and solutions 400 mM, 300 mM, 50 mM, 10 mM and 5 mM were obtained by dilution.

Preparation of [Omim][Cl] solutions at various concentrations

A stock solution of 1-octyl-3-methylimidazolium chloride 99%, [Omim][Cl] (purchased from IoLiTec), 6 mM in HBS buffer was prepared and solutions 100 µM, 10 µM and 1 µM were obtained by dilution.

SLB conditioning with IL solution

After completing the AFM measurement on the bare phospholipid bilayer, 3 mL of the ionic liquid solution, at the chosen concentration, were gently injected in the fluid cell (MTFML-V2, Bruker) and allowed to condition the supported lipid bilayer for 20 minutes before the measurements. The nanomechanical measurements on the conditioned IL were performed as described above.

5.2.2. Force spectroscopy experiments

Silicon functionalization with APTES

A silicon wafer was cut into rectangular fragments (around 5 mm x 10 mm), rinsed with ethanol and dried with a stream of nitrogen. Two cleaning protocols were tested. Half of the silicon samples were cleaned with piranha solution (H_2SO_4/H_2O_2 3:1) kept at 90°C for 1 hour, then rinsed with Milli-Q water (5 minutes, 3 times). The other half were cleaned with a Helizime and Alconox according to the following protocol: the silicon fragments were cleaned overnight in a solution of Helizime (Enzymatic cleaner, Braun) 1% at rt and then in a solution of Alconox® Powder Precision Cleaner (Alconox) 1% for 1 hour at rt. Finally, the samples were rinsed with Milli-Q water (5 minutes, 3 times). The clean silicon pieces were functionalized by APTES vapors, half of them in nitrogen atmosphere and the others under static vacuum. To perform the functionalization, a customized desiccator connected to a Schlenk line, that allow creating APTES vapors both under vacuum or in a nitrogen atmosphere was used. Just before the APTES treatment, the silicon fragments underwent a plasma treatment to recover the pristine density of surface -OH groups using a surface plasma cleaner (Zepto, Diener electronic) at 80W for 5 minutes. Then, 500 µL of APTES were introduced into the dedicated desiccator containing the silicon, and a vacuum or nitrogen atmosphere was created. The samples were incubated for 10, 5 and 2 minutes, then rinsed with anhydrous toluene (3 times for 5 minutes) and cured in the oven at 120°C.

Contact angle characterization of the Si-APTES samples

Contact angle measurements were performed on the APTES functionalized silicon samples with a custom sessile drop instrument. A droplet of Milli-Q water was settled down on the sample and three pictures on both the right and left side of the drop were acquired using a CCD camera. The profiles of the droplet were digitized and fitted to evaluate the slope (the contact angle) at the liquid-solid-air interface.

ATR-FTIR characterization of the Si-APTES samples

ATR-FTIR spectra were recorded on a Jasco 6000 spectrometer. The ATR accessory (ATR PRO550S-S) contained a ZnSe crystal (1,5 mm diameter) at a nominal incident angle of 45°, yielding 1 internal reflection at the sample surface.

AFM probe functionalization

Step 1, APTES functionalization

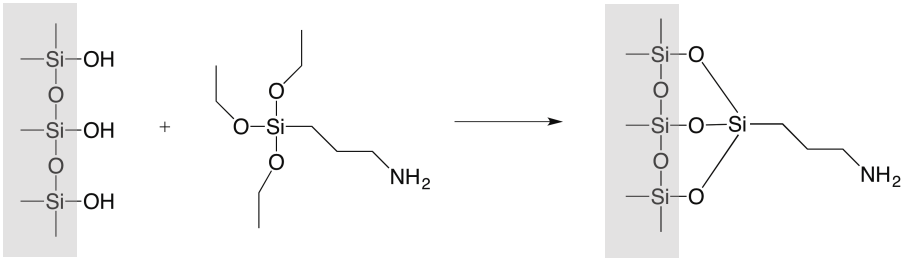

Scheme 18 Reaction scheme of the APTES functionalization of an AFM probe.

Before the APTES functionalization the probes have been treated with piranha solution to increase the -OH groups on the surface of the tips, made of Si_3N_4. On a Teflon tip-holder, 8 AFM contact mode probes DNP-10 purchased from Bruker (spring constant of 0.175-0.7 N/m and nominal tip radius: 20 nm) were secured and cleaned with piranha solution at 90 °C for 40 minutes, then rinsed with milli-Q water (5 minutes, 3 times). Two tips were kept as reference while the others were

introduced into the desiccator designated to the APTES functionalization (see paragraph 5.2.2. “silicon functionalization with aptes”). A N_2 atmosphere was obtained in the desiccator to avoid polymerization of the the aminosilane caused by moisture[250]. Under a gentle stream of nitrogen, 500 µL of APTES were introduced into the desiccator and its vapors let react with the probes under static vacuum, for 10 minutes. Then, the probes were rinsed with distilled toluene (5 minutes, 2 times), dried under a gentle stream of nitrogen and cured in the oven at 120°C for 2 hours. Two probes were kept as reference, the others proceeded through the next step.

Step 2, PEG functionalization.

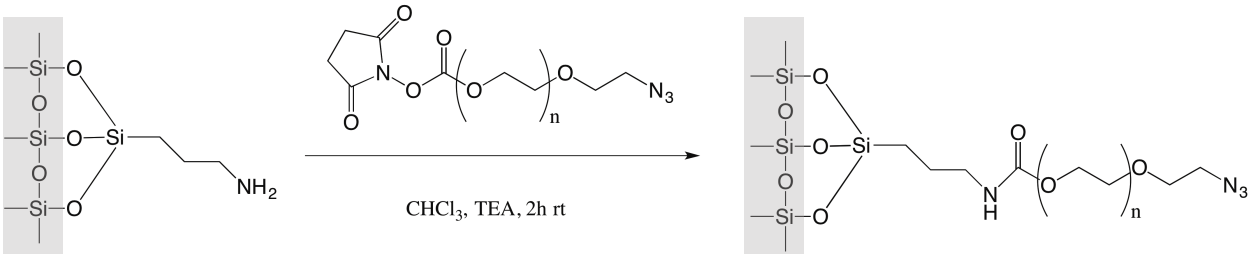

Scheme 19 Reaction scheme of the PEG functionalization of an AFM probe.

The AFM probes, secured in the tip-holder, were immersed into a solution of 20 mL of distilled chloroform, 40 mg of heterobifunctional PEG (NHS-PEG-N_3 2K) and 1,2 mL of distilled TEA. After 2 hours the probes were rinsed with distilled chloroform (10 minutes, 3 times) and dried under vacuum. Two probes were kept as reference, the others proceeded through the next step.

Step 3, *n*-octyl functionalization.

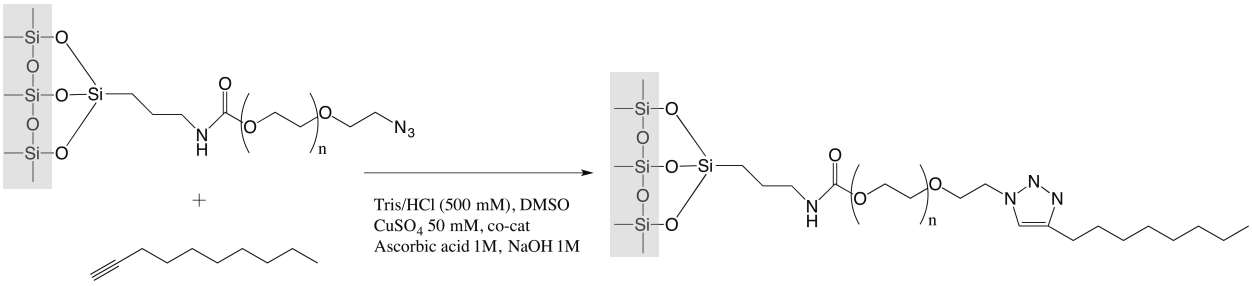

Scheme 20 Reaction scheme of the octyl functionalization of an AFM probe.

This step was performed working under nitrogen atmosphere, in a Schlenk flask. A solution of 15 mL Tris/HCl 500 mM pH 8.6, 4,5 mL DMSO, 125 µL $CuSO_4$ 50 mM, 625 µL Co-cat (Bathophenanthrolinedisulfonic acid disodium salt hydrate) 10 mM and 3,75 mL 1-decyne 6,5 mM in DMSO was degassed, then were quickly added 0,5 ml ascorbic acid 1 M, 0,5 mL NaOH 1 M and the solution degassed again. The probes were immersed overnight in the solution at RT, then rinsed with milli-Q water.

Force spectroscopy measurements

3 auto ramps (grid of 15 x 15 force curves, step 50 nm) were acquired on macroscopically separated areas of a freshly prepared SLB (see paragraph 5.2.1. “Supported lipid bilayer (SLB) preparation by vesicle fusion”) with a contact mode DNP-10 (Bruker) test probe, to confirm the presence of the bilayer, through the observation of the typical breakthrough event in the force curve (see paragraph 3.2.1, Fig. 47). Once the presence of a single bilayer was verified, auto ramps in different areas were

acquired as descripted above, using the functionalized probes of paragraph5.2.2. “AFM probe functionalization”. The contact time of the probe with the sample during each force curve was set at 2 seconds. The setpoint was set at 2 nN in order to avoid the penetration of the tip into the bilayer, at the same time allowing a stable contact and interaction of the octyl group with the lipid bilayer. Since the acquisition of all the auto ramps required around 10 hours, the condition of the SLB with the test probe was periodically checked.

5.2.3. Data analysis

Conversion of force curves

A force-distance curve consists of the measured cantilever deflection I_{PSD}, in the raw unit of the photodector (V), as a function of the distance Z_p travelled by the z-piezo (in nm), see Figure 19, section 1.6.2.1.

The abscissa and ordinate must be converted in Force (nN) and tip-sample distance (nm) respectively[78]. To this purpose, from the force curve itself, two parameters have to be extracted: the zero distance and the sensitivity, Z_{sens}. The linear part of the “contact regime” in a force curve is assumed to be the zero distance and the inverse of its slope is the sensitivity (nm/V). Therefore, the PSD signal can be converted into a cantilever deflection, Z_c (nm), by multiplying the PSD signal by the sensitivity

$$Z_c = I_{PSD} \cdot Z_{sens} \tag{10}$$

And multiplying the deflection by the spring constant of the cantilever, *k* (N/m), the force is easily obtained

$$F = Z_c \cdot k \tag{11}$$

To convert Z_p into a tip-sample distance, d, which become indentation, δ, after the contact point, the deflection of the cantilever must be considered

$$d = Z_p + Z_c \tag{12}$$

Nanomechanics data analysis

Thousands of force curves were analyzed on MATLAB by means of custom data analysis routines, in order to identify the force and the distance at which the AFM probe causes the breakage of the supported phospholipid bilayer. To this purpose, only approaching FC were considered: the anomalous force curves (with no physical meaning) were deleted (generally less than the 10 %) and operations of alignment on the remaining curves were performed, along baseline subtraction to eliminate artifacts of the optical system for the measurement of the deflection (e.g. periodic signal due to the interference of the laser reflected from the back of the cantilever or the sample). Once the curves were organized, the conversion of the axis to obtain force and tip-sample distance (see previous paragraph) was performed[251]. Typically, each FC shows a sudden drop in the force corresponding to the penetration of the tip into the bilayer. In Figure 19 (section 1.6.2.1.) are highlighted the main events of an approach FC on a SLB:

1. The probe is approaching the surface of the SLB
2. The sample resists to the compression of the tip
3. The bilayer breaks,
4. The probe penetrates through it
5. And pushes against the rigid substrate until the force reaches the setpoint.

From this discontinuity in the FCs, the force and the distance from the substrate at which the tip penetrates into the sample, respectively the values of Breakthrough Force (F_b) and Breakthrough Distance (d_b), can be obtained. Creating a tip-sample distance distribution histogram in the zone of compression, a maximum is observed due to the fact that nearby the d_b, the slope of the curve increases and so the number of points whose abscissa falls within the same interval increases. That

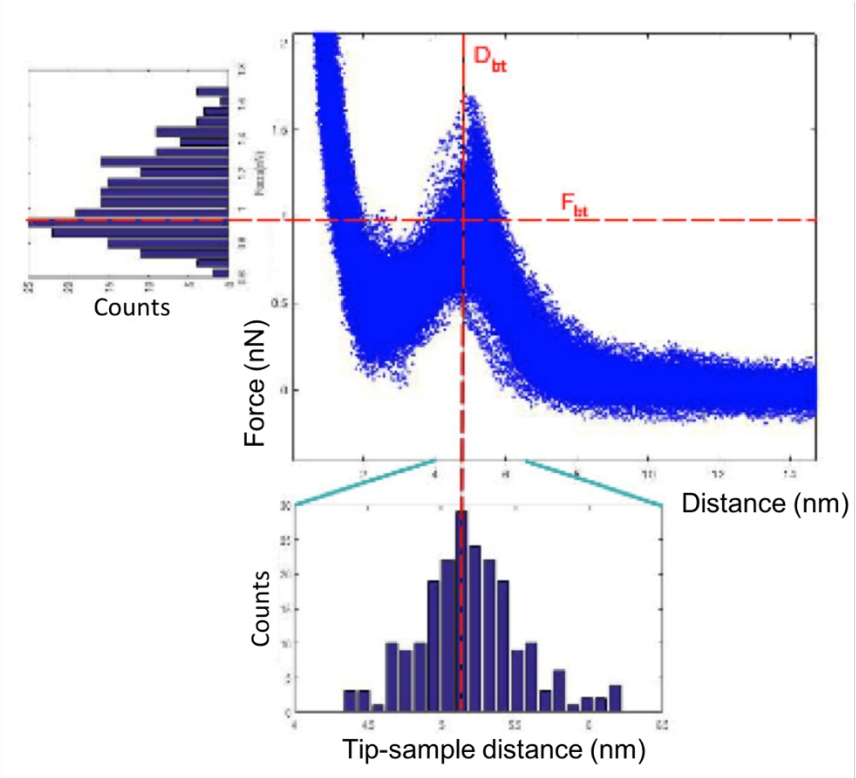

Figure 58 Examples of histograms that identify respectively the breakthrough force and the breakthrough distance

maximum corresponds with d_b. F_b can be obtained analogously (Fig. 58).

Force Spectroscopy data analysis

The analysis of the specific interaction events between the functionalized probe C8 (see paragraph 3.2.2.) and the SLB was performed by mean of a custom MATLAB function. From a set of retracting FCs it enables to manually select the peculiar specific events, providing the following parameters: the number of events (n) in each FC, the force of interaction (F) of each event and the distance (in nm) from the tip-sample contact region at which the event occurs (x1).

5.3. Synthesis and characterization of highly conjugated heterocyclic molecules with interesting photophysical properties

5.3.1. General Remarks

All chemicals and solvents are commercially available and were used after distillation or treatment with drying agents. All the reactions that involve the use of reagents sensitive to oxygen or water were carried out under nitrogen.

Chromatographic column separations were performed by a flash technique, using silica gel 40– 63 micron/60 Å with a particle size 230–400 mesh. TLC Alu foils with a fluorescent indicator (254 nm)

and silica gel F254 thin-layer plates were employed for thin-layer chromatography (TLC). The detection was performed by irradiation with UV light (λ = 254 nm and/or 366 nm).

^{1}H and ^{13}C-NMR spectra were determined with a Varian-Gemini 300, a Bruker 300 or Bruker 500 spectrometers at room temperature in $CDCl_3$, CD_2Cl_2 or DMSO with residual solvent peaks as the internal reference. Some ^{13}C NMR analyses were performed with the same instruments at 75 MHz Two-dimensional NMR experiments were performed, where appropriate, to aid the assignment of structures. The coupling constants (*J*) are expressed in hertz (Hz), and the chemical shifts (*δ*) are expressed in ppm. An Attached Proton Test (APT) sequence was used to distinguish the methine and methyl carbon signals from those arising from methylene and quaternary carbon atoms. All ^{13}C NMR spectra were recorded with complete proton decoupling.

Low-resolution MS spectra were recorded with a Thermo-Finnigan LCQ advantage AP electrospray/ion trap equipped instrument using a syringe pump device to directly inject sample solutions. The values are reported as mass–charge ratio and the relative intensities of the most significant peaks are shown in brackets. UV- visible and fluorescence spectra were collected at 20 °C. Absolute photoluminescence QYs were measured using an absolute PL quantum yield spectrometer (C11347, Hamamatsu) at rt.

High-resolution MS spectra were recorded with Fisions-VG autospec M246 electron ionization/ion trap equipped instrument using a syringe pump device to directly inject sample solutions. Slow additions were performed using NE-1000 Programmable Single Syringe Pump of the New Era Pump Systems Inc.

EFISH measurements were carried out by using a non-resonant incident wavelength of 1.907 µm, achieved by Raman-shifting the fundamental 1.064 µm wavelength given by a Q-switched, mode-locked Nd^{3+}:YAG laser (from Atalaser).

Melting points were measured with a PerkinElmer DSC 6 calorimeter at a heating rate of 5 °C/min and are uncorrected.

5.3.2. Synthesis and photophysical evaluation of polarity sensitive push-pull isoquinolines and their alkynyl precursors

5.3.2.1. General procedure for the synthesis of 5-nitro-2- alkynylbenzaldehydes 3a–e

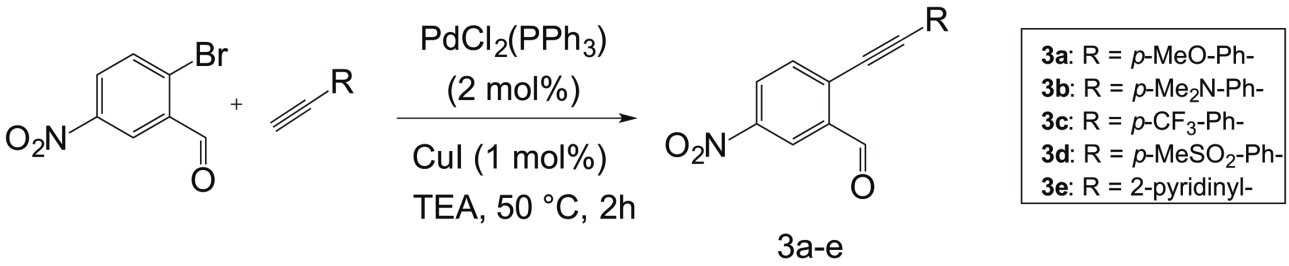

Scheme 21 Reaction scheme for the synthesis of compounds **3a-e**.

In a round-bottom flask, $PdCl_2(PPh_3)_2$ (2 mol%) was added to a well-stirred N_2-flushed solution of commercially available 2-bromo-5-nitro-benzaldehyde (1.0 equiv.) and the suitable terminal arylalkyne (1.2 equiv.) in anhydrous triethylamine. The reaction mixture was stirred for 15 minutes at rt, and then CuI (1 mol%) was added. The reaction mixture was warmed at 50 °C and stirred for 2 h. The reaction mixture was filtered on a thin diatomite pad and the triethylamine was removed under reduced pressure. The crude product obtained was purified by flash column chromatography over silica gel affording 2-alkynyl-5-nitrobenzadehydes **3a–e**.

2-((4-Methoxyphenyl)ethynyl)-5-nitrobenzaldehyde 3a. The general procedure was followed by using 2-bromo-5-nitrobenzaldehyde (400 mg, 1.73 mmol), $PdCl_2(PPh_3)_2$ (38 mg, 0.03 mmol), 2-ethynyl-4-methoxybenzene (274 mg, 2.08 mmol) and CuI (5 mg, 0.02 mmol). Eluent for chromatography: Hexane/EtOAc (9:1). Yellow solid. Yield 95% (464 mg). **^{1}H NMR** (300 MHz, $CDCl_3$): *δ* 10.64 (s, 1H), 8.75 (d, *J* = 2.4 Hz, 1H), 8.39 (dd, *J* = 8.6, 2.4 Hz, 1H), 7.77 (d, *J* = 8.6 Hz, 1H), 7.54 (d, *J* = 8.9Hz,2H), 6.94 (d, *J* = 8.9Hz,2H), 3.86 (s, 3H). NMR data are in agreement with those reported in the literature[18].

2-((4(Dimethylamino)phenyl)ethynyl)-5-nitrobenzaldehyde **3b**. The general procedure was followed by using 2-bromo-5-nitrobenzaldehyde (400 mg, 1.73 mmol), $PdCl_2(PPh_3)_2$ (38 mg, 0.03 mmol), 4-ethynyl-N,N-dimethylaniline (301 mg, 2.08 mmol) and CuI (5 mg, 0.02 mmol). Eluent for chromatography: Hexane/EtOAc (from 9 : 1 to 3 : 1). Yellow solid. Yield 92% (467 mg). **^{1}H NMR** (300 MHz, $CDCl_3$): *δ* 10.64 (s, 1H), 8.71 (d, *J* = 2.5 Hz, 1H), 8.34 (dd, *J* = 8.6, 2.5 Hz, 1H), 7.71 (d, *J* = 8.6 Hz, 1H), 7.44 (d, *J* = 9.1 Hz, 2H), 6.67 (d, *J* = 9.1 Hz, 2H), 3.04 (s, 6H). **^{13}C NMR** (75 MHz, $CDCl_3$) *δ* 189.7 (CH), 151.3 (C), 146.4 (C), 135.6 (C), 133.7 (C), 133.6 (CH), 133.5 (2 × CH), 127.5 (CH), 122.7 (CH), 111.7 (2 × CH), 107.3 (C), 104.9 (C), 83.1 (C), 40.0 (2 × CH_3). **ESI(+)-MS**: *m/z* (%) = 295.25 (100) $[MH]^+$; 296.30 (20). Calcd for $C_{17}H_{14}N_2O_3$ (294.31): C, 69.38; H, 4.79; N, 9.52; found: C, 69.21; H, 4.70; N, 9.61.

5-Nitro-2-((4-(trifluoromethyl)phenyl)ethynyl)benzaldehyde **3c**. The general procedure was followed by using 2-bromo-5-nitrobenzaldehyde 3 (400 mg, 1.73 mmol), $PdCl_2(PPh_3)_2$ (38 mg, 0.03 mmol), 1-ethynyl-4-(trifluoromethyl)benzene (353 mg, 2.08 mmol) and CuI (5 mg, 0.02 mmol). Eluent for chromatography: Hexane/EtOAc (9 : 1). Yellow solid. Yield 88% (487 mg). **^{1}H NMR** (300 MHz, $CDCl_3$): *δ* 10.63 (s, 1H), 8.79 (dd, *J* = 2.4, 0.5 Hz, 1H), 8.45 (dd, *J* = 8.5, 2.4 Hz, 1H), 7.86 (dd, *J* = 8.5, 0.5 Hz, 1H), 7.79–7.62 (m, 4H). **^{13}C NMR** (75 MHz, $CDCl_3$) *δ* 188.8 (CH), 147.7 (C), 136.8 (C), 134.6 (CH), 132.3 (2 × CH), 131.7 (q, $^2J_{(C,F)}$ = 32.9 Hz, C), 131.3 (C), 129.0, (C) 127.7 (CH), 125.7 (q, $^3J_{(C,F)}$ = 3.8 Hz, 2 × CH), 125.4 (C), 125.0 (C), 123.6 (q, $^1J_{(C,F)}$ = 272.5 Hz, C), 122.9 (CH), 99.4 (C), 85.5 (C). **ESI(−)-MS**: *m/z* (%) = 319.63 (45) $[M]^-$; 336.71 (100) $[M + OH]^-$; 351.63 (100) $[M + MeOH]^-$. Calcd for $C_{16}H_8F_3NO_3$ (319.04): C, 60.20; H, 2.53; N, 4.39; found: C, 60.36; H, 2.48; N, 4.35.

2-((4-(Methylsulfonyl)ethynyl)-5-nitrobenzaldehyde **3d**. The general procedure was followed by using 2-bromo-5-nitrobenzaldehyde 3 (300 mg, 1.30 mmol), $PdCl_2(PPh_3)_2$ (18 mg, 0.026 mmol), 1-ethynyl-4-methylsulfonylbenzene (282 mg, 1.56 mmol) and CuI (2 mg, 0.01 mmol). Eluent for chromatography: Hexane/EtOAc (from 9 : 1 to 8 : 2). Yellow solid. Yield 95% (408 mg). **^{1}H NMR** (300 MHz, $CDCl_3$) *δ* 10.61 (s, 1H), 8.79 (d, *J* =2.4 Hz, 1H), 8.46 (dd, *J* =8.5, 2.4 Hz, 1H), 8.02 (d, *J* =8.6 Hz, 2H), 7.87 (d, *J* = 8.5 Hz, 1H), 7.80 (d, *J* = 8.6 Hz, 2H), 3.10 (s, 3H). **^{13}C NMR** (75 MHz, $CDCl_3$) *δ* 188.5 (CH), 141.6 (C), 137.0 (C), 134.7 (CH), 132.7 (2 × CH), 130.7 (C), 127.74 (2 × CH), 127.71 (CH), 126.9 (C), 123.1 (CH), 120.5 (C), 98.6 (C), 86.8 (C), 44.4 (CH_3). **ESI(−)-MS**: *m/z* (%) = 329.63 (35) $[M]^-$; 346.61 (100) $[M + OH]^-$; 361.58 (100) $[M + MeOH]^-$. Calcd for $C_{16}H_{11}NO_5S$ (329.33): C, 58.35; H, 3.37; N, 4.25; found: C, 58.22; H, 3.34; N, 4.25.

5-Nitro-2-(pyridin-2-ylethynyl)benzaldehyde **3e**. The general procedure was followed by using 2-bromo-5-nitrobenzaldehyde 3 (400 mg, 1.73 mmol), $PdCl_2(PPh_3)_2$ (38 mg, 0.03 mmol), 2-ethynylpyridine (214 mg, 2.08 mmol) and CuI (5 mg, 0.02 mmol). Eluent for chromatography: Hexane/EtOAc (2 : 1). Violet solid. Yield 76% (331 mg). **^{1}H NMR** (300 MHz, $CDCl_3$) *δ* 10.67 (s, 1H),

8.78 (dd, *J* = 2.4, 0.4 Hz, 1H), 8.70 (ddd, *J* = 4.9, 1.7, 1.2 Hz, 1H), 8.44 (dd, *J* = 8.5, 2.4 Hz, 1H), 7.90 (dd, *J* = 8.5, 0.4 Hz, 1H), 7.78 (td, *J* = 7.7, 1.7 Hz, 1H), 7.63 (dt, *J* = 7.7, 1.2 Hz, 1H), 7.37 (ddd, *J* = 7.7, 4.9, 1.2 Hz, 1H). **^{13}C NMR** (75 MHz, $CDCl_3$) *δ* 188.8 (CH), 150.6 (CH), 147.9 (C), 141.7 (C), 137.2 (C), 136.5 (CH), 134.8 (CH), 131.1 (C), 127.8 (CH), 127.6 (CH), 124.2 (CH), 122.7 (CH), 99.6 (C), 82.5 (C). **ESI(+)-MS**: *m/z* (%) = 253.25 (9) $[MH]^+$; 275.25 (6) $[M + Na]^+$; 307.13 (100) $[M + Na + MeOH]^+$. Calcd for $C_{14}H_8N_2O_3$ (252.22): C, 66.67; H, 3.20; N, 11.11; found: C, 66.51; H, 3.17; N, 11.03.

5.3.2.2. General procedure for the microwave-assisted synthesis of isoquinolines 1a–c

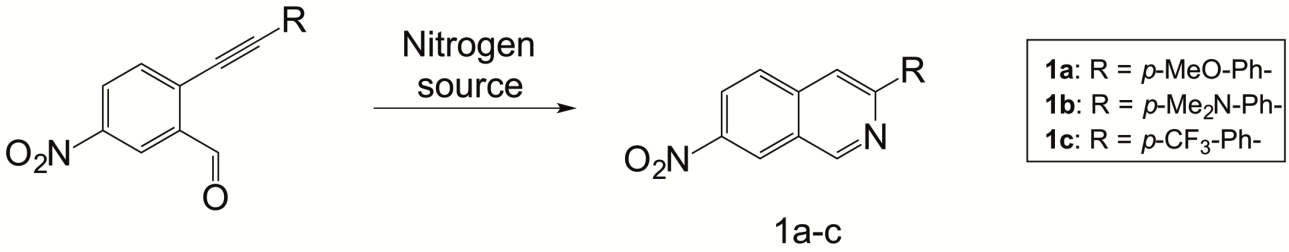

Scheme 22 Reaction sceme for the synthesis of compounds **1a-c**.

A stirred solution of an appropriate amount of 2-alkynyl-5-nitrobenzaldehyde (0.28 mmol) in ammonia in methanol (2 M, 3 mL) was heated at 100 °C in a microwave test tube with a screw cap under microwave irradiation for 2 h. The solvent was removed under reduced pressure. The crude product obtained was purified by flash chromatography over silica gel affording the corresponding isoquinolines **1a–c**.

3-(4-Methoxyphenyl)-7-nitroisoquinoline **1a**. Eluent for chromatography: Hexane/DCM (1 : 2 to 1 : 4). Yellow solid. Yield 56% (47 mg). **^{1}H NMR** (300 MHz, $CDCl_3$): *δ* 9.48 (s, 1H), 8.93 (d, *J* = 2.1 Hz, 1H), 8.43 (dd, *J* = 9.1, 2.2 Hz, 1H), 8.14 (d, *J* = 8.9 Hz, 2H), 8.08 (s, 1H), 7.97 (d, *J* = 9.1 Hz, 1H), 7.06 (d, *J* = 8.9 Hz, 2H), 3.90 (s, 3H). **^{13}C NMR** (75 MHz, DMSO): *δ* 161.1 (C), 155.0 (CH), 153.5 (C), 145.7 (C), 139.4 (C), 130.8 (C), 129.4 (CH), 128.9 (2 × CH), 125.9 (C), 125.3 (CH), 124.3 (CH), 114.88 (CH), 114.85 (2 × CH), 55.8 (CH_3). **ESI(+)-MS**: *m/z* (%) = 170.00 (50); 178.56 (33) $[M–Ph–NMe_2]^+$ 281.14 (100) $[MH]^+$; 282.12 (20). Calcd for $C_{16}H_{12}N_2O_3$ (280.28): C, 68.56; H, 4.32; N, 9.99; found: C, 68.69; H, 4.38; N, 10.10.

N,N-Dimethyl-4-(7-nitroisoquinolin-3-yl)anilina **1b**. Eluent for chromatography: Hexane/DCM (1 : 2 to 1 : 4). Violet solid. Yield 58% (47 mg). **^{1}H NMR** (300 MHz, CD_2Cl_2) *δ* 9.43 (s, 1H), 8.89 (d, *J* = 2.3 Hz, 1H), 8.37 (dd, *J* = 9.1, 2.3 Hz, 1H), 8.13 (d, *J* = 9.1 Hz, 2H), 8.06 (s, 1H), 7.94 (d, *J* = 9.1 Hz, 1H), 6.84 (d, *J* = 9.1 Hz, 2H), 3.07 (s, 7H). **^{13}C NMR** (75 MHz, CD_2Cl_2): *δ* 155.0 (C), 154.9 (C), 153.9 (CH), 151.6 (C), 139.4 (C), 128.2 (CH), 128.1 (2 × CH), 125.6 (C), 125.3 (C), 124.6 (CH), 123.5 (CH), 112.9 (CH), 112.0 (2 × CH), 40.0 (2 × CH_3). **ESI(+)-MS**: *m/z* (%) = 248.21 (100) $[MH–NO_2]^+$; 294.23 (80) $[MH]^+$; 295.24 (20). Calcd for $C_{17}H_{15}N_3O_2$ (293.33): C, 69.61; H, 5.15; N, 14.33; found: C, 69.39; H, 5.06; N, 14.28.

7-Nitro-3-(4-(trifluoromethyl)phenyl)isoquinoline **1c**. Eluent for chromatography: Hexane/DCM (1 : 2 to 1 : 4). Violet solid. Yield 19% (15 mg). **^{1}H NMR** (300 MHz, $CDCl_3$) *δ* 9.55 (s, 1H), 8.98 (d, *J* = 2.2 Hz, 1H), 8.50 (dd, *J* = 9.0, 2.2 Hz, 1H), 8.30 (d, *J* =8.1 Hz, 2H), 8.22 (s, 1H) , 8.06 (d, *J* = 9.0 Hz, 1H), 7.79 (d, *J* = 8.1 Hz, 2H). **^{13}C NMR** (75 MHz, $CDCl_3$) *δ* 154.3 (CH), 153.1 (C), 146.4 (C), 141.7 (C), 139.0 (C), 131.4 (q, $^2J_{(C,F)}$ = 32.6 Hz, C), 128.9 (CH), 127.6 (2 × CH), 126.6 (C), 125.9 (q, $^3J_{(C,F)}$ = 3.8 Hz, 2 × CH), 124.4 (CH), 124.2 (CH), 124.1 (q, $^1J_{(C,F)}$ = 272.4 Hz, C), 116.6 (CH). **ESI(+)-MS**: *m/z* (%) = 319.32

(100) $[MH]^+$; 320.33 (20). Calcd for $C_{16}H_9F_3N_2O_2$ (318.26): C, 60.38; H, 2.85; N, 8.80; found: C, 60.15; H, 2.77; N, 8.75.

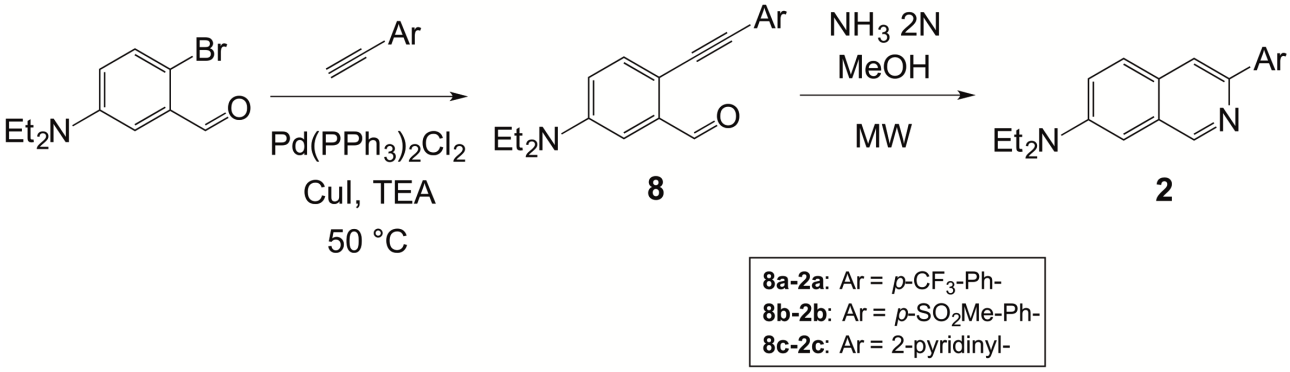

Scheme 23 Reaction scheme for the synthesis of compounds **2a-c**.

5-(Diethylamino)-2-((4-(trifluoromethyl)phenyl)ethynyl)benzaldehyde **8a**. In a round-bottom flask, $PdCl_2(PPh_3)_2$ (41 mg, 0.059 mmol, 5 mol%) was added to a well-stirred N_2-flushed solution of 2-bromo-5-(diethylamino)benzaldehyde **7** (300 mg, 1.71 mmol), 1-ethynyl-4-(trifluoromethyl)benzene (219 mg, 1.29 mmol) and trimethylamine (178 mg, 0.245 mL, 1.76 mmol) in anhydrous acetonitrile (1.3 mL). The reaction mixture was stirred for 15 minutes at rt, and then CuI (2.0 mg, 0.012 mmol, 1 mol%) was added. The reaction mixture was warmed at 50 °C and stirred for 5 h. The reaction mixture was filtered on a thin diatomite pad and the solvent was removed under reduced pressure. The crude product obtained was purified by flash column chromatography over silica gel (eluent: hexane/EtOAc (2 : 1)) affording **8a** in 67% yield (278 mg). **^{1}H NMR** (300 MHz, $CDCl_3$) δ 10.60 (s, 1H), 7.63 (m, 4H), 7.52 (d, J = 8.7 Hz, 1H), 7.24 (bs, 1H), 6.96 (bs, 1H), 3.46 (q, J = 7.1 Hz, 1H), 1.23 (t, J = 7.1 Hz, 1H). **^{13}C NMR** (75 MHz, $CDCl_3$) δ 192.1 (CH), 147.6 (C), 137.0 (C), 134.7 (CH), 131.4 (2 × CH), 129.6 (q, $^2J_{(C,F)}$ = 31.2 Hz, C), 128.7 (C), 127.2 (C), 125.3 (q, $^3J_{(C,F)}$ = 3.9 Hz, 2 × CH), 124.0 (q, $^1J_{(C,F)}$ = 272.8 Hz, C), 117.3 (CH), 109.2 (CH), 92.3 (C), 88.7 (C), 44.8 (2 × CH_2), 12.4 (2 × CH_3). **ESI (+)-MS**: *m/z* (%) = 346.14 (55) $[MH]^+$; 378.23 (100) $[MH + MeOH]^+$. Calcd for $C_{20}H_{18}F_3NO$ (345.37): C, 69.56; H, 5.25; N, 4.06; found: C, 69.42; H, 5.32; N, 3.99.

5-(Diethylamino)-2-((4-(methylsulfonyl)phenyl)ethynyl)benzaldehyde 8b. In a round-bottom flask, $PdCl_2(PPh_3)_2$ (32 mg, 0.045 mmol, 5 mol%) was added to a well-stirred N_2-flushed solution of 2-bromo-5-(diethylamino)benzaldehyde **7** (236 mg, 0.92 mmol), 1-ethynyl-4-(methylsulfonyl)benzene (183 mg, 1.01 mmol) and trimethylamine (137 mg, 0.188 mL, 1.35 mmol) in anhydrous acetonitrile (1.0 mL). The reaction mixture was stirred for 15 minutes at rt, and then CuI (1.7 mg, 0.00 mmol, 1 mol%) was added. The reaction mixture was warmed at 50 °C and stirred for 2 h. The reaction mixture was filtered on a thin diatomite pad and the solvent was removed under reduced pressure. The crude product obtained was purified by flash column chromatography over silica gel (eluent: hexane/EtOAc (7 : 3)) affording **8b** in 41% yield (134 mg). **^{1}H NMR** (300 MHz, $CDCl_3$) δ 10.54 (s, 1H), 7.91 (d, J = 8.7 Hz, 2H), 7.66 (d, J = 8.7 Hz, 2H), 7.48 (d, J = 8.7 Hz, 1H), 6.85 (dd, J = 8.8, 2.9 Hz, 1H), 3.43 (q, J = 7.1 Hz, 4H), 3.06 (s, 3H), 1.20 (t, J = 7.1 Hz, 6H). **^{13}C NMR** (75 MHz, $CDCl_3$) δ 191.9 (CH), 148.2 (C), 139.3 (C), 137.2 (C), 134.8 (CH), 131.8 (2 × CH), 129.4 (C), 127.4 (2 × CH), 116.5 (CH), 111.1 (C), 109.1 (CH), 91.7 (C), 90.9 (C), 44.48 (CH_3), 44.5 (2 × CH_2), 12.4 (2 × CH_3). **ESI(+)-MS**: *m/z* (%) = 356.21 (18) $[MH]^+$; 378.02 (100) $[M + Na]^+$. Calcd for $C_{20}H_{21}NO_3S$ (355.45): C, 67.58; H, 5.96; N, 3.94; found: C, 67.75; H, 5.91; N, 4.02.

5-(Diethylamino)-2-(pyridin-2-ylethynyl)benzaldehyde **8c**. In a round-bottom flask, $PdCl_2(PPh_3)_2$ (41 mg, 0.059 mmol, 5 mol%) was added to a well-stirred N_2-flushed solution of 2-bromo-5-(diethylamino)benzaldehyde **7** (300 mg, 1.71 mmol), 2-ethynylpyridine (145 mg, 1.41 mmol), K_2CO_3 (810 mg, 5.86 mmol) and trimethylamine (178 mg, 0.245 mL, 1.76 mmol) in anhydrous DMF (5 mL). The reaction mixture was stirred for 15 minutes at rt, and then CuI (2.0 mg, 0.012 mmol, 1 mol%) was added. The reaction mixture was warmed at 50 °C and stirred for 4 h. The reaction mixture was poured in water (70 mL) and extracted with EtOAc (3 × 20 mL). The solvent was removed under reduced pressure. The crude product obtained was purified by flash column chromatography over silica gel (eluent: hexane/EtOAc/isopropanol (80 : 20 : 1)) affording **8c** in 76% yield (248 mg). **^{1}H NMR** (300 MHz, $CDCl_3$) δ 10.60 (s, 1H), 8.60 (d, J = 4.8 Hz, 1H), 7.66 (td, J = 7.7, 1.8 Hz, 1H), 7.54 (d, J = 8.7 Hz, 1H), 7.49 (d, J = 7.8 Hz, 1H), 7.21 (ddd, J = 7.5, 4.9, 1.1 Hz, 1H), 7.16 (d, J = 2.9 Hz, 1H), 6.84 (dd, J = 8.8, 2.9 Hz, 1H), 3.41 (q, J = 7.1 Hz, 4H), 1.18 (t, J = 7.1 Hz, 6H). **^{13}C NMR** (75 MHz, $CDCl_3$) δ 192.1 (CH), 150.1 (CH), 148.1 (C), 143.7 (C), 137.3 (C), 136.1 (CH), 135.0 (CH), 126.9 (CH), 122.4 (CH), 116.5 (CH), 111.4 (C), 108.7 (CH), 92.8 (C), 86.5 (C), 44.4 (2 × CH_2), 12.4 (2 × CH_3). **ESI(+)-MS**: *m/z* (%) = 279.27 (100) $[MH]^+$; 280.27 (22). Calcd for $C_{18}H_{18}N_2O$ (278.36): C, 77.67; H, 6.52; N, 10.06; found: C, 77.62; H, 6.50; N, 10.02.

N,N-Diethyl-3-(4-(trifluoromethyl)phenyl)isoquinolin-7-amine **2a**. A stirred solution of **8a** (69 mg, 0.20 mmol) in ammonia in methanol (2 M, 3 mL) was heated at 140 °C in a microwave test tube with a screw cap under microwave irradiation for 1 h. The solvent was removed under reduced pressure. The crude product obtained was purified by flash chromatography over silica gel (eluent: heptane/EtOAc (9 : 1)) affording **2a** in 26% yield (18 mg). **^{1}H NMR** (300 MHz, $CDCl_3$) δ 9.10 (s, 1H), 8.26 (d, J = 8.1 Hz, 2H), 8.00 (s, 1H), 7.75 (m, 3H), 7.33 (dd, J = 9.1, 2.6 Hz, 1H), 6.97 (d, J = 2.5 Hz, 1H), 3.52 (q, J = 7.1 Hz, 4H), 1.26 (t, J = 7.1 Hz, 6H). **^{13}C NMR** (75 MHz, $CDCl_3$) δ 150.4 (CH), 147.2 (C), 144.9 (C), 143.7 (C), 130.5 (C), 128.9 (q, $^2J_{(C,F)}$ = 31.2 Hz, C), 128.4 (C), 128.0 (CH), 126.2 (2 × CH), 125.4 (q, $^3J_{(C,F)}$ = 4.3 Hz, 2 × CH), 124.6 (q, $^1J_{(C,F)}$ = 271.4 Hz, C), 120.0 (CH), 116.6 (CH), 103.5 (CH), 44.5 (2 × CH_2), 12.3 (2 × CH_3). **ESI (+)-MS**: *m/z* (%) = 345.23 (100) $[MH]^+$; 346.25 (17). Calcd for $C_{20}H_{19}F_3N_2$ (344.38): C, 69.75; H, 5.56; N, 8.13; found: C, 69.68; H, 5.52; N, 8.18.

N,N-Diethyl-3-(4-(methylsulfonyl)phenyl)isoquinolin-7-amine **2b**. A stirred solution of **8b** (71 mg, 0.20 mmol) in ammonia in methanol (2 M, 2 mL) was heated at 80 °C in a microwave test tube with a screw cap under microwave irradiation for 1 h. The solvent was removed under reduced pressure. The crude product obtained was purified by flash chromatography over silica gel (eluent: hexane/EtOAc (6 : 4)) affording **2b** in 18% yield (13 mg). **^{1}H NMR** (300 MHz, $CDCl_3$) δ 9.16 (s, 1H), 8.31 (d, J = 8.6 Hz, 1H), 8.15–8.00 (m, 3H), 7.79 (d, J = 9.1 Hz, 1H), 7.37 (dd, J = 9.2, 2.4 Hz, 1H), 7.00 (bs, 1H), 3.54 (q, J = 7.1 Hz, 2H), 3.12 (s, 1H), 1.29 (t, J = 7.0 Hz, 4H). **^{13}C NMR** (75 MHz, $CDCl_3$) δ 149.6 (CH), 147.5 (C), 143.8 (C), 142.9 (C), 139.4 (C), 130.3 (C), 128.9 (C), 128.5 (CH), 127.9 (2 × CH), 127.2 (2 × CH), 121.1 (CH) 118.5 (CH), 103.7 (CH), 44.8 (2 × CH_2), 44.7 (CH_3), 12.5 (2 × CH_3). **ESI(+)-MS**: *m/z* (%) = 355.24 (100) $[MH]^+$; 356.27 (25). Calcd for $C_{20}H_{22}N_2O_2S$ (354.47): C, 67.77; H, 6.26; N, 7.90; found: C, 67.65; H, 6.21; N, 7.94.

N,N-Diethyl-3-(pyridin-2-yl)isoquinolin-7-amine **2c**. A stirred solution of **8c** (56 mg, 0.20 mmol) in ammonia in methanol (2 M, 2 mL) was heated at 100 °C in a microwave test tube with a screw cap under microwave irradiation for 2 h. The solvent was removed under reduced pressure. The crude

product obtained was purified by flash chromatography over silica gel (eluent: heptane/EtOAc/TEA (70 : 30 : 1)) affording **2c** in 18% yield (13 mg). **^{1}H NMR** (300 MHz, $CDCl_3$) δ 9.08 (s, 1H), 8.68 (ddd, *J* = 4.8, 1.8, 0.9 Hz, 1H), 8.59 (s, 1H), 8.43 (d, *J* = 8.0 Hz, 1H), 7.85–7.74 (m, 2H), 7.33–7.18 (m, 2H), 6.94 (d, *J* = 2.4 Hz, 1H), 3.50 (q, *J* = 7.1 Hz, 4H), 1.25 (t, *J* = 7.1 Hz, 6H). **^{13}C NMR** (75 MHz, $CDCl_3$) δ 157.2 (C), 149.9 (CH), 149.1 (CH), 147.1 (C), 145.9 (C), 136.7 (CH), 131.0 (C), 128.8 (CH), 122.3 (CH), 120.5 (CH), 119.9 (CH), 117.5 (CH), 103.7 (CH) 44.6 (2 × CH_2), 12.6 (2 × CH_3). **ESI(+)-MS**: *m/z* (%) = 278.22 (100) $[MH]^+$; 279.21 (27). Calcd for $C_{18}H_{19}N_3$ (277.37): C, 77.95; H, 6.90; N, 15.15; found: C, 78.09; H, 6.82; N, 15.14.

5.3.3.3. Absorption spectroscopy

Stock solutions of **2a**, **2b**, **2c**, **3a**, **3b**, **8a**, **8b**, **8c** (1 mg mL^{-1}) and **1a**, **1b** (0,5 mg mL^{-1}) were prepared by dissolving the powders in DMSO. Absorption spectra were acquired in increasing polarity solvents (Toluene, $CHCl_3$, EtOAc, THF, DCM, Acetone, EtOH, DMF, DMSO and H_2O), to study the effect of the solvent. For each absorption spectrum, stock solution of **1a**, **2a**, **2b**, **2c**, **3a**, **3b**, **8a**, **8b**, **8c** were dissolved in the suitable media, to obtain a final concentration of 0,014 mg mL^{-1}. **1b** was dissolved in the suitable media, to obtain a final concentration of 0,010 mg mL^{-1}. The molar extinction coefficient was obtained from the linear regression method. Absorption spectra of **1a**, **1b**, **2a**, **2b**, **2c**, **3a**, **3b**, **8a**, **8b**, **8c** at the concentration of 0,004 mg mL^{-1}, 0,008 mg mL^{-1}, 0,01 mg mL^{-1} and 0,02 mg mL^{-1} in DMSO were acquired. Absorption spectra were recorded at 300 nm min^{-1} at 20 °C with a 1 cm path length quartz cuvette on a spectrophotometer equipped with a thermostated cell-holder.

5.3.3.4. Fluorescence spectroscopy

Fluorescence spectra were collected by recording the emission signal upon excitation at the maximum absorbance wavelength, with slits set at 2 nm and an integration time of 0.1 seconds. The concentration of compounds was 0.014 mg mL^{-1} for **1a**, **1b**, **2a**, **2c**, **3a**, and **3b**, and 0.007 mg mL^{-1} for **2b**, **8a**, **8b**, and **8c**.

Absolute QY determination

The fluorescence quantum yield (Φ) was measured with an absolute photoluminescence quantum yield spectrometer (C11347, Hamamatsu). Stock solutions of **1a**,**1b**, **2a**, **2b**, **2c**, **3a**, **3b**, **8a**, **8b**, **8c** (1 mg mL^{-1}) were prepared by dissolving the powders in DMSO. To determine the quantum yield, samples (2 µg mL^{-1}) were prepared from the stock solutions by dilutions in DMSO, toluene and EtOH. For any fixed excitation wavelength, Φ is given by:

$$\Phi = \frac{PN(Em)}{PN(Abs)} = \frac{\int \frac{\lambda}{hc}\left[I_{em}^{sample}(\lambda) - I_{em}^{reference}(\lambda)\right]\mathrm{d}\lambda}{\int \frac{\lambda}{hc}\left[I_{ex}^{reference}(\lambda) - I_{ex}^{sample}(\lambda)\right]\mathrm{d}\lambda} \quad (13)$$

where PN(Em) is the number of photons emitted from a sample and PN(Abs) is the number of photons absorbed by a sample, λ is the wavelength, *h* is Planck's constant, *c* is the velocity of light, $I_{em}^{sample}(\lambda)$ and $I_{em}^{reference}(\lambda)$ are the photoluminescence intensities with and without a sample, respectively, $I_{ex}^{sample}(\lambda)$ and $I_{ex}^{reference}(\lambda)$ are the integrated intensities of the excitation light with

and without a sample, respectively. PN(Em) is calculated in the wavelength interval [λ_i,λ_f], where λ_i is taken 10 nm below the excitation wavelength, while λ_f is the upper end wavelength in the emission spectrum.

5.3.3. Gold-catalyzed cascade reactions of 4H-furo[3,2-*b*]indoles with propargyl esters: synthesis of 2-alkenylidene-3-oxoindolines

Furoindole **9a**-**b** are known compound and were prepared according to literature procedures[252]. Indole **9f**-**g** are known compound and were prepared according to literature procedures[191,206,192,193,194,253,254]. Propargyl esters **10a-f** are known compounds and were prepared according to literature procedures[195,196,197,198,255,256,193,257]. Catalysts **A**-**E** are known compounds and were purchased from commercial suppliers and used as received (**A** = JhonPhosAuSbF$_6$, **C** = tris(aryl)phosphiteSbF$_6$) or prepared following literature procedures (**B** = iPrAuNTf$_2$, **D** = Ph$_3$PAuNTf$_2$, **E** = JhonPhosAuNTf$_2$)[258,259,260,261,262].

5.3.3.1. Preparation and characterization data for 4H-furo[3,2-b]indole 9b-d

tert-butyl 4*H*-furo[3,2-*b*]indole-4-carboxylate **9b**.

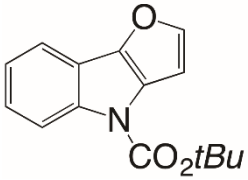

Figure 59 Chemical structure of compound **9b**.

To a N$_2$-flushed solution of 4*H*-furo[3,2-*b*]indole[252] (157 mg, 1 mmol) in dichloromethane (5 mL), Boc$_2$O (659 mg, 3 mmol) and DMAP (12 mg, 0.1 mmol) were added at 0 °C. The mixture was warmed up to room temperature and stirred for 2.5 h. Then the solvent was evaporated and the crude was purified by flash column chromatography (SiO$_2$, hexane/ethyl acetate 98:2) to yield **9b** (252 mg, 98%) as white solid (m.p. 82.4-84.6 °C). **^{1}H NMR** (300 MHz, CDCl$_3$): 8.32 (bs, 1H), 7.66 (ddd, *J* = 6.7, 3.3, 2.1 Hz, 1H), 7.56 (t, *J* = 16.1 Hz, 1H), 7.38 – 7.19 (m, 2H), 6.79 (bs, 1H), 1.71 (s, 9H). **^{13}C NMR** (75 MHz, CDCl$_3$): 149.77 (C), 145.59 (CH), 143.24 (C), 138.80 (C), 129.67 (C), 123.74 (CH), 123.03 (CH), 117.88 (C), 116.33 (CH), 116.23 (CH), 103.07 (CH), 83.42 (C), 28.25 (3xCH$_3$). **ESI(+)-MS**: *m/z* (%) = 258 (100) [M+H] $^+$; C$_{15}$H$_{15}$NO$_3$ [257.29]: calcd. for C, 70.02; H, 5.88; N, 5.44; found C, 70.15; H, 5.86, N 5.46.

4-methyl-4*H*-furo[3,2-*b*]indole **9c**.

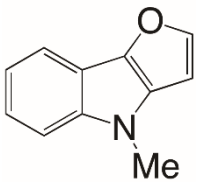

Figure 60 Chemical structure of compound **9c**.

To a N$_2$-flushed solution of NaH (28 mg, 1.1 mmol) in DMF (6 ml) 4*H*-furo[3,2-*b*]indole[252] (157 mg, 1 mmol) was added in small portions at 0 °C and the mixture was stirred for 30 min at 0 °C. Then MeI (156 mg, 1.1 mmol) was added and the reaction was warmed to room temperature and stirred for 1 h before being quenched with water. The organic layer was extracted with ethyl acetate, dried over Na$_2$SO$_4$ and the solvent concentrated under reduced pression. The crude was purified by flash

column chromatography (SiO_2, hexane/ethyl acetate 98:2) to yield **9c** (153 mg, 89%) as pink oil. **^{1}H NMR** (300 MHz, $CDCl_3$): 7.75 (dd, *J* = 7.1, 0.8 Hz, 1H), 7.56 (d, *J* = 2.1 Hz, 1H), 7.36 (d, *J* = 8.1 Hz, 1H), 7.29 – 7.09 (m, 2H), 6.61 (d, *J* = 2.1 Hz, 1H), 3.81 (s, 3H). **^{13}C NMR** (75 MHz, $CDCl_3$): 145.69 (CH), 140.82 (C), 140.44 (C), 133.10 (C), 121.15 (CH), 118.94 (CH), 116.25 (CH), 113.96 (C), 109.63 (CH), 98.18 (CH), 31.21 (CH_3). **ESI(+)-MS**: *m/z* (%) = 172 (100) $[M+H]^+$; $C_{11}H_9NO$ [171.20]: calcd. for C, 77.17; H, 5.30; N, 8.18; found C, 76.89; H, 5.33; N, 8.15.

2-(2-azido-5-methoxyphenyl)furan.

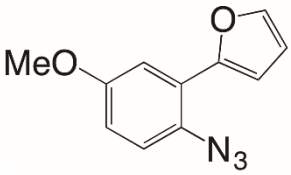

Figure 61 Chemical structure of 2-(2-azido-5-methoxyphenyl)furan.

To a solution of 2-(furan-2-yl)-4-methoxyaniline (1.30 g, 6.9 mmol), an aqueous solution of hydrochloric acid (15%, 6.9 mL) was added dropwise at 0 °C. Then a solution of sodium nitrite (573 mg, 8.3 mmol) in water (19 mL) was added dropwise. The mixture was stirred for 1 h at 0 °C. Then a solution of sodium azide (728 mg, 11.2 mmol) in water (2.6 mL) was added dropwise at 0 °C and the mixture was stirred for 1 h at room temperature. The mixture was diluted with water, extracted with ethyl acetate, washed with sodium bicarbonate saturated solution and brine. The organic layer was dried over Na_2SO_4 and the solvent concentrated under reduced pression. The crude was purified by flash column chromatography (SiO_2, hexane 100%) to yield 2-(2-azido-5-methoxyphenyl)furan (1.47 g, 99%) as brownish oil. **^{1}H NMR** (300 MHz, $CDCl_3$): 7.47 (dd, *J* = 1.8, 0.7 Hz, 1H), 7.38 (d, *J* = 2.9 Hz, 1H), 7.13 (d, *J* = 8.8 Hz, 1H), 7.10 (dd, *J* = 3.4, 0.7 Hz, 1H), 6.85 (dd, *J* = 8.8, 3.0 Hz, 1H), 6.51 (dd, *J* = 3.4, 1.8 Hz, 1H), 3.85 (s, 3H). **^{13}C NMR** (75 MHz, $CDCl_3$): 156.89 (C), 149.47 (C), 141.74 (CH), 127.61 (C), 123.21 (C), 119.99 (CH), 114.44 (CH), 111.81 (CH), 111.21 (CH), 110.62 (CH), 55.61 (CH_3). **ESI(+)-MS**: $C_{11}H_9N_3O_2$ [215.21]: calcd. for C, 61.39; H, 4.22; N, 19.53; found C, 61.67; H, 4.20; N, 19.48.

7-methoxy-4*H*-furo[3,2-*b*]indole.

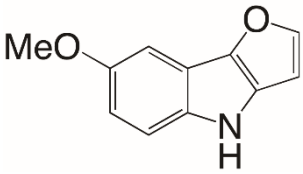

Figure 62 Chemical structure of 7-methoxy-4H-furo[3,2-*b*]índole.

A solution of 2-(2-azido-5-methoxyphenyl)furan (1.34 g, 6.2 mmol) in 1,2-dichlorobenzene (4 mL) was added dropwise to 1,2-dichlorobenzene (8 mL) heated at 160 °C. The reaction mixture was stirred for 1 h. Then, the solvent was concentrated under reduced pression. The crude was purified by flash column chromatography (SiO_2, hexane/ ethyl acetate 95:5 to 9:1) to yield 7-methoxy-4*H*-furo[3,2-*b*]indole (279 mg, 24%) as brownish oil. **^{1}H NMR** (300 MHz, CD_2Cl_2): 7.69 (bs, 1H), 7.56 (d, *J* = 2.1 Hz, 1H), 7.32 (dd, *J* = 8.9, 0.5 Hz, 1H), 7.19 (d, *J* = 2.5 Hz, 1H), 6.83 (dd, *J* = 8.9, 2.5 Hz, 1H), 6.62 (d, *J* = 2.1 Hz, 1H), 3.87 (s, 3H). **^{13}C NMR** (75 MHz, CD_2Cl_2): 154.20 (C), 145.88 (CH), 142.22 (C), 135.10 (C), 131.10 (C), 114.49 (C), 112.91 (CH), 111.06 (CH), 99.52 (CH), 98.54 (CH), 55.71 (CH_3). **ESI(+)-MS**:

m/z (%) = 188 (100) $[M+H]^+$; $C_{11}H_9NO_2$ [187.19]: calcd. for C, 70.58; H, 4.85; N, 7.48; found for C, 70.84; H, 4.86; N, 7.45.

Ethyl 7-methoxy-4*H*-furo[3,2-*b*]indole-4-carboxylate **9d**.

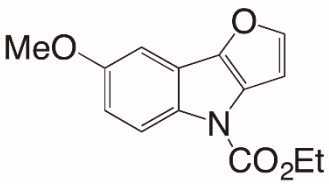

Figure 63 Chemical structure of compound **9d**.

To a N_2-flushed solution of 7-methoxy-4*H*-furo[3,2-*b*]indole (250 mg, 1.3 mmol) in tetrahydrofuran (13 mL), a solution of n-butyllithium (1.6 M in hexane, 893 µL, 1.43 mmol), was added dropwise at -78 °C. The reaction mixture was stirred for 30 minutes. Ethyl chloroformate (186 µL, 1.95 mmol) was added dropwise and the reaction was brought to room temperature and stirred for 2 h before of being quenched with ammonium chloride saturated solution. The organic layer was extracted with ethyl acetate, dried over Na_2SO_4 and the solvent concentrated under reduced pression. The crude was purified by flash column chromatography (SiO_2, hexane/ethyl acetate 95:5) to yield **9d** (288 mg, 86%) as orange solid (m.p. 74.5-76.2 °C). **^{1}H NMR** (300 MHz, $CDCl_3$): 8.20 (bs, 1H), 7.52 (d, *J* = 2.0 Hz, 1H), 7.14 (d, *J* = 2.6 Hz, 1H), 6.90 (dd, *J* = 9.1, 2.6 Hz, 1H), 6.79 (s, 1H), 4.50 (q, *J* = 7.1 Hz, 2H), 3.88 (s, 3H), 1.49 (t, *J* = 7.1 Hz, 3H). **^{13}C NMR** (75 MHz, $CDCl_3$): 156.31 (C), 151.04 (C) 145.85 (CH), 143.34 (C), 133.38 (C), 130.06 (C), 118.69 (C), 117.12 (CH), 111.80 (CH), 103.10 (CH), 99.87 (CH), 62.94 (CH_2), 55.72 (CH_3), 14.47 (CH_3) **ESI(+)-MS**: *m/z* (%) = 260 (100) $[M+H]^+$; $C_{14}H_{13}NO_4$ [259.26]: calcd. for C, 64.86; H, 5.05; N, 5.40; found C, 65.09; H, 5.03; N, 5.42.

5.3.3.2. Preparation and characterization data for propargylic esters 10e,f

(*E*)-1-(4-fluorophenyl)pent-1-en-4-yn-3-ol.

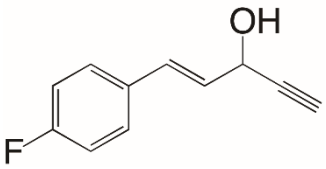

Figure 64 Chemical structure of (E)-1-(4-fluorophenyl)pent-1-en-4-yn-3-ol.

To a N_2-flushed solution of (*E*)-3-(4-fluorophenyl)acrylaldehyde (753 mg, 5 mmol) in tetrahydrofuran (10 mL), a solution of ethynylmagnesium bromide (0.5 M in tetrahydrofuran, 12 mL, 6 mmol) was added dropwise at 0 °C. The mixture was warmed up to room temperature and stirred for 1h before of being quenched with ammonium chloride saturated solution. The organic layer was extracted with ethyl acetate, dried over Na_2SO_4 and the solvent concentrated under vacuum. The crude was used directly for the next step, quantitative yield.

(*E*)-1-(4-fluorophenyl)pent-1-en-4-yn-3-yl pivalate **10e**.

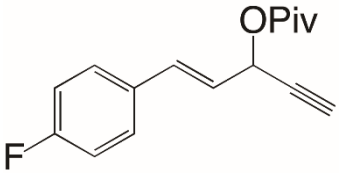

Figure 65 Chemical structure of compound **10e**.

To a solution of (*E*)-1-(4-fluorophenyl)pent-1-en-4-yn-3-ol (889 mg, 5 mmol), triethylamine (1.52 g, 15 mmol), DMAP (61 mg, 0.5 mmol) in dichloromethane (21.5 mL), pivaloyl chloride (720 mg, 6 mmol) was added at 0 °C. The mixture was warmed up to room temperature and stirred for 2h before of being quenched with ammonium chloride saturated solution. The organic layer was extracted with dichloromethane, washed with brine, dried over Na_2SO_4 and the solvent concentrated under vacuum. The crude was purified by flash column chromatography (SiO_2, hexane/ethyl acetate 98:2) to yield **10e** (1.3 g, quantitative) as a yellow oil. **^{1}H NMR** (300 MHz, $CDCl_3$): 7.49 – 7.27 (m, 2H), 7.06 – 6.98 (m, 2H), 6.83 (d, *J* = 15.6 Hz, 1H), 6.14 (dd, *J* = 15.7, 6.3 Hz, 1H), 6.01 (ddd, *J* = 6.3, 2.2, 1.2 Hz, 1H), 2.61 (d, *J* = 2.2 Hz, 1H), 1.24 (s, 9H). **^{13}C NMR** (75 MHz, $CDCl_3$): 177.08 (C), 162.78 (d, *J* = 248.1 Hz, C), 133.18 (CH), 131.87 (d, *J* = 3.4 Hz, C), 128.51 (d, *J* = 8.2 Hz, 2xCH), 123.39 (d, *J* = 2.2 Hz, CH), 115.57 (d, *J* = 21.6 Hz, 2xCH), 79.48 (C), 74.99 (CH), 63.69 (CH), 38.76 (C), 26.98 (3xCH_3). **ESI(-)-MS**: *m/z* (%) = 520 (100) [dimer] - ; $C_{16}H_{17}FO_2$ [260.30]: calcd. for C, 73.83; H, 6.58; found C, 73.57; H, 6.60.

1-ethynylcyclohexyl pivalate **10f**.

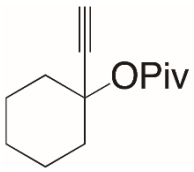

Figure 66 Chemical structure of compound **10f.**

1-ethynylcyclohexanol (500 mg, 4 mmol) and pivalic anhydride (815 mg, 4.4 mmol) were stirred at 80 °C for 1h in presence of magnesium perchlorate (9 mg, 0.04 mmol). The mixture was diluted with water, saturated solution of $NaHCO_3$ and extracted with Et_2O. The organic layers were washed with saturated solution of $NaHCO_3$, brine, dried over Na_2SO_4 and the solvent concentrated under vacuum. The crude was purified by flash column chromatography (SiO_2, hexane/ethyl acetate 99:1 to 98:2) to yield **10f** (781 g, 94%) as a yellow oil. **^{1}H NMR** (300 MHz, $CDCl_3$): 2.54 (s, 1H), 2.06 – 1.90 (m, 4H), 1.66 – 1.52 (m, 4H), 1.51 – 1.34 (m, 2H), 1.19 (s, 9H). **^{13}C NMR** (75 MHz, $CDCl_3$): 176.43 (C), 84.08 (C), 74.15 (C), 73.44 (CH), 39.16 (C), 36.75 (2xCH_2), 27.08 (3xCH_3), 25.08(CH_2), 22.16 (2xCH_2). **ESI(+)-MS**: *m/z* (%) = 209 (100) $[M+H]^+$; $C_{13}H_{20}O_2$ [208.30]: calcd. for C, 74.96; H, 9.68; found C, 75.23; H, 9.64.

5.3.3.3. Preliminary reactions between 9a and 10a-c

Reaction between 9a and 10a

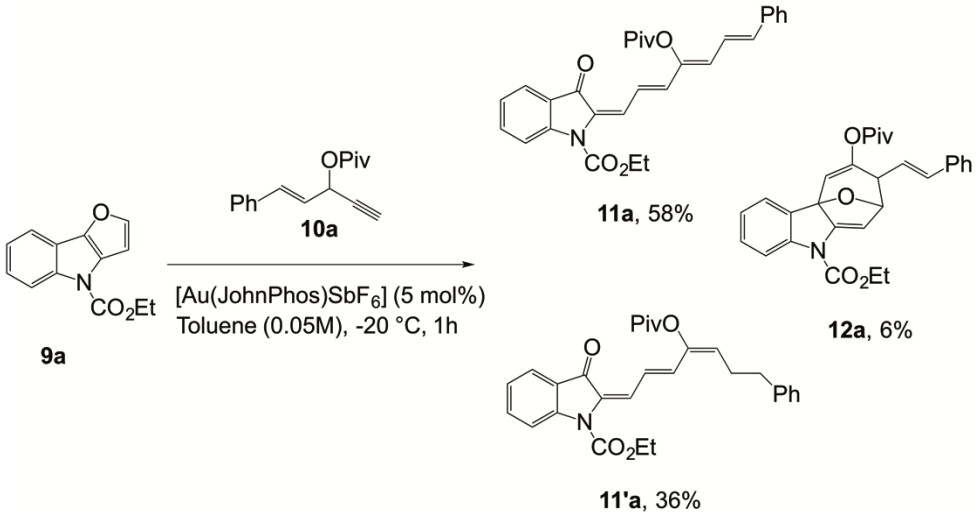

Scheme 24 Reaction scheme for the synthesis of compounds **11a, 11'a and 12a**.

To a N_2-flushed solution of ethyl 4*H*-furo[3,2-*b*]indole-4-carboxylate **9a** (46 mg, 0.2 mmol) and [Au(JohnPhos)SbF_6] (5 mol%) in anhydrous toluene (2 mL), a solution of (*E*)-1-phenylpent-1-en-4-yn-3-yl pivalate **10a** (58 mg, 0.24 mmol) in toluene (2 mL, final concentration 0.05 M) was added dropwise at -20 °C. The reaction mixture was stirred for 1 h at -20 °C and then quenched with PPh_3 (15 mol%). Purification by flash chromatography (SiO_2, toluene/ethyl acetate 99:1) yielded progressively **12a** (6 mg, 6%) as pale oil, **11'a** (34 mg, 36%) as a red solid (m.p. 174.2-176.3 °C) and **11a** (55 mg, 58%) as a red solid (m.p. 171.3-173.6 °C).

(*E*)-ethyl 9-(pivaloyloxy)-8-styryl-7,8-dihydro-5*H*-7,10a-epoxycyclohepta[*b*]indole-5-carboxylate **12a**.

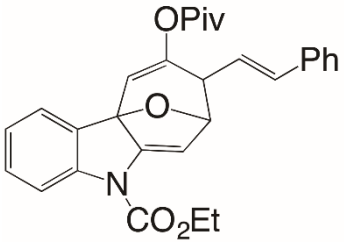

Figure 67 Chemical structure of compound **12a.**

^{1}H NMR (300 MHz, $CDCl_3$): 7.92 (bs, 1H), 7.51 (d, *J* = 6.7 Hz, 1H), 7.44 – 7.20 (m, 6H), 7.16 (t, *J* = 7.5 Hz, 1H), 6.56 (d, *J* = 15.9 Hz, 1H), 6.44 (dd, *J* = 15.8, 8.8 Hz, 1H), 5.89 (d, *J* = 1.1 Hz, 1H), 5.68 (bs, 1H), 5.15 (d, *J* = 2.6 Hz, 1H), 4.58 – 4.21 (m, 2H), 3.29 (d, *J* = 9.0 Hz, 1H), 1.43 (t, *J* = 7.1 Hz, 3H), 1.14 (s, 9H). **^{13}C NMR** (75 MHz, $CDCl_3$): 176.43 (C), 156.41 (C), 151.50 (C), 146.87 (C), 146.03 (C), 136.84 (C), 133.13 (CH), 130.40 (CH), 128.81 (CH), 128.53 (2xCH), 128.45 (C), 127.54 (CH), 126.35 (2xCH), 124.86 (CH), 124.37 (CH), 120.74 (CH), 115.82 (CH), 104.10 (CH), 89.27 (CH), 62.75 (CH_2), 45.48 (CH), 39.05 (C), 29.66 (C), 26.99 (3xCH_3), 14.39 (CH_3). **ESI(+)-MS**: *m/z* (%) = 472 (100) $[M+H]^+$; $C_{29}H_{29}NO_5$ [471.54]: calcd. for C, 73.87; H, 6.20; N, 2.97; found C, 73.76; H, 6.17; N, 2.98.

(*E*)-ethyl 3-oxo-2-((2*E*,4*E*,6*E*)-7-phenyl-4-(pivaloyloxy)hepta-2,4,6-trien-1-ylidene)indoline-1-carboxylate **11'a**.

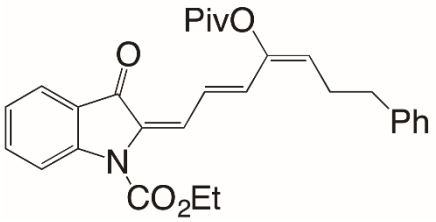

Figure 68 Chemical structure of compound **11'a.**

^{1}H NMR (300 MHz, CD_2Cl_2): 8.23 (dd, *J* = 14.8, 12.1 Hz, 1H), 8.07 (d, *J* = 8.4 Hz, 1H), 7.93 (d, *J* = 12.1 Hz, 1H), 7.80 (m, 1H), 7.65 (ddd, *J* = 8.6, 7.3, 1.4 Hz, 1H), 7.54 (d, *J* = 7.3 Hz, 2H), 7.45 – 7.36 (m, 2) 7.35 – 7.14 (m, 4H), 6.74 (d, *J* = 15.3 Hz, 1H), 6.21 (d, *J* = 11.9 Hz, 1H), 4.54 (q, *J* = 7.1 Hz, 2H), 1.54 (t, *J* = 7.1 Hz, 3H), 1.50 (s, 9H). **^{13}C NMR** (75 MHz, CD_2Cl_2): 184.10 (C), 176.76 (C), 151.75 (C), 146.88 (C), 146.85 (C), 136.95 (C), 135.53 (CH), 135.49 (CH), 132.57 (C), 130.62 (CH), 128.72 (2xCH), 128.23 (CH), 126.98 (CH), 126.71 (2xCH), 125.19 (CH), 125.07 (CH), 124.18 (CH), 123.87 (C), 123.58 (CH), 122.01 (CH), 117.28 (CH), 63.27 (CH_2), 39.11 (C), 27.07 (3xCH_3), 14.23 (CH_3). **ESI(+)-MS**: *m/z* (%) = 472 (100) $[M+H]^+$; $C_{29}H_{29}NO_5$ [471.54]: calcd. for C, 73.87; H, 6.20; N, 32.97; found C, 74.15; H, 6.22; N, 2.96.

(*E*)-ethyl 3-oxo-2-((2*E*,4*Z*,6*E*)-7-phenyl-4-(pivaloyloxy)hepta-2,4,6-trien-1-ylidene)indoline-1-carboxylate **11a**.

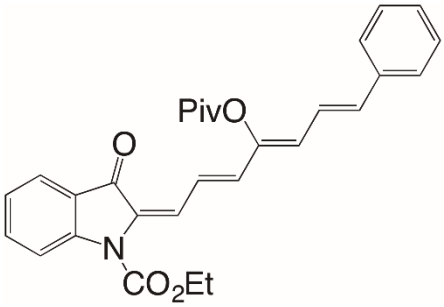

Figure 69 Chemical structure of compound **11a.**

^{1}H NMR (300 MHz, CD_2Cl_2): 8.17 (dd, *J* = 15.1, 12.0 Hz, 1H), 8.06 (d, *J* = 8.4 Hz, 1H), 7.88 – 7.74 (m, 2H), 7.63 (ddd, *J* = 8.6, 7.3, 1.5 Hz, 1H), 7.52 – 7.14 (m, 6H), 6.92 (dd, *J* = 15.6, 10.9 Hz, 1H) 6.81 (s, 1H), 6.68 (d, *J* = 15.1 Hz, 1H), 6.39 (d, *J* = 10.8 Hz, 1H), 4.50 (q, *J* = 7.1 Hz, 2H), 1.60 (s, 9H), 1.52 (d, *J* = 7.1, 3H). **^{13}C NMR** (75 MHz, CD_2Cl_2): 184.03 (C), 175.86 (C), 151.69 (C), 146.99 (C), 146.86 (C), 136.87 (C), 135.84 (CH), 135.78 (CH), 135.43 (CH), 132.15 (C), 128.73 (2xCH), 128.38 (CH), 127.11 (2xCH), 126.71 (CH), 124.87 (CH), 124.58 (CH), 124.22 (C), 123.81 (CH), 123.50 (CH), 121.79 (CH), 117.25 (CH), 63.21 (CH_2), 39.38 (C), 27.20 (3xCH_3), 14.16 (CH_3). **ESI(+)-MS**: *m/z* (%) = 472 (100) $[M+H]^+$; $C_{29}H_{29}NO_5$ [471.54]: calcd. for C, 73.87; H, 6.20; N, 32.97; found C, 73.67; H, 6.18; N, 2.96.

*Reaction between **9a** and **10b***

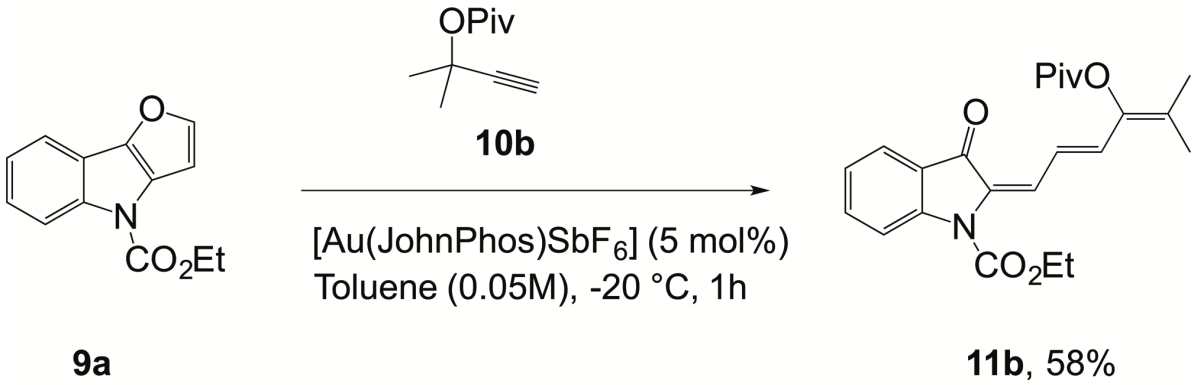

Scheme 25 Reaction scheme for the synthesis of compounds **11b.**

To a N_2-flushed solution of ethyl 4*H*-furo[3,2-*b*]indole-4-carboxylate **9a** (46 mg, 0.2 mmol) and [Au(JohnPhos)SbF_6] (5 mol%) in anhydrous toluene (2 mL), a solution of 2-methylbut-3-yn-2-yl pivalate **10b** (67 mg, 0.4 mmol) in toluene (2 mL, final concentration 0.05 M) was added dropwise at -20 °C. The reaction mixture was stirred for 1 h at -20 °C and then quenched with PPh_3 (15 mol%). Purification by flash chromatography (SiO_2, hexane/ ethyl acetate 95:5 to 9:1) yielded **11b** (46 mg, 58%) as a yellow solid (138.4 °C dec.).

(*E*)-ethyl 2-((*E*)-5-methyl-4-(pivaloyloxy)hexa-2,4-dien-1-ylidene)-3-oxoindoline-1-carboxylate **11b**.

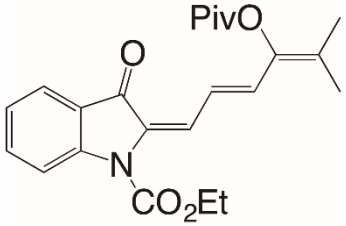

Figure 70 Chemical structure of compound **11b.**

^{1}H NMR (300 MHz, $CDCl_3$): 8.06 – 7.93 (m, 2H), 7.90 – 7.74 (m, 2H), 7.58 (t, *J* = 7.4 Hz, 1H), 7.21 (t, *J* = 7.4 Hz, 1H), 6.93 (d, *J* = 14.7 Hz, 1H), 4.50 (q, *J* = 7.1 Hz, 2H), 1.99 (s, 3H), 1.75 (s, 3H), 1.61 – 1.42 (m, 12H). **^{13}C NMR** (75 MHz, $CDCl_3$): 184.00 (C), 176.23 (C), 151.81 (C), 146.64 (C), 141.46 (C), 135.23 (CH), 133.11 (CH), 131.56 (C), 129.80 (C), 128.86 (CH), 124.45 (C), 123.79 (CH), 123.72 (CH), 122.36 (CH), 117.19 (CH), 62.98 (CH_2), 39.20 (C), 27.42 (3xCH_3), 19.27 (CH_3), 18.98 (CH_3), 14.41 (CH_3). **ESI(+)-MS**: *m/z* (%) = 420 (100) $[M+Na]^+$; $C_{23}H_{27}NO_5$ [397.46]: calcd. for C, 69.50; H, 6.85; N, 3.52; found C, 69.36; H, 6.87; N, 3.54.

*Reaction between **9a** and **10c***

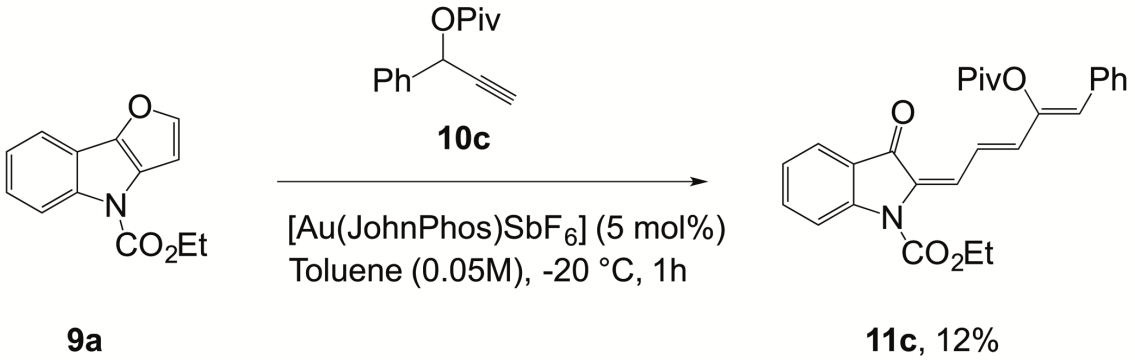

9a **11c**, 12%

Scheme 26 Reaction scheme for the synthesis of compounds **11c.**

To a N_2-flushed solution of ethyl 4*H*-furo[3,2-*b*]indole-4-carboxylate **9a** (46 mg, 0.2 mmol) and [Au(JohnPhos)SbF_6] (5 mol%) in anhydrous toluene (2 mL), a solution of 1-phenylprop-2-yn-1-yl pivalate **10c** (86 mg, 0.4 mmol) in toluene (2 mL, final concentration 0.05 M) was added dropwise at -20 °C. The reaction mixture was stirred for 1 h at -20 °C and then quenched with PPh_3 (15 mol%). Purification by flash chromatography (SiO_2, hexane/ ethyl acetate 95:5 to 9:1) yielded **11c** (11 mg, 12%) as a yellow oil.

(*E*)-ethyl 3-oxo-2-((2*E*,4*Z*)-5-phenyl-4-(pivaloyloxy)penta-2,4-dien-1-ylidene)indoline-1-carboxylate **11c**.

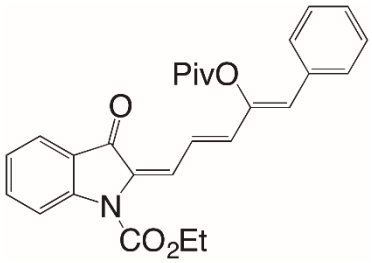

Figure 71 Chemical structure of compound **11c.**

^{1}H NMR (300 MHz, $CDCl_3$): 8.15 (dd, *J* = 15.0, 11.8 Hz, 1H), 8.02 (d, *J* = 8.5 Hz, 1H), 7.81 (m, 2H), 7.58 (ddd, *J* = 8.6, 7.3, 1.4 Hz, 1H), 7.49 (m, 2H), 7.37 – 7.27 (m, 3H), 7.20 (t, *J* = 7.5 Hz, 1H), 6.66 (s, 1H), 6.46 (s, 1H), 4.49 (q, *J* = 7.1 Hz, 3H), 1.58 – 1.41 (m, 12H). **^{13}C NMR** (75 MHz, $CDCl_3$): 184.17 (C), 175.53 (C), 151.76 (C), 146.83 (C), 146.49 (C), 137.64 (CH), 135.48 (CH), 134.04 (C), 132.08 (C), 129.13 (2xCH), 128.38 (2xCH), 128.25 (CH), 127.64 (CH), 124.61 (CH), 124.37 (CH), 124.29 (C), 123.89 (CH), 117.24 (CH), 63.12 (CH_2), 39.30 (C), 27.47 (3xCH_3), 14.42 (CH_3). One CH is missing, probably overlapping. **ESI(+)-MS**: *m/z* (%) = 468 (100) $[M+Na]^+$; $C_{27}H_{27}NO_5$ [445.51]: calcd. for C, 72.79; H, 6.11; N, 3.14; found 73.08; H, 6.09; N, 3.15.

*Reaction of **10a** under standard reaction conditions*

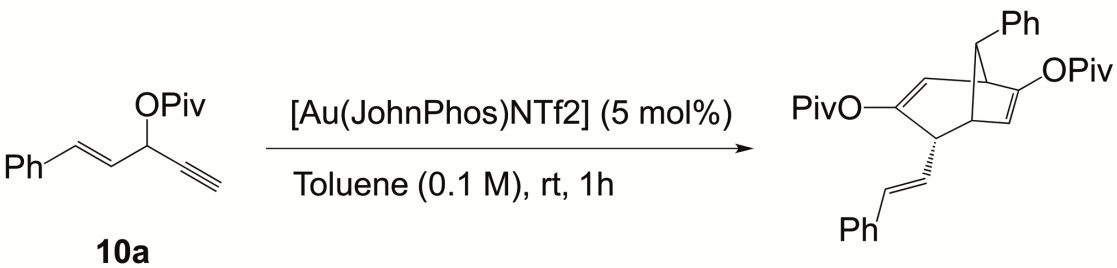

10a

Scheme 27 Scheme reaction of compound **10a** under standard reaction conditions.

To a N_2-flushed solution of (*E*)-1-phenylpent-1-en-4-yn-3-yl pivalate **10a** (97 mg, 0.4 mmol) in toluene (4 ml) was added [Au(JohnPhos)SbF_6]. The reaction mixture was stirred for 1h at room temperature and then quenched with PPh_3 (15 mol%). Purification by flash chromatography (SiO_2, hexane/ ethyl acetate 98:2) yielded cycloadduct (45 mg, 46%) as a yellow oil. **^{1}H NMR** (300 MHz, $CDCl_3$): 7.45 – 7.06 (m, 10H), 6.52 (d, *J* = 15.7 Hz, 1H), 6.20 (dd, *J* = 6.9, 1.8 Hz, 1H), 6.07 (dd, *J* = 15.7, 9.8 Hz, 1H), 5.38 (d, *J* = 3.0 Hz, 1H), 3.95 – 3.76 (m, 1H), 3.55 (s, 1H), 3.19 (m, 1H), 3.12 (d, *J* = 7.0 Hz, 1H), 1.28 (s, 9H), 1.15 (s, 9H). Data are in agreement with those reported in literature[199].

5.3.3.4. Preparation and characterization data for products 11a-n

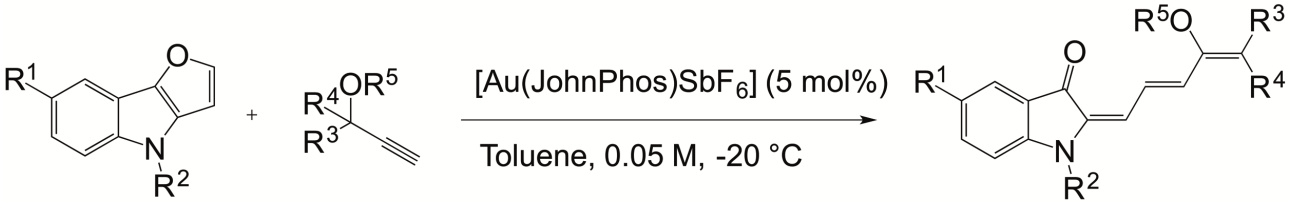

Scheme 28 Scheme reaction for the synthesis of compounds **11a-n**.

(*E*)-ethyl 3-oxo-2-((2*E*,4*Z*,6*E*)-7-phenyl-4-(pivaloyloxy)hepta-2,4,6-trien-1-ylidene)indoline-1-carboxylate **11a**.

General procedure was followed using ethyl 4*H*-furo[3,2-*b*]indole-4-carboxylate **9a** (46 mg, 0.2 mmol), (*E*)-1-phenylpent-1-en-4-yn-3-yl pivalate **10a** (58 mg, 0.24 mmol) and [Au(JohnPhos)SbF_6] (7.7 mg, 0.01 mmol) in anhydrous toluene (2+2 mL) at -20 °C for 1 h, followed by isomerization with I_2 for 4 h at rt. Purification by flash chromatography (SiO_2, toluene/ethyl acetate 99:1) yielded **11a** (89 mg, 98%). Data analysis are reported previously.

(*E*)-tert-butyl 3-oxo-2-((2*E*,4*Z*,6*E*)-7-phenyl-4-(pivaloyloxy)hepta-2,4,6-trien-1-ylidene)indoline-1-carboxylate **11d**.

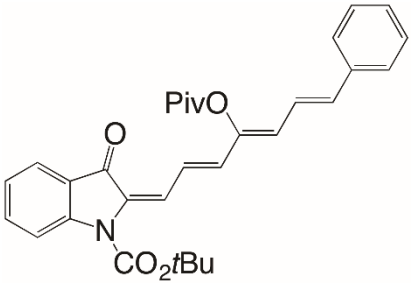

Figure 72 Chemical structure of compound **11d.**

General procedure was followed using tert-butyl 4*H*-furo[3,2-*b*]indole-4-carboxylate **9b** (52 mg, 0.2 mmol), (*E*)-1-phenylpent-1-en-4-yn-3-yl pivalate **10a** (58 mg, 0.24 mmol) and [Au(JohnPhos)SbF_6] (7.7 mg, 0.01 mmol) in anhydrous toluene (2+2 mL) at -20 °C for 1 h, followed by isomerization with I_2 for 4 h at rt. Purification by flash chromatography (SiO_2,toluene to toluene/ethyl acetate 98:2) yielded **11d** (75 mg, 75%) as a red solid (170.2 °C, dec). **^{1}H NMR** (300 MHz, $CDCl_3$): 8.15 (dd, *J* = 14.9, 12.1 Hz, 1H), 8.00 (d, *J* = 8.5 Hz, 1H), 7.86 – 7.68 (m, 2H), 7.56 (m, 1H), 7.44 – 7.06 (m, 6H), 6.85 (dd, *J* = 15.5, 11.0 Hz, 1H), 6.71 (d, *J* = 15.7 Hz, 1H), 6.60 (d, *J* = 15.1 Hz, 1H), 6.31 (d, *J* = 11.0 Hz, 1H), 1.68 (s, 9H), 1.57 (s, 9H). **^{13}C NMR** (75 MHz, $CDCl_3$): 184.31 (C), 176.03 (C), 150.41 (C), 147.09 (C), 146.89 (C), 136.94 (C), 135.83 (CH), 135.75 (CH), 135.30 (CH), 132.32 (C), 128.74 (2xCH), 128.32 (CH), 127.54 (CH), 126.70 (2xCH), 124.88 (CH), 124.79 (CH), 124.19 (C), 123.80 (CH), 123.56 (CH), 121.89 (CH),

117.16 (CH), 84.21 (C), 39.50 (C), 28.32 (3xCH_3), 27.46 (3xCH_3). **ESI(+)-MS**: *m/z* (%) = 500 (100) $[M+H]^+$; $C_{31}H_{33}NO_5$ [499.60]: calcd. for C, 74.53; H, 6.66; N, 2.80; found C, 74.78; H, 6.64; N, 2.79.

(*E*)-tert-butyl 3-oxo-2-((2*E*,4*E*,6*E*)-7-phenyl-4-(pivaloyloxy)hepta-2,4,6-trien-1-ylidene)indoline-1-carboxylate **11'd**.

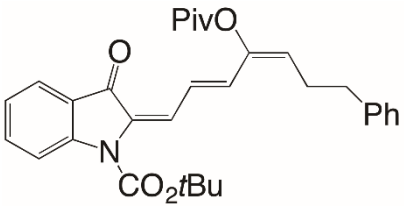

Figure 73 Chemical structure of compound **11'd.**

General procedure was followed using tert-butyl 4*H*-furo[3,2-*b*]indole-4-carboxylate **9b** (52 mg, 0.2 mmol), (*E*)-1-phenylpent-1-en-4-yn-3-yl pivalate **10a** (58 mg, 0.24 mmol) and [Au(JohnPhos)SbF_6] (7.7 mg, 0.01 mmol) in anhydrous toluene (2+2 mL) at -20 °C for 1 h, avoiding the isomerization step with I_2. Purification by flash chromatography (SiO_2, toluene to toluene/ethyl acetate 98:2) yielded progressively **11'd** (35 mg, 35%) as red solid (177.3 °C, dec.) and **11d** (48 mg, 48%). **^{1}H NMR** (500 MHz, $CDCl_3$): 8.24 (dd, *J* = 14.9, 12.1 Hz, 1H), 7.96 (dd, *J* = 22.2, 10.2 Hz, 2H), 7.82 (d, *J* = 7.0 Hz, 1H), 7.59 (m, 1H), 7.49 (d, *J* = 7.4 Hz, 2H), 7.38 (t, *J* = 7.6 Hz, 2H), 7.31 (m, 1H), 7.26 – 7.15 (m, 2H), 7.12 (d, *J* = 14.9 Hz, 1H), 6.70 (d, *J* = 15.3 Hz, 1H), 6.19 (d, *J* = 11.7 Hz, 1H), 1.74 (s, 9H), 1.51 (s, 9H). **^{13}C NMR** (126 MHz, $CDCl_3$): 184.35 (C), 177.00 (C), 150.50 (C), 147.05 (C), 146.76 (C), 137.00 (C), 135.52 (CH), 135.39 (CH), 132.77 (C), 130.72 (CH), 128.76 (2xCH), 128.20 (CH), 127.51 (CH), 126.74 (2xCH), 125.34 (CH), 125.20 (CH), 124.20 (C), 123.93 (CH), 123.65 (CH), 122.10 (CH), 117.18 (CH), 84.33 (C), 39.28 (C), 28.38 (3xCH_3), 27.37 (3xCH_3). **ESI(+)-MS**: *m/z* (%) = 500 (100) $[M+H]^+$; $C_{31}H_{33}NO_5$ [499.60]: calcd. for C, 74.53; H, 6.66; N, 2.80; found C, 74.73; H, 6.68; N, 2.81.

(1*E*,3*Z*,5*E*,7*E*)-7-(1-methyl-3-oxoindolin-2-ylidene)-1-phenylhepta-1,3,5-trien-4-yl pivalate **11e**.

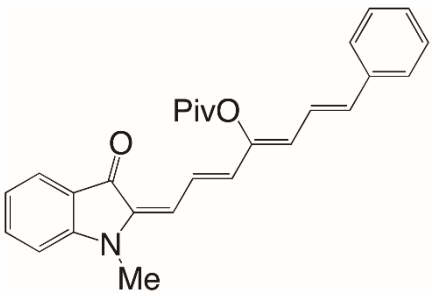

Figure 74 Chemical structure of compound **11e.**

General procedure was followed using 4-methyl-4*H*-furo[3,2-*b*]indole **9c** (34 mg, 0.2 mmol), (*E*)-1-phenylpent-1-en-4-yn-3-yl pivalate **10a** (58 mg, 0.24 mmol) and [Au(JohnPhos)SbF_6] (7.7 mg, 0.01 mmol) in anhydrous toluene (2+2 mL) at -20 °C for 1 h, followed by isomerization with I_2 for 4 h at rt. Purification by flash chromatography (SiO_2, toluene/ethyl acetate 99:1 to 98:2) yielded **11e** (33 mg, 40%) as a purple solid (m.p. 189.8-191.2 °C). **^{1}H NMR** (300 MHz, $CDCl_3$): 7.99 (dd, *J* = 15.0, 12.0 Hz, 1H), 7.66 (d, *J* = 7.5 Hz, 1H), 7.50 – 7.13 (m, 6H), 6.99 – 6.77 (m, 3H), 6.67 (d, *J* = 15.6 Hz, 1H), 6.46 (d, *J* = 15.1 Hz, 1H), 6.25 (d, *J* = 11.2 Hz, 1H), 6.09 (d, *J* = 11.9 Hz, 1H), 3.22 (s, 3H), 1.60 (s, 9H). **^{13}C NMR** (75 MHz, $CDCl_3$): 185.44 (C), 176.22 (C), 151.90 (C), 147.32 (C), 137.17 (C), 136.45 (C), 135.40 (CH), 134.61 (CH), 131.23 (CH), 128.75 (2xCH), 128.09 (CH), 126.60 (2xCH), 124.92 (CH),

124.47 (CH), 122.99 (CH), 122.12 (CH), 121.34 (C), 119.19 (CH), 115.14 (CH), 108.58 (CH), 39.53 (C), 28.53 (CH_3), 27.52 (3xCH_3). **ESI(+)-MS**: *m/z* (%) = 414 (100) $[M+H]^+$; $C_{27}H_{27}NO_3$ [413.51]: calcd. for C, 78.42; H, 6.58; N, 3.39; found C, 78.35; H, 6.61; N, 3.38.

(*E*)-ethyl 2-((2*E*,4*Z*,6*E*)-7-(4-methoxyphenyl)-4-(pivaloyloxy)hepta-2,4,6-trien-1-ylidene)-3-oxoindoline1-carboxylate **11f**.

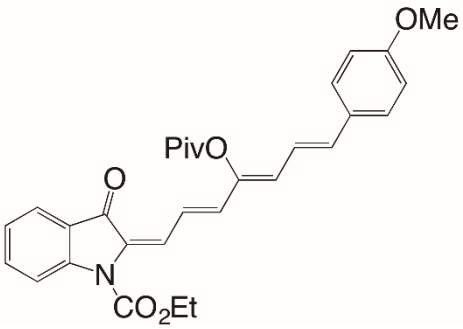

Figure 75 Chemical structure of compound **11f.**

General procedure was followed using ethyl 4*H*-furo[3,2-*b*]indole-4-carboxylate **9a** (46 mg, 0.2 mmol), (*E*)-1-(4-methoxyphenyl)pent-1-en-4-yn-3-yl pivalate **10d** (109 mg, 0.4 mmol) and [Au(JohnPhos)SbF_6] (7.7 mg, 0.01 mmol) in anhydrous toluene (2+2 mL) at -20 °C for 1 h, followed by isomerization with I_2 for 4 h at rt. Purification by flash chromatography (SiO_2, hexane/ethyl acetate 9:1 to 8:2) yielded **11f** (89 mg, 89%) as a red solid (m.p. 154.3-156.8 °C). **^{1}H NMR** (300 MHz, $CDCl_3$): 8.11 (dd, *J* = 14.9, 11.9 Hz, 1H), 8.01 (d, *J* = 8.4 Hz, 1H), 7.81 (s, 1H), 7.78 (m, 1H), 7.57 (ddd, *J* = 8.6, 7.3, 1.5 Hz, 1H), 7.32 (d, *J* = 8.8 Hz, 2H), 7.19 (m, 1H), 6.86 (d, *J* = 8.8 Hz, 2H), 6.70 (d, *J* = 8.8 Hz, 2H), 6.61 (d, *J* = 15.0 Hz, 1H), 6.30 (d, *J* = 9.9 Hz, 1H), 4.48 (q, *J* = 7.1 Hz, 2H), 3.82 (s, 3H), 1.57 (s, 9H), 1.49 (t, *J* = 7.1 Hz, 3H). **^{13}C NMR** (75 MHz, $CDCl_3$): 184.01 (C), 176.01 (C), 159.95 (C), 151.75 (C), 146.65 (C), 146.05 (C), 136.40 (CH), 135.68 (CH), 135.28 (CH), 131.81 (C), 129.83 (C), 128.10 (2xCH), 127.97 (CH), 125.49 (CH), 124.40 (C), 124.09 (CH), 123.80 (2xCH), 119.90 (CH), 117.21 (CH), 114.28 (2xCH), 63.06 (CH_2), 55.30 (CH_3), 39.48 (C), 27.46 (3xCH_3), 14.40 (CH_3). **ESI(+)-MS**: *m/z* (%) = 502 (100) $[M+H]^+$; $C_{30}H_{31}NO_6$ [501.57]: calcd. for C, 71.84; H, 6.23; N, 2.79; found C, 72.10; H, 6.25; N, 2.80.

(*E*)-ethyl 2-((2*E*,4*Z*,6*E*)-7-(4-fluorophenyl)-4-(pivaloyloxy)hepta-2,4,6-trien-1-ylidene)-3-oxoindoline-1- carboxylate **11g**.

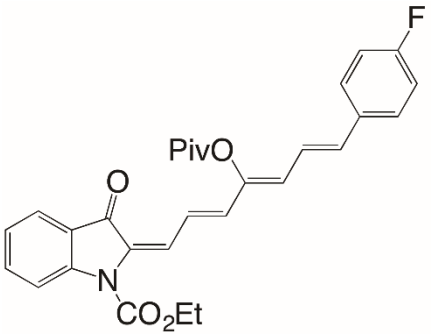

Figure 76 Chemical structure of compound **11g.**

General procedure was followed using ethyl 4*H*-furo[3,2-*b*]indole-4-carboxylate **9a** (46 mg, 0.2 mmol), (*E*)-1-(4-fluorophenyl)pent-1-en-4-yn-3-yl pivalate **10e** (62 mg, 0.24 mmol) and [Au(JohnPhos)SbF_6] (7.7 mg, 0.01 mmol) in anhydrous toluene (2+2 mL) at -20 °C for 1 h, followed

by isomerization with I_2 for 4 h at rt. Purification by flash chromatography (SiO_2, toluene/ethyl acetate 99:1) yielded **11g** (54 mg, 55%) as a red solid (m.p. 162.2-164.3 °C). **^{1}H NMR** (300 MHz, $CDCl_3$): 8.16 (dd, *J* = 14.9, 12.1 Hz, 1H), 8.02 (d, *J* = 8.5 Hz, 1H), 7.88 – 7.73 (m, 2H), 7.59 (t, *J* = 7.9 Hz, 1H), 7.40 – 7.32 (m, 2H), 7.22 (t, *J* = 7.4 Hz, 1H),7.03 (t, *J* = 8.6 Hz, 2H), 6.85 – 6.56 (m, 3H), 6.32 (d, *J* = 10.3 Hz, 1H), 4.50 (q, *J* = 7.1 Hz, 2H), 1.59 (s, 9H), 1.51 (t, *J* = 7.1 Hz, 3H). **^{13}C NMR** (75 MHz, $CDCl_3$): 184.14 (C), 176.09 (C), 162.69 (d, J = 249.1 Hz, C), 151.75 (C), 146.83 (d, J = 1.1 Hz, C),146.68 (C), 136.13 (CH), 135.46 (CH), 134.55 (CH), 133.15 (d, J = 3.4 Hz, C), 132.03 (C), 128.28 (d, J = 8.0 Hz, 2xCH), 127.72 (CH), 124.87 (CH), 124.71 (CH), 124.30 (C), 123.90 (CH), 123.87 (CH), 121.57 (d, J = 2.3 Hz, CH), 117.26 (CH), 115.83 (d, J = 21.9 Hz, 2xCH), 63.15 (CH_2), 39.53 (C), 27.47 (3xCH_3), 14.43 (CH_3). **ESI(+)-MS**: *m/z* (%) = 490 (100) $[M+H]^+$; $C_{29}H_{28}FNO_5$ [489.53]: calcd. for C, 71.15; H, 5.77; N, 2.86; found C, 71.37; H, 5.79; N, 2.86.

(*E*)-ethyl 2-((*E*)-4-cyclohexylidene-4-(pivaloyloxy)but-2-en-1-ylidene)-3-oxoindoline-1-carboxylate **11h**.

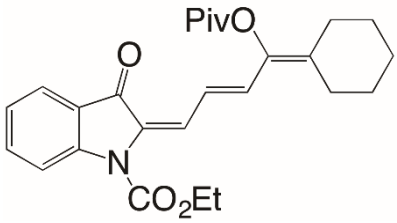

Figure 77 Chemical structure of compound **11h.**

General procedure was followed using ethyl 4*H*-furo[3,2-*b*]indole-4-carboxylate **9a** (46 mg, 0.2 mmol), 1-ethynylcyclohexyl acetate **10f** (83 mg, 0.4 mmol) and [Au(JohnPhos)SbF_6] (7.7 mg, 0.01 mmol) in anhydrous toluene (2+2 mL) at -20 °C for 22 h, followed by isomerization with I_2 for 4 h at rt. Purification by flash chromatography (SiO_2, hexane/ethyl acetate 95:5 to 9:1) yielded **11h** (32 mg, 36%) as a yellow oil. **^{1}H NMR** (300 MHz, $CDCl^3$): 8.06 – 7.94 (m, 2H), 7.86 – 7.72 (m, 2H), 7.56 (m, 1H), 7.19 (t, *J* = 7.4 Hz, 1H), 6.97 (d, *J* = 14.8 Hz, 1H), 4.48 (q, *J* = 7.1 Hz, 2H), 2.58 – 2.34 (m, 2H), 2.16 (d, *J* = 6.6 Hz, 2H), 1.77 – 1.01 (m, 18H). **^{13}C NMR** (75 MHz, $CDCl_3$): 184.00 (C), 176.48 (C), 151.82 (C), 146.64 (C), 138.65 (C), 137.83 (C), 135.21 (CH), 132.88 (CH), 131.44 (C), 129.06 (CH), 124.47 (C), 123.79 (CH), 123.71 (CH), 122.64 (CH), 117.20 (CH), 62.98 (CH2), 39.19 (C), 29.76 (CH2), 28.89 (CH_2), 27.76 (CH_2), 27.46 (3xCH_3), 27.07 (CH_2), 26.29 (CH_2), 14.43 (CH_3). **ESI(+)-MS**: *m/z* (%) = 438 (100) $[M+H]^+$; $C_{26}H_{31}NO_5$ [437.53]: calcd. for C, 71.37; H, 7.14; N, 3.20; found C, 71.18; H, 7.11; N, 3.22.

(I)-ethyl 2-((2E,4Z,6I)-4-acetoxy-7-phenylhepta-2,4,6-trien-1-ylidene)-3-oxoindoline-1-carboxylate **11i**.

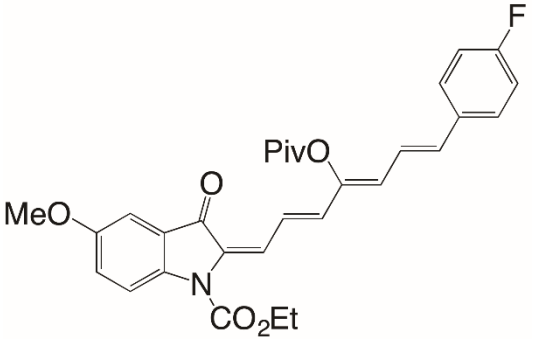

Figure 78 Chemical structure of compound **11i.**

General procedure was followed using ethyl 4*H*-furo[3,2-*b*]indole-4-carboxylate **9a** (46 mg, 0.2 mmol), (*E*)-1-phenylpent-1-en-4-yn-3-yl acetate **10g** (48 mg, 0.24 mmol) and [Au(JohnPhos)SbF_6] (7.7 mg, 0.01 mmol) in anhydrous toluene (2+2 mL) at -20 °C for 2 h, followed by isomerization with I_2 for 4 h at rt. Purification by flash chromatography (SiO_2, hexane/ethyl acetate 9:1 to 8:2) yielded **11i** (48 mg, 56%) as a red solid (m.p. 88.2- 90.1 °C). **^{1}H NMR** (300 MHz, $CDCl_3$): 8.21 (dd, *J* = 15.0, 12.0 Hz, 1H), 8.02 (d, *J* = 8.4 Hz, 1H), 7.86 – 7.77 (m, 2H), 7.61 (m, 1H), 7.53 – 7.41 (m, 2H), 7.37 – 7.17 (m, 4H), 6.87 (d, *J* = 10.9 Hz, 1H), 6.75 (d, *J* = 15.8 Hz, 1H), 6.62 (d, *J* = 15.0 Hz, 1H), 6.35 (d, *J* = 10.9 Hz, 1H), 4.50 (q, *J* = 7.1 Hz, 2H), 2.53 (s, 3H), 1.51 (t, *J* = 7.1 Hz, 3H). **^{13}C NMR** (75 MHz, $CDCl_3$): 184.37 (C), 168.72 (C), 151.73 (C), 146.73 (C), 146.59 (C), 136.81 (C), 136.43 (CH), 135.79 (CH), 135.57 (CH), 132.08 (C), 128.72 (2xCH), 128.47 (CH), 127.74 (CH), 126.94 (2xCH), 125.39 (CH), 124.81 (CH), 124.31 (C), 123.99 (CH), 123.76 (CH), 121.92 (CH), 117.31 (CH), 63.18 (CH_2), (CH_3), 14.42 (CH_3). **ESI(+)-MS**: *m/z* (%) = 452 (100) $[M+Na]^+$; $C_{26}H_{23}NO_5$ [429.46].

(*E*)-ethyl 3-oxo-2-((2*E*,4*Z*,6*E*)-7-phenyl-4-((thiophene-2-carbonyl)oxy)hepta-2,4,6-trien-1-ylidene)indoline-1-carboxylate **11j**.

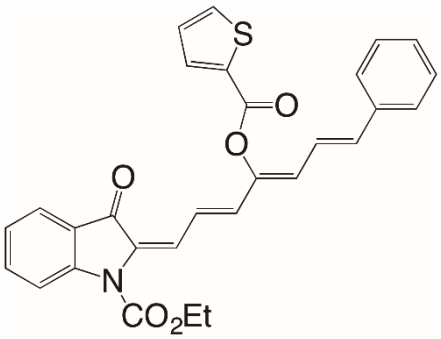

Figure 79 Chemical structure of compound **11j.**

General procedure was followed using ethyl 4*H*-furo[3,2-*b*]indole-4-carboxylate **9a** (46 mg, 0.2 mmol (*E*)-1-phenylpent-1-en-4-yn-3-yl thiophene-2-carboxylate **10h** (65 mg, 0.24 mmol) and [Au(JohnPhos)SbF_6] (7.7 mg, 0.01 mmol) in anhydrous toluene (2+2 mL) at -20 °C for 22 h, followed by isomerization with I_2 for 4 h at rt. Purification by flash chromatography (SiO_2, hexane/ethyl acetate 9:1+1% dichloromethane) yielded **11j** (98 mg, 98%) as a red solid (m.p. 172.3-174.5 °C). **^{1}H NMR** (300 MHz, $CDCl_3$): 8.29 (dd, *J* = 15.0, 12.0 Hz, 1H), 8.14 (dd, *J* = 3.7, 1.1 Hz, 1H), 8.00 (d, *J* = 8.4 Hz, 1H), 7.83 (d, *J* = 12.0 Hz, 1H), 7.79 – 7.70 (m, 2H), 7.56 (m, 1H), 7.43 – 7.36 (m, 2H), 7.34 – 7.14 (m, 5H), 6.95 (dd, *J* = 15.5, 11.0 Hz, 1H), 6.78 (d, *J* = 15.7 Hz, 1H), 6.71 (d, *J* = 15.1 Hz, 1H), 6.46 (d, *J* = 11.0 Hz, 1H), 4.49 (q, *J* = 7.1 Hz, 2H), 1.51 (t, *J* = 7.1 Hz, 3H). **^{13}C NMR** (75 MHz, $CDCl_3$): 184.56 (C), 160.12 (C), 152.13 (C), 147.13 (C), 146.59 (C), 137.16 (C), 137.02 (CH), 136.58 (CH), 135.83 (CH), 135.61 (CH), 134.34 (CH), 132.45 (C), 132.40 (C), 129.06 (2xCH), 128.84 (CH), 128.71 (CH), 128.19 (CH), 127.38 (2xCH), 126.04 (CH), 125.39 (CH), 124.67 (C), 124.29 (CH), 124.22 (CH), 122.41 (CH), 117.65 (CH), 63.55 (CH_2), 14.81 (CH_3). **ESI(+)-MS**: *m/z* (%) = 520 (100) $[M+Na]^+$; $C_{29}H_{23}NO_5S$ [497.56].

(*E*)-ethyl 5-methoxy-3-oxo-2-((2*E*,4*Z*,6*E*)-7-phenyl-4-(pivaloyloxy)hepta-2,4,6-trien-1-ylidene)indoline1-carboxylate **11k**.

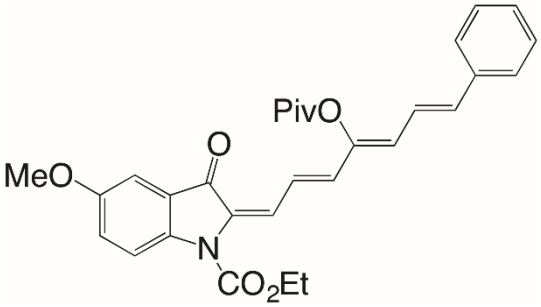

Figure 80 Chemical structure of compound **11k.**

General procedure was followed using ethyl 7-methoxy-4*H*-furo[3,2-*b*]indole-4-carboxylate **9d** (52 mg, 0.2 mmol), (*E*)-1-phenylpent-1-en-4-yn-3-yl pivalate **10a** (58 mg, 0.24 mmol) and [Au(JohnPhos)SbF_6] (7.7 mg, 0.01 mmol) in anhydrous toluene (2+2 mL) at -20 °C for 2 h, followed by isomerization with I_2 for 4 h at rt. Purification by flash chromatography (SiO_2, toluene/ethyl acetate 99:1 to 98:2) yielded **11k** (77 mg, 75%) as a red solid (m.p. 164.2-166.5 °C). **^{1}H NMR** (300 MHz, $CDCl_3$): 8.12 (dd, *J* = 14.9, 12.1 Hz, 1H), 7.89 (d, *J* = 9.0 Hz, 1H), 7.79 (d, *J* = 12.2 Hz, 1H), 7.45 – 7.08 (m, 7H), 6.85 (dd, *J* = 15.6, 10.9 Hz, 1H), 6.76 – 6.56 (m, 2H), 6.32 (d, *J* = 10.8 Hz, 1H), 4.45 (q, *J* = 7.1 Hz, 2H), 3.83 (s, 3H), 1.58 (s, 9H), 1.48 (t, *J* = 7.1 Hz, 3H). **^{13}C NMR** (75 MHz, $CDCl_3$): 183.92 (C), 175.96 (C), 156.43 (C), 151.60 (C), 146.85 (C), 141.25 (C), 136.93 (C), 136.20 (CH), 135.90 (CH), 132.52 (C), 128.73 (2xCH), 128.33 (CH), 127.92 (CH), 126.71 (2xCH), 125.05 (CH), 124.68 (CH), 124.13 (CH), 121.87 (CH), 118.40 (CH), 105.09 (CH), 62.92 (CH_2), 55.77 (CH_3), 39.49 (C), 27.46 (3xCH_3), 14.41 (CH_3), one quaternary carbon is missing, probably overlapping. **ESI(+)-MS**: *m/z* (%) = 502 (100) $[M+H]^+$; $C_{30}H_{31}NO_6$ [501.57]: calcd. for C, 71.84; H, 6.23; N, 2.79; found C, 71.62; H, 6.20; N, 2.80.

(*E*)-ethyl 2-((2*E*,4*Z*,6*E*)-7-(4-fluorophenyl)-4-(pivaloyloxy)hepta-2,4,6-trien-1-ylidene)-5-methoxy-3-oxoindoline-1-carboxylate **11l**.

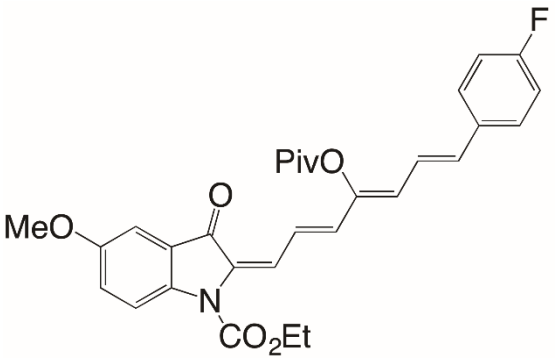

Figure 81 Chemical structure of compound **11l.**

General procedure was followed using ethyl 7-methoxy-4*H*-furo[3,2-*b*]indole-4-carboxylate **9d** (52 mg, 0.2 mmol), (*E*)-1-(4-fluorophenyl)pent-1-en-4-yn-3-yl pivalate **10e** (62 mg, 0.24 mmol) and [Au(JohnPhos)SbF_6] (7.7 mg, 0.01 mmol) in anhydrous toluene (2+2 mL) at -20 °C for 2 h, followed by isomerization with I_2 for 4 h at rt. Purification by flash chromatography (SiO_2, hexane/ethyl acetate 95:5 to 91) yielded **11l** (70 mg, 67%) as a red solid (m.p. 161.5-163.7 °C). **^{1}H NMR** (300 MHz, $CDCl_3$): 8.12 (dd, *J* = 15.0, 12.1 Hz, 1H), 7.90 (d, *J* = 9.1 Hz, 1H), 7.79 (d, *J* = 12.1 Hz, 1H), 7.33 (dd, *J* = 8.7, 5.4 Hz, 2H), 7.22 (d, *J* = 2.7 Hz, 1H), 7.15 (dd, *J* = 9.0, 2.8 Hz, 1H), 7.01 (t, *J* = 8.6 Hz, 2H), 6.76 – 6.55 (m, 3H), 6.29 (d, *J* = 10.2 Hz, 1H), 4.45 (q, *J* = 7.1 Hz, 2H), 3.83 (s, 3H), 1.57 (s, 9H), 1.48 (t, *J* = 7.1 Hz, 3H). **^{13}C NMR** (75 MHz, $CDCl_3$): 183.95 (C), 175.96 (C), 162.69 (d, *J* = 249.1 Hz, C), 156.45 (C),

151.61 (C), 146.86 (C), 141.26 (C), 136.07 (CH), 134.48 (CH), 133.18 (d, *J* = 3.4 Hz, C), 132.57 (C), 128.24 (d, *J* = 8.0 Hz, 2xCH), 127.85 (CH), 125.05 (C), 124.78 (CH),124.75 (CH), 124.17 (CH), 121.63 (CH), 118.41 (CH), 115.79 (d, *J* = 21.9 Hz, 2xCH), 105.10 (CH), 62.93 (CH_2), 55.77 (CH_3), 39.49 (C), 27.45 (3xCH_3), 14.41 (CH_3). **ESI(+)-MS**: *m/z* (%) = 520 (100) $[M+H]^+$; $C_{30}H_{30}FNO_6$ [519.56]: calcd. for C, 69.35; H, 5.82; N, 2.70; found C, 69.13; H, 5.84; N, 2.69.

(*E*)-ethyl 5-fluoro-3-oxo-2-((2*E*,4*Z*,6*E*)-7-phenyl-4-(pivaloyloxy)hepta-2,4,6-trien-1-ylidene)indoline-1-carboxylate **11m**.

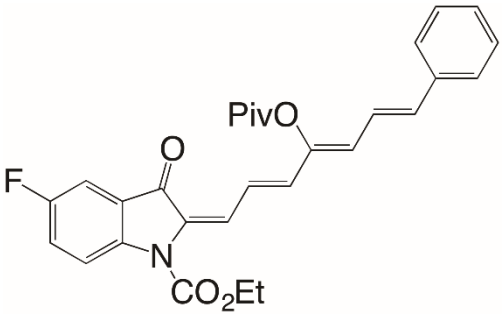

Figure 82 Chemical structure of compound **11m.**

General procedure was followed using ethyl 7-fluoro-4*H*-furo[3,2-*b*]indole-4-carboxylate **9e** (49 mg, 0.2 mmol), (*E*)-1-phenylpent-1-en-4-yn-3-yl pivalate **10a** (97 mg, 0.4 mmol) and [Au(JohnPhos)SbF_6] (7.7 mg, 0.01 mmol) in anhydrous toluene (2+2 mL) at -20 °C for 1 h, followed by isomerization with I_2 for 4 h at rt. Purification by flash chromatography (SiO_2, hexane/ethyl acetate 95:5 to 9:1) yielded **11m** (82 mg, 84%) as a red solid (m.p.144.6-146.1 °C). **^{1}H NMR** (300 MHz, $CDCl_3$): 8.10 (dd, *J* = 14.9, 12.2 Hz, 1H), 7.98 (dd, *J* = 9.0, 3.9 Hz, 1H), 7.78 (d, *J* = 12.1 Hz, 1H), 7.44 (dd, *J* = 6.8, 2.7 Hz, 1H), 7.40 – 7.22 (m, 6H), 6.85 (dd, *J* = 15.6, 10.9 Hz, 1H), 6.76 – 6.59 (m, 2H), 6.33 (d, *J* = 10.9 Hz, 1H), 4.47 (q, *J* = 7.1 Hz, 2H), 1.57 (s, 9H), 1.48 (t, *J* = 7.1 Hz, 3H). **^{13}C NMR** (75 MHz, $CDCl_3$): 183.00 (C), 175.98 (C), 159.27 (d, *J* = 245.6 Hz, C), 151.50 (C), 146.77 (C), 142.82 (C), 136.86 (C), 136.83 (CH), 136.20 (CH), 132.15 (C), 128.74 (2xCH), 128.58 (CH), 128.42 (CH), 126.74 (2xCH), 125.49 (d, *J* = 7.7 Hz, C), 125.50 (CH), 124.46 (CH), 122.46 (d, *J* = 24.3 Hz, CH), 121.81 (CH), 118.76 (d, *J* = 7.4 Hz, CH), 109.47 (d, *J* = 23.4 Hz, CH), 63.21 (CH_2), 39.50 (C), 27.43 (3xCH_3), 14.38 (CH_3). **ESI(+)-MS**: *m/z* (%) = 490 (100) $[M+H]^+$; $C_{29}H_{28}FNO_5$ [489.53]: calcd. for C, 71.15; H, 5.77; N, 2.86; found C, 71.43; H, 5.75; N, 2.85.

(*E*)-ethyl 5-fluoro-2-((2*E*,4*Z*,6*E*)-7-(4-methoxyphenyl)-4-(pivaloyloxy)hepta-2,4,6-trien-1-ylidene)-3-oxoindoline-1-carboxylate **11n**.

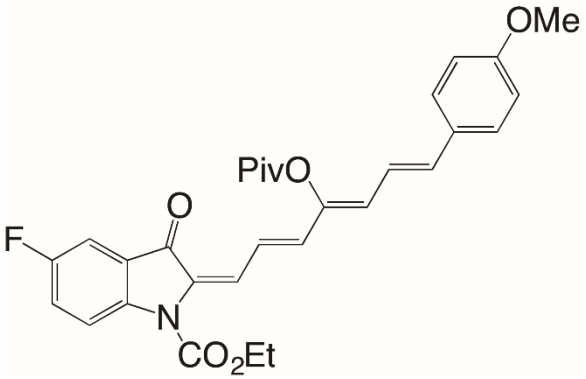

Figure 83 Chemical structure of compound **11n.**

General procedure was followed using ethyl 7-fluoro-4*H*-furo[3,2-*b*]indole-4-carboxylate **9e** (49 mg, 0.2 mmol), (*E*)-1-(4-methoxyphenyl)pent-1-en-4-yn-3-yl pivalate **10d** (109 mg, 0.4 mmol) and [Au(JohnPhos)SbF_6] (7.7 mg, 0.01 mmol) in anhydrous toluene (2+2 mL) at -20 °C for 1 h, followed by isomerization with I_2 for 4 h at rt. Purification by flash chromatography (SiO_2, dichloromethane/hexane 95:5) yielded **11n** (102 mg, 98%) as a red solid (m.p. 175.9-177.6 °C). **^{1}H NMR** (300 MHz, $CDCl_3$): 8.22 – 7.94 (m, 2H), 7.77 (d, *J* = 12.1 Hz, 1H), 7.43 (dd, *J* = 6.9, 2.7 Hz, 1H), 7.36 – 7.24 (m, 3H), 6.85 (d, *J* = 8.7 Hz, 2H), 6.76 – 6.55 (m, 3H), 6.31 (d, *J* = 9.3 Hz, 1H), 4.46 (q, *J* = 7.1 Hz, 2H), 3.81 (s, 3H), 1.57 (s, 9H), 1.48 (t, *J* = 7.2 Hz, 3H). **^{13}C NMR** (75 MHz, $CDCl_3$): 182.94 (C), 176.00 (C), 160.01 (C), 159.25 (d, *J* = 245.5 Hz, C), 151.49 (C), 145.98 (C), 142.74 (C), 137.10 (CH), 136.03 (CH), 131.92 (C), 129.75 (C), 128.86 (CH), 128.15 (2xCH), 126.05 (CH), 125.55 (d, *J* = 7.6 Hz, C), 123.87 (CH), 122.35 (d, *J* = 24.2 Hz, CH), 119.82 (CH), 118.73 (d, *J* = 7.4 Hz, CH), 114.28 (2xCH), 109.40 (d, *J* = 23.3 Hz, CH), 63.17 (CH_2), 55.28 (CH_3), 39.48 (C), 27.45 (3xCH_3), 14.38 (CH_3). **ESI(+)-MS**: *m/z* (%) = 542 (100) $[M+Na]^+$; $C_{30}H_{30}FNO_6$ [519.56]: calcd. for C, 69.35; H, 5.82; N, 2.70; found C, 69.64; H, 5.80; N, 2.69.

5.3.3.5. Preparation and characterization data for products 11o, 13a-b, 14 and 15

(1*E*,3*Z*,5*E*,7*E*)-7-(3-oxoindolin-2-ylidene)-1-phenylhepta-1,3,5-trien-4-yl pivalate **11o**.

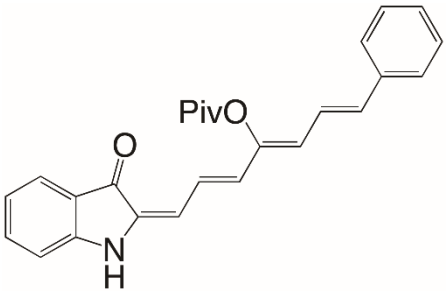

Figure 84 Chemical structure of compound **11o.**

To a solution of (*E*)-tert-butyl 3-oxo-2-((2*E*,4*Z*,6*E*)-7-phenyl-4-(pivaloyloxy)hepta-2,4,6-trien-1-ylidene)indoline-1-carboxylate **11d** (57 mg, 0.11 mmol) in dichloromethane (1 ml), trifluoroacetic acid (0.1 mL) was added. The mixture was stirred at room temperature for 2 h, then the reaction was quenched with 1 N sodium hydroxide aqueous solution and extracted with dichloromethane. The combined organic layers were dried over anhydrous sodium sulfate and concentrated under reduced pressure. The crude residue was purified by flash column chromatography (SiO_2, hexane/ethyl acetate 3:1) to yield (1*E*,3*Z*,5*E*,7*E*)-7-(3-oxoindolin-2- ylidene)-1-phenylhepta-1,3,5-trien-4-yl pivalate **11o** (30 mg, 68%) as a red solid (m.p. 198.2-200.1 °C). Alternatively, **11o** was prepared from **11a** according to the following procedure. To a solution of (*E*)-ethyl 3-oxo-2-((2*E*,4*Z*,6*E*)-7-phenyl-4-(pivaloyloxy)hepta-2,4,6-trien-1-ylidene)indoline-1-carboxylate **11a** (35 mg, 0.07 mmol) in methanol (0.7 ml), K_2CO_3 (10 mg, 0.07 mmol) was added. The mixture was stirred at 60 °C for 2 h, then the reaction extracted with ethyl acetate. The combined organic layers were dried over anhydrous sodium sulfate and concentrated under reduced pressure. The crude residue was purified by flash column chromatography (SiO_2, hexane/ethyl acetate 3:1) to yield (1*E*,3*Z*,5*E*,7*E*)-7-(3-oxoindolin-2-ylidene)-1- phenylhepta-1,3,5-trien-4-yl pivalate **11o** (8 mg, 29%). **^{1}H NMR** (300 MHz, DMSO): 10.06 (s, 1H), 7.63 – 7.23 (m, 7H), 7.06 (d, *J* = 8.0 Hz, 1H), 6.94 – 6.65 (m, 4H), 6.64 – 6.52 (m, 1H), 6.51 – 6.42 (m, 2H), 1.43 (d, *J* = 24.0 Hz, 9H). **^{13}C NMR** (75 MHz, DMSO): 185.70 (C), 175.93 (C), 152.89 (C), 146.98 (C), 136.99 (C), 136.49 (CH), 136.41 (C), 135.80 (CH),

133.25 (CH), 129.43 (2xCH), 128.92 (CH), 126.99 (2xCH), 124.47 (CH), 124.07 (CH), 123.09 (CH), 121.95 (CH), 121.16 (C), 120.00 (CH), 112.49 (CH), 110.94 (CH), 139.50 (C) 27.57 (3xCH_3). **ESI(+)-MS**: *m/z* (%) = 400 (100) $[M+H]^+$; $C_{26}H_{25}NO_3$ [399.48]: calcd. for C, 78.17; H, 6.31; N, 3.51; found C, 77.95; H, 6.30; N, 3.53.

Ethyl 3-oxo-2-(7-phenyl-4-(pivaloyloxy)heptyl)indoline-1-carboxylate **13a**.

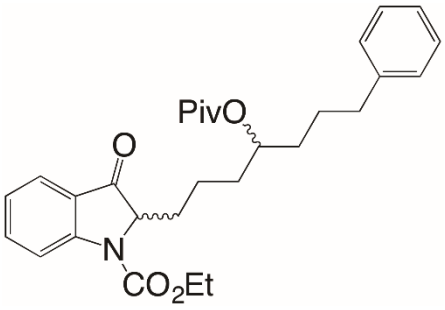

Figure 85 Chemical structure of compound **13a.**

To a solution of (*E*)-ethyl 3-oxo-2-((2*E*,4*Z*,6*E*)-7-phenyl-4-(pivaloyloxy)hepta-2,4,6-trien-1-ylidene)indoline1-carboxylate **11a** (70 mg, 0.15 mmol) in ethyl acetate, Pd/C (7 mg, 10% wt) was added. The reaction mixture was stirred under H_2 at room temperature overnight, then was filtered over a pad of celite and the solvent was evaporated under reduced pression. The crude residue was purified by flash column chromatography (SiO_2, hexane/ethyl acetate 9:1) to yield ethyl 3-oxo-2-(7-phenyl-4-(pivaloyloxy)heptyl)indoline-1-carboxylate **13a** as a mixture of two diastereoisomers (45 mg, 63%, 1:1) as a pale oil. **^{1}H NMR** (300 MHz, $CDCl_3$): 8.14 (s, 2H), 7.71 (dd, *J* = 7.7, 3.5 Hz, 2H), 7.68 – 7.58 (m, 2H), 7.33 – 7.22 (m, 4H), 7.22 – 7.08 (m, 8H), 4.86 – 4.74 (m, 2H), 4.44 – 4.22 (m, 6H), 2.67 – 2.49 (m, 4H), 2.32 – 1.96 (m, 4H), 1.66 – 1.45 (m, 12H), 1.41 (t, *J* = 7.1 Hz, 6H), 1.30 – 1.17 (m, 4H), 1.14 (s, 9H), 1.11 (s, 9H). Most signals are overlapped for two diastereoisomers. **^{13}C NMR** (75 MHz, $CDCl_3$): 199.57 (C), 199.39 (C), 178.41 (2xC), 152.42 (2xC), 142.48 (4xC), 137.46 (CH), 137.34 (CH), 128.70 (3xCH), 128.67 (3xCH), 126.13 (4xCH), 124.63 (2xC) 124.15 (CH), 124.03 (CH), 123.71 (CH), 123.64 (CH), 117.28 (CH), 117.24 (CH), 73.24 (CH), 72.93 (CH), 65.54 (2xCH), 62.80 (CH2), 62.76 (CH2), 39.16 (C), 39.14 (C), 35.97 (2x CH_2), 34.40 (CH_2), 34.30 (CH_2), 34.13 (CH_2), 33.98 (CH_2), 31.14 (CH_2), 30.98 (CH_2), 27.52 (3xCH_3), 27.50 (3xCH_3), 27.32 (CH_2), 27.28 (CH_2), 19.29 (CH_2), 19.02 (CH_2), 14.92 (CH_3), 14.90 (CH_3). **ESI(+)-MS**: *m/z* (%) = 502 (100) $[M+Na]^+$; $C_{29}H_{37}NO_5$ [479.27].

Tert-butyl 3-oxo-2-(7-phenyl-4-(pivaloyloxy)heptyl)indoline-1-carboxylate **13b**.

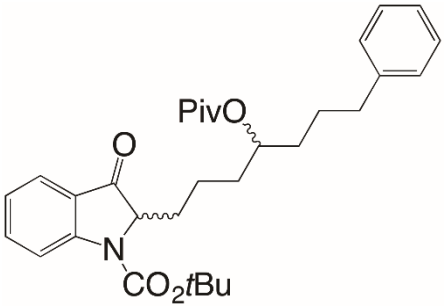

Figure 86 Chemical structure of compound **13b.**

To a solution of (*E*)-tert-butyl 3-oxo-2-((2*E*,4*Z*,6*E*)-7-phenyl-4-(pivaloyloxy)hepta-2,4,6-trien-1-ylidene)indoline-1-carboxylate **11d** (88 mg, 0.17 mmol) in ethyl acetate, Pd/C (9 mg, 10% wt) was added. The reaction mixture was stirred under H_2 at room temperature overnight, then was filtered

over a pad of celite and the solvent was evaporated under reduced pression. The crude residue was purified by flash column chromatography (SiO_2, hexane/ethyl acetate 9:1 to 8:2) to yield **13b** as a mixture of two diastereoisomers (41 mg, 47%, 1:1) as a yellow oil. **^{1}H NMR** (300 MHz, $CDCl_3$): 8.09 (bs, 2H), 7.71 – 7.64 (m, 2H), 7.60 (ddd, *J* = 8.5, 7.3, 1.4 Hz, 2H), 7.30 – 7.21 (m, 4H), 7.19 – 7.04 (m, 8H), 4.85 – 4.72 (m, 2H), 4.23 (bs, 2H), 2.60 – 2.51 (m, 4H), 2.16 – 2.00 (m, 4H), 1.64 – 1.43 (m, 34H), 1.11 (s, 9H), 1.08 (s, 9 H). Most signals are overlapped for two diastereoisomers. **^{13}C NMR** (75 MHz, $CDCl_3$): 199.28 (2xC), 177.98 (2xC), 150.88 (2xC), 142.08 (2xC), 136.93 (2xCH), 128.29 (3xCH), 128.25 (3xCH), 125.70 (4xCH), 124.16 (2xC), 123.67 (CH), 123.58 (CH), 122.95 (CH), 122.89 (CH), 116.85 (CH), 116.75 (CH), 82.42 (2xC), 72.90 (CH), 72.82 (CH), 65.21 (2xCH), 38.74 (2xC), 35.58 (2xCH_2), 34.09 (CH_2), 34.02 (CH_2), 33.57 (2xCH_2), 30.84 (2xCH_2), 28.32 (6xCH_3), 27.11 (3xCH_3), 27.08 (3xCH_3), 26.86 (2xCH_2), 18.92 (CH_2), 18.82(CH_2). 2 quaternary carbons are missing, probably overlapped. **ESI(+)-MS**: *m/z* (%) = 530 (100) $[M+Na]^+$; $C_{31}H_{41}NO_5$ [507.66].

Ethyl 2-(2-methyl-3-((1*Z*,3*E*)-4-phenyl-1-(pivaloyloxy)buta-1,3-dien-1-yl)cyclopropyl)-1H-indole-1-carboxylate **14**.

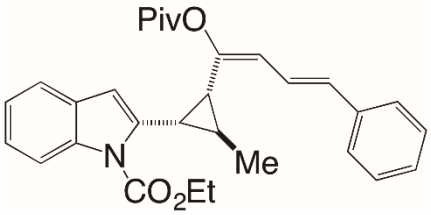

Figure 87 Chemical structure of compound **14.**

To a N_2-flushed solution of (*E*)-ethyl 2-(prop-1-en-1-yl)-1*H*-indole-1-carboxylate **9f** (46 mg, 0.2 mmol) and [Au(JohnPhos)SbF_6] (5 mol%) in anhydrous toluene (2 mL), (*E*)-1-phenylpent-1-en-4-yn-3-yl pivalate **10a** (97 mg, 0.4 mmol) in toluene (2 mL, final concentration 0.05 M) was added dropwise at -20 °C. The reaction mixture was stirred for 1 h at -20 °C and then quenched with PPh_3 (15 mol%). Purification by flash chromatography (SiO_2, hexane/ ethyl acetate 98:2) yielded **14** (41 mg, 43%) as a yellow oil. **^{1}H NMR** (300 MHz, CD_2Cl_2): 7.99 (d, *J* = 8.3 Hz, 1H), 7.55 – 7.44 (m, 3H), 7.42 – 7.34 (m, 2H), 7.31 – 7.10 (m, 4H), 6.46 (d, *J* = 15.6 Hz, 1H), 6.37 (s, 1H), 5.89 (d, *J* = 11.3 Hz, 1H), 4.43 – 4.18 (m, 2H), 2.89 (dd, *J* = 8.1, 6.4 Hz, 1H), 2.35 (dd, *J* = 8.6, 5.6 Hz, 1H), 1.77 (m, 1H), 1.46 – 1.27 (m, 6H), 1.12 (s, 9H). **^{13}C NMR** (75 MHz, CD_2Cl_2): 176.28(C), 151.80 (C), 148.19 (C), 139.13 (C), 137.63 (C), 136.42 (C), 131.81 (CH), 129.09 (C),128.55 (2xCH), 127.35 (CH), 126.27 (2xCH), 123.41 (CH), 123.24 (CH), 122.61 (CH), 120.37 (CH), 119.79 (CH), 115.42 (CH), 107.60 (CH), 63.06 (CH_2), 38.68 (C), 29.00 (CH), 27.95 (CH), 26.70 (3xCH_3), 19.65 (CH), 17.74 (CH_3), 13.99 (CH_3). **ESI(+)-MS**: *m/z* (%) = 494 (100) $[M+Na]^+$; $C_{30}H_{33}NO_4$ [471.59]: calcd. for C, 76.41; H, 7.05; N, 2.97; found C, 76.25; H, 7.02; N, 2.98.

Ethyl 2-methyl-3-((1*Z*,4*E*)-5-phenyl-2-(pivaloyloxy)penta-1,4-dien-1-yl)-1*H*-indole-1-carboxylate **15**.

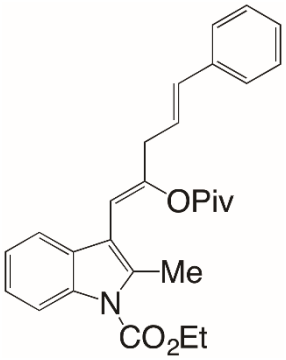

Figure 88 Chemical structure of compound **15.**

To a N_2-flushed solution of (*E*)-ethyl 2-(prop-1-en-1-yl)-1*H*-indole-1-carboxylate **9g** (46 mg, 0.2 mmol) and [Au(JohnPhos)SbF_6] (5 mol%) in anhydrous toluene (2 mL), (*E*)-1-phenylpent-1-en-4-yn-3-yl pivalate **10a** (97 mg, 0.4 mmol) in toluene (2 mL, final concentration 0.05 M) was added dropwise at -20 °C. The reaction mixture was stirred for 1 h at -20 °C and then quenched with PPh_3 (15 mol%). Purification by flash chromatography (SiO_2, hexane/ ethyl acetate 98:2) yielded **15** (44 mg, 50%) as a yellow oil. **^{1}H NMR** (300 MHz, C_6D_6): 8.52 (dd, *J* = 7.0, 1.8 Hz, 1H), 7.81 (dd, *J* = 6.5, 2.2 Hz, 1H), 7.53 – 6.90 (m, 7H), 6.58 (d, *J* = 15.7 Hz, 1H), 6.35 (dt, *J* = 15.8, 7.0 Hz, 1H), 6.09 (s, 1H), 4.08 (q, *J* = 7.1 Hz, 2H), 3.47 (d, *J* = 7.0 Hz, 2H), 2.65 (s, 3H), 1.16 – 0.88 (m, 12H). **^{13}C NMR** (75 MHz, C_6D_6): 175.46 (C), 151.78 (C), 151.07 (C), 137.39 (C), 136.09 (C), 134.69 (C), 133.53 (CH), 129.47 (C),128.64 (3xCH), 126.37 (2xCH), 125.15 (CH), 123.84 (CH), 122.90 (CH), 119.99 (CH), 115.72 (CH), 114.21 (C), 108.30 (CH), 62.47 (CH_2), 38.68 (C), 37.62 (CH_2), 26.75 (3xCH_3), 14.90 (CH_3), 13.75 (CH_3). **ESI(+)-MS**: *m/z* (%) = 446 (100) $[M+H]^+$; $C_{28}H_{31}NO_4$ [445.55].

5.3.3.6. UV-Vis analysis for compound 11a, 11'a, 11d and 11'd

The determination of UV-Vis spectra was made for compounds **11a**, **11'a**, **11d** and **11'd**. In order to obtain the UV-Vis spectra, standard solution with 2.35 mg of **11a** and **11'a** in 10 mL volumetric flask and 1.25 mg of **11d** and **11'd** in 5 mL volumetric flask were prepared in toluene, thetrahydrofuran and dimethyl sulfoxide. The standard solutions were used for the preparation of $1\cdot10^{-5}$M, $2\cdot10^{-5}$ M, $4\cdot10^{-5}$ M, $5\cdot10^{-5}$ M and $1\cdot10^{-4}$ M solutions of each compound. The extinction coefficients were determined using Lambert-Beer law after the determination of UV-Vis spectra using Agilent 1453E and open top UV quartz cell, 10 mm, 3.0 ml vol. In the conversion experiments, two solutions of pure **11'a** and **11'd** at the concentration of $2\cdot10^{-5}$ M in dimethyl sulfoxide were prepared. Experiments were conducted in a rotaflo equipped quartz cuvette and the cuvette was irradiated with a 200 W lamp for a period of 6h. Measurements have been taken every 20 minutes to monitor the isomerization. Relative concentrations of E and Z isomers in the reaction mixture were calculated using Lambert-Beer law by the following equation (1):

$$[\boldsymbol{E}]_t = \frac{\boldsymbol{A_t - E_z C_0}}{\varepsilon_{\boldsymbol{E}} - \varepsilon_{\boldsymbol{Z}}} \qquad (14)$$

Where:

$[E]_t$ = concentration of the E isomer at time t;

A_t = Absorbance at time t at 354 nm;

ε_Z = molar extinction coefficient for the isomer Z at 354 nm;

ε_E = molar extinction coefficient for the isomer E at 354 nm;

C_0 = starting concentration of **11'a** or **11'd**, respectively

5.3.4. Synthesis of 2-alkenylidene-3-oxoindolines: cascade reactions of 4H-furo[3,2-*b*]indoles with diazoacetates catalysed by a Cu(I) macrocyclic pyridine-containing ligand (PcL) complex

4*H*-furo[3,2-*b*]indole compounds **16a-e,g**[212] and methyl 2-diazo-2-phenylacetate[218,219,213,220,221] are known compounds and were prepared according to literature procedures

$Rh_2(Oct)_4$, JohnPhosAuSbF$_6$, IPrAuCl, $Cu(OTf)_2$ were purchased from commercial suppliers and used as received, while $(ArO)_3PAuNTf_2$[214,222] and [Cu(OTf)]-Np-Pc-L[199] were prepared following literature procedures.

5.3.4.1. Preparation and characterization data for ethyl 4H-furo[3,2-b]indole-4-carboxylates 16f,h

2-(furan-2-yl)-5-methoxyaniline.

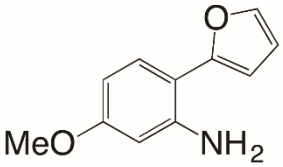

Figure 89 Chemical structure of 2-(furan-2-yl)-5-methoxyaniline.

To a N_2-flushed solution of furan-2-ylboronic acid (1.24 g, 11.1 mmol), potassium carbonate (4.10 g, 29.7 mmol), $PdCl_2(PPh_3)_2$ (260 mg, 0.37 mmol) in DMF (33 mL) and water (7.5 mL), 2-bromo-5-methoxyaniline (1.5 mg, 7.4 mmol) was added. The reaction mixture was heated at reflux for 3 h and then cooled at room temperature. The mixture was diluted with water and extracted with ethyl acetate. The organic layer was washed with brine, dried over Na_2SO_4 and the solvent concentrated under reduced pression. The crude was purified by flash column chromatography (SiO_2, hexane/ethyl acetate 95:5) to yield 2-(furan-2-yl)-5-methoxyaniline (1.04 g, 74%) as brownish oil. **^{1}H NMR** (300 MHz, $CDCl_3$): 7.49 (dd, *J* = 1.7, 0.6 Hz, 1H), 7.41 (d, *J* = 8.6 Hz, 1H), 6.51 (dd, *J* = 3.3, 1.8 Hz, 1H), 6.48 (dd, *J* = 3.3, 0.5 Hz, 1H), 6.41 (dd, *J* = 8.6, 2.5 Hz, 1H), 6.30 (d, *J* = 2.5 Hz, 1H), 4.25 (bs, 2H), 3.81 (s, 3H). **^{13}C NMR** (75 MHz, $CDCl_3$): 160.39 (C), 153.56 (C), 144.78 (C), 140.77 (CH), 129.08 (CH), 111.26 (CH), 109.84 (C), 105.17 (CH), 104.75 (CH), 101.45 (CH), 55.17 (CH_3). **ESI(+)-MS**: m/z (%) = 190 (100) $[M+H]^+$; $C_{11}H_{11}NO_2$ [189.21]: calcd. for: C, 69.83; H, 5.86; N, 7.40; found: C, 69.65; H, 5.88; N, 7.37.

2-(2-azido-4-methoxyphenyl)furan.

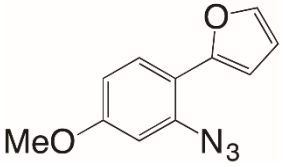

Figure 90 Chemical structure of 2-(2-azido-4-methoxyphenyl)furan.

To a solution of 2-(furan-2-yl)-5-methoxyaniline (980 g, 5.17 mmol) in CH_3CN (10 mL) at 0 °C, *t*-BuONO (801 Mg, 7.77 mmol) was added, followed by $TMSN_3$ (895 Mg, 7.77) dropwise. The resulting solution was stirred at room temperature for 1 h and then concentrated in vacuum. The crude was purified by flash column chromatography (SiO_2, hexane 100%) to yield 2-(2-azido-4-methoxyphenyl)furan (614 Mg, 55%) as brownish oil. **^{1}H NMR** (300 MHz, $CDCl_3$): 7.75 (m, 1H), 7.43 (dd, *J* = 1.8, 0.7 Hz, 1H), 6.90 (dd, *J* = 3.4, 0.7 Hz, 1H), 6.81 – 6.70 (m, 2H), 6.48 (dd, *J* = 3.4, 1.8 Hz, 1H), 3.85 (s, 3H). **^{13}C NM**R (75 MHz, $CDCl_3$): 159.57 (C), 149.76 (C), 141.10 (CH), 136.32 (C), 128.11 (CH), 115.95 (C), 111.54 (CH), 110.71 (CH), 108.47 (CH), 104.59 (CH), 55.47 (CH_3). **ESI(+)-MS**: $C_{11}H_9N_3O_2$ [215.21]: calcd. for: C, 61.39; H, 4.22; N, 19.53; found: C, 61.57; H, 4.20; N, 19.48.

6-methoxy-4*H*-furo[3,2-*b*]indole.

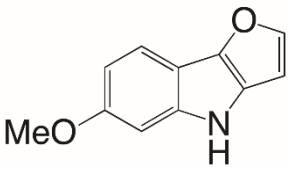

Figure 91 Chemical structure of 6-methoxy-4H-furo[3,2-*b*]indole

A solution of 2-(2-azido-4-methoxyphenyl)furan (590 Mg, 2.74 mmol) in 1,2-dichlorobenzene (2 mL) was added dropwise to 1,2-dichlorobenzene (4 mL) heated at 160 °C. The reaction mixture was stirred for 1 h. Then solvent was concentrated under reduced pression. The crude was purified by flash column chromatography (SiO_2, hexane/ ethyl acetate 95:5) to yield 6-methoxy-4*H*-furo[3,2-*b*]indole (138 mg, 27%) as brownish oil. **^{1}H NMR** (300 MHz, $CDCl_3$): 7.60 (d, *J* = 8.6 Hz, 1H), 7.53 (bs, 1H), 7.48 (d, *J* = 2.1 Hz, 1H), 6.89 (d, *J* = 2.1 Hz, 1H), 6.84 (dd, *J* = 8.6, 2.1 Hz, 1H), 6.55 (d, *J* = 2.1 Hz, 1H), 3.86 (s, 3H).
^{13}C NMR (75 MHz, CDC_3): 156.02 (C), 144.62 (CH), 142.46 (C), 141.04 (C), 128.93 (C), 116.77 (CH), 109.56 (C), 108.89 (CH), 99.50 (CH), 96.61 (CH), 55.70 (CH_3).
ESI(+)-MS: m/z (%) = 188 (100) $[M+H]^+$; $C_{11}H_9NO_2$ [187.19]: calcd. for: C, 70.58; H, 4.85; N, 7.48; found: C, 70.84; H, 4.86; N, 7.45.

Ethyl 6-methoxy-4*H*-furo[3,2-*b*]indole-4-carboxylate **16f**.

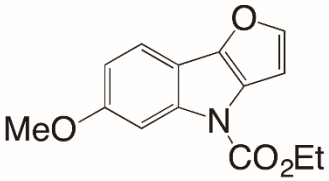

Figure 92 Chemical structure of compound **16f**.

To a N_2-flushed solution of 6-methoxy-4*H*-furo[3,2-*b*]indole (98 mg, 0.52 mmol) in tetrahydrofuran (5 mL), a solution of *n*-butyllithium (1.6 M in hexane, 362 µL, 0.58 mmol), was added dropwise at -78 °C. The reaction mixture was stirred for 30 minutes. Ethyl chloroformate (75 µL, 0.78 mmol) was added dropwise and the reaction was brought to room temperature and stirred for 2 h before of being quenched with ammonium chloride saturated solution. The organic layer was extracted with ethyl acetate, dried over Na_2SO_4 and the solvent concentrated under reduced pression. The crude was purified by flash column chromatography (SiO_2, hexane/ethyl acetate 98:2) to yield **16f** (114 mg, 85%) as orange solid (m.p. 70-72 °C). **^{1}H NMR** (300 MHz, $CDCl_3$): 7.94 (bs, 1H), 7.52 (d, *J* = 8.6 Hz, 1H), 7.46 (d, *J* = 2.0 Hz, 1H), 6.92 (dd, *J* = 8.6, 2.0 Hz, 1H), 6.76 (s, 1H), 4.50 (q, *J* = 7.1 Hz, 2H), 3.89 (s, 3H), 1.50 (t, *J* = 7.1 Hz, 3H). **^{13}C NMR** (75 MHz, $CDCl_3$): 157.40 (C), 151.10 (C), 144.62 (CH), 143.54 (C), 139.97 (C), 128.19 (C), 116.76 (CH), 112.33 (C), 111.71 (CH), 103.12 (CH), 101.40 (CH), 62.92 (CH_2), 55.68 (CH_3), 14.40 (CH_3).
ESI(+)-MS: m/z (%) = 260 (100) $[M+H]^+$; $C_{14}H_{13}NO_4$ [259.26]: calcd. for: C, 64.86; H, 5.05; N, 5.40; found: C, 64.71; H, 5.03; N, 5.42.

5-fluoro-2-(furan-2-yl)aniline.

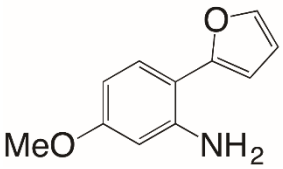

Figure 93 Chemical structure of 5-fluoro-2-(furan-2-yl)aniline.

To a N_2-flushed solution of furan-2-ylboronic acid (1.32 g, 11.8 mmol), potassium carbonate (4.36 g, 31.5 mmol), $PdCl_2(PPh_3)_2$ (276 mg, 0.39 mmol) in DMF (35 mL) and water (8 mL), 2-bromo-5-fluoroaniline (1.50 mg, 7.89 mmol) was added. The reaction mixture was heated at reflux for 3 h and then cooled at room temperature. The mixture was diluted with water and extracted with ethyl acetate. The organic layer was washed with brine, dried over Na_2SO_4 and the solvent concentrated under reduced pression. The crude was purified by flash column chromatography (SiO_2, hexane/ethyl acetate 95:5) to yield 5-fluoro-2-(furan-2-yl)aniline (1.21 g, 87%) as yellow oil. **^{1}H NMR** (300 MHz, $CDCl_3$): 7.48 (t, *J* = 1.2 Hz, 1H), 7.39 (dd, *J* = 8.6, 6.4 Hz, 1H), 6.59 – 6.33 (m, 3H), 4.43 (bs, 2H). **^{13}C NMR** (75 MHz, $CDCl_3$): 163.29 (d, *J* = 245.4 Hz, C), 152.76 (C), 145.10 (d, *J* = 10.9 Hz, C), 141.24 (CH), 129.43 (d, *J* = 10.1 Hz, CH), 112.54 (d, *J* = 2.5 Hz, C), 111.31 (CH), 106.12 (CH),105.39 (d, *J* = 22.1 Hz, CH), 102.87 (d, *J* = 24.8 Hz, CH).
ESI(+)-MS: m/z (%) = 178 (100) $[M+H]^+$; $C_{10}H_8FNO$ [177.18]: calcd. for: C, 67.79; H, 4.55; N, 7.91; found: C, 67.97; H, 4.56; N, 7.09.

2-(2-azido-4-fluorophenyl)furan.

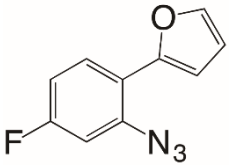

Figure 94 Chemical structure of 2-(2-azido-4-fluorophenyl)furan.

To a solution of 5-fluoro-2-(furan-2-yl)aniline (1.18 g, 6.65 mmol) in CH_3CN (13 mL) at 0 °C, *t*-BuONO (1.03 g, 9.97 mmol) was added, followed by $TMSN_3$ (1.15 g, 9.97) dropwise. The resulting solution was stirred at room temperature for 1 h and then concentrated in vacuum. The crude was purified by flash column chromatography (SiO_2, hexane 100%) to yield 2-(2-azido-4-fluorophenyl)furan (1.02 g, 76%) as brownish oil. **^{1}H NMR** (300 MHz, $CDCl_3$): 7.80 (m, 1H), 7.46 (dd, *J* = 1.8, 0.7 Hz, 1H), 6.99 (m, 1H), 6.96 – 6.86 (m, 2H), 6.50 (dd, *J* = 3.4, 1.8 Hz, 1H). **^{13}C NMR** (75 MHz, $CDCl_3$): 162.05 (d, *J* = 249.4 Hz, C), 148.90 (C), 141.69 (CH), 136.69 (d, *J* = 8.3 Hz, C), 128.40 (d, *J* = 9.0 Hz, CH), 119.02 (C), 112.24 (d, *J* = 21.6 Hz, CH), 111.68 (CH), 109.76 (CH), 106.12 (d, *J* = 25.2 Hz, CH). **ESI(+)-MS**: $C_{10}H_6FN_3O$ [203.18]: calcd. for: C, 59.12; H, 2.98; N, 20.68; found: C, 59.04; H, 2.99; N 20.66.

6-fluoro-4*H*-furo[3,2-*b*]indole.

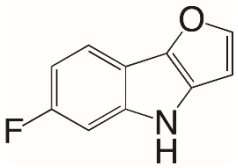

Figure 95 Chemical structure of 6-fluoro-4H-furo[3,2-b]indole.

A solution of 2-(2-azido-4-fluorophenyl)furan (983 mg, 4.84 mmol) in 1,2-dichlorobenzene (3.5 mL) was added dropwise to 1,2-dichlorobenzene (7 mL) heated at 160 °C. The reaction mixture was

stirred for 1 h. Then solvent was concentrated under reduced pression. The crude was purified by flash column chromatography (SiO_2, hexane/ ethyl acetate 95:5) to yield 6-fluoro-4*H*-furo[3,2-*b*]indole (650 mg, 76%) as brownish oil. **^{1}H NMR** (300 MHz, $CDCl_3$): 7.77 – 7.61 (m, 2H), 7.54 (d, *J* = 2.0 Hz, 1H), 7.10 (dd, *J* = 9.8, 2.2 Hz, 1H), 6.97 (td, *J* = 9.2, 2.2 Hz, 1H), 6.59 (d, *J* = 2.0 Hz, 1H). **^{13}C NMR** (75 MHz, $CDCl_3$): 159.38 (d, *J* = 238.1 Hz, C), 145.52 (CH), 142.03 (C), 140.00 (d, *J* = 11.9 Hz, C), 130.21 (C), 116.77 (d, *J* = 10.0 Hz, CH), 111.55 (C), 108.24 (d, *J* = 24.5 Hz, CH), 99.54 (CH), 98.95 (d, *J* = 26.6 Hz, CH). **ESI(+)-MS**: m/z (%) = 176 (100) $[M+H]^+$; $C_{10}H_6FNO$ [175.16]: calcd. for: C, 68.57; H, 3.45; N, 8.00; found: C, 68.48; H, 3.46; N, 8.02.

Ethyl 6-fluoro-4*H*-furo[3,2-*b*]indole-4-carboxylate **16h**.

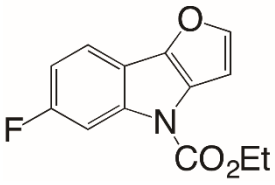

Figure 96 Chemical structure of compound **16h**.

To a N_2-flushed solution of 6-fluoro-4*H*-furo[3,2-*b*]indole (538 mg, 3.07 mmol) in tetrahydrofuran (30 mL), a solution of *n*-butyllithium (1.6 M in hexane, 2.1 mL, 3.36 mmol), was added dropwise at -78 °C. The reaction mixture was stirred for 30 minutes. Ethyl chloroformate (728 µL, 4.58 mmol) was added dropwise and the reaction was brought to room temperature and stirred for 2 h before of being quenched with ammonium chloride saturated solution. The organic layer was extracted with ethyl acetate, dried over Na_2SO_4 and the solvent concentrated under reduced pression. The crude was purified by flash column chromatography (SiO_2, hexane/ethyl acetate 98:2) to yield **16h** (672 mg, 89%) as orange solid (m.p. 53-55 °C). **^{1}H NMR** (300 MHz, $CDCl_3$): 8.07 (bs, 1H), 7.57 (dd, *J* = 8.6, 5.4 Hz, 1H), 7.52 (d, *J* = 2.0 Hz, 1H), 7.06 (td, *J* = 8.9, 2.4 Hz, 1H), 6.80 (s, 1H), 4.53 (q, *J* = 7.1 Hz, 2H), 1.52 (t, *J* = 7.1 Hz, 3H). **^{13}C NMR** (75 MHz, $CDCl_3$) : 160.27 (d, *J* = 240.9 Hz, C), 150.82 (C), 145.58 (CH), 142.87 (C), 139.07 (C), 129.57 (C), 116.78 (d, *J* = 9.7 Hz, CH), 114.64 (C), 111.20 (d, *J* = 24.3 Hz, CH), 104.23 (d, *J* = 29.2 Hz, CH), 103.08 (CH), 63.30 (CH_2), 14.41 (CH_3). **ESI(+)-MS**: m/z (%) = 248 (100) $[M+H]^+$; $C_{13}H_{10}FNO_3$ [247.23]: calcd. for: C, 63.16; H, 4.08; N, 5.67; found: C, 63.39; H, 4.08; N, 5.68.

5.3.4.2. Preparation and characterization data for product 17a-m

General procedure

To a N_2-flushed solution of 4*H*-furo[3,2-*b*]indole **16** (0.2 mmol, 1 equiv), [Cu(OTf)]Np-Pc-L (8 mol%) and 4 Å molecular sieves (200 mg) in anhydrous toluene (1 mL), a solution of diazo compound (1.5 equiv.) in anhydrous toluene (2 mL) was added dropwise in 2 h with a syringe pump at room temperature. Then, the solvent was removed under reduced pression and the crude residue was purified by flash column chromatography to yield the desired product **17**.

Ethyl (*E*)-2-((*Z*)-4-ethoxy-4-oxobut-2-en-1-ylidene)-3-oxoindoline-1-carboxylate **17'a**.

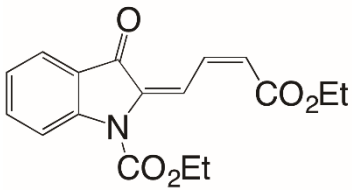

Figure 97 Chemical structure of compound **17'a**.

To a N_2-flushed solution of ethyl 4*H*-furo[3,2-*b*]indole-4-carboxylate **16a** (45.8 mg, 0.2 mmol), [$Cu^{(I)}$(PcL)] (13.8 mg, 0.016 mmol),and 4 Å molecular sieves (200 mg) in anhydrous toluene (1 mL), a solution of ethyl 2-diazoacetate (34.2 mg, 0.3 mmol) in anhydrous DCE (2 mL) was added dropwise in 2 h with a syringe pump at room temperature. The crude residue was purified by flash column chromatography (SiO_2, hexane/ethyl acetate 95:5) to yield **17'a** (62.5 mg, 25%) as a yellow solid with an inseparable impurity probably deriving from the dimerization of diazo compound. (Reaction of the screening, entry 8). **^{1}H NMR** (300 MHz, $CDCl_3$): 9.02 (dd, *J* = 12.1, 1.2 Hz, 1H), 8.45 (t, *J* = 11.7 Hz, 1H), 8.09 (d, *J* = 8.4 Hz, 1H), 7.79 (d, *J* = 6.8 Hz, 1H), 7.62 (t, *J* = 7.9 Hz, 1H), 7.23 (m, 1H), 6.05 (dd, *J* = 11.4, 1.2 Hz, 1H), 4.51 (m, 2H), 4.24 (qd, *J* = 7.1, 3.7 Hz, 2H, overlapped with the impurity), 1.52 (t, *J* = 7.1 Hz, 3H), 1.39 – 1.16 (m, 3H, overlapped with impurity). **^{13}C NMR** (75 MHz, $CDCl_3$): 185.16 (C), 165.75 (C), 151.60 (C), 147.90 (C), 137.27 (CH), 136.31 (CH), 135.08 (C), 129.74 (CH), 124.73 (CH), 124.13 (CH), 123.73 (C), 121.64 (CH), 117.28 (CH),63.52 (CH_2), 60.22 (CH_2), 14.25 (CH_3), 14.21 (CH_3). **ESI(+)-MS**: m/z (%) = 316 (100) $[M+H]^+$; $C_{17}H_{17}NO_5$ [315.33]: calcd. for: C, 64.75; H, 5.43; N, 4.44; found: C, 64.56; H, 5.43; N, 4.45.

Ethyl (*E*)-2-((*E*)-4-ethoxy-4-oxobut-2-en-1-ylidene)-3-oxoindoline-1-carboxylate **17a**.

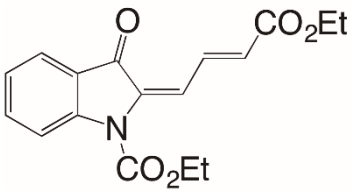

Figure 98 Chemical structure of compound **17a**.

General procedure was followed using ethyl 4*H*-furo[3,2-*b*]indole-4-carboxylate **16a** (45.8 mg, 0.2 mmol), [$Cu^{(I)}$(PcL)] (13.8 mg, 0.016 mmol), ethyl 2-diazoacetate (34.2 mg, 0.3 mmol) in anhydrous DCE (1+2 mL). Purification by flash chromatography (SiO_2, hexane/ethyl acetate 95:5) yielded **17a** (62.5 mg, 99%) as a yellow solid (m.p. 99-102 °C). **^{1}H NMR** (300 MHz, CD_2Cl_2): 8.92 (dd, *J* = 15.4, 12.0 Hz, 1H), 8.04 (m, 1H), 7.79 (ddd, *J* = 7.6, 1.5, 0.7 Hz, 1H), 7.73 (dd, *J* = 12.0, 1.0 Hz, 1H), 7.65 (m, 1H), 7.26 (td, *J* = 7.6, 0.8 Hz, 1H), 6.25 (dd, *J* = 15.4, 1.0 Hz, 1H), 4.49 (q, *J* = 7.1 Hz, 2H), 4.25 (q, *J* = 7.1 Hz, 2H), 1.49 (t, *J* = 7.1 Hz, 3H), 1.34 (t, *J* = 7.1 Hz, 3H). **^{13}C NMR** (75 MHz, CD_2Cl_2): 184.51 (C), 166.11 (C), 151.56 (C), 147.62 (C), 137.83 (CH), 136.31 (CH), 135.19 (C), 129.33 (CH), 124.23 (CH), 124.00 (CH), 123.60 (C), 123.27 (CH), 117.28 (CH), 63.51 (CH_2), 60.55 (CH_2), 14.08 (CH_3), 14.03 (CH_3). **EI(+)-HRMS**: m/z (%) = calcd for $C_{17}H_{17}NO_5$: 315.110673, found: 315.110760 (40) $[M]^+$

tert-butyl (*E*)-2-((*E*)-4-ethoxy-4-oxobut-2-en-1-ylidene)-3-oxoindoline-1-carboxylate **17b**.

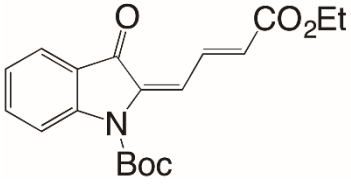

Figure 99 Chemical structure of compound **17b**.

General procedure was followed using *tert*-butyl 4*H*-furo[3,2-*b*]indole-4-carboxylate **16b** (51.5 mg, 0.2 mmol), [$Cu^{(I)}$(PcL)] (13.8 mg, 0.016 mmol), ethyl 2-diazoacetate (34.2 mg, 0.3 mmol) in anhydrous DCE (1+2 mL). Purification by flash chromatography (SiO_2, hexane/ethyl acetate 95:5)

yielded **17b** (47.0 mg, 68%) as a yellow solid (m.p. 128-131 °C). **^{1}H NMR** (300 MHz, $CDCl_3$): 8.99 (m, 1H), 8.02 (d, *J* = 8.3 Hz, 1H), 7.81 (d, *J* = 7.3 Hz, 1H), 7.71 (d, *J* = 12.0 Hz, 1H), 7.62 (t, *J* = 7.6 Hz, 1H), 7.24 (m, 1H overlapped with $CDCl_3$), 6.22 (d, *J* = 15.4 Hz, 1H), 4.28 (q, *J* = 6.8 Hz, 2H), 1.71 (s, 9H), 1.36 (t, *J* = 6.8 Hz, 3H). **^{13}C NMR** (75 MHz, $CDCl_3$): 184.71 (C), 166.33 (C), 150.23 (C), 147.93 (C), 138.32 (CH), 136.23 (CH), 135.33 (C), 129.37 (CH), 124.24 (CH), 124.08 (CH), 123.67 (CH), 123.60 (C), 117.25 (CH), 84.83 (C), 60.61 (CH_2), 28.28 (3xCH_3), 14.28 (CH_3). **ESI(+)-HRMS**: m/z (%) = calcd for $C_{19}H_{21}NO_5$: 343.141973, found: 343.141340 (60) $[M]^+$.

Ethyl (*E*)-4-((*E*)-1-methyl-3-oxoindolin-2-ylidene)but-2-enoate 17c.

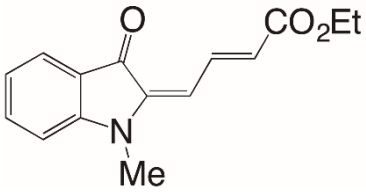

Figure 100 Chemical structure of compound **17c**.

General procedure was followed using 4-methyl-4*H*-furo[3,2-*b*]indole **16c** (34.2 mg, 0.2 mmol), $[Cu^{(I)}(PcL)]$ (13.8 mg, 0.016 mmol), ethyl 2-diazoacetate (34.2 mg, 0.3 mmol) in anhydrous DCE (1+2 mL). Purification by flash chromatography (SiO_2, hexane/ethyl acetate 9:1) yielded **17c** (39.5 mg, 77%) as a purple solid (m.p. 150-152 °C). **^{1}H NMR** (300 MHz, $CDCl_3$): 8.84 (dd, *J* = 15.3, 12.0 Hz, 1H), 7.66 (d, *J* = 7.5 Hz, 1H), 7.49 (t, *J* = 7.7 Hz, 1H), 7.00 – 6.78 (m, 2H), 6.10 – 5.95 (m, 2H), 4.26 (q, *J* = 7.1 Hz, 2H), 3.27 (s, 3H), 1.35 (t, *J* = 7.1 Hz, 3H). **^{13}C NMR** (75 MHz, $CDCl_3$): 185.99 (C), 166.87 (C), 152.73 (C), 139.36 (C), 138.48 (CH), 136.36 (CH), 124.91 (CH), 124.30 (CH), 121.15 (C), 120.17 (CH), 110.45 (CH), 108.73 (CH), 60.36 (CH_2), 28.63 (CH_3), 14.35 (CH_3). **ESI(+)-HRMS**: m/z (%) = calcd for $C_{15}H_{15}NO_3$: 257.105194, found: 257.105930 (45) $[M]^+$.

Ethyl (*E*)-2-((*E*)-4-ethoxy-4-oxobut-2-en-1-ylidene)-5-methoxy-3-oxoindoline-1-carboxylate **17d**.

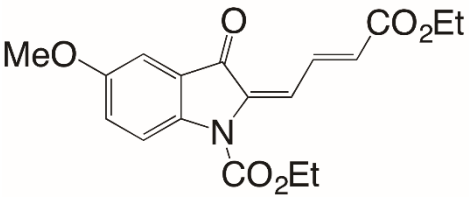

Figure 101 Chemical structure of compound **17d**.

General procedure was followed using ethyl 7-methoxy-4*H*-furo[3,2-*b*]indole-4-carboxylate **16d** (51.8 mg, 0.2 mmol), $[Cu^{(I)}(PcL)]$ (13.8 mg, 0.016 mmol), ethyl 2-diazoacetate (34.2 mg, 0.3 mmol) in anhydrous DCE (1+2 mL). Purification by flash chromatography (SiO_2, hexane/ethyl acetate 95:5) yielded **17d** (50.0 mg, 73%) as a yellow solid (m.p. 155-157 °C). **^{1}H NMR** (300 MHz, $CDCl_3$): 8.96 (m, 1H), 7.91 (d, *J* = 8.7 Hz, 1H), 7.72 (d, *J* = 11.9 Hz, 1H), 7.32 – 7.13 (m, *J* = 15.0 Hz, 2H), 6.24 (d, *J* = 15.4 Hz, 1H), 4.49 (m, 2H), 4.28 (m, 2H), 3.86 (s, 3H), 1.50 (t, *J* = 6.8 Hz, 3H), 1.36 (t, *J* = 6.7 Hz, 3H). **^{13}C NMR** (75 MHz, $CDCl_3$): 184.32 (C), 166.29 (C), 156.74 (C), 151.50 (C), 141.97 (C), 138.14 (CH), 135.53 (C), 129.62 (CH), 124.82 (CH), 124.45 (C), 123.97 (CH), 118.51 (CH), 105.63 (CH), 63.30 (CH_2), 60.63 (CH_2), 55.80 (CH_3), 14.37 (CH_3), 14.27 (CH_3). **ESI(+)-HRMS**: m/z (%) = calcd for $C_{18}H_{19}NO_6$: 345.121238, found: 345.121340 (60) $[M]^+$.

Ethyl (*E*)-2-((*E*)-4-ethoxy-4-oxobut-2-en-1-ylidene)-5-methyl-3-oxoindoline-1-carboxylate **17e**.

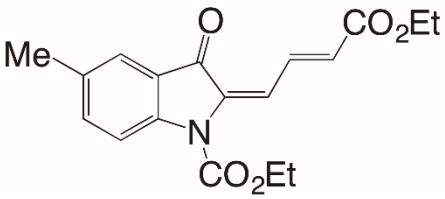

Figure 102 Chemical structure of compound **17e**.

General procedure was followed using ethyl 7-methyl-4*H*-furo[3,2-*b*]indole-4-carboxylate **16d** (48.6 mg, 0.2 mmol), [$Cu^{(I)}$(PcL)] (13.8 mg, 0.016 mmol), ethyl 2-diazoacetate (34.2 mg, 0.3 mmol) in anhydrous DCE (1+2 mL). Purification by flash chromatography (SiO_2, hexane/ethyl acetate 9:1) yielded **17d** (62.0 mg, 94%) as a yellow solid (m.p. 106-108 °C). **^{1}H NMR** (300 MHz, $CDCl_3$): 8.98 (dd, *J* = 15.4, 12.0 Hz, 1H), 7.89 (d, *J* = 8.5 Hz, 1H), 7.72 (d, *J* = 11.9 Hz, 1H), 7.60 (s, 1H), 7.44 (d, *J* = 8.5 Hz, 1H), 6.23 (d, *J* = 15.4 Hz, 1H), 4.50 (q, *J* = 7.1 Hz, 2H), 4.28 (q, 7.1 Hz, 2H), 2.41 (s, 3H), 1.51 (t, *J* = 7.1 Hz, 3H), 1.36 (t, *J* = 7.1 Hz, 3H). **^{13}C NMR** (75 MHz, $CDCl_3$): 184.55 (C), 166.32 (C), 151.64 (C), 145.63 (C), 138.18 (CH), 137.37 (CH), 135.37 (C), 134.31 (C), 129.49 (CH), 124.13 (CH), 123.78 (C), 123.62 (CH), 117.08 (CH), 63.34 (CH_2), 60.63 (CH_2), 20.64 (CH_3), 14.38 (CH_3), 14.29 (CH_3). **ESI(+)-HRMS**: m/z (%) = calcd for $C_{18}H_{19}NO_5$: 329.126323, found: 329.126700 (50) $[M]^+$.

Ethyl (*E*)-2-((*E*)-4-ethoxy-4-oxobut-2-en-1-ylidene)-6-methoxy-3-oxoindoline-1-carboxylate **17f**.

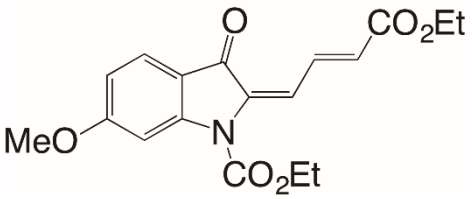

Figure 103 Chemical structure of compound **17f**.

General procedure was followed using ethyl 6-methoxy-4*H*-furo[3,2-*b*]indole-4-carboxylate **16f** (51.8 mg, 0.2 mmol), [$Cu^{(I)}$(PcL)] (13.8 mg, 0.016 mmol), ethyl 2-diazoacetate (34.2 mg, 0.3 mmol) in anhydrous DCE (1+2 mL). Purification by flash chromatography (SiO_2, hexane/ethyl acetate 9:1) yielded **17f** (45.5 mg, 66%) as a yellow solid (m.p. 157-159 °C). **^{1}H NMR** (300 MHz, $CDCl_3$): 8.96 (dd, *J* = 15.5, 11.9 Hz, 1H), 7.67 (d, *J* = 8.5 Hz, 1H), 7.57 (dd, *J* = 11.9, 0.8 Hz, 1H), 7.51 (d, *J* = 2.1 Hz, 1H), 6.72 (dd, *J* = 8.5, 2.1 Hz, 1H), 6.15 (dd, *J* = 15.5, 0.8 Hz, 1H), 4.46 (q, *J* = 7.1 Hz, 2H), 4.24 (q, *J* = 7.1 Hz, 2H), 3.89 (s, 3H), 1.46 (t, *J* = 7.1 Hz, 3H), 1.29 (t, *J* = 7.1 Hz, 3H). **^{13}C NMR** (75 MHz, $CDCl_3$): 182.58 (C), 166.59 (C), 166.26 (C), 151.47 (C), 149.69 (C), 138.17 (CH), 135.83 (C), 129.01 (CH), 125.81 (CH), 122.85 (CH), 117.26 (C), 111.69 (CH), 102.15 (CH), 63.40 (CH_2), 60.52 (CH_2), 55.81 (CH_3), 14.25 (CH_3), 14.24 (CH_3). **ESI(+)-MS**: m/z (%) = 368 (100) $[M+H]^+$; $C_{18}H_{19}NO_6$ [345.35]: calcd. for: C, 62.60; H, 5.55; N, 4.06; found: C, 62.44; H, 5.56; N, 4.08.

Ethyl (*E*)-2-((*E*)-4-ethoxy-4-oxobut-2-en-1-ylidene)-5-fluoro-3-oxoindoline-1-carboxylate **17g**.

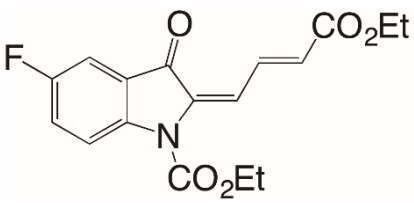

Figure 104 Chemical structure of compound **17g**.

General procedure was followed using ethyl 7-fluoro-4*H*-furo[3,2-*b*]indole-4-carboxylate **16g** (49.4 mg, 0.2 mmol), [$Cu^{(I)}$(PcL)] (13.8 mg, 0.016 mmol), ethyl 2-diazoacetate (34.2 mg, 0.3 mmol) in anhydrous DCE (1+2 mL). Purification by flash chromatography (SiO_2, toluene) yielded **17g** (48.5 mg, 73%) as a yellow solid (m.p. 106-109 °C). **^{1}H NMR** (300 MHz, $CDCl_3$): 8.94 (dd, *J* = 14.8, 12.6 Hz, 1H), 8.03 (m, 1H), 7.74 (d, *J* = 12.1 Hz, 1H), 7.57 – 7.19 (m, 2H), 6.27 (d, *J* = 15.2 Hz, 1H), 4.52 (q, *J* = 7.1 Hz, 2H), 4.29 (q, *J* = 7.1 Hz, 2H), 1.52 (t, *J* = 7.1 Hz, 3H), 1.36 (t, *J* = 7.1 Hz, 3H). **^{13}C NMR** (75 MHz, $CDCl_3$): 183.57 (C), 166.16 (C), 159.50 (d, *J* = 246.8 Hz, C), 151.42 (C), 143.69 (d, *J* = 1.7 Hz, C), 137.77 (CH), 135.16 (C), 130.31 (CH), 124.73 (CH), 123.45 (d, *J* = 24.3 Hz, CH), 118.94 (d, *J* = 7.3 Hz, CH), 110.04 (d, *J* = 23.5 Hz, CH), 63.61 (CH_2), 60.73 (CH_2), 14.36 (CH_3), 14.26 (CH_3). One quaternary carbon is missing, probably overlapped. **ESI(+)-HRMS**: m/z (%) = calcd for $C_{17}H_{16}FNO_5$: 333.101251, found: 333.101330 (10) $[M]^+$.

Ethyl (*E*)-2-((*E*)-4-ethoxy-4-oxobut-2-en-1-ylidene)-5-fluoro-3-oxoindoline-1-carboxylate **17h**.

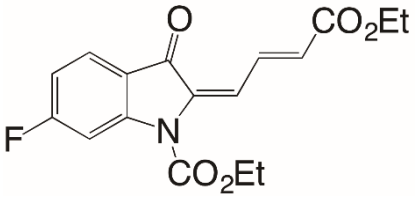

Figure 105 Chemical structure of compound **17h**.

General procedure was followed using ethyl 6-fluoro-4*H*-furo[3,2-*b*]indole-4-carboxylate **16h** (49.4 mg, 0.2 mmol), [$Cu^{(I)}$(PcL)] (13.8 mg, 0.016 mmol), ethyl 2-diazoacetate (34.2 mg, 0.3 mmol) in anhydrous DCE (1+2 mL). Purification by flash chromatography (SiO_2, hexane/ethyl acetate 95:5) yielded **17h** (40.5 mg, 61%) as a yellow solid (m.p. 111.5-113.8 °C). **^{1}H NMR** (300 MHz, $CDCl_3$): 8.92 (dd, *J* = 15.5, 12.0 Hz, 1H), 7.79 (dd, *J* = 8.5, 5.8 Hz, 1H), 7.74 – 7.65 (m, 2H), 6.93 (td, *J* = 8.5, 2.2 Hz, 1H), 6.22 (dd, *J* = 15.5, 0.9 Hz, 1H), 4.50 (q, *J* = 7.1 Hz, 2H), 4.26 (q, *J* = 7.1 Hz, 2H), 1.50 (t, *J* = 7.1 Hz, 3H), 1.33 (t, *J* = 7.1 Hz, 3H). **^{13}C NMR** (75 MHz, $CDCl_3$): 182.71 (C), 167.78 (d, *J* = 255.3 Hz, C), 166.12 (C), 151.24 (C), 149.03 (d, *J* = 13.9 Hz, C), 137.66 (CH), 135.13 (C), 130.08 (CH), 126.36 (d, *J* = 11.6 Hz, CH), 124.03 (CH), 120.14 (C), 112.37 (d, *J* = 24.1 Hz, CH), 105.38 (d, *J* = 30.0 Hz, CH), 63.78 (CH_2), 60.66 (CH_2), 14.29 (CH_3), 14.23 (CH_3). **ESI(+)-MS**: m/z (%) = 334 (100) $[M+H]^+$; $C_{17}H_{16}FNO_5$ [333.32]: calcd. for: C, 61.26; H, 4.84; N, 4.20; found: C, 61.39; H, 4.84; N, 4.21.

Ethyl (*E*)-2-((*E*)-4-methoxy-4-oxo-3-phenylbut-2-en-1-ylidene)-3-oxoindoline-1-carboxylate **17i**.

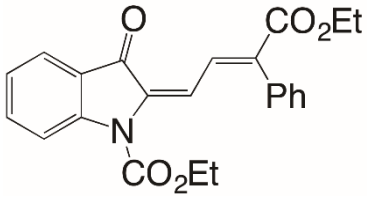

Figure 106 Chemical structure of compound **17i**.

General procedure was followed using ethyl 4*H*-furo[3,2-*b*]indole-4-carboxylate **16a** (45.8 mg, 0.2 mmol), [$Cu^{(I)}$(PcL)] (13.8 mg, 0.016 mmol), methyl 2-diazo-2-phenylacetate (52.8 mg, 0.3 mmol) in anhydrous DCE (1+2 mL). Purification by flash chromatography (SiO_2, toluene) yielded **17i** (52.0 mg, 69%) as a yellow solid with traces of minor isomer (*E/Z* = 95:5)
(m.p. 102-104 °C). **^{1}H NMR** (400 MHz, $CDCl_3$): 9.19 (d, *J* = 12.2 Hz, 1H), 8.13 (d, *J* = 8.5 Hz, 1H), 7.84 (dd, *J* = 7.6, 0.6 Hz, 1H), 7.63 (t, *J* = 7.9 Hz, 1H), 7.58 (d, *J* = 12.2 Hz, 1H), 7.47 – 7.40 (m, 3H), 7.35 –

7.30 (m, 2H), 7.25 (t, *J* = 7.5 Hz, 1H), 4.29 (q, *J* = 7.0 Hz, 2H), 3.88 (d, *J* = 0.5 Hz, 3H), 1.15 (t, *J* = 7.1 Hz, 3H). **^{13}C NMR** (101 MHz,, $CDCl_3$): 184.73 (C), 167.49 (C), 151.47 (C), 147.79 (C), 140.11 (C), 136.32 (CH), 134.70 (C), 134.49 (C), 133.63 (CH), 130.47 (2xCH), 128.38 (CH), 128.07 (2xCH), 124.32 (CH), 124.17 (CH), 123.78 (C), 122.55 (CH), 117.26 (CH), 63.32 (CH_2), 52.44 (CH_3), 13.90 (CH_3). **ESI(+)-MS**: m/z (%) = 378 (100) $[M+H]^+$; $C_{22}H_{19}NO_5$ [377.40]: calcd. for: C, 70.02; H, 5.07; N, 3.71; found: C, 69.83; H, 5.09; N, 3.70.

Ethyl (*E*)-5-methoxy-2-((*E*)-4-methoxy-4-oxo-3-phenylbut-2-en-1-ylidene)-3-oxoindoline-1-carboxylate **17j**.

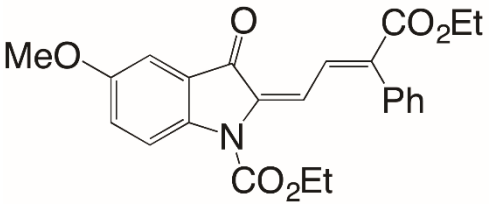

Figure 107 Chemical structure of compound **17j**.

General procedure was followed using ethyl 7-methoxy-4*H*-furo[3,2-*b*]indole-4-carboxylate **16d** (51.8 mg, 0.2 mmol), [$Cu^{(I)}$(PcL)] (13.8 mg, 0.016 mmol), methyl 2-diazo-2-phenylacetate (52.8 mg, 0.3 mmol) in anhydrous DCE (1+2 mL). Purification by flash chromatography (SiO_2, hexane/ethyl acetate 98:2) yielded **17j** (75.5 mg, 93%) as a yellow solid (m.p. 136-138 °C). **^{1}H NMR** (300 MHz, $CDCl_3$): 9.17 (d, *J* = 12.2 Hz, 1H), 8.03 (d, *J* = 9.0 Hz, 1H), 7.57 (d, *J* = 12.2 Hz, 1H), 7.47 – 7.38 (m, 3H), 7.32 (dd, *J* = 7.6, 1.8 Hz, 2H), 7.27 (d, *J* = 5.2 Hz, 1H), 7.20 (dd, *J* = 9.0, 2.8 Hz, 1H), 4.27 (q, *J* = 7.1 Hz, 2H), 3.88 (s, 3H) 3.87 (s, 3H), 1.14 (t, *J* = 7.1 Hz, 3H). **^{13}C NMR** (75 MHz, $CDCl_3$): 184.55 (C), 167.50 (C), 156.72 (C), 151.39 (C), 142.31 (C), 140.07 (C), 135.18 (C), 134.50 (C), 133.68 (CH), 130.45 (2xCH), 128.36 (CH), 128.05 (2xCH), 124.75 (CH), 124.53 (C), 122.66 (CH), 118.44 (CH), 105.54 (CH), 63.15 (CH_2), 55.81 ,(CH_3) 52.41 (CH_3), 13.92 (CH_3). **ESI(+)-MS**: m/z (%) = 430 (100) $[M+H]^+$; $C_{23}H_{21}NO_6$ [407.42]: calcd. for: C, 67.81; H, 5.20; N, 3.44; found: C, 67.65; H, 5.19; N, 3.44.

Ethyl (*E*)-6-methoxy-2-((*E*)-4-methoxy-4-oxo-3-phenylbut-2-en-1-ylidene)-3-oxoindoline-1-carboxylate **17k**.

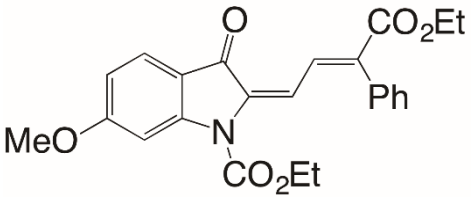

Figure 108 Chemical structure of compound **17k**.

General procedure was followed using ethyl 6-methoxy-4*H*-furo[3,2-*b*]indole-4-carboxylate **16f** (51.8 mg, 0.2 mmol), [$Cu^{(I)}$(PcL)] (13.8 mg, 0.016 mmol), methyl 2-diazo-2-phenylacetate (52.8 mg, 0.3 mmol) in anhydrous DCE (1+2 mL). Purification by flash chromatography (SiO_2, hexane/ethyl acetate 95:5) yielded **17k** (77.0 mg, 95%) as a yellow solid with traces of the minor isomer(*E/Z* = 88:12) (m.p. 140-142 °C). **^{1}H NMR** (300 MHz, $CDCl_3$): 9.19 (d, *J* = 12.1 Hz, 1H), 7.72 (d, *J* = 8.6 Hz, 1H), 7.66 (d, *J* = 2.1 Hz, 1H), 7.50 – 7.36 (m, 4H), 7.29 (dd, *J* = 7.7, 1.8 Hz, 2H), 6.75 (dd, *J* = 8.6, 2.2 Hz, 1H), 4.23 (q, *J* = 7.2 Hz, 2H), 3.90 (s, 3H), 3.84 (s, 3H), 1.08 (t, *J* = 7.2 Hz, 3H). **^{13}C NMR** (75 MHz, $CDCl_3$): 182.83 (C), 167.46 (C), 166.63 (C), 151.45 (C), 150.13 (C), 139.50 (C), 135.50 (C), 134.63 (C),

133.70 (CH), 130.43 (2xCH), 128.19 (CH), 127.98 (2xCH), 125.67 (CH), 121.54 (CH), 117.38 (C), 112.11 (CH), 101.67 (CH), 63.24 (CH_2), 55.83 (CH_3), 52.29 (CH_3), 13.79 (CH_3). **ESI(+)-MS**: m/z (%) = 430 (100) $[M+Na]^+$; $C_{23}H_{21}NO_6$ [407.42]: calcd. for: C, 67.81; H, 5.20; N, 3.44; found: C, 67.93; H, 5.18; N, 3.45.

Ethyl (*E*)-5-fluoro-2-((*E*)-4-methoxy-4-oxo-3-phenylbut-2-en-1-ylidene)-3-oxoindoline-1-carboxylate **17l**.

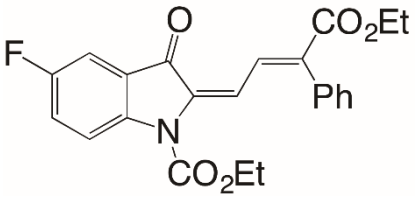

Figure 109 Chemical structure of compound **17l**.

General procedure was followed using ethyl 7-fluoro-4*H*-furo[3,2-*b*]indole-4-carboxylate **16g** (49.4 mg, 0.2 mmol), [$Cu^{(I)}$(PcL)] (13.8 mg, 0.016 mmol), methyl 2-diazo-2-phenylacetate (52.8 mg, 0.3 mmol) in anhydrous DCE (1+2 mL). Purification by flash chromatography (SiO_2, toluene/ethyl acetate 98:2) yielded **17l** (73.0 mg, 92%) as a yellow solid with traces of the minor isomer, (*E/Z* = 85:15) (m.p. 146-148 °C). **^{1}H NMR** (300 MHz, $CDCl_3$): 9.12 (d, *J* = 12.2 Hz, 1H), 8.13 (dd, *J* = 9.1, 4.0 Hz, 1H), 7.57 (d, J = 12.2 Hz, 1H), 7.48 – 7.38 (m, 4H), 7.35 – 7.28 (m, *J* = 3.2, 2.1 Hz, 3H), 4.27 (q, *J* = 7.2 Hz, 2H), 3.88 (s, 3H), 1.12 (t, *J* = 7.2 Hz, 3H). **^{13}C NMR** (75 MHz, $CDCl_3$): 183.75 (C), 167.36 (C), 159.47 (d, *J* = 246.5 Hz, C), 151.31 (C), 143.93 (C), 140.73 (C), 134.75 (C), 134.39 (C), 133.32 (CH), 130.44 (2xCH), 128.46 (CH), 128.08 (2xCH), 124.91 (d, *J* = 7.6 Hz, C), 123.39 (d, *J* = 24.0 Hz, CH), 123.39 (CH),118.91 (t, *J* = 6.2 Hz, CH), 109.74 (d, *J* = 23.5, 11.8 Hz, CH), 63.45 (CH_2), 52.48 (CH_3), 13.86 (CH_3). **ESI(+)-MS**: m/z (%) = 396 (100) [M+H]+ ; C22H18FNO5 [395.39]: calcd. for: C, 66.83; H, 4.59; N, 3.54; found: C, 67.02; H, 4.58; N, 3.53.

Ethyl (*E*)-6-fluoro-2-((*E*)-4-methoxy-4-oxo-3-phenylbut-2-en-1-ylidene)-3-oxoindoline-1-carboxylate **17m**.

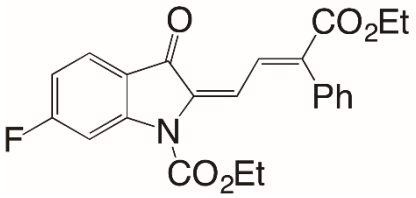

Figure 110 Chemical structure of compound **17m**.

General procedure was followed using ethyl 6-fluoro-4*H*-furo[3,2-*b*]indole-4-carboxylate **16h** (49.4 mg, 0.2 mmol), [$Cu^{(I)}$(PcL)] (13.8 mg, 0.016 mmol), methyl 2-diazo-2-phenylacetate (52.8 mg, 0.3 mmol) in anhydrous DCE (1+2 mL). Purification by flash chromatography (SiO_2, hexane/ethyl acetate 95:1) yielded **17m** (63.0 mg, 80%) as a yellow solid with traces of minor isomer (E/Z = 94:6) (m.p. 136.7-139.2 °C). **^{1}H NMR** (300 MHz, $CDCl_3$): 9.14 (d, *J* = 12.2 Hz, 1H), 7.92 – 7.78 (m, 2H), 7.55 (d, *J* = 12.2 Hz, 1H), 7.49 – 7.36 (m, 3H), 7.36 – 7.23 (m, 2H), 6.95 (td, *J* = 8.5, 2.2 Hz, 1H), 4.29 (q, *J* = 7.2 Hz, 2H), 3.87 (s, 3H), 1.13 (t, *J* = 7.2 Hz, 3H). **^{13}C NMR** (75 MHz, $CDCl_3$): 182.97 (C), 167.78 (d, *J* = 255.4 Hz, C), 167.38 (C), 151.19 (C), 149.33 (d, *J* = 14.0 Hz, C), 140.52 (C), 134.80 (C), 134.41 (C), 133.24 (CH), 130.44 (2xCH), 128.43 (CH), 128.08 (2xCH), 126.15 (t, *J* = 11.1 Hz, CH), 122.70 (CH), 120.24 (C), 112.28 (dd, *J* = 24.1, 10.8 Hz, CH), 105.29 (d, *J* = 30.0 Hz, CH), 63.64 (CH_2), 52.45 (CH_3),

13.84 (CH_3). **ESI(+)-MS**: m/z (%) = 396 (100) $[M+H]^+$; $C_{22}H_{18}FNO_5$ [395.39]: calcd. for: C, 66.83; H, 4.59; N, 3.54; found: C, 66.74; H, 4.59; N, 3.55.

5.3.4.3. Absorption spectroscopy

UV-visible absorption spectra were carried out on compounds **17a**, **17c**, **17d**, **17e**, **17g**, **17h**, **17l** and **17m** in chloroform solution.

References

1. Marth JD. A unified vision of the building blocks of life. *Nat Cell Biol*. 2008;10(9):1015. doi:10.1038/ncb0908-1015
2. Van Meer G, De Kroon AIPM. Lipid map of the mammalian cell. *J Cell Sci*. 2011;124(1):5-8. doi:10.1242/jcs.071233
3. Hjort Ipsen J, Karlström G, Mourtisen OG, Wennerström H, Zuckermann MJ. Phase equilibria in the phosphatidylcholine-cholesterol system. *BBA - Biomembr*. 1987;905(1):162-172. doi:10.1016/0005-2736(87)90020-4
4. Mouritsen OG, Zuckermann MJ. Mouritsen_Zuckermann_2004. 2004;39(11):1101-1113.
5. Maxfield FR, van Meer G. Cholesterol, the central lipid of mammalian cells. *Curr Opin Cell Biol*. 2010;22(4):422-429. doi:10.1016/j.ceb.2010.05.004
6. Fraenkel G, Hopf HS. The physiological action of abnormally high temperatures on poikilothermic animals. *Biochem J*. 1940;34(7):1085-1092. doi:10.1042/bj0341085
7. Buda C, Dey I, Balogh N, et al. Structural order of membranes and composition of phospholipids in fish brain cells during thermal acclimatization. *Proc Natl Acad Sci U S A*. 1994;91(17):8234-8238. doi:10.1073/pnas.91.17.8234
8. Luby-Phelps K, Mujumdar S, Mujumdar RB, Ernst LA, Galbraith W, Waggoner AS. A novel fluorescence ratiometric method confirms the low solvent viscosity of the cytoplasm. *Biophys J*. 1993;65(1):236-242. doi:10.1016/S0006-3495(93)81075-0
9. Plant95-AnalBioChem-PLAlkanethiole bilayers SPR.pdf.
10. Pum D, Stangl G, Sponer C, et al. P a t t e r n i n g of M o n o l a y e r s of Crystalline S-layer P r o t e i n s on a Silicon Surface by D e e p Ultraviolet R a d i a t i o n. 1997;35:297-300.
11. Yang T, Jung SY, Mao H, Cremer PS. Fabrication of phospholipid bilayer-coated microchannels for on-chip immunoassays. *Anal Chem*. 2001;73(2):165-169. doi:10.1021/ac000997o
12. Yang T, Baryshnikova OK, Mao H, Holden MA, Cremer PS. Investigations of bivalent antibody binding on fluid-supported phospholipid membranes: The effect of hapten density. *J Am Chem Soc*. 2003;125(16):4779-4784. doi:10.1021/ja029469f
13. Ono A, Freed EO. Plasma membrane rafts play a critical role in HIV-1 assembly and release. *Proc Natl Acad Sci U S A*. 2001;98(24):13925-13930. doi:10.1073/pnas.241320298
14. Kasahara K, Watanabe K, Kozutsumi Y, Oohira A, Yamamoto T, Sanai Y. Association of GPI-anchored protein TAG-1 with Src-family kinase Lyn in lipid rafts of cerebellar granule cells. *Neurochem Res*. 2002;27(7-8):823-829. doi:10.1023/A:1020265225916
15. Stoddart A, Dykstra ML, Brown BK, Song W, Pierce SK, Brodsky FM. Lipid rafts unite signaling cascades with clathrin to regulate BCR internalization. *Immunity*. 2002;17(4):451-462. doi:10.1016/S1074-7613(02)00416-8
16. Qi SY, Groves JT, Chakraborty AK. Synaptic pattern formation during immune recognition. *Proc Natl Acad Sci*. 2001;98(12):6548-6553.
17. Tamm LK, McConnell HM. Supported phospholipid bilayers. *Biophys J*. 1985;47(1):105-113. doi:10.1016/S0006-3495(85)83882-0
18. Johnson SJ, Bayerl TM, McDermott DC, et al. Structure of an adsorbed dimyristoylphosphatidylcholine bilayer measured with specular reflection of neutrons. *Biophys J*. 1991;59(2):289-294. doi:10.1016/S0006-3495(91)82222-6
19. Lagerholm BC, Starr TE, Volovyk ZN, Thompson NL. Rebinding of IgE Fabs at haptenated planar membranes: Measurement by total internal reflection with fluorescence photobleaching recovery. *Biochemistry*. 2000;39(8):2042-2051. doi:10.1021/bi9917434
20. Cremer PS, Boxer SG. Formation and spreading of lipid bilayers on planar glass supports. *J*

Phys Chem B. 1999;103(13):2554-2559. doi:10.1021/jp983996x
21. Egawa H, Furusawa K. Liposome adhesion on mica surface studied by atomic force microscopy. *Langmuir*. 1999;15(5):1660-1666. doi:10.1021/la980923w
22. Reimhult E, Höök F, Kasemo B. Intact vesicle adsorption and supported biomembrane formation from vesicles in solution: Influence of surface chemistry, vesicle size, temperature, and osmotic pressure. *Langmuir*. 2003;19(5):1681-1691. doi:10.1021/la0263920
23. Stelzle M, Weissmüller G, Sackmann E. On the application of supported bilayers as receptive layers for biosensors with electrical detection. *J Phys Chem*. 1993;97(12):2974-2981. doi:10.1021/j100114a025
24. Et B, Acta B. BsN. 1998;1369:61-70.
25. Yang J, Kleijn JM. Order in phospholipid Langmuir-Blodgett layers and the effect of the electrical potential of the substrate. *Biophys J*. 1999;76(1 I):323-332. doi:10.1016/S0006-3495(99)77199-7
26. Gritsch S, Nollert P, Jähnig F, Sackmann E. Impedance spectroscopy of porin and gramicidin pores reconstituted into supported lipid bilayers on indium-tin-oxide electrodes. *Langmuir*. 1998;14(11):3118-3125. doi:10.1021/la9710381
27. Erdelen C, Häussling L, Naumann R, et al. Self-Assembled Disulfide-Functionalized Amphiphilic Copolymers on Gold. *Langmuir*. 1994;10(4):1246-1250. doi:10.1021/la00016a044
28. Castellana ET, Cremer PS. Solid supported lipid bilayers: From biophysical studies to sensor design. *Surf Sci Rep*. 2006;61(10):429-444. doi:10.1016/j.surfrep.2006.06.001
29. Puu G, Gustafson I. Planar lipid bilayers on solid supports from liposomes - factors of importance for kinetics and stability. *Biochim Biophys Acta - Biomembr*. 1997;1327(2):149-161. doi:10.1016/S0005-2736(97)00052-7
30. Picas L, Milhiet PE, Hernández-Borrell J. Atomic force microscopy: A versatile tool to probe the physical and chemical properties of supported membranes at the nanoscale. *Chem Phys Lipids*. 2012;165(8):845-860. doi:10.1016/j.chemphyslip.2012.10.005
31. Morrissey JH. Morrissey Lab Protocol for Preparing Phospholipid Vesicles by Extrusion. *Methods Enzymol*. 2005;(June):1-3.
32. Hempstead PD, Yewdall SJ, Fernie AR, et al. Comparison of the three-dimensional structures of recombinant human H and horse L ferritins at high resolution. *J Mol Biol*. 1997;268(2):424-448. doi:10.1006/jmbi.1997.0970
33. Van Wuytswinkel O, Briat JF. Conformational changes and in vitro core-formation modifications induced by site-directed mutagenesis of the specific N-terminus of pea seed ferritin. *Biochem J*. 1995;305(3):959-965. doi:10.1042/bj3050959
34. Wardrop AJ, Wicks RE, Entsch B. Occurrence end expression of members of the ferritin gene family in cowpeas. *Biochem J*. 1999;337(3):523-530. doi:10.1042/0264-6021:3370523
35. Theil EC, Matzapetakis M, Liu X. Ferritins: Iron/oxygen biominerals in protein nanocages. *J Biol Inorg Chem*. 2006;11(7):803-810. doi:10.1007/s00775-006-0125-6
36. Zhang Y, Orner BP. Self-assembly in the ferritin nano-cage protein superfamily. *Int J Mol Sci*. 2011;12(8):5406-5421. doi:10.3390/ijms12085406
37. Heli H, Mirtorabi S, Karimian K. Advances in iron chelation: An update. *Expert Opin Ther Pat*. 2011;21(6):819-856. doi:10.1517/13543776.2011.569493
38. Theil EC, Tosha T, Behera RK. Solving Biologys Iron Chemistry Problem with Ferritin Protein Nanocages. *Acc Chem Res*. 2016;49(5):784-791. doi:10.1021/ar500469e
39. Zhao G, Arosio P, Chasteen ND. Iron(II) and hydrogen peroxide detoxification by human H-chain ferritin. An EPR spin-trapping study. *Biochemistry*. 2006;45(10):3429-3436.

doi:10.1021/bi052443r
40. Penner-Hahn JE. A short Fe-Fe distance in peroxodiferric ferritin: Control of Fe substrate versus cofactor decay? *Science (80-)*. 2000;287(5450):122-125. doi:10.1126/science.287.5450.122
41. Yasmin S, Andrews SC, Moore GR, Le Brun NE. A new role for heme, facilitating release of iron from the bacterioferritin iron biomineral. *J Biol Chem*. 2011;286(5):3473-3483. doi:10.1074/jbc.M110.175034
42. Andrews SC. *Iron Storage in Bacteria*. Vol 40.; 1998. doi:10.1016/s0065-2911(08)60134-4
43. Theil EC. Ferritin protein nanocages use ion channels, catalytic sites, and nucleation channels to manage iron/oxygen chemistry. *Curr Opin Chem Biol*. 2011;15(2):304-311. doi:10.1016/j.cbpa.2011.01.004
44. Hough WL, Smiglak M, Rodríguez H, et al. The third evolution of ionic liquids: Active pharmaceutical ingredients. *New J Chem*. 2007;31(8):1429-1436. doi:10.1039/b706677p
45. Smiglak M, Reichert WM, Holbrey JD, et al. Combustible ionic liquids by design: Is laboratory safety another ionic liquid myth? *Chem Commun*. 2006;(24):2554-2556. doi:10.1039/b602086k
46. Thomas welton. Room-temperature ionic liquids: Solvents for synthesis and catalysis. *Chem Rev*. 1999;99(8):2071-2083. doi:10.1021/cr1003248
47. Swatloski RP, Spear SK, Holbrey JD, Rogers RD. Dissolution of cellose with ionic liquids. *J Am Chem Soc*. 2002;124(18):4974-4975. doi:10.1021/ja025790m
48. Borra EF, Seddiki O, Angel R, et al. Deposition of metal films on an ionic liquid as a basis for a lunar telescope. *Nature*. 2007;447(7147):979-981. doi:10.1038/nature05909
49. Fabregat-Santiago F, Bisquert J, Palomares E, et al. Correlation between photovoltaic performance and impedance spectroscopy of dye-sensitized solar cells based on ionic liquids. *J Phys Chem C*. 2007;111(17):6550-6560. doi:10.1021/jp066178a
50. Samorì C, Torri C, Samorì G, et al. Extraction of hydrocarbons from microalga Botryococcus braunii with switchable solvents. *Bioresour Technol*. 2010;101(9):3274-3279. doi:10.1016/j.biortech.2009.12.068
51. Jastorff B, Störmann R, Ranke J, et al. How hazardous are ionic liquids? Structure-activity relationships and biological testing as important elements for sustainability evaluation. *Green Chem*. 2003;5(2):136-142. doi:10.1039/b211971d
52. Jastorff B, Mölter K, Behrend P, et al. Progress in evaluation of risk potential of ionic liquids - Basis for an eco-design of sustainable products. *Green Chem*. 2005;7(5):362-372. doi:10.1039/b418518h
53. Ranke J, Stolte S, Störmann R, Aming J, Jastorff B. Design of sustainable chemical products - The example of ionic liquids. *Chem Rev*. 2007;107(6):2183-2206. doi:10.1021/cr050942s
54. Thuy Pham TP, Cho CW, Yun YS. Environmental fate and toxicity of ionic liquids: A review. *Water Res*. 2010;44(2):352-372. doi:10.1016/j.watres.2009.09.030
55. Stolte S, Arning J, Bottin-Weber U, et al. Anion effects on the cytotoxicity of ionic liquids. *Green Chem*. 2006;8(7):621-629. doi:10.1039/b602161a
56. Frade RFM, Matias A, Branco LC, Afonso CAM, Duarte CMM. Effect of ionic liquids on human colon carcinoma HT-29 and CaCo-2 cell lines. *Green Chem*. 2007;9(8):873-887. doi:10.1039/b617526k
57. García-Lorenzo A, Tojo E, Tojo J, et al. Cytotoxicity of selected imidazolium-derived ionic liquids in the human Caco-2 cell line. Sub-structural toxicological interpretation through a QSAR study. *Green Chem*. 2008;10(5):508-551. doi:10.1039/b718860a
58. Ranke J, Müller A, Bottin-Weber U, et al. Lipophilicity parameters for ionic liquid cations and their correlation to in vitro cytotoxicity. *Ecotoxicol Environ Saf*. 2007;67(3):430-438.

doi:10.1016/j.ecoenv.2006.08.008
59. Wang X, Ohlin CA, Lu Q, Fei Z, Hu J, Dyson PJ. Cytotoxicity of ionic liquids and precursor compounds towards human cell line HeLa. *Green Chem*. 2007;9(11):1191-1197. doi:10.1039/b704503d
60. Larson JH, Frost PC, Lamberti GA. Variable toxicity of ionic liquid-forming chemicals to Lemna minor and the influence of dissolved organic matter. *Environ Toxicol Chem*. 2008;27(3):676-681. doi:10.1897/06-540.1
61. Pretti C, Chiappe C, Pieraccini D, et al. Acute toxicity of ionic liquids to the zebrafish (Danio rerio). *Green Chem*. 2006;8(3):238-240. doi:10.1039/b511554j
62. Yu M, Li SM, Li XY, Zhang BJ, Wang JJ. Acute effects of 1-octyl-3-methylimidazolium bromide ionic liquid on the antioxidant enzyme system of mouse liver. *Ecotoxicol Environ Saf*. 2008;71(3):903-908. doi:10.1016/j.ecoenv.2008.02.022
63. Wells AS, Coombe VT. On the freshwater ecotoxicity and biodegradation properties of some common ionic liquids. *Org Process Res Dev*. 2006;10(4):794-798. doi:10.1021/op060048i
64. Suoninen EJ. Optical microscopy. *Surf Charact A User's Sourceb*. 2007;(April):54-56. doi:10.1002/9783527612451.ch1
65. Elson EL, Magde D. Fluorescence correlation spectroscopy. I. Conceptual basis and theory. *Biopolymers*. 1974;13(1):1-27. doi:10.1002/bip.1974.360130102
66. Yu L, Lei Y, Ma Y, et al. A Comprehensive Review of Fluorescence Correlation Spectroscopy. *Front Phys*. 2021;9(April):1-21. doi:10.3389/fphy.2021.644450
67. Albrecht TR, Akamine S, Carver TE, Quate CF. Microfabrication of cantilever styli for the atomic force microscope. *J Vac Sci Technol A Vacuum, Surfaces, Film*. 1990;8(4):3386-3396. doi:10.1116/1.576520
68. Zhong Q, Inniss D, Kjoller K, Elings VB. Fractured polymer/silica fiber surface studied by tapping mode atomic force microscopy. *Surf Sci Lett*. 1993;290(1-2):L688-L692. doi:10.1016/0167-2584(93)90906-y
69. Karrasch S, Dolder M, Schabert F, Ramsden J, Engel A. Covalent binding of biological samples to solid supports for scanning probe microscopy in buffer solution. *Biophys J*. 1993;65(6):2437-2446. doi:10.1016/S0006-3495(93)81327-4
70. García R, Pérez R. *Dynamic Atomic Force Microscopy Methods*. Vol 47.; 2002. doi:10.1016/s0167-5729(02)00077-8
71. Schäffer TE, Cleveland JP, Ohnesorge F, Walters DA, Hansma PK. Studies of vibrating atomic force microscope cantilevers in liquid. *J Appl Phys*. 1996;80(7):3622-3627. doi:10.1063/1.363308
72. Sirghi L, Rossi F. Adhesion and elasticity in nanoscale indentation. *Appl Phys Lett*. 2006;89(24). doi:10.1063/1.2404981
73. Leya T, Rother A, Torsten M, Fuhr G, Gropius M, Watermann B. 10th International Congress on Marine Corrosion and Fouling, University of Melbourne, February 1999. *DSTO Aeronaut Marit Res Lab*. 1999;(February):98-110. http://www.dsto.defence.gov.au/publications/2396/DSTO-GD-0287.pdf.
74. Volle CB, Ferguson MA, Aidala KE, Spain EM, Núñez ME. Spring constants and adhesive properties of native bacterial biofilm cells measured by atomic force microscopy. *Colloids Surfaces B Biointerfaces*. 2008;67(1):32-40. doi:10.1016/j.colsurfb.2008.07.021
75. Wampler HP, Ivanisevic A. Nanoindentation of gold nanoparticles functionalized with proteins. *Micron*. 2009;40(4):444-448. doi:10.1016/j.micron.2009.01.002
76. Vakarelski IU, Toritani A, Nakayama M, Higashitani K. Effects of particle deformability on interaction between surfaces in solutions. *Langmuir*. 2003;19(1):110-117. doi:10.1021/la026581i

77. Götzinger M, Peukert W. Adhesion forces of spherical alumina particles on ceramic substrates. *J Adhes*. 2004;80(3):223-242. doi:10.1080/00218460490279297
78. Butt HJ, Cappella B, Kappl M. Force measurements with the atomic force microscope: Technique, interpretation and applications. *Surf Sci Rep*. 2005;59(1-6):1-152. doi:10.1016/j.surfrep.2005.08.003
79. Hinterdorfer P, Baumgartner W, Gruber HJ, Schilcher K, Schindler H. Detection and localization of individual antibody-antigen recognition events by atomic force microscopy. *Proc Natl Acad Sci U S A*. 1996;93(8):3477-3481. doi:10.1073/pnas.93.8.3477
80. Clausen-Schaumann H, Seitz M, Krautbauer R, Gaub HE. Force spectroscopy with single bio-molecules. *Curr Opin Chem Biol*. 2000;4(5):524-530. doi:10.1016/S1367-5931(00)00126-5
81. Eaton PJ, Graham P, Smith JR, Smart JD, Nevell TG, Tsibouklis J. Mapping the surface heterogeneity of a polymer blend: An adhesion-force-distribution study using the atomic force microscope. *Langmuir*. 2000;16(21):7887-7890. doi:10.1021/la000159p
82. Subramanian S, Sampath S. Effect of chain length on the adhesion behaviour of n-alkanethiol self-assembled monolayers on Au(111): An atomic force microscopy study. *Pramana - J Phys*. 2005;65(4 SPEC. ISS.):753-761. doi:10.1007/bf03010464
83. Emerson IV RJ, Camesano TA. Nanoscale investigation of pathogenic microbial adhesion to a biomaterial. *Appl Environ Microbiol*. 2004;70(10):6012-6022. doi:10.1128/AEM.70.10.6012-6022.2004
84. Bowen WR, Lovitt RW, Wright CJ. Atomic force microscopy study of the adhesion of Saccharomyces cerevisiae. *J Colloid Interface Sci*. 2001;237(1):54-61. doi:10.1006/jcis.2001.7437
85. Butt HJ. Measuring local surface charge densities in electrolyte solutions with a scanning force microscope. *Biophys J*. 1992;63(2):578-582. doi:10.1016/S0006-3495(92)81601-6
86. Dufrêne YF, Boonaert CJP, Van der Mei HC, Busscher HJ, Rouxhet PG. Probing molecular interactions and mechanical properties of microbial cell surfaces by atomic force microscopy. *Ultramicroscopy*. 2001;86(1-2):113-120. doi:10.1016/S0304-3991(00)00079-6
87. Dupres V, Menozzi FD, Locht C, et al. Nanoscale mapping and functional analysis of individual adhesins on living bacteria. *Nat Methods*. 2005;2(7):515-520. doi:10.1038/nmeth769
88. Muller DJ. AFM: A nanotool in membrane biology. *Biochemistry*. 2008;47(31):7986-7998. doi:10.1021/bi800753x
89. Ducker WA, Senden TJ, Pashley RM. Measurement of Forces in Liquids Using a Force Microscope. *Langmuir*. 1992;8(7):1831-1836. doi:10.1021/la00043a024
90. Eaton P, Smith JR, Graham P, Smart JD, Nevell TG, Tsibouklis J. Adhesion force mapping of polymer surfaces: Factors influencing force of adhesion. *Langmuir*. 2002;18(8):3387-3389. doi:10.1021/la015633l
91. Vancso GJ, Hillborg H, Schönherr H. Erratum to Chemical Composition of Polymer Surfaces Imaged by Atomic ForceMicroscopy and Complementary Approaches. *Adv Polym Sci*. 2005;182(July):309. doi:10.1007/12_046
92. Nagao E, Dvorak JA. Phase imaging by atomic force microscopy: Analysis of living homoiothermic vertebrate cells. *Biophys J*. 1999;76(6):3289-3297. doi:10.1016/S0006-3495(99)77481-3
93. Abelmann L, Porthun S, Haast M, et al. Comparing the resolution of magnetic force microscopes using the CAMST reference samples. *J Magn Magn Mater*. 1998;190(1-2):135-147. doi:10.1016/S0304-8853(98)00281-9
94. Porthun S, Abelmann L, Lodder C. Magnetic force microscopy of thin film media for high density magnetic recording. *J Magn Magn Mater*. 1998;182(1-2):238-273.

doi:10.1016/S0304-8853(97)01010-X
95. Hillner PE, Manne S, Gratz AJ, Hansma PK. AFM images of dissolution and growth on a calcite crystal. *Ultramicroscopy*. 1992;42-44(PART 2):1387-1393. doi:10.1016/0304-3991(92)90454-R
96. Review T. Micro-thermal analysis : techniques and. 2001.
97. Day HC, Allee DR. Selective area oxidation of silicon with a scanning force microscope. *Appl Phys Lett*. 1993;62(21):2691-2693. doi:10.1063/1.109259
98. Stiévenard D, Legrand B. Silicon surface nano-oxidation using scanning probe microscopy. *Prog Surf Sci*. 2006;81(2-3):112-140. doi:10.1016/j.progsurf.2006.01.003
99. Piner RD, Zhu J, Xu F, Hong S, Mirkin CA. "Dip-pen" nanolithography. *Science (80-)*. 1999;283(5402):661-663. doi:10.1126/science.283.5402.661
100. Christman KL, Enriquez-Rios VD, Maynard HD. Nanopatterning proteins and peptides. *Soft Matter*. 2006;2(11):928-939. doi:10.1039/b611000b
101. Noy A, Miller AE, Klare JE, Weeks BL, Woods BW, DeYoreo JJ. Fabrication of Luminescent Nanostructures and Polymer Nanowires Using Dip-Pen Nanolithography. *Nano Lett*. 2002;2(2):109-112. doi:10.1021/nl010081c
102. Agarwal G, Sowards LA, Naik RR, Stone MO. Dip-pen nanolithography in tapping mode. *J Am Chem Soc*. 2003;125(2):580-583. doi:10.1021/ja020471g
103. Ginger DS, Zhang H, Mirkin CA. The Evolution of Dip-Pen Nanolithography. *Angew Chemie - Int Ed*. 2004;43(1):30-45. doi:10.1002/anie.200300608
104. Fu L, Liu X, Zhang Y, Dravid VP, Mirkin CA. Nanopatterning of "hard" magnetic nanostructures via dip-pen nanolithography and a sol-based ink. *Nano Lett*. 2003;3(6):757-760. doi:10.1021/nl034172g
105. Xie XN, Chung HJ, Sow CH, Wee ATS. Nanoscale materials patterning and engineering by atomic force microscopy nanolithography. *Mater Sci Eng R Reports*. 2006;54(1-2):1-48. doi:10.1016/j.mser.2006.10.001
106. Darbeau R. Nuclear magnetic resonance (NMR) spectroscopy: A review and a look at its use as a probative tool in deamination chemistry. *Appl Spectrosc Rev*. 2006;41(4):401-425. doi:10.1080/05704920600726175
107. Johnson CS. Diffusion ordered nuclear magnetic resonance spectroscopy: Principles and applications. *Prog Nucl Magn Reson Spectrosc*. 1999;34(3-4):203-256. doi:10.1016/S0079-6565(99)00003-5
108. Morris GA. Diffusion-Ordered Spectroscopy. *Encycl Magn Reson*. 2009:1-13. doi:10.1002/9780470034590.emrstm0119.pub2
109. Kaszuba M. The measurement of nanoparticles using photon correlation spectroscopy and avalanche photo diodes. *J Nanoparticle Res*. 1999;1(3):405-409. doi:10.1023/A:1010072129578
110. Divizione F, Della F, Hayden B, Holloway D, Simons JP. Versammlungen und Veranstaltungen. *Berichte der Bunsengesellschaft für Phys Chemie*. 1989;93(4):539-539. doi:10.1002/bbpc.19890930432
111. Feigin LA, Svergun DI. *Structure Analysis by Small-Angle X-Ray and Neutron Scattering*.; 1987. doi:10.1007/978-1-4757-6624-0
112. Svergun DI, Koch MHJ. Small-angle scattering studies of biological macromolecules in solution. *Reports Prog Phys*. 2003;66(10):1735-1782. doi:10.1088/0034-4885/66/10/R05
113. Poitevin F, Orland H, Doniach S, Koehl P, Delarue M. AquaSAXS: A web server for computation and fitting of SAXS profiles with non-uniformally hydrated atomic models. *Nucleic Acids Res*. 2011;39(SUPPL. 2):184-189. doi:10.1093/nar/gkr430
114. Overington JP, Al-Lazikani B, Hopkins AL. How many drug targets are there? *Nat Rev Drug*

Discov. 2006;5(12):993-996. doi:10.1038/nrd2199
115. Paoletti P, Ellis-Davies GCR, Mourot A. Optical control of neuronal ion channels and receptors. *Nat Rev Neurosci*. 2019;20(9):514-532. doi:10.1038/s41583-019-0197-2
116. Waszkielewicz AM, Gunia A, Szkaradek N, Sloczynska K, Krupinska S, Marona H. Ion Channels as Drug Targets in Central Nervous System Disorders. *Curr Med Chem*. 2013;999(999):29-35. doi:10.2174/09298673113209990109
117. Fenno L, Yizhar O, Deisseroth K. The development and application of optogenetics. *Annu Rev Neurosci*. 2011;34:389-412. doi:10.1146/annurev-neuro-061010-113817
118. Boyden ES, Zhang F, Bamberg E, Nagel G, Deisseroth K. Millisecond-timescale, genetically targeted optical control of neural activity. *Nat Neurosci*. 2005;8(9):1263-1268. doi:10.1038/nn1525
119. Johansen JP, Hamanaka H, Monfils MH, et al. Optical activation of lateral amygdala pyramidal cells instructs associative fear learning. *Proc Natl Acad Sci U S A*. 2010;107(28):12692-12697. doi:10.1073/pnas.1002418107
120. Kravitz A V., Freeze BS, Parker PRL, et al. Regulation of parkinsonian motor behaviours by optogenetic control of basal ganglia circuitry. *Nature*. 2010;466(7306):622-626. doi:10.1038/nature09159
121. Berndt A, Yizhar O, Gunaydin LA, Hegemann P, Deisseroth K. Bi-stable neural state switches. *Nat Neurosci*. 2009;12(2):229-234. doi:10.1038/nn.2247
122. Gunaydin LA, Yizhar O, Berndt A, Sohal VS, Deisseroth K, Hegemann P. Ultrafast optogenetic control. *Nat Neurosci*. 2010;13(3):387-392. doi:10.1038/nn.2495
123. Cardin JA, Carlén M, Meletis K, et al. Targeted optogenetic stimulation and recording of neurons in vivo using cell-type-specific expression of Channelrhodopsin-2. *Nat Protoc*. 2010;5(2):247-254. doi:10.1038/nprot.2009.228
124. Cruikshank SJ, Urabe H, Nurmikko A V., Connors BW. Pathway-Specific Feedforward Circuits between Thalamus and Neocortex Revealed by Selective Optical Stimulation of Axons. *Neuron*. 2010;65(2):230-245. doi:10.1016/j.neuron.2009.12.025
125. Petreanu L, Mao T, Sternson SM, Svoboda K. The subcellular organization of neocortical excitatory connections. *Nature*. 2009;457(7233):1142-1145. doi:10.1038/nature07709
126. Adesnik H, Scanziani M. Lateral competition for cortical space by layer-specific horizontal circuits. *Nature*. 2010;464(7292):1155-1160. doi:10.1038/nature08935
127. Grubb MS, Burrone J. Activity-dependent relocation of the axon initial segment fine-tunes neuronal excitability. *Nature*. 2010;465(7301):1070-1074. doi:10.1038/nature09160
128. Adamantidis AR, Zhang F, Aravanis AM, Deisseroth K, De Lecea L. Neural substrates of awakening probed with optogenetic control of hypocretin neurons. *Nature*. 2007;450(7168):420-424. doi:10.1038/nature06310
129. Aravanis AM, Wang LP, Zhang F, et al. An optical neural interface: in vivo control of rodent motor cortex with integrated fiberoptic and optogenetic technology. *J Neural Eng*. 2007;4(3). doi:10.1088/1741-2560/4/3/S02
130. Zhang F, Gradinaru V, Adamantidis AR, et al. Optogenetic interrogation of neural circuits: Technology for probing mammalian brain structures. *Nat Protoc*. 2010;5(3):439-456. doi:10.1038/nprot.2009.226
131. Hockberger PE, Skimina TA, Centonze VE, et al. Activation of flavin-containing oxidases underlies light-induced production of H2O2 in mammalian cells. *Proc Natl Acad Sci U S A*. 1999;96(11):6255-6260. doi:10.1073/pnas.96.11.6255
132. Pasek J, Pasek T, Sieroń-Stołtny K, Cieślar G, Sieroń A. Electromagnetic fields in medicine – The state of art. *Electromagn Biol Med*. 2016;35(2):170-175. doi:10.3109/15368378.2015.1048549

133. Wiltschko W, Wiltschko R. Magnetic orientation and magnetoreception in birds and other animals. *J Comp Physiol A Neuroethol Sensory, Neural, Behav Physiol*. 2005;191(8):675-693. doi:10.1007/s00359-005-0627-7
134. Eder SHK, Cadiou H, Muhamad A, McNaughton PA, Kirschvink JL, Winklhofer M. Magnetic characterization of isolated candidate vertebrate magnetoreceptor cells. *Proc Natl Acad Sci U S A*. 2012;109(30):12022-12027. doi:10.1073/pnas.1205653109
135. C. Knight L, E. Romano J, Krynska B, Faro S, B. Mohamed F. Binding and Internalization of Iron Oxide Nanoparticles Targeted To Nuclear Oncoprotein. *J Mol Biomark Diagn*. 2010;01(01):1-15. doi:10.4172/2155-9929.1000102
136. Stanley SA, Sauer J, Kane RS, Dordick JS, Friedman JM. Remote regulation of glucose homeostasis in mice using genetically encoded nanoparticles. *Nat Med*. 2015;21(1):92-98. doi:10.1038/nm.3730
137. Suppiramaniam V, Abdel-Rahman EA, Buabeid MA, Parameshwaran K. Ion Channels. *Compr Toxicol Second Ed*. 2010;13(November):129-171. doi:10.1016/B978-0-08-046884-6.01310-5
138. Tatur J, Hagedoorn PL, Overeijnder ML, Hagen WR. A highly thermostable ferritin from the hyperthermophilic archaeal anaerobe Pyrococcus furiosus. *Extremophiles*. 2006;10(2):139-148. doi:10.1007/s00792-005-0484-x
139. Barinov NA, Prokhorov V V., Dubrovin E V., Klinov D V. AFM visualization at a single-molecule level of denaturated states of proteins on graphite. *Colloids Surfaces B Biointerfaces*. 2016;146:777-784. doi:10.1016/j.colsurfb.2016.07.014
140. Tatur J, Hagen WR, Matias PM. Crystal structure of the ferritin from the hyperthermophilic archaeal anaerobe Pyrococcus furiosus. *J Biol Inorg Chem*. 2007;12(5):615-630. doi:10.1007/s00775-007-0212-3
141. Nieto G. © 1978 Nature Publishing Group - Unknown - 1978.pdf. 2012;33:23-33.
142. Gerl M, Jaenicke R. Mechanism of the self-assembly of apoferritin from horse spleen - Cross-linking and spectroscopic analysis. *Eur Biophys J*. 1987;15(2):103-109. doi:10.1007/BF00257503
143. Stefanini S, Vecchini P, Chiancone E. On the Mechanism of Horse Spleen Apoferritin Assembly: A Sedimentation Velocity and Circular Dichroism Study. *Biochemistry*. 1987;26(7):1831-1837. doi:10.1021/bi00381a007
144. Ferguson WJ, Braunschweiger KI, Braunschweiger WR, et al. Hydrogen ion buffers for biological research. *Anal Biochem*. 1980;104(2):300-310. doi:10.1016/0003-2697(80)90079-2
145. Good NE, Izawa S. Hydrogen Ion Buffers. *Methods Enzymol*. 1972;24(C):53-68. doi:10.1016/0076-6879(72)24054-X
146. Zhen Z, Tang W, Todd T, Xie J. Ferritins as nanoplatforms for imaging and drug delivery. *Expert Opin Drug Deliv*. 2014;11(12):1913-1922. doi:10.1517/17425247.2014.941354
147. De Turris V, Cardoso Trabuco M, Peruzzi G, et al. Humanized archaeal ferritin as a tool for cell targeted delivery. *Nanoscale*. 2017;9(2):647-655. doi:10.1039/c6nr07129e
148. Xu D, Watt GD, Harb JN, Davis RC. Electrical conductivity of ferritin proteins by conductive AFM. *Nano Lett*. 2005;5(4):571-577. doi:10.1021/nl048218x
149. Rakshit T. Differentiating Holo-and Apoferritin on Surface by Atomic Force Microscopy Approach. 2016;(January 2015).
150. Ohnishi S, Hara M, Furuno T, Okada T, Sasabe H. Direct visualization of polypeptide shell of ferritin molecule by atomic force microscopy. *Biophys J*. 1993;65(2):573-577. doi:10.1016/S0006-3495(93)81125-1
151. Satriano C, Svedhem S, Kasemo B. Well-defined lipid interfaces for protein adsorption studies. *Phys Chem Chem Phys*. 2012;14(48):16695-16698. doi:10.1039/c2cp43254d

152. Daniels SL, Ngunjiri JN, Garno JC. Investigation of the magnetic properties of ferritin by AFM imaging with magnetic sample modulation. *Anal Bioanal Chem*. 2009;394(1):215-223. doi:10.1007/s00216-009-2618-y
153. Stühn L, Auernhammer J, Dietz C. pH-depended protein shell dis- and reassembly of ferritin nanoparticles revealed by atomic force microscopy. *Sci Rep*. 2019;9(1):1-9. doi:10.1038/s41598-019-53943-3
154. Hernández-Morales M, Shang T, Chen J, Han V, Liu C. Lipid Oxidation Induced by RF Waves and Mediated by Ferritin Iron Causes Activation of Ferritin-Tagged Ion Channels. *Cell Rep*. 2020;30(10):3250-3260.e7. doi:10.1016/j.celrep.2020.02.070
155. Chaganti LK, Venkatakrishnan N, Bose K. An efficient method for FITC labelling of proteins using tandem affinity purification. *Biosci Rep*. 2018;38(6):1-8. doi:10.1042/BSR20181764
156. Carmona F, Palacios Ò, Gálvez N, et al. Ferritin iron uptake and release in the presence of metals and metalloproteins: Chemical implications in the brain. *Coord Chem Rev*. 2013;257(19-20):2752-2764. doi:10.1016/j.ccr.2013.03.034
157. Jain N, Kumar A, Chauhan S, Chauhan SMS. Chemical and biochemical transformations in ionic liquids. *Tetrahedron*. 2005;61(5):1015-1060. doi:10.1016/j.tet.2004.10.070
158. Hallett JP, Welton T. Room-Temperature Ionic Liquids: Solvents for Synthesis and Catalysis. 2. *Chem Rev*. 2011;111(5):3508-3576. doi:10.1021/cr1003248
159. Cull SG, Holbrey JD, Vargas-Mora V, Seddon KR, Lye GJ. Room-temperature ionic liquids as replacements for organic solvents in multiphase bioprocess operations. *Biotechnol Bioeng*. 2000;69(2):227-233. doi:10.1002/(SICI)1097-0290(20000720)69:2<227::AID-BIT12>3.0.CO;2-0
160. Romero A, Santos A, Tojo J, Rodríguez A. Toxicity and biodegradability of imidazolium ionic liquids. *J Hazard Mater*. 2008;151(1):268-273. doi:10.1016/j.jhazmat.2007.10.079
161. Lee H, Jeonb TJ. The binding and insertion of imidazolium-based ionic surfactants into lipid bilayers: The effects of the surfactant size and salt concentration. *Phys Chem Chem Phys*. 2015;17(8):5725-5733. doi:10.1039/c4cp05537c
162. Bingham RJ, Ballone P. Computational study of room-temperature ionic liquids interacting with a POPC phospholipid bilayer. *J Phys Chem B*. 2012;116(36):11205-11216. doi:10.1021/jp306126q
163. Benedetto A, Heinrich F, Gonzalez MA, Fragneto G, Watkins E, Ballone P. Structure and stability of phospholipid bilayers hydrated by a room-temperature ionic liquid/water solution: A neutron reflectometry study. *J Phys Chem B*. 2014;118(42):12192-12206. doi:10.1021/jp507631h
164. Gower CN, Garrott RA, White PJ, Cherry S, Yoccoz NG. Chapter 19 Elk Group Size and Wolf Predation. 2008;8(24):401-422. doi:10.1016/s1936-7961(08)00219-4
165. Vandenberg ET, Bertilsson L, Liedberg B, et al. Structure of 3-aminopropyl triethoxy silane on silicon oxide. *J Colloid Interface Sci*. 1991;147(1):103-118. doi:10.1016/0021-9797(91)90139-Y
166. Parisio G, Marini A, Biancardi A, Ferrarini A, Mennucci B. Polarity-sensitive fluorescent probes in lipid bilayers: Bridging spectroscopic behavior and microenvironment properties. *J Phys Chem B*. 2011;115(33):9980-9989. doi:10.1021/jp205163w
167. Signore G, Nifosì R, Albertazzi L, Bizzarri R. A novel coumarin fluorescent sensor to probe polarity around biomolecules. *J Biomed Nanotechnol*. 2009;5(6):722-729. doi:10.1166/jbn.2009.1089
168. Klymchenko AS. Solvatochromic and Fluorogenic Dyes as Environment-Sensitive Probes: Design and Biological Applications. *Acc Chem Res*. 2017;50(2):366-375. doi:10.1021/acs.accounts.6b00517

169. Bureš F. Fundamental aspects of property tuning in push-pull molecules. *RSC Adv*. 2014;4(102):58826-58851. doi:10.1039/c4ra11264d
170. Dell'Acqua M, Ronda L, Piano R, et al. MediaChrom: Discovering a Class of Pyrimidoindolone-Based Polarity-Sensitive Dyes. *J Org Chem*. 2015;80(21):10939-10954. doi:10.1021/acs.joc.5b02066
171. Pirovano V, Marchetti M, Carbonaro J, et al. Synthesis and photophysical properties of isocoumarin-based D-π-A systems. *Dye Pigment*. 2020;173(September 2019):107917. doi:10.1016/j.dyepig.2019.107917
172. Arcadi A, Abbiati G, Rossi E. Tandem imination/annulation of γ- And δ-ketoalkynes in the presence of ammonia/amines. *J Organomet Chem*. 2011;696(1):87-98. doi:10.1016/j.jorganchem.2010.08.011
173. Dell'Acqua M, Pirovano V, Confalonieri G, Arcadi A, Rossi E, Abbiati G. Synthesis of 3-benzylisoquinolines by domino imination/cycloisomerisation of 2-propargylbenzaldehydes. *Org Biomol Chem*. 2014;12(40):8019-8030. doi:10.1039/c4ob01583e
174. Dell'Acqua M, Abbiati G, Arcadi A, Rossi E. Silver-catalysed intramolecular cyclisation of 2-alkynylacetophenones and 3-acetyl-2-alkynylpyridines in the presence of ammonia. *Org Biomol Chem*. 2011;9(22):7836-7848. doi:10.1039/c1ob06271a
175. Alfonsi M, Dell'Acqua M, Facoetti D, Arcadi A, Abbiati G, Rossi E. Microwave-promoted synthesis of N-heterocycles by tandem imination/ annulation of γ- and δ-ketoalkynes in the presence of ammonia. *European J Org Chem*. 2009;(17):2852-2862. doi:10.1002/ejoc.200900014
176. Dellacqua M, Abbiati G, Rossi E. Palladium-catalyzed, microwave-enhanced three-component synthesis of isoquinolines with aqueous ammonia. *Synlett*. 2010;(17):2672-2676. doi:10.1055/s-0030-1258571
177. Balewski Ł, Sa¸czewski F, Gdaniec M, Kornicka A, Cicha K, Jalińska A. Synthesis and fluorescent properties of novel isoquinoline derivatives. *Molecules*. 2019;24(22). doi:10.3390/molecules24224070
178. Balog J, Riedl Z, Hajós G, Miskolczy Z, Biczók L. Novel fluorescent isoquinoline derivatives obtained via Buchwald-Hartwig coupling of isoquinolin-3-amines. *Arkivoc*. 2012;2012(5):109-119. doi:10.3998/ark.5550190.0013.511
179. Balog J, Riedl Z, Hajós G, Miskolczy Z, Biczók L. New fluorescent isoquinoline derivatives. *Tetrahedron Lett*. 2011;52(41):5264-5266. doi:10.1016/j.tetlet.2011.07.143
180. Wan Y, Niu W, Behof WJ, Wang Y, Boyle P, Gorman CB. Aminoisoquinolines as colorimetric Hg2+ sensors: the importance of molecular structure and sacrificial base. *Tetrahedron*. 2009;65(22):4293-4297. doi:10.1016/j.tet.2009.03.063
181. Wei CY, Yu WS, Chou PT, Hung FT, Chang CP, Lin TC. Conjugated dual hydrogen-bond mediating proton-transfer reaction in 3-hydroxyisoquinoline. *J Phys Chem B*. 1998;102(6):1053-1064. doi:10.1021/jp973173s
182. Gomez Pinheiro GE, Ihmels H, Dohmen C. Mild Synthesis of Fluorosolvatochromic and Acidochromic 3-Hydroxy-4-pyridylisoquinoline Derivatives from Easily Available Substrates. *J Org Chem*. 2019;84(5):3011-3016. doi:10.1021/acs.joc.8b03272
183. Chen DG, Ranganathan R, Lin JA, et al. Ratiometric tuning of luminescence: interplay between the locally excited and interligand charge-transfer states in pyrazolate-based boron compounds. *J Phys Chem C*. 2019;123(7):4022-4028. doi:10.1021/acs.jpcc.8b11100
184. Ibrahim Mohamed Allaoui Z, le Gall E, Fihey A, et al. Push–Pull (Iso)quinoline Chromophores: Synthesis, Photophysical Properties, and Use for White-Light Emission. *Chem - A Eur J*. 2020;26(36):8153-8161. doi:10.1002/chem.202000817
185. Jones G, Jackson WR, Choi CY, Bergmark WR. Solvent effects on emission yield and lifetime

for coumarin laser dyes. Requirements for a rotatory decay mechanism. *J Phys Chem*. 1985;89(2):294-300. doi:10.1021/j100248a024
186. Weusmann J, Mahmoodi B, Kordsmeyer K, Azaripour A, Walter C, Willershausen B. Die zahnärztliche selektive Intensivprophylaxe in Rheinland-Pfalz: Untersuchungen an Erstklässlern im Schuljahr 2013/2014. *Gesundheitswesen*. 2017;79(4):247-251. doi:10.1055/s-0042-108582
187. Chinchilla R, Nájera C. The Sonogashira reaction: A booming methodology in synthetic organic chemistry. *Chem Rev*. 2007;107(3):874-922. doi:10.1021/cr050992x
188. Klymchenko AS. Solvatochromic fluorescent dyes research. 2012:1-7.
189. Klymchenko AS, Mely Y. *Fluorescent Environment-Sensitive Dyes as Reporters of Biomolecular Interactions*. Vol 113. 1st ed. Elsevier Inc.; 2013. doi:10.1016/B978-0-12-386932-6.00002-8
190. Hashmi ASK, Toste FD. Modern Gold Catalyzed Synthesis. *Mod Gold Catalyzed Synth*. 2012. doi:10.1002/9783527646869
191. Lee YC, Kumar K, Waldmann H. Ligand-Directed Divergent Synthesis of Carbo- and Heterocyclic Ring Systems. *Angew Chemie - Int Ed*. 2018;57(19):5212-5226. doi:10.1002/anie.201710247
192. Asiri AM, Hashmi ASK. Gold-catalysed reactions of diynes. *Chem Soc Rev*. 2016;45(16):4471-4503. doi:10.1039/c6cs00023a
193. Wagner B, Belger K, Minkler S, Belting V, Krause N. Sustainable gold catalysis: Synthesis of new spiroacetals. *Pure Appl Chem*. 2016;88(4):391-399. doi:10.1515/pac-2016-0406
194. Dorel R, Echavarren AM. Gold(I)-Catalyzed Activation of Alkynes for the Construction of Molecular Complexity. *Chem Rev*. 2015;115(17):9028-9072. doi:10.1021/cr500691k
195. Fang W, Shi M. Recent Advances in the Cycloisomerizations of Methylenecyclopropanes using Gold Catalysis. *Chem - A Eur J*. 2018;24(40):9998-10005. doi:10.1002/chem.201705788
196. Fürstner A. Gold Catalysis for Heterocyclic Chemistry: A Representative Case Study on Pyrone Natural Products. *Angew Chemie - Int Ed*. 2018;57(16):4215-4233. doi:10.1002/anie.201707260
197. Quach R, Furkert DP, Brimble MA. Gold catalysis: synthesis of spiro, bridged, and fused ketal natural products. *Org Biomol Chem*. 2017;15(15):3098-3104. doi:10.1039/C7OB00496F
198. Wang Q, Shi M. Synthesis of Cyclic and Heterocyclic Compounds via Gold-Catalyzed Reactions. *Synlett*. 2017;28(17):2230-2240. doi:10.1055/s-0036-1590827
199. Pirovano V, Brambilla E, Rizzato S, Abbiati G, Bozzi M, Rossi E. Gold-Catalyzed Cascade Reactions of 4 H-Furo[3,2-b]indoles with Allenamides: Synthesis of Indolin-3-one Derivatives. *J Org Chem*. 2019;84(9):5150-5166. doi:10.1021/acs.joc.9b00143
200. Leb D, Gaydou M, Echavarren AM. ORGANIC CHEMISTRY FRONTIERS furans by related mechanisms †‡. 2014:759-764. doi:10.1039/c4qo00130c
201. Wang S. Transition metal-catalyzed reactions of propargylic carboxylates via an initial 1,2-acyloxy migration. *Tetrahedron Lett*. 2018;59(14):1317-1327. doi:10.1016/j.tetlet.2018.02.054
202. García-Morales C, Pei XL, Sarria Toro JM, Echavarren AM. Direct Observation of Aryl Gold(I) Carbenes that Undergo Cyclopropanation, C−H Insertion, and Dimerization Reactions. *Angew Chemie - Int Ed*. 2019;58(12):3957-3961. doi:10.1002/anie.201814577
203. Harris RJ, Widenhoefer RA. Gold carbenes, gold-stabilized carbocations, and cationic intermediates relevant to gold-catalysed enyne cycloaddition. *Chem Soc Rev*. 2016;45(16):4533-4551. doi:10.1039/c6cs00171h
204. Wang Y, Muratore ME, Echavarren AM. Gold carbene or carbenoid: Is there a difference?

Chem - A Eur J. 2015;21(20):7332-7339. doi:10.1002/chem.201406318
205. Shi X, Gorin DJ, Toste FD. Synthesis of 2-cyclopentenones by gold(I)-catalyzed rautenstrauch rearrangement. *J Am Chem Soc*. 2005;127(16):5802-5803. doi:10.1021/ja051689g
206. Mascarenas JL, Varela I, López F. Allenes and derivatives in gold(I)- And platinum(II)-catalyzed formal cycloadditions. *Acc Chem Res*. 2019;52(2):465-479. doi:10.1021/acs.accounts.8b00567
207. Zhao J, Yang S, Xie X, Li X, Liu Y. Ligand-Effect in Gold(I)-Catalyzed Rautenstrauch Rearrangement: Regio- and Stereoselective Synthesis of Bicyclo[3.2.1]octa-3,6-dienes through Cyclodimerization of 1-Ethynyl-2-propenyl Esters. *J Org Chem*. 2018;83(3):1287-1297. doi:10.1021/acs.joc.7b02816
208. Mathiew M, Tan JK, Chan PWH. Gold-Catalyzed Double Cycloisomerization of 1-Ene-4,10-diynyl Esters to Bicyclo[6.3.0]undeca-2,4,9-trienyl Esters. *Angew Chemie - Int Ed*. 2018;57(43):14235-14239. doi:10.1002/anie.201809376
209. Chen X, Day DP, Teo WT, Chan PWH. Gold- and Brønsted Acid-Catalyzed Cycloisomerization of 1,8-Diynyl Vinyl Acetates to Bicyclo[2.2.1]hept-2-en-7-ones. *Org Lett*. 2016;18(22):5936-5939. doi:10.1021/acs.orglett.6b03049
210. Bürki C, Whyte A, Arndt S, Hashmi ASK, Lautens M. Expanding the Scope of the Gold(I)-Catalyzed Rautenstrauch Rearrangement: Protic Additives. *Org Lett*. 2016;18(19):5058-5061. doi:10.1021/acs.orglett.6b02505
211. Qiana D, Zhang J. Gold-catalyzed cyclopropanation reactions using a carbenoid precursor toolbox. *Chem Soc Rev*. 2015;44(3):677-698. doi:10.1039/c4cs00304g
212. Trushkov I V., Uchuskin MG, Butin A V. Furan's gambit: Electrophile-attack-triggered sacrifice of furan rings for the intramolecular construction of azaheterocycles. *European J Org Chem*. 2015;2015(14):2999-3016. doi:10.1002/ejoc.201403580
213. Kaïm L El, Grimaud L, Wagschal S. Palladium catalyzed ring opening of furans as a route to α,β-unsaturated aldehydes. *Chem Commun*. 2011;47(6):1887-1889. doi:10.1039/c0cc04164e
214. Alves AJS, Lopes SMM, Henriques MSC, Paixão JA, Pinho e Melo TMVD. Hetero-Diels–Alder and Ring-Opening Reactions of Furans Applied to the Synthesis of Functionalized Heterocycles. *European J Org Chem*. 2017;2017(27):4011-4025. doi:10.1002/ejoc.201700453
215. Rao W, Sally, Berry SN, Chan PWH. Gold-Catalyzed Cycloisomerization of 1,6,8-Dienyne Carbonates and Esters to cis-Cyclohepta-4,8-diene-Fused Pyrrolidines. *Chem - A Eur J*. 2014;20(41):13174-13180. doi:10.1002/chem.201402500
216. Matsumoto A, Yoshida M, Simamura O, et al. l ...;,.., Jl ' Tittll. 2009;(9):1171-1176.
217. Flitsch W, Jones RA, Hohenhorst M. 3a-Azaazulenones containing a carbonyl group in the 5-membered ring. *Tetrahedron Lett*. 1987;28(38):4397-4398. doi:10.1016/S0040-4039(00)96520-1
218. Abaev VT, Plieva AT, Chalikidi PN, Uchuskin MG, Trushkov I V., Butin A V. A simple route to polysubstituted indoles exploiting azide induced furan ring opening. *Org Lett*. 2014;16(16):4150-4153. doi:10.1021/ol5018504
219. Yin B, Cai C, Zeng G, Zhang R, Li X, Jiang H. A novel entry to functionalized benzofurans and indoles via palladium(0)-catalyzed arylative dearomatization of furans. *Org Lett*. 2012;14(4):1098-1101. doi:10.1021/ol300008d
220. Butin A V., Uchuskin MG, Pilipenko AS, Tsiunchik FA, Cheshkov DA, Trushkov I V. Furan ring-opening/indole ring-closure: Pictet-spengler-like reaction of 2-(o-aminophenyl)furans with aldehydes. *European J Org Chem*. 2010;(5):920-926. doi:10.1002/ejoc.200901241
221. Yamamura K, Kawabata S, Kimura T, Eda K, Hashimoto M. Novel synthesis of benzalacetone

analogues of naphth[a]azulenes by intramolecular tropylium ion-mediated furan ring-opening reaction and X-ray investigation of a naphth[1,2-a]azulene derivative. *J Org Chem*. 2005;70(22):8902-8906. doi:10.1021/jo051409f
222. Chen Y, Li G, Liu Y. Gold-catalyzed cascade friedel-crafts/furan-yne cyclization/heteroenyne metathesis for the highly efficient construction of phenanthrene derivatives. *Adv Synth Catal*. 2011;353(2-3):392-400. doi:10.1002/adsc.201000644
223. Brambilla E, Pirovano V, Giannangeli M, Abbiati G, Caselli A, Rossi E. Gold-catalyzed cascade reactions of 4: H -furo[3,2- b] indoles with propargyl esters: Synthesis of 2-alkenylidene-3-oxoindolines. *Org Chem Front*. 2019;6(17):3078-3084. doi:10.1039/c9qo00647h
224. Castano B, Pedrazzini T, Sisti M, et al. Henry reaction catalyzed by copper(I) complexes of a new pyridine-containing macrocyclic ligand. *Appl Organomet Chem*. 2011;25(11):824-829. doi:10.1002/aoc.1846
225. Rodríguez AM, Molina F, Díaz-Requejo MM, Pérez PJ. Copper-Catalyzed Selective Pyrrole Functionalization by Carbene Transfer Reaction. *Adv Synth Catal*. 2020;362(10):1998-2004. doi:10.1002/adsc.201901629
226. Caballero A, Díaz-Requejo MM, Trofimenko S, Belderrain TR, Pérez PJ. Copper-Catalyzed Addition of Ethyl Diazoacetate to Furans : An Alternative to Dirhodium (II) Tetraacetate The reaction of furan and diazo compounds has been known for decades since the first report of copper salts diene being obtained as the major produ. *J Org Chem*. 2005;70(Ii):6101-6104.
227. Salomon RG, Kochi JK. Copper(I) Catalysis in Cyclopropanations with Diazo Compounds. The Role of Olefin Coordination. *J Am Chem Soc*. 1973;95(10):3300-3310. doi:10.1021/ja00791a038
228. Castano B, Gallo E, Cole-Hamilton DJ, Dal Santo V, Psaro R, Caselli A. Continuous flow asymmetric cyclopropanation reactions using Cu(i) complexes of Pc-L* ligands supported on silica as catalysts with carbon dioxide as a carrier. *Green Chem*. 2014;16(6):3202-3209. doi:10.1039/c4gc00119b
229. Castano B, Guidone S, Gallo E, et al. Asymmetric cyclopropanation of olefins catalysed by Cu(i) complexes of chiral pyridine-containing macrocyclic ligands (Pc-L*). *Dalt Trans*. 2013;42(7):2451-2462. doi:10.1039/c2dt32347h
230. Castano B, Zardi P, Hönemann YC, et al. Silica “sHB” chiral Pc-L* copper complexes for halogen-free solvent cyclopropanation reactions. *RSC Adv*. 2013;3(44):22199-22205. doi:10.1039/c3ra44806a
231. Caselli A, Cesana F, Gallo E, et al. Designing new ligands: Asymmetric cyclopropanation by Cu(I) complexes based on functionalised pyridine-containing macrocyclic ligands. *Dalt Trans*. 2008;(32):4202-4205. doi:10.1039/b809317m
232. Tseberlidis G, Caselli A, Vicente R. Carbene X[sbnd]H bond insertions catalyzed by copper(I) macrocyclic pyridine-containing ligand (PcL) complexes. *J Organomet Chem*. 2017;835(I):1-5. doi:10.1016/j.jorganchem.2017.02.027
233. Pirovano V, Brambilla E, Tseberlidis G. [Copper(I)(Pyridine-Containing Ligand)] Catalyzed Regio- and Steroselective Synthesis of 2-Vinylcyclopropa[b]indolines from 2-Vinylindoles. *Org Lett*. 2018;20(2):405-408. doi:10.1021/acs.orglett.7b03704
234. H. Wee A. Rhodium(II)-Catalyzed Reaction of Diazocompounds in the Service of Organic Synthesis of Natural and Non-Natural Products. *Curr Org Synth*. 2006;3(4):499-555. doi:10.2174/157017906778699512
235. Grirrane A, Álvarez E, García H, Corma A. Double A3-Coupling of Primary Amines Catalysed by Gold Complexes. *Chem - A Eur J*. 2018;24(61):16356-16367. doi:10.1002/chem.201803020

236. Zhang Z, Wang J. Recent studies on the reactions of α-diazocarbonyl compounds. *Tetrahedron*. 2008;64(28):6577-6605. doi:10.1016/j.tet.2008.04.074
237. Dalton LR, Sullivan PA, Bale DH. Electric field poled organic electro-optic materials: State of the art and future prospects. *Chem Rev*. 2010;110(1):25-55. doi:10.1021/cr9000429
238. Colombo A, Dragonetti C, Guerchais V, Hierlinger C, Zysman-Colman E, Roberto D. A trip in the nonlinear optical properties of iridium complexes. *Coord Chem Rev*. 2020;414:213293. doi:10.1016/j.ccr.2020.213293
239. Kanis DR, Ratner MA, Marks TJ. Design and Construction of Molecular Assemblies with Large Second-Order Optical Nonlinearities. Quantum Chemical Aspects. *Chem Rev*. 1994;94(1):195-242. doi:10.1021/cr00025a007
240. Tessore F, Roberto D, Ugo R, et al. Acetate by Triflate **. 2003;(4):456-459.
241. Beverina L, Ruffo R, Patriarca G, et al. Second harmonic generation in nonsymmetrical squaraines: Tuning of the directional charge transfer character in highly delocalized dyes. *J Mater Chem*. 2009;19(43):8190-8197. doi:10.1039/b914716k
242. Cariati E, Dragonetti C, Lucenti E, et al. An acido-triggered reversible luminescent and nonlinear optical switch based on a substituted styrylpyridine: EFISH measurements as an unusual method to reveal a protonation-deprotonation NLO contrast. *Chem Commun*. 2014;50(13):1608-1610. doi:10.1039/c3cc48149b
243. Ledoux I, Zyss J. Influence of the molecular environment in solution measurements of the Second-order optical susceptibility for urea and derivatives. *Chem Phys*. 1982;73(1-2):203-213. doi:10.1016/0301-0104(82)85161-6
244. Levine BF, Bethea CG. Molecular hyperpolarizabilities determined from conjugated and nonconjugated organic liquids. *Appl Phys Lett*. 1974;24(9):445-447. doi:10.1063/1.1655254
245. Levine BF, Bethea CG. Second and third order hyperpolarizabilities of organic molecules. *J Chem Phys*. 1975;63(6):2666-2682. doi:10.1063/1.431660
246. Rossi E, Colombo A, Dragonetti C, et al. Tuning the dipolar second-order nonlinear optical properties of cyclometalated platinum(II) complexes with tridentate N^C^N binding ligands. *Chem - A Eur J*. 2013;19(30):9875-9883. doi:10.1002/chem.201301131
247. Oudar JL. Optical nonlinearities of conjugated molecules. Stilbene derivatives and highly polar aromatic compounds. *J Chem Phys*. 1977;67(2):446-457. doi:10.1063/1.434888
248. Singer KD, Katz HE, Dirk CW, Sohn JE, King LA, Gordon HM. Second-order nonlinear-optical properties of donor- and acceptor-substituted aromatic compounds. *J Opt Soc Am B*. 1989;6(7):1339. doi:10.1364/josab.6.001339
249. Kirmse W. Kurzaufsätze Kupfer-Carben-Komplexe : hochentwickelte. *Angew Chemie*. 2003;(10):1120-1125.
250. Foust KD, Kaspar BK. An overview of GFR testing in dogs and cats. *Vet J*. 2011;188(2):156-165. doi:10.1021/la203638g.How
251. Puricelli L, Galluzzi M, Schulte C, Podestà A, Milani P. Nanomechanical and topographical imaging of living cells by atomic force microscopy with colloidal probes. *Rev Sci Instrum*. 2015;86(3). doi:10.1063/1.4915896
252. Gandon V. Modern Gold Catalyzed Synthesis. Edited by A. Stephen K. Hashmi and F. Dean Toste. *Angew Chemie Int Ed*. 2012;51(45):11200-11200. doi:10.1002/anie.201207733
253. Pirovano V, Caselli A, Colombo A, et al. Synthesis of 2-alkenylidene-3-oxoindolines: cascade reactions of 4H-furo [3,2-b]indoles with diazoacetates catalyzed by a Cu(I) macrocyclic pyridine-containing ligand (PcL) complex. *ChemCatChem*. 2020;12(20):5250-5255. doi:10.1002/cctc.202000887
254. Yang W, Hashmi ASK. Mechanistic insights into the gold chemistry of allenes. *Chem Soc Rev*. 2014;43(9):2941-2955. doi:10.1039/c3cs60441a

255. Pan F, Shu C, Ye LW. Recent progress towards gold-catalyzed synthesis of N-containing tricyclic compounds based on ynamides. *Org Biomol Chem*. 2016;14(40):9456-9465. doi:10.1039/c6ob01774f
256. Blanc A, Bénéteau V, Weibel JM, Pale P. Silver & gold-catalyzed routes to furans and benzofurans. *Org Biomol Chem*. 2016;14(39):9184-9205. doi:10.1039/c6ob01468b
257. Zhang Y, Luo T, Yang Z. Strategic innovation in the total synthesis of complex natural products using gold catalysis. *Nat Prod Rep*. 2014;31(4):489-503. doi:10.1039/c3np70075e
258. Rossi E, Abbiati G, Pirovano V. 2- and 3-Vinylindoles as 4π Components in Cycloaddition Reactions. *European J Org Chem*. 2017;2017(31):4512-4529. doi:10.1002/ejoc.201700120
259. Pirovano V. Gold-Catalyzed Functionalization Reactions of Indole. *European J Org Chem*. 2018;2018(17):1925-1945. doi:10.1002/ejoc.201800125
260. Pirovano V, Borri M, Abbiati G, Rizzato S, Rossi E. Gold(I)-Catalyzed Enantioselective Synthesis of Tetrahydrocarbazoles through Dearomative [4+2] Cycloadditions of 3/2-Substituted 2/3-Vinylindoles. *Adv Synth Catal*. 2017;359(11):1912-1918. doi:10.1002/adsc.201700280
261. Pirovano V, Negrato M, Abbiati G, Dell'Acqua M, Rossi E. Gold-Catalyzed cis-Hydroarylation of Ynamides with Indoles: Regio- and Stereoselective Synthesis of a Class of 2-Vinylindoles. *Org Lett*. 2016;18(19):4798-4801. doi:10.1021/acs.orglett.6b02189
262. Rossi E, Abbiati G, Dell'Acqua M, Negrato M, Paganoni A, Pirovano V. Exploiting the σ-phylic properties of cationic gold(i) catalysts in the ring opening reactions of aziridines with indoles. *Org Biomol Chem*. 2016;14(25):6095-6110. doi:10.1039/c6ob00672h